Polymeric microfibers mimicking hair cell like sensors fabrication
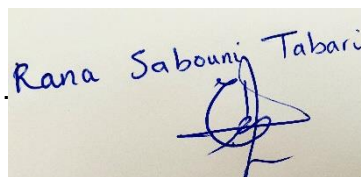
Submitted by **Rana Sabouni Tabari** to the University of Exeter

As a thesis for the degree of

Doctor of Philosophy in Engineering

In July 2022

I certify that all material in this thesis which is not my own work has been identified and that no material has previously been submitted and approved for the award of a degree by this or any other University.

Signature: …………… Rana Sabouni Tabari ………………………..

Abstract

In mammals, hair cell loss due to acoustic over-stimulation, ototoxic drugs, ageing, and genetic defects is irreversible, leading to a permanent loss of function. Any loss occurred in cochlea hair cells can lead to an unavoidable loss in hearing. Tiny nerves called 'hair cells' are hit with sound so hard that the hair cells are bent, broken, and sometimes sheared off. Hair cells in the cochlea are not capable of regenerating themselves. Dissimilar to skin, hair and other cells in the body, once cochlear damage happens, no "growing" is available. The natural hair cell includes pillars in different heights which are connected with tip-links on top. The main role of hair cells is the conversion of acoustic signal to electrical ones which is exactly the piezoelectric materials functionality performance.

For the purpose of mimicking the artificial hair cell like sensors like a prototype, this research fabricated and tested an acoustic prototype device including two main parts. The base part is required be flexible and stable. On top of the based structure, there must be a thin sheet of piezoelectric structure capable of mimicking the tip-links role.

Firstly, this thesis presents how to fabricate a semi-permanent designed negative photoresist SU-8 mould to work as a template for peeling up the cured and formed Polydimethylsiloxane (PDMS) pillars in microscale. Secondly, to get the same function of tip-links in the hair cells, Polyvinylidene fluoride (PVDF) nanofibers are fabricated which is an important part of the main hair cell structure. Thirdly, electrospinning is applied to achieve piezoelectric electrospun nanofibers. Fourthly, the behavior of 5 different additives by reason of their biocompatibility and possibility of presenting different properties on the produced PVDF composites will be evaluated. Finally, the thesis will evaluate the prototype performance based on acoustic sensing experiments. The main findings are as follows:

- Successfully synthesized a semi-permanent SU-8 molud in microscale using UV-lithography and achieved a triangular mould including 4 rows of exposed holes at different depths. A series of preparations steps is needed following

Abstract

up the fabrication processes to get the best geometrical structure of the semi-permanent SU-8 mould.

- The fabrication of PDMS pillars of different heights starting from 100 µm for the first row to 400 µm in the fourth row with an increment of 100 µm and the diameter of almost 50 µm for each single pillar was done. The PDMS solution contains two agents a 10:1 mixture of PDMS elastomer (Sylgard 184) to cross-linker which is combined and mixed well.

- Conducted electrospinning method to achieve the phase transition of PVDF material from α and γ phases to β-phase due to the mechanically drawing fabrication process. The pure PVDF powder is compared with pure electrospun PVDF nanofibers in different concentrations for their crystal structures and phase change behavior. For the group of pure PVDF electrospun nanofibers, the comparison includes further investigation into piezoelectricity and triboelectric properties by use of PFM and a linear acoustic actuator as well as morphology and structure analysis including SEM, TEM, XRD, FTIR, XPS, DSC and Raman spectroscopy.

- By use of electrospinning method, we have identified that changing the concentration of PVDF powder from 1.50 to 1.80 g with an increment of 0.15 into the mixture of DMF (Dimethylformamide) /Acetone (3/7) volume ratio of solution plays an effective role in the content of β-phase, leading to the change of piezoelectricity and triboelectric properties. Moreover, the thinnest mean diameter of electrospun fibers allocates to the sample with highest value of open circuit voltage (170 mV) which is equal to 213 nm. A layer of 0.015 mm thick of such sample with the highest β-phase content has generated the highest output voltage and current values of 124 V and 174 nA, respectively.

- To evaluate the piezoelectricity properties for the current PVDF electrospun fibers in response to various additives, CNTs, LiCl, TiO_2, WO_3 and ZnO particles in different size have been added to the prepared solution separately. The piezoelectric properties depend on the highest β-phase content reached in each sample. When the additives are WO_3, ZnO and CNTs, they achieved a uniform dispersion within the fibers that exhibiting a

mean diameter around 150, 780 and 970 nm, respectively. However, both TiO$_2$ and LiCl acted differently from other additives on the morphology, piezoelectric and triboelectric properties, leading to thicker fibers and negative impact on the β-phase formation.

- Successfully produced hybrid samples including additives have been investigated thoroughly. For TENG/PENG devices in sound energy harvesting evaluation of pure PVDF electrospun fibers and the incorporation of additives into the PVDF solution, an acoustic sensing measurement is applied. Among all of samples, the device with WO$_3$ electrospun nanofibers shows highest values of output amongst all composites tested, being 2.12 mV at a frequency of approximately 6 kHz. For the artificial device including the pure PVDF electrospun nanofibers on top and PDMS pillars as the based part, the application of cell cultures including the HCT-116 (human colon cancer) and HEK-293 (embryonic kidney) approved that they continued to grow around the device and no sign of toxicity was evident.

List of Publications and Presentations

➢ Piezoelectric Property of Electrospun PVDF Nanofibers as Linking Tips of Artificial-Hair Cell Structures in Cochlea. Rana Sabouni Tabari, Yu Chen, Kunyapat Thummavichai, Yan Zhang, Zakaria Saadi, Ana I. S. Neves, Yongde Xia and Yanqiu Zhu. Nanomaterials 2022, 12, 1466.

https://doi.org/10.3390/nano12091466

➢ The effect of additives on piezoelectricity properties of PVDF in acoustic triboelectric nanogenerator energy harvester for hearing impairment application. Rana Sabouni Tabari, Yu Chen, Hong Chang, Kunyapat Thummavichai, Zakaria Saadi, Ana Neves, Agnes Bacon, Konstantinos Anastasiou, Saverio Russo, Yongde Xia and Yanqiu Zhu (In preparation).

➢ International Conference on Nano Science and Nanotechnology (IC2N) Stuttgart. Oral presentation November 2021.

➢ International Women in Engineering Day (INWED21), University of Exeter Oral Presentation.

➢ International Women in Engineering Day (INWED20), University of Exeter Oral Presentation.

➢ International Women in Engineering Day (INWED19), University of Exeter Oral and Poster Presentations.

Table of Contents

Table of Contents

Table of Contents

Table of Contents

Table of Contents

Acknowledgement

At the outset, I would like to give my deep sincere appreciation and gratitude to my supervisor, Professor Yanqiu Zhu, for his patience, meaningful support, and superb instructions. His exceptional guidance and knowledge on the field have shaped me to become a better scholar. This work would not be possible without his insight, guidance, and good humor. I am also grateful for Dr. Yongde Xia's feedback and technical insight.

I feel very thankful to my laboratory teammates: Drs. Zhuxian Yang, Bahareh Yazdani Damavandi, Kunyapat Thummavicai (Ploy), Yu Chen, Zakaria Saadi, William Ferguson, Ms. Agnes Bacon, Ms. Evelina Lucinskaite, Ms. Zheng Huang, Mr. Konstantinos Anastasiou, Mr. Sunil Poudel for their help, support, and meaningful cooperation.

I would also thank the staff at engineering department Drs. Yat-Tarng (Tommy) Shyng, Peter Armitage who helped me with DSC characterization and accosting sensing setup, and Hong Chang for her expressive support and collaboration with imagine suite facilities. I do appreciate Dr. Mark Heath from the Physic department who guided and helped me with the clean-rooms facilities application. Thank Prof. Russo Saverio, Prof. Christian Soeller and Dr. Ana Neves, for providing the acoustic sensing facilities, viability characterization of my device in available cell cultures and triboelectric properties investigation in Physics, engineering and LSI departments which led to mutual collaborations in some results and analyses. Thank Dr Ellen Green for her guidance on Raman Spectroscopy analysis. Thank Prof. Yan Zhang from CSU university in China for providing the PFM results of my samples and Dr. David Morgan in Cardiff university for the XPS results.

Last but not least, I would particularly like to express my gratitude for my loyal and supportive husband and my parents as my solid bedrock throughout my years in University of Exeter, who showed faith in me and gave me million words of encouragement and kindness.

List of Figures

List of Tables

List of Abbreviation

AAO	Anodic Aluminum oxide
AC	Alternating current
AFM	Atomic Force Microscopy'
Ag	Silver
AgCl	Silver Chloride
AHL	Artificial hair cells
Au	Gold
BaTiO$_3$	Barium Titanate
BM	Basilar Membrane
BTE	Behind-The-Ear
CAD	Computer-Aided-Design
CIC	Completely-In-the-Canal
Cis	Cochlear Implants
CVD	Chemical Vapor Deposition
CNTs	Carbon nanotubes
dB	Decibels
DC	Direct current
DMAC	Dimethyl acetamide
DMF	Dimethylformamide
DMSO	Dimethyl sulfoxide
Dpi	Dots per inch
DRIE	Deep reactive ion etching
DSC	Differential scanning calorimetry
EC solvent	(2-methoxy-1-methylethyl acetate)
EDX	Energy-dispersive X-ray
FSRs	Force Sensitive Resistors
FWHM	Full width at half maximum
FTIR	Fourier transform infrared radiation
GPa	Gigapascal
Gr	Graphene
H	Hour
Has	Hearing aids
HRTEM	High-resolution transmission electron microscopy
Hz	Hertz
IC	Integrated circuit
IHCs	Inner hair cells
IPA	Isopropyl alcohol
iPANS	inorganic piezoelectric acoustic nanosensor
Ir	Iridium
ITC	In the canal
ITE	In the ear
KBr	Potassium Bromide
kV	Kilovolts
LiCl	Lithium Chloride

MEIs	middle ear implants
MEMS	Micro electro mechanical system
MET	mechanoelectrical transduction
MMPF	metal core piezoelectric fiber
mW	Megawatt
MWCNTs	Multi-walled Carbon Nanotubes
NBL	NanoBeam Lithography
NDT	Non-destructive testing
Nm	Nanometer
NPs	Nanoparticles
OHCs	Outer hair cells
PANi	Polyaniline
PCDH15	Protocadherin Related 15
Pd	Palladium
PDMS	Polydimethylsiloxane
PET	Polyethylene terephthalate
PFM	Piezoresponse Force Microscopy
PLGA	Poly (d,l-lactide-co-glycolide acid)
PMMA	Poly (methyl methacrylate)
Pt	Platinum
PVD	Physical Vapor Deposition
PVDF	Polyvinylidene fluoride
PZT	(Pb [Zr_xTi_{1-x}] O_3,$0 \leq x \leq 1$) Lead zirconate titanate
RIC	Receiver in the canal/ear
Rpm	Revolutions per minute
S	Second (s)
SAED	Selected Area Electron Diffraction
SEM	Scanning electron microscope
SNHL	Sensorineural hearing loss
SU-8	Negative EPON SU-8 epoxy resin
T	Temperature
TEM	Transmission electron microscope
TiO_2	Titanium oxide
TRPA1	Transient receptor potential vanilloid 1 ion channel
TGTG'	Alpha
TTTGTTTG'	Gama
TTTT	Beta
UV	Ultraviolet
VIVLAD	Vibrating Intravascular Lung Assist Device
WHO	World Health Organization
WD40	Water Displacement, 40th formula
WO_3	Tungsten (VI) Oxide
X_c	Degree of crystallinity
XPS	X-Ray Photoelectron Spectroscopy
XRD	X-Ray Diffraction
ΔH_m	Apparent enthalpy of fusion

List of Abbreviation

ZnO	Zinc Oxide
Ω	Ohms
μA	Microamps
μm	Micrometer
$\mu W/Cm^2$	Microwatt per square
T_m	Melting point

Chapter 1: Introduction

Biology has provided inspiration and creativeness for a number of technologies. Engineers are turning to nature for finding solutions to difficult problems in locomotion, material design, sensor development, artificial fabrications for body implantation and a multitude of other fields [1]. One of the famous biological mechanisms is hearing, which has attracted great research interest in the past few decades. When the human ears are healthy, they can detect a range of frequencies between 20 Hz and 20,000 Hz [2]. However, permanent hearing loss happens when the hair cells in the cochlea are broken or lost.

For the increasing number of people who are suffering from hearing loss, the use of hearing aids (HAs) has been proven beneficial. Besides all the great advantages of existing HAs which are becoming more versatile than the past, they exhibit some disadvantages and could cause discomfort to the users. Disadvantage features such as short service cycle owing to limited batteries that requires frequent changing, clogging with ear wax, trapping moisture within the ears, not helpful in restoring the hearing loss, risk of losing hearing loss for implanted types of hearing aids, not ideal for using while doing physical activities and for higher degrees of hearing losses, need to be tackled urgently, to improve the quality of life for those who suffer from hearing losses. This becomes the driving force for this thesis.

Recent progresses on bio-inspired HA devices have shed light on this area. By the use of advanced nanotechnology to mimic the sensing mechanism in the mammalian auditory system, transducing of sound into highly sensitive and detectable electrical signals, it is possible to replace damaged components in the ear and to restore hearing [3-4]. Such bio-inspired ideas, combined with recent advances in nanotechnologies, enlightens us with useful directions to approach the challenges.

At current stage, the constitutive components of the cochlea are not repairable if they are damaged [5]. As a result, existing HAs could only act as a magnifier and work with those having survival hearing hair cells.

In spite of the fact that artificially cochlear developments presented a great progress in recent years, they are currently not expected to solve all degrees of hearing loss. Furthermore, current artificial cochlear devices are not capable of fixing hearing loss as a nerve result damage and their use on ear will cause a human to lose all his natural hearing. A close biomimetic approach to develop new generation of artificial hair cell like sensors could solve these issues.

The next generation of HAs should completely or partly overcome these disadvantages, exhibiting features such as small in size, bendable and durable, biocompatible, extended battery life or completely eliminate the requirements of charging, low cost etc. Further desirable features include the capacity of replacing or restoring damaged and broken hair cells by using artificial hair cells, to allow some recovery of auditory operation. Those requirements define the scope of the thesis.

Therefore, the main aim of this thesis is to create an artificial hair cell sensor that is able to convert sound into electric signal, with self-power capability. To remove any further need of an external battery, this artificial hair cell HA is introduced. The main methods for the fabrication of this structure are such as lithography and electrospinning following the steps of gold coating using thermal evaporation process.

The objective characterizations are mainly done on top and base structures of this artificial HA. These include optical and Scanning electron microscope (SEM) investigations for the polydimethylsiloxane (PDMS) micropillars base part and further morphology as well as structure characterizations for the electrospun fibers on top of PDMS micropillars surface. For the group of pure PVDF electrospun nanofibers and its composites, SEM, Transmission electron microscope (TEM), X-Ray Diffraction (XRD), Fourier transform infrared radiation (FTIR), X-Ray Photoelectron Spectroscopy (XPS), Differential scanning calorimetry (DSC) and Raman spectroscopy analysis are detailed and presented. The whole assembly of artificial HA is tested for accosting sensing properties and its response under different ranges of frequencies and applied voltages are recorded. The engagement of both piezoelectric and triboelectric properties for better demonstration of the artificial HA is also carried out.

To construct an artificial hair cell HA, we first need to create the key components that are required for its structures, including the elastic PDMS micropillars of graded heights, a SU-8 semi-permanent mould for PDMS micropillars fabrication, polyvinylidene fluoride (PVDF) fibers sheet for the piezoelectric properties of the tip-links session, PVDF fibers sheet on the surface of PDMS micropillars and gold coated layers to provide the conductivity for the device on the surface of PDMS and the PVDF mate illustrated in Fig. 1.1(a-f).
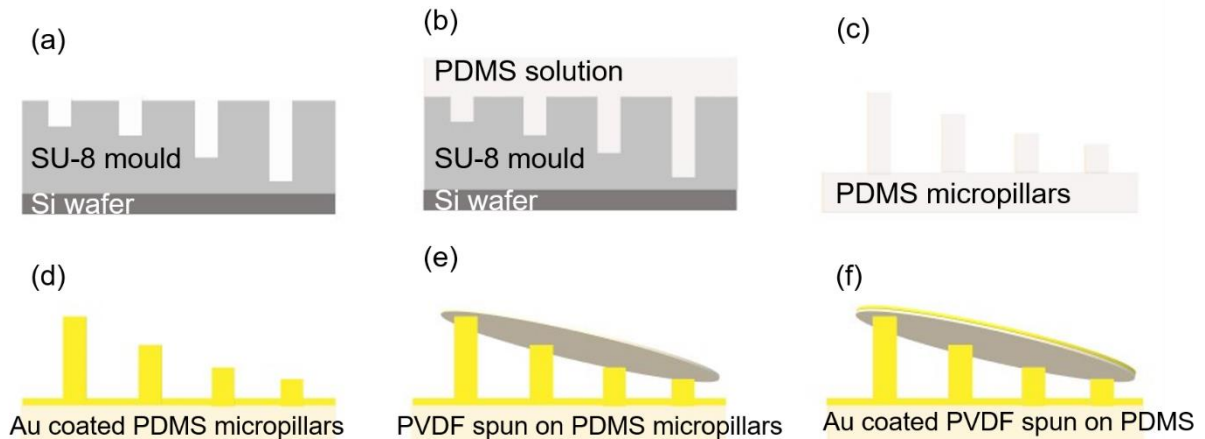
Fig. 1.1 (a) The exposed SU-8 mould fabricated on the Si wafer, (b) PDMS solution cast on the SU-8 mould, (c) cured PDMS micropillars, (d) Au-coated surface of PDMS micropillars as the underneath electrode, (e) PVDF electrospun sheet on the Au-coated PDMS substrate, and (f) the final Au-coated surface on the as-spun PVDF sheet playing the top electrode role.

We then characterize each component, investigate their properties, understand their performance, seek for further improvement, and finally demonstrate the assembled structure. Starting from materials science and engineering, we would face various challenges of multidisciplinary feature. To accomplish the above aim, we have carefully selected the following objectives, to tackle each of the challenges, as defined below:

- Fabrication of a HA sensor device prototype by means of advanced nanomaterials.
- A low cost, very well operative and biocompatible device.

- Easily removal of any need for the external battery with self-powered feature for the device.

The system developed in this research is fabricated using a soft and flexible polymer PDMS, PVDF electrospun nanofibers on top playing the artificial tip-link's role and sputtered Au electrodes. Specifically, the sensor device consists of a PDMS micro pillar structure inspired by cilia found in biological organisms. Cilia are high aspect ratio structures that play an important role in multi-stimulus sensing, locomotion and acoustic in many living organisms [6].

The demonstration of the structure mimicking the natural hair cells structure and sensing principles of these proposed regions in the cochlea, present practical functions for hearing senses in the damaged hair cells' part causing severe hearing losses. The simplified and relatively similar construction of this created device to natural hair cells is ideally different from the previous studies and the sensitive transduction mechanism for the mechanical (acoustic) input to electrical output helps to improvement of its effectiveness, high sensitivity, and efficient frequency responses.

The transduction function of hair cells can be mimicked when suitable material is applied. Smart materials which can pick up the surrounding energy such as motion as the external stimuli and convert it to another form of energy. Nature offers examples of energy conversions by using piezoelectric materials. These materials are highly desirable for many researchers, due to the promising potential for the development of a self-powered sensor without the need of an external power source.

As a piezoelectric material, polyvinylidene fluoride (PVDF) is an important candidate for future energy harvesting, due to its excellent structural stability, higher voltage sensitivity, better acoustic impedance with air and water, biocompatibility, easier manufacturing over ceramic piezoelectric [7]. Its promising triboelectric performance and wide combination possibilities with other materials have made it particular attractive in energy conversion.

To achieve enhanced piezoelectric and triboelectric performance of the produced electrospun PVDF nanofibers, incorporated additives will be studied. Carbon nanotubes (CNTs), graphene, nanoclays and Barium titanate ($BaTiO_3$) showed higher piezo response in the electrospun PVDF [8]. To further investigate the behavior of other additives, a set of additives such as Tungsten (VI) Oxide (WO_3), Zinc Oxide (ZnO), CNTs, Titanium Oxide (TiO_2) and Lithium Chloride (LiCl) are chosen in this thesis. The comparison of their performances can lead to the best filler to serve as the tip-links in the artificial structure.

The main contents of the thesis consist of following:

With the aim to design, synthesize and evaluation of the target device, the experimental work is principally presented. This part comprises the fabrication processes for the different heights of PDMS pillars for which a semi-permanent SU-8 mould was fabricated and chosen. The challenge in this step is to get succeed different holes in the SU-8 exposed photoresist. This can be done by controlling the development time for each row on the SU-8 template.

The main focus of this thesis is to obtain the highest piezoelectric and triboelectric electrospun pure PVDF and its composites by the help of electrospinning method. This part of fabrication in the designed device is due to the purpose of battery removal needed in the previous and current generations of hearing aids devices. The prospect of responding to the acoustic signals and electrical signal generation is another objective of this study. This thesis also sets insight into the investigation of biocompatibility of the device in two different cell cultures to obtain its safety for the approval of non-harmful selection of polymeric materials in this study. Another confronted challenge is the exact cell medium application which is not precisely achieved because of the shortage of time and available facilities for pursuing this purpose. Another target of this study is to a COMSOL model presentation for the smaller size close to the natural hair cells for a better demonstration of a more realistic perspective of smaller scale for this design.

The structure of the thesis is presented as follow:

Starting from the motivation of the thesis in Chapter 1, following to the presentation of hearing loss, hearing aids and their limitations in Chapter 2, the analysis methods for characterizations, methodologies for the fabrications, and the processes for two individual parts of the device as the underneath PDMS based and top PVDF sheet are demonstrated in chapters 3, 4 and 5 respectively. Chapters 6 and 7 provide the characterizations and comparisons of pure PVDF and the composites. Additionally, the device is thoroughly investigated for its acoustic and viability of non-toxic conditions in Chapter 7. In Chapter 8 the conclusion and all key findings from this thesis are presented, and some future work to continue research in related areas are also undertaken.

Chapter 2: Literature review

This Chapter will present the background information associated with existing strategies for hearing aids (HAs), which is the key technique to tackle the hearing loss problems. We will focus on the materials and processes used for the construction of HAs, which will lead to the need for further investigations of next generation of HAs.

2.1 Hearing loss and hearing fundamental

A person who could not recognize a hearing threshold of 20 dB for one or both ears together is defined as suffering from hearing loss. World Health Organization (WHO) reported that one of the most common diseases in the world is hearing loss, and that more and more of the population suffer from the disease. Up to now, there are around 466 million people (over 5% of the global population) in the world living through hearing loss of various levels, which could increase to more than 900 million by 2050.

Causes to hearing loss include genetic origins, impediments at birth, particular infectious illnesses, side effect of medicine, experiencing to unnecessary and unwanted loud noise for longer time, and aging, of which noise-induced hearing loss is the main cause for hearing deficiency and deafness [9]. People older than 65, young adults and children are prone to the noise-induced hearing impairment [10-12]. Since the hearing loss deteriorates gradually, early diagnosing is important. Hearing loss starting from the birth or in older age, affects the communication abilities, mental health, and the value of life. Major impacts of hearing loss compromise individual and the whole society in different scales which lead to excessive costs.

The anatomy of the ear entails the external ear, the middle, and the inner ear (Fig. 2.1).
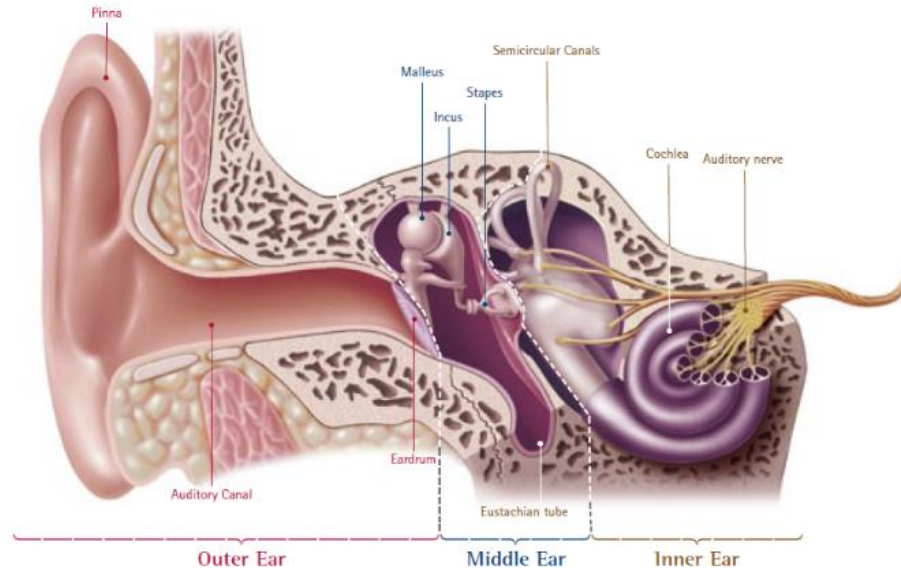
Fig. 2.1 The anatomy of ear [13].

To recognise sounds, our ears transduce the airborne acoustical energy into electrical energy which is processable for the brain [14]. The pressure fluctuations transiting through the air from sounds consist of sinusoidal oscillations of different frequencies. To expedite the perception of sound, the nervous system converts the acoustic signals to the electromechanical signals [15]. Fig. 2.2 illustrates the whole process of the sound perception from the outer ear to the hearing system.
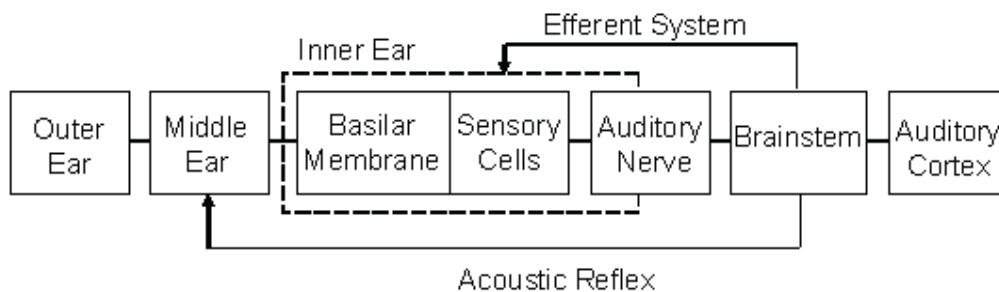
Fig. 2.2 Hearing and auditory system [15].

When the sound reaches the head of a person, the sound process part starts and the head creates a pulse to reflect, captivate and deflect the sound to the processing function by the auditory system which is in the outer and middle ears. After the diffraction, absorption, and reflection of acoustic waves by the ears, the mechanical

energy that converted from the acoustic energy of the waves passes around the middle part of the ear. The movement of the fluids of the inner ear results in the shakings of the basilar membrane between the middle and inner ears [15]. In the organ of Corti, there are several hair cells working as the sensual receptors and they are two classes, the inner and outer hair cells (OHCs). While the inner hair cells (IHCs) are in a single row in the Corti and are round and square in shape, the outer hair cells are in three parallel rows and their shape is longer and trimmer [16-17].

2.2 Hair cells as the sensory receptors

In the inner ear, there are several hair cells which perceive sound as the mechanoreceptors [18-19]. A summary of some main differences between the inner and outer hair cells is illustrated in Table 2.1.

Table 2.1 Differences between inner and outer hair cells.

Features	Inner hair cells	Outer hair cells	References
Assembly	A single row arrangement	A three parallel rows arrangement.	[20-22]
Appearance	Round and small	Long and slim.	[23]
Function	Mechanical energy to neural signal transduction	Affective on the sensitivity of the cochlea more than 32 dB for better regulation.	[23]
Consequences	Sensory Neural Hearing loss	Alter properties of cochlear input to the brain.	[24]
Estimated number	3000 to 3500	9000 to 12000	[21-22]

2.2.1 Hair cells properties and roles in sound receiving process

In mammals, the inner ear, named as cochlea, is filled with a fluid tube curled up like a snail's shell, in which the auditory sensing arises. In the cochlea, there are several steps to receive the sound pressure oscillations, including: eardrum vibration, transmission throughout the small middle ear bones acting as a lever, and the pressure waves recognition by the cochlea, as shown in Fig. 2.3 [25].
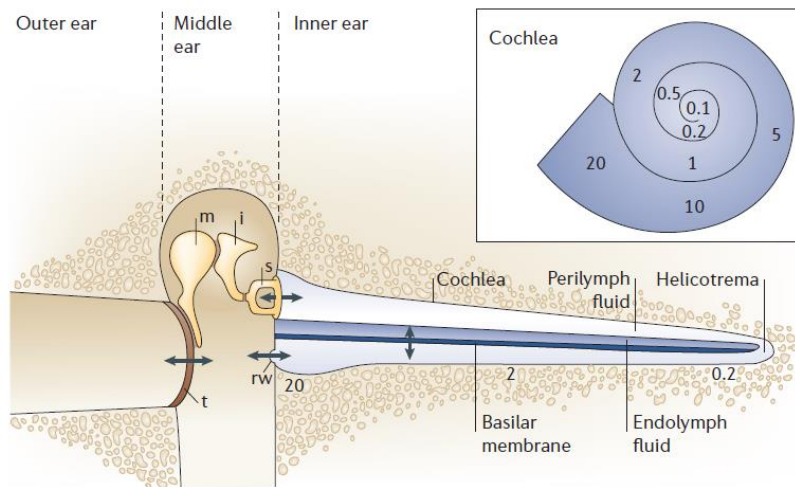
Fig. 2.3 The sound transition trail [25].

The auditory or hearing system involves the outer, middle and inner ears, as well as central hearing nervous system [26]. The sound detection happens when the IHCs as mechanoreceptors got excited. Submicrometric shakings of the stereo ciliary hair bundles soaking in an extracellular fluid could excite the hair cells. To proceed the transduction step in IHCs, the fluid that is low in cytoplasmic calcium and high in potassium, dissimilar to OHCs, generates a potential of 100 mV [27]. IHCs and OHCs are incongruent in these purposes, and the permission of current flow in one direction can be achieved by IHCs containing larger depolarization element. The generation of force from a piezoelectric motor protein to intensify the mechanical inducement would occur to the outer hair cells, while inner hair cells interconnect with auditory nerve fibres as the cochlear output [28-29]. For a vestibular type of hair cell, the filamentous tip-links connect the stereocilia at the top, as illustrated in Fig. 2.4. These tip-links of sensory hair cells in the inner ear play a

critical role in the mechanoelectrical transduction (MET), by converting mechanical stimuli arising from sound and head movements into electrochemical signals [30-32].

The acoustomechanic transduction is the foremost function of the middle ear which links the air-filled outer ear and the fluid-filled inner ear [15].The acoustic energy conversion into physical vibrations of the ossicular chain happens when the sound waves arrive at the tympanic membrane. If this conversion of sound energy does not take place, the volume of energy to vibrate the tympanic membrane would not be adequate. The tension of the tympanic membrane must be sufficient to convert the sound energy into the mechanical movement of the ossicles in the middle ear [26].
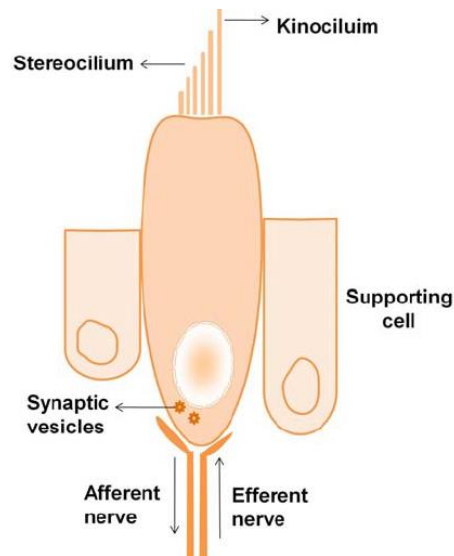
Fig. 2.4 A vestibular hair cell structure [28].

The arrangement of microvilli or stereocilia, a set of steps of different heights, is the key part of hair cells for efficient transduction, as shown in Fig. 2.5. Bending of the filaments deflects the stereocilia at their elongated base, opens the mechanoelectrical transduction (MET) channels, whereas shifts to the opposite direction closes these channels [31]. A TEM image (Fig. 2.5a) illustrates three rows of stereocilia containing osmophilia areas at the stereociliary tips, the side walls, and the rootlets for a guinea pig outer hair cell. Around 30 to 100 stereocilia are in the hair bundle of a mammalian outer hair cell with a maximum height of 1 to 6 µm [32].

Some of the protein elements of the stereocilia are shown in Fig. 2.5b. The mechanoelectrical transduction MET, transient receptor potential channel A1 (TRPA1) are shown as the other constituents of the stereociliary bundle.
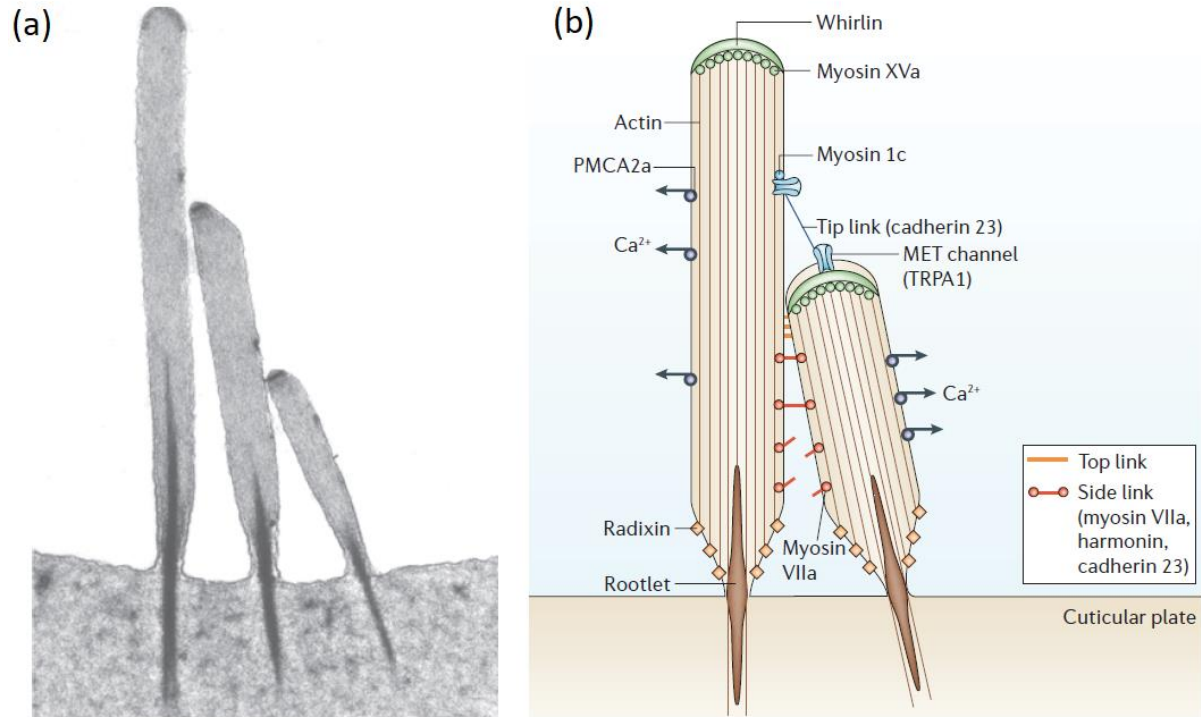
Fig. 2.5 (a) The stereociliary bundle structure and its protein component [25], and (b) The diameter of tallest stereocilium is around 0.25 µm for a mammalian outer hair cell. There are almost 30 to 100 stereocilia having a height range from 1 to 6 µm [32].

A series of thin extracellular threads interconnects with the stereocilia in a hair bundle. Tip-links expand from the peak of each stereocilium to the side of the tallest one in each hair bundle [33-34]. The principal function of tip-links is the mechanoelectrical transduction. Dissimilar to the outer hair cells, the polarization could happen in two ways in the inner hair cells in the mammalian cochlea. Forming the polarity could be a result of the height differences in the rows of stereocilia, and of the two dimensional division of the stereocilia [35]. To measure the irregular strains of the bundles bending to the tall stereocilia which depolarizes the cell and provides the force more than bending in the opposite direction, tip-links are vital [36-37]. The differences among the heights of hair cell structures are essential in this

context [38]. Three crucial features of hair cells for the transduction receptiveness are as follows. Firstly, the transduction process is remarkably fast due to its pure mechanical nature which is helpful for humans to hear frequencies greater than 20 kHz, and more than 100 kHz for bats or even higher for whales [39-40]. Secondly, the sensitivity of the transduction process of the hair cells for the weakest sounds could produce vibrations at ±0.3 nm within the ear which is very high [41]. Thirdly, this process could distort hearing surprisingly, as proven by Italian violinist Tartini who heard tones at frequencies as a combination of f_1 and f_2, actually two pure notes were played on his instrument [42-43].

When the sound is high in frequency, the hair cells near the base vibrate which are closer to the eardrum; whilst the sound in low frequency excites the hair cells close to their distal end [44].

2.2.2 Hearing loss types

Hearing impairment, based on the classification of the World Health Organization, (WHO) has several grades which change due to different conditions and ages. Table 2.2 summarises the classifications of hearing impairment ranging from "no impairment" to "intense impairment" status, based on the threshold [45].

Table 2.2 Different grades of hearing impairment according to WHO classification [45].

Grade of Impairment	Audiometric ISO value (average of 500, 1000, 2000, 4000 Hz)	Impairment description
0 (no impairment)	25 dBHL or less (better ear)	No or very slight hearing problems. Able to hear whispers
1 (Slight impairment)	26-40 dBHL (better ear)	Able to hear and repeat words spoken in normal voice at 1 metre
2 (Moderate impairment)	41-60 dBHL (better ear)	Able to hear and repeat words using raised voice at 1 metre
3 (severe impairment)	61-80 dBHL (better ear)	Able to hear some words when shouted into better ear
4 (Profound impairment including deafness)	81 dBHL or greater (better ear)	Unable to hear and understand even a shouted voice

In general, based on the damaged area of the auditory system, there are three main categories for the hearing loss, which are conductive, sensorineural, and mixed type of hearing loss [46].

- Conductive hearing loss: When the external ear canal does not conduct sound to the eardrum and the middle ear parts, this type of hearing loss starts to happen. Sound vibrations could pass through the inner ear without passing through the middle ear. Those suffering from this type of hearing loss could get comfort through the bone conduction HAs devices behind the ears, or via surgery if needed. Medication, physicians or audiologists could find a way to help retrieve hearing by getting rid of wax, infection blockages in the middle ear [47].

- Sensorineural hearing loss (SNHL): This type of hearing loss happens when the inner ear (cochlea) or the nerves passing through the inner ear to the brain got damaged. The loss and damages in the cochlear hair cells could result in sensorineural hearing loss. Severe hearing loss happens when the damage is substantial. Both the sensitivity and clarity of hearing could be affected [47]. The common treatment includes the use of usual HAs or cochlear implants, which could raise some disorders in auditory daily routine function, and not recommended to be used for a long period of time [48].

- Mixed hearing loss: When both of conductive and sensorineural hearing losses exist in the same ear together, it is defined as mixed hearing loss. In such conditions, ear wax in the ear canal can be treated, however the sensorineural hearing loss cannot be effectively treated therapeutically [47].

2.3 Hearing aid devices

A hearing aid (HA) device is an electro-acoustic body-worn apparatus that can amplify and modulate sounds for the user. Some HAs could be useful for some of nerve damage caused by loud noises, side effects of certain medicines or other causes [49].

In both hearing loss types, HA categories are slightly unalike, while for the mixed hearing loss, HAs could be applied only to the conductive part that can be cured medically. Also, a small portion of sensorineural hearing loss can be compensated by the use of HAs [50-51].

2.3.1 Hearing aid device elements

HAs are made of at least four main components, including microphones, circuitry, receiver or speaker and the battery, details of main elements are as follows:

1) Microphones pick up an external sound and convert it to an electrical signal, then feed the signal into an amplifier. For the piezoelectric type of microphone, an amplifier is needed. When the piezoelectric crystal gets stressed physically, small electrical signals will be generated [52-53].

2) A preamplifier to enhance the electrical signal, which will be transformed into acoustic energy.

3) A receiver to convert the output of the signal processor to the sound. Most issues relevant to HAs system from a wide range of frequencies are originated in this part [53].

4) A battery is required for the operation of the receiver and the circuitry and the compensation of the signal difference between the acoustic energy delivered to the ear and the amount which the microphone receives. The source of energy in HAs is the battery, not the amplifiers [54-55].

For almost all of the previous HAs, size reduction was pleading [45], [56-58]. Though the conversion of the acoustic signal into an electrical signal seems easy to understand, this transducing function could be more complicated for the digital type of HAs [59].

2.3.2 Hearing aid devices reviews

HA application for older patients proved a huge advantage in different areas including social, emotional, and communicational after 12 months of use for a group of 192 elderly people who were over 64 years old [60-61]. In contrast, some people could not stand wearing HAs due to being discomfort, feeling inconvenience and social stigma problems. Some recent advances in technology have made the HA devices invisible. A total implantable HA device has been proposed to overcome the current HA devices' limitations [62-66]. Diverse kinds of hearing loss have been treated by use of various hearing devices including HAs, middle ear implants (MEIs)

or cochlear implants (CIs). Main limitations for the available commercial HAs and their features have been summarized in Table 2.3 [67-69].

Table 2.3 Commercially available types of hearing aids and their features.

Type	Severity of hearing loss level	Key advantages	Disadvantages
Body worn aids	-	-	• The size is like a pack of playing card and heavy.
Behind the ear aids (BTE)	Those who suffer from a placid to overwhelming hearing loss, and not suitable for higher levels of hearing loss.	• Comfortable to wear and affordable for most budgets.	• BTE is large and massive in general and doesn't let both of ears to act individualistically. • Easily noticeable
Receiver in the canal/ear (CRT/RIC/RITE)	Mild to moderate level of hearing loss.	• Comfortable, easy to wear. • The receiver is in the ear canal instead of in the BTE case [67]. • For the RITE type, the cochlea and external auditory canal include all parts of amplifier, microphone, and receiver together in a plastic container	• Frequently repairs to the receiver. • Although it seems more comfortable dissimilar to the rest styles, however users might not notice if they lose them. • Expensive.
In the Canal (ITC)	Not very suitable for hearing losses intensities higher than gentle or moderate.	• Direct microphone to hear voices in a noise. • Fits entirely into the external auditory canal. • ITCs are smaller than ITEs	• Occupies the ear canal. • The size of battery is small and can be tricky for removal or changing purposes. • Poor in background noise and in groups. • Hard to clean and change the battery
In The Ear (ITE)	-	• As an advantage, the connection of ITE hearing aids to FM systems is possible wirelessly [68]. • Completely customizable for all users.	• For young children ITEs are not fit as they grow, and most people could not afford buying new hearing aids, however new ITEs hearing aids are mostly silicone-based material which are less expensive. • Higher level of cleaning up to prevent ear wax build-up. • Its high sound quality and amplification to provide for most types of hearing loss coming with being more comfortable than the BTE aids

Cochlear implants (CI)	Severe to profound sensorineural	• Allow deaf people to hear.	• Auditory nerves are stimulated directly • Expensive. • Invasive surgery and some side effects possibility after that. • The batteries will need to be replaced or charged every day. • Not very easy to care during physical activity. • The limitation of stimulation of the cochlear nerve at low frequencies [69].

2.3.3 The mechanism of recent hearing aid devices

HAs include several types, such as middle ear implants (MEIs) and cochlear implants (CIs) which have treated numerous classes of hearing loss so far. While HAs transfer sound into the ear canal using speakers that are receivers, MEIs could transfer the signal to excite the ossicular chain. Severe and profound sensorineural hearing loss can be treated by CIs which can stimulate the auditory nerves directly. To provide the required energy for the amplifier, battery is a must in the HA devices [53]. Fig. 2.6 shows two common types of HAs as a reference. The category of HAs can be also divided into four styles, the In-the-canal (ITC) and completely-in-the-canal (CIC) Aids, In-The-Ear (ITE) Aids, and Behind-The-Ear (BTE) Aids. Patients suffering from moderate to rigorous hearing loss usually use this type of HA devices which accounts for around 38% of all HA customers [67-70].

Fig. 2.6 (a) A body worn HA/BTE device [53] and (b) A RTE HA [71].

2.3.4 Limitations of traditional hearing aids

Patient satisfaction with HAs is always important. Technology has been improved for microphones and other parts in HAs, however limitations still remain [72-74]. Low cost, small size, long-lasting battery endurance, easy operating are the notable demands [75-77]. The other reasons are the high cost in terms of changing the HAs which is significantly empower the need of manual tuning processes and labor-demanding manufacturing [52]. Furthermore, even for the most updated and sophisticated types of HA devices could not restore all hearing loss and they just work as reading glasses to correct the vision, but they could help people to make the most of their remaining hearing by making sounds louder [52].

The increased need of sensor devices for medical and environmental technologies during the last 20 years led to an apparent revolution in sensor research. Although both HAs and CIs can enhance hearing, they are unsuccessful when hair cells are broken or harshly impaired. Regardless of the great progress for in vitro studies in CIs, a huge challenge is still noticeable for the subtle nature of the inner ear in terms of major surgical treatment. Nature has been always the best pattern for the synthesis of artificial biomimetic structures of hair cells. This structure can contain materials mimicking the behaviour of the natural hair cells in the cochlea. The mechanism of transduction can be obtained from the appropriate materials having the equivalent properties to act as an artificial structure. The engineering hair cells manufacturing could hypothetically lead to a new generation of fully implantable devices overcoming current issues and removing the battery use.

2.3.5. Nanomaterials application as a potential for hearing impairment

The weight and volume of battery in biomedical devices can unavoidably increase the whole size of the biomedical systems. The working life of implanted devices can be extended by in-situ energy harvesters, which could be an excellent idea to explore for medical implants applications, such as in HAs.

The study of hearing mechanisms and hearing losses challenges highlight the need of in vivo energy harvester in implanted HA devices for miniaturized microphone and micro speakers', by omitting the battery requirement. By using

advanced nanomaterials, a single chip consisting of nanomaterial-based structures can be created for the future HA devices.

The classification of nanomaterials is based on the different features of 0D, 1D, 2D and 3D nanostructures, such as carbon nanotubes (CNTs), quantum dots, nanoparticles, nanowires, nanofibers and nanotubes [78-83]. Research of nanomaterials for medical applications and biological systems is increasing [84]. Biologically ultrasensitive sensors could be developed by using nanomaterials. Example applications of nanomaterials to improve the sensitivity in nanobiosensors are listed in Table 2.4.

Table 2.4 Nanomaterials application in nanobiosensors.

No.	Nanomaterial structure used	Key advantages	References
1	Carbon nanotubes	Enzyme loading improvement, higher aspect rate and enhanced electrical communication	[85-87]
2	Nanoparticles	Better loading of bioanalyte as well as including catalytic properties	[88-90]
3	Quantum dots	High fluorescence level and size tunable band energy	[91-93]
4	Nanowires/Nanofibers	Better charge conduction, high level of electrical and sensing properties for biosensing	[94-95]
5	Nanorodes	Appropriate for MEMS (Micro-Electro-Mechanical System) with good couple sensing properties	[96-97]

To tackle the current limitations addressed in Table 2.3, MEMS technology which is less expensive, more precise, and smaller in size could provide the solution. Smaller electronic device consumes less energy, and their fabrication could be batched that would benefit end-users. The development of MEMS-type nanosensors in HA has huge potentials, and has been rarely studied [98].

Moreover, while the moderate type of conductive hearing loss can be cured by HAs and MEIs, CIs using an electrode array stimulating the auditory nerve fibers could be applied for severe or profound sensorineural hearing loss. However, for the transduction channels at stereo ciliary tips, when the tip-links are broken, the mechanical sensitivity of hair bundle will be lost.

Recently, a group of researchers regenerated tip-link in a two-step process, starting with PCDH15 (protocadherin-related 15) formation followed with the development of CDH23 (cadherin related 23) as the upper half of tip-links as shown in Fig. 2.7. This temporary tip-link adaption of the MET was not completely practical, as the MET current was impaired for up to 36 hours, and the amplitude of MET current was fully fixed within 12 hours [99].
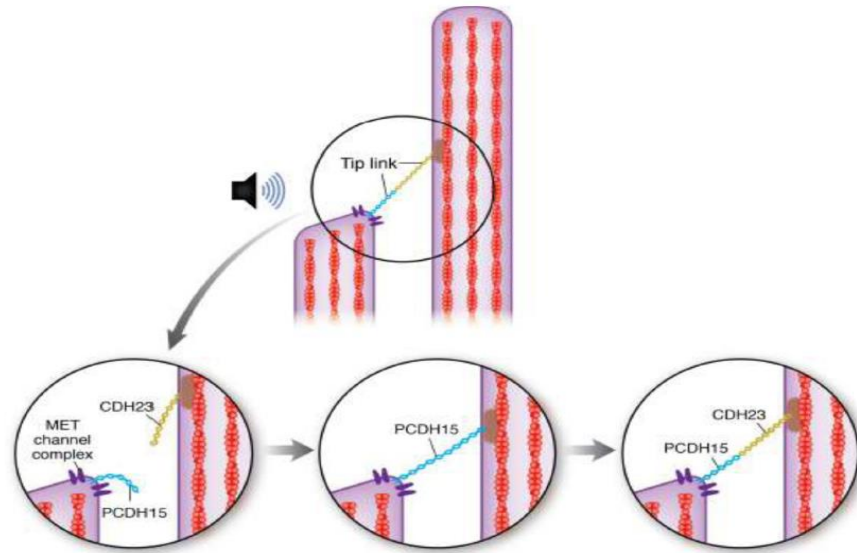
Fig. 2.7 The repair processes of tip-link model, (Top) tip-link connecting the MET channel, (bottom left) tip-link breakage, (bottom middle) a temporary tip-link formed within 12 hours of damage, and (bottom right) the full restoration of MET within 36 hours after damage [99].

Artificial biological sensors based on mechanotransduction using nanomaterials have been developed to mimic the natural hair cell functions in human ears. For example, a long cilia close to the rest part of cells acts as a mechanical converter to electrical signals [100]. The Artificial hair like (AHL) sensors can be divided into four main categories: piezoresistive, piezoelectric, capacitive, and magnetic sensors. Ko et al reported a piezoresistive AHL sensor, which included a liquid metal capsulation in a piezo-sensitive PDMS substrate, as shown in Fig. 2.8a. A thin layer of PDMS cured at $70^{\circ}C$ in a convection oven was then attached to the piezoresistors by an oxygen plasma technique, which showed a linear relationship between the

resistance and applied normal loads [101]. Maschmann et al. reported another piezoresistive AHL. It was a sputter-coated Au/Pd cylinder deposited electrode. Also, a deep hole containing carbon nanotubes (CNTs) encapsulated in a single glass fiber was included in the electrode cylinder. Due to the CNTs, as the piezoresistance element, the sensitivity of this piezoresistive AHL sensor was approved very high at low-speed air flow [102]. Another piezoresistive sensor, a composite of PDMS and CNTs was suggested by Ji-Eun Han et al to improve the higher conductivity of piezoresistive sensor types [103].
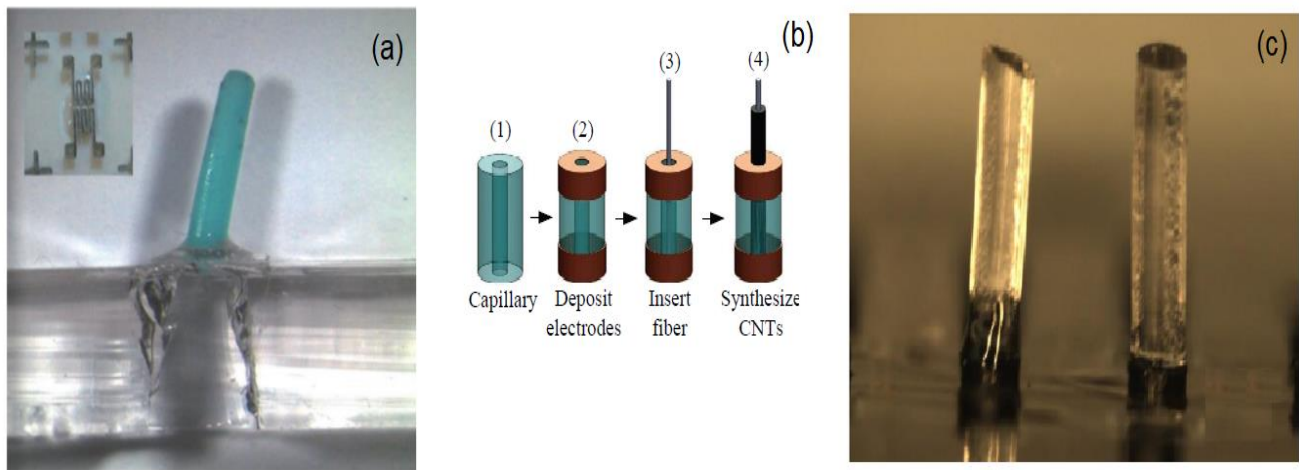
Fig. 2.8 (a) Piezoresistive sensors developed by Ko et al. [101] (b) Piezoresistive sensors developed by Maschmann et al. [102] and (c) another piezoresistive sensor fabricated by Ji-Eun Han et al. [103].

An all-polymer based artificial hair cell sensor made of polyurethane was fabricated by Nannan et al. They used force sensitive resistors as the sensing elements, whose conductivity was provided with carbon black and CNTs fillers [104]. In another effort, Kottapalli et al. fabricated an artificial MEMS neuromast flow sensor by using a liquid crystal polymer membrane. The polycarbonate hair cells can boost the flow sensitivity for fish-like underwater sensing [105].

Next category of AHL sensor is the piezoelectric type, based on piezoelectric metals and ceramics. For instance, an improvement in airflow sensing was reported by Bian et al., and by squeezing and pressing, they achieved a multi-electrode metal

core piezoelectric fiber (MMPF)-based sensor, which is complicated and time consuming [106]. Dagamesh et al. developed a MEMS accelerometer hair cell based sensor using surface micromachining and lithography methods, and they reported a damping factor for the hair flow sensor of 10^{-12} nm (rad s^{-1})$^{-1}$, which is more than the calculated value in crickets (2×10^{-14} nm (rad s^{-1})$^{-1}$ [107]. Magnetic polymeric structure-based sensor responses quickly and is sensitive for air flow detections, which comprised a hair-shaped PDMS pillar wrapped by iron nanowires [108]. These AHL sensors suffer from common challenges and problems which are listed as below [109] :

- The effect of thermal drift on the accuracy and sensitivity of piezoresistive AHL sensor could not be neglected.
- There is still charge leakage for some of piezoelectric materials used in the piezoelectric AHL sensor.
- Capacitive AHL sensors suffer from significant loss in sensitivity because of high output impedance.
- Magnetic AHL sensors are affected by external magnetic field.

The selection of materials depends on the type and function of each AHL sensor. Besides liquid metal alloy, single-wall, or multi-wall CNTs, macromolecule polymer materials, including PDMS, Poly (methyl methacrylate) (PMMA), Polyvinylidene fluoride (PVDF) etc. can be considered. Materials with a low elasticity modulus is important in a sensing component, as the flexibility plays a main role in the sensor. Metallic materials such as Au, Gr and Pt are good candidate for the fabrication of electrodes in AHL sensors [110]. The design of AHL sensor is dependent on the final application, and the framework of each AHL sensor can be completely different from another type of AHL sensor, having different thickness, length, and width. For an example, when the aspect ratio of AHL sensor needs to be taken into account, the fabrication methods, such as UV (Ultraviolet) lithography, Deep reactive ion etching (DRIE), followed with Physical Vapor Deposition (PVD) or Chemical Vapor Deposition (CVD), can be applied [111-114].

The technology for MEMS-based micro speakers and microphones has been applied in CIC-type HAs to overcome existing problems [115]. The acoustic-induced vibration of bio-inspired approach to be transduced to an electrical signal can be realised through different methods. Many researchers used piezoelectric materials in an effort of achieving a self-powered sensor without the need of an external power source. One example was PVDF-based cantilever beams for cochlear implant construction, conducted in early 2000s [116]. The reason for using PVDF instead of ceramic piezoelectric materials was its greater range of motion, higher voltage sensitivity, better acoustic impedance in air and water, and higher voltage output [115 -117]. Another MEMS scale hair sensor based on piezoresistive materials was developed for application as strain gauges. Designing HAs with features of simple, sensitive, self-powered and small in size is highly demanding in future.

2.4 Polydimethylsiloxane (PDMS) pillars introduction as artificial hair like sensor of stereo ciliary (stereocilia)

Hair cells' role is to transduce mechanical vibration into electrical signals in the cochlea membrane [103], [117-118]. The flexibility of the materials able to detect minute vibration is important. For implantable devices, biocompatibility is vital. It relates to the complete chemical and biological interaction between the body and device surface [119-120].

Low toxicity, durability, high dielectric strength, low surface energy (hydrophobic surface) properties of PDMS, made it an excellent choice for such a sensor device. For mass production reason and increasing the chance of using a mould repeatedly, a semi-permanent mould for PDMS pillars fabrication is preferred [121-128]. The most challenging and critical step in PDMS micro pillars fabrication is the demoulding process.

2.4.1 Microfabrication technique

Industries such as microsystems/MEMS, Integrated circuit, and solar cells are based on microfabrication technologies which are in the dimension ranges of 0.1 µm to 100 µm in width and the typical thickness ranges from 10 nm to 1 µm. Fig. 2.9 illustrates the processes for microfabrication [125].
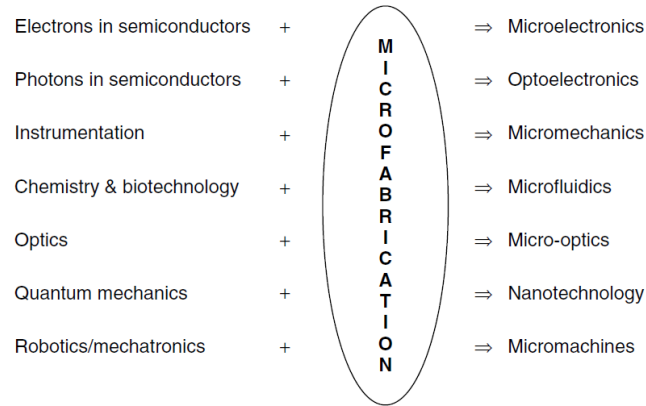
Fig. 2.9 Microfabrication technology and its applications [125].

Various processes for the fabrication of high aspect ratio pillar (or cilia) arrays for mimicking micro/nanoscale structures can be divided into two types basically, the top-down and bottom-up methods, as illustrated in Fig. 2.10. The fabrication of hierarchical structures, like micro-pillars, is usually involving the standard and micropatterning techniques which make the entire fabrication more challenging.
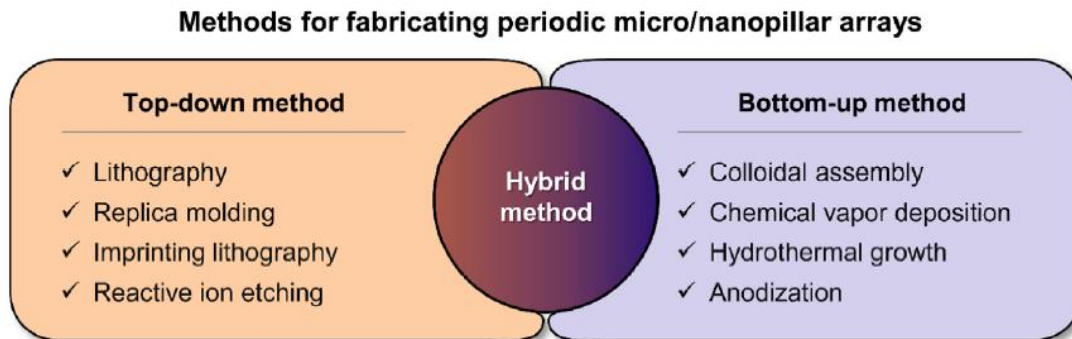
Fig. 2.10 Fabrication methods for micro/nanopillar arrays [126].

Most of top-down methods have been developed by using techniques such as deep-reactive ion etching (DRIE), X-ray lithography, laser abrasion and UV lithography [129-132]. In addition, electron beam and ion beam lithography have been studied. However, among these methods, UV lithography is dominant, since it is suitable for mask making in manufacturing [133-134]. Due to the minimum feature size and limitation of printing below the microscale, imprinting lithography is not recommended for pillar fabrication. The shrinkage rate of polymers for higher aspect

ratio and smaller sizes still remained a technical challenge [135-138]. Although manufacturing advanced microstructured devices with a high degree of precision can be achieved by laser micromachining, one of the biggest challenges of laser micromachining is the requirement of chemical modification to the material after this process. This is not precisely achievable when handling PDMS [135]. These fabrication methods are less cost-effective, and demoulding the structure from these methods is always challenging [131], [138-139].

Regarding DRIE, apart from its advantage on upright morphology of pillars fabrication, multiple steps of complicated mould fabrication are required. Furthermore, fluoro-coating for the mould is an inevitable step, which usually involves an evacuation coating step by using (1H, 1H, 2H, 2H-perfluorooctyl) silane on the mould [140-143], which raises biocompatible concerns.

Bottom-up methods are mainly based on the fabrication of a rigid static arrays of pillars from CNTs or metal oxides. One of these methods is the use of Anode Aluminium Oxide (AAO) as a master template to grow pillar arrays of metal oxides or CNTs, via a Physical vapour deposition (PVD) or chemical vapour deposition (CVD) process. Other template materials, such as titanium oxide (TiO_2) ring arrays, have also been used for the growth of zinc oxide (ZnO) nanorod arrays for optoelectronic devices [140].

Polymers could be fabricated using direct lithography patterning if they are photosensitive (when there is no reaction with the light as the resist solution forms) or by the use of a template to form moulds (which is usually SU-8 resin or silicon). Based on low optical absorption in the UV range, the SU-8 could be applied for the UV light with 365 nm wavelength. The use of UV lithography is an economical method for the industrial applications compared with the other methods. PDMS pillars had been moulded by this technique in a wide range of scales from μm to nm sizes. For direct fabrication of devices, the polymer could be patterned out of SU-8 moulds by the use of UV light and a mask [143-144]. The pattern needs an accurate master which is mainly fabricated by photolithography [145-147]. For high aspect ratio fabrication of mould of 1-100 μm and lengths of 100-500 μm, photolithography uses a negative photoresist (SU-8) on a silicon wafer [143].

The modern microfabrication technology is available in the IC industry with or without silicon. For the semiconducting properties of silicon materials, they could be used in several applications like MEMS (micro electro-mechanical systems). As an example, a silicon chip achieving protection of the sensor from the atmosphere can be covered by a glass layer on the top [144]. For microstructure fabrication, the integration of different materials with silicon or glass is advantageous for the final products which results in low cost in some cases, good biocompatibility and easy bonding between polymers and glass at low temperature [143], [147-148]. To achieve longer PDMS pillars, higher thickness of the master template is required, and SU-8 resin was suitable for this purpose [149-151].

2.4.2 Photolithography technique introduction

In photolithography, light is used to transfer a geometric pattern from a photomask. The range of wavelengths for the light source is from short to extremely long. It starts from very short value of UV wavelength (10-14 nm) to longer UV wavelength levels of (150-300 nm) and higher values equal to UV (350-500nm) [148]. The procedure could be applied to produce small patterns down to a few tens of nanometres in size by using shorter light source. The standard process steps of photolithography and pattern transfer are illustrated in Fig. 2.11, using an oxidized Si wafer and a negative photoresist system. First, 1 µm thick layer of negative photoresist is spin-coated on the oxidized wafer surface (Fig. 2.11a and 2.11b). Next, after the exposure step (Fig. 2.11c), the wafer should be rinsed in a developing solution to get rid of the unexposed areas on the photoresist and leave a pattern of the exposed regions on the wafer surface (Fig. 2.11d). There are four main steps for UV lithography process which are summarized as below:

1. The appropriate photoresist films.
2. The mask alignment with the wafer.
3. The exposure.
4. Pattern development in development solution.

SiO$_2$ ($-$1μm)

n-type silicon

(a) Oxidation

Negative photoresist coat ($\pm$1μm)

SiO$_2$

SI

(b) Lithography preparation

UV light

Glass plate

Opaque pattern

Hardened resist

(c) Exposure

(d) Unexposed photoresist removed by developer
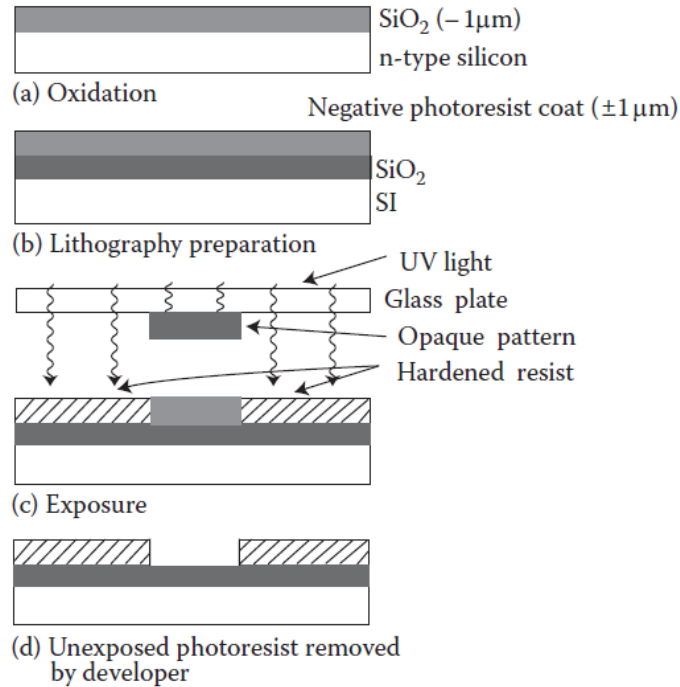
Fig. 2.11 The photolithography procedure consisting of several steps: (a) oxidation of the layer, (b) photoresist coating, (c) exposure, and (d) development [148].

After proper alignment between the photomask and the photoresist coated wafer, the radiation of UV light exposure will change the solubility of photoresist for selective areas in the development step. Three factors, including optics for radiation generation, responses of the photoresist and mechanical alignment of the photomask and wafer, determine the resolution of the final patterns.

After irradiation with UV light through the mask, the exposed area of the SU-8 photoresist layer will turn into the cross-linked part, and the baking step is to improve further and complete the cross-linking. Due to its high cross-linked matrix and high thermal stability, an incredibly good resolution could be achieved for the fine features.

According to the absorption, reflection and diffraction laws, the profile of microstructures may be determined by the dose of the incident light, however the actual behaviour of SU-8 resist is still beyond theoretical understanding, as no

reliable references are available. Further development and modification of current exposure data are needed.

2.4.3 Pattern Generation

To transfer a precisely geometric design from an optical mask to a light sensitive photoresist coated on the substrate, a pattern is made [125]. A computer-aided design (CAD) tool or Solid Work software can be used, and different features from lower dimensions of 500 nm to higher values of 500 µm patterns can be designed and printed on a transparency mask. When dimensions are more than 8 µm, a transparent polymer sheet is applied for the pattern fabrication, however a thin layer of metal mostly chrome on a glass slide for dimensions less than 8 µm is used which is higher in resolution compared with the polymer sheet [149]. The fabricated photomask is positioned between the UV lamp source and the photoresist surface thin layer on the silicon (Si) wafer.

2.4.4 The negative SU-8 photoresist

There are two types of photoresists, negative and positive. For the negative photoresists, they are less soluble in the developer solution after getting exposed to light, and the solidified area will be remained on the surface of the wafer, while the positive photoresists are more soluble after getting exposed to light in the developer solution. The exposure reaction is to separate the main and side chains of polymers, making them more soluble in development solutions for positive type of photoresist (almost 10 times more soluble). The difference between these two photoresists are illustrated in Fig. 2.12 [148].

(a) Negative photoresist. Photoresist is photopolymerized where exposed and rendered insoluble to the developer solution.

(b) Positive photoresist. Exposure decomposes a development inhibitor, and developer solution only dissolves photoresist in the exposed areas.
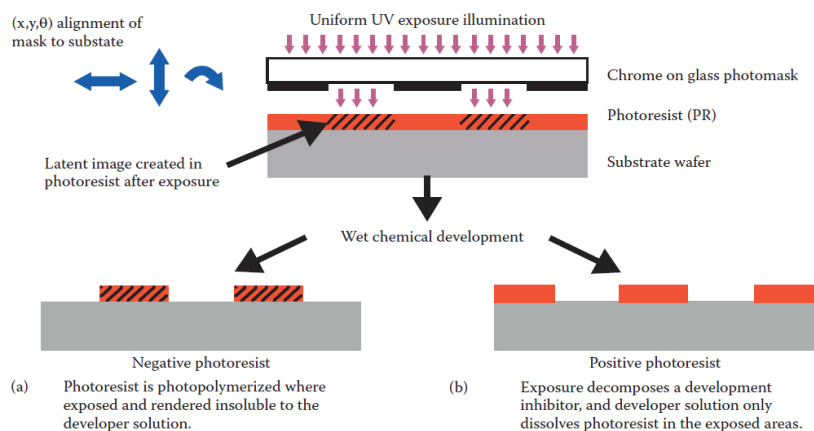
Fig. 2.12 (a) Behavior of negative photoresist to exposure, development and pattern transfer in the exposed region (b) and Positive photoresist properties after exposure, development and pattern transfer in the exposed region [148].

Diverse types of photomasks are available for different feature sizes. When they are small, laser-written chrome photomasks could be helpful, while for larger dimensions (≥20 µm), masks could be written onto plastic films by using a high resolution printer (≥3000 dpi) [150]. The precise microscale fabrication of PDMS pillars can be achieved by the application of a negative photoresist and UV lithography, using two steps. SU-8 is a negative acid-catalysed chemical amplification photoresist, with a full name of EPON SU-8 epoxy resin, patented (US Patent No.4882245 (1989) by IBM [150]. It is viscous enough to be spun from a range below 1 µm up to above 1000 µm on the surface of wafer [151]. The main elements of SU-8 are a Bisphenol A Novolak epoxy oligomer (EPON® SU-8 resin, Shell Chemical) and a photo acid generator up to 10 wt.% triarylsulfonium hexafluroantimonate salt (CYRACURE® UVI, Union Carbide), and they react via heating to cross-link [152]. Eight groups of epoxy sites for each monomer molecule make the high degree of cross-linking possible (Fig. 2.13).
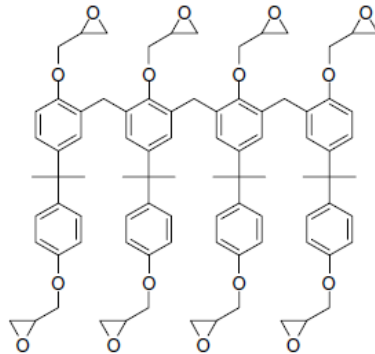
Fig. 2.13 Eight epoxy groups in the chemical structure of SU-8 to help the photoresist polymerization upon heating [152].

At the highest level of cross-linking for SU-8, a glass-transition temperature around ~200 °C, degradation temperature around ~380 °C and a Young's modulus E~4-5 GPa could be achieved (Table 2.5), which makes it suitable for the fabrication of high aspect ratio and three-dimensional lithographic patterns.

Table 2.5 Physical and chemical properties of SU-8 [153].

Property	Value
Young's modulus, E (post-bake at 95 °C)	4.02 GPa
Young's modulus, E (hard bake at 200 °C)	4.95 ± 0.42 GPa
Biaxial modulus of elasticity, $E/(1 - v)$	5.18 ± 0.89 GPa
Film stress (post-bake at 95 °C)	16–19 MPa
Maximum stress (hard bake at 200 °C)	34 MPa
Friction coefficient (post bake at 95 °C)	0.19
Glass temperature, T_g (unexposed)	~50 °C
Glass temperature, T_g (fully cross-linked)	>200 °C
Degradation temperature (fully cross-linked)	~380 °C
Thermal expansion coefficient (post-bake at 95 °C)	52 ± 5.1 ppm K^{-1}
Polymer shrinkage upon cross-linking	7.5%

To achieve a uniform coating of the SU-8, spin coating is normally used. The thickness T of the polymer during spin coating could be calculated according to the Eq. 2.1 [154].

$$T = \frac{KC^{\beta}\eta^{\gamma}}{\omega^{\alpha}}$$

Eq. 2.1

where K is the overall calibration constant, C is the polymer concentration in g/100-mL solution, η is the intrinsic viscosity and ω is the number of rotations per minute, for the various exponential factors of α, β and γ values.

2.5 Piezoelectric properties

The "piezoelectricity" word stems from the Greek words "piezō'' (πιέζω) and "ēlektron" (ήλεκτρον), meaning "electricity conversion out of the pressure". There are some particular materials which could produce electricity when exposed to a mechanical stress [155]. Piezoelectric materials have 20 sub-classes and are a sub-class of dielectric materials. When an external force is applied on a piezoelectric material, the lattice will be polarized due to the charges of unit cells, as illustrated in Fig. 2.14.
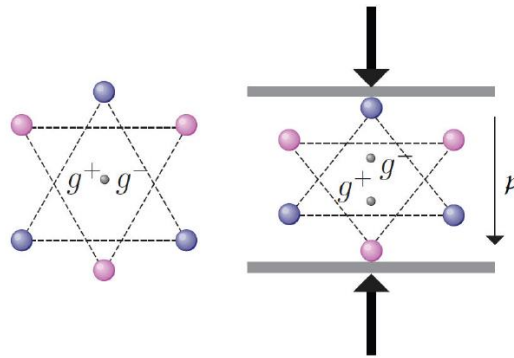
Fig. 2.14 piezoelectric unit cell with or without applied external forces. The centers of electric charges are as g^+ and g^- [156].

In 1880, Pierre and Jacques Curie, stated the phenomenon of piezoelectricity. The piezoelectricity properties have been found in a few crystals that have no center of symmetry along the piezoelectric axes. A mass of individual dipole areas in ferroelectric ceramics is dispersed in various crystallographic orientations, which could result in a net dipole moment of zero [157]. When the process of poling takes place, the dipole regions will be aligned due to the electrical field applying through the whole material. An electric field is developed in these crystals when a stress is applied, and a mechanical deformation happens when an electric field is applied [158-162].

2.5.1 Piezoelectricity formation

For piezoelectric materials, depending on the crystal orientation, an anisotropic structure is essential. They contain 3 axes and 3 rotations, as illustrated in Fig. 2.15.
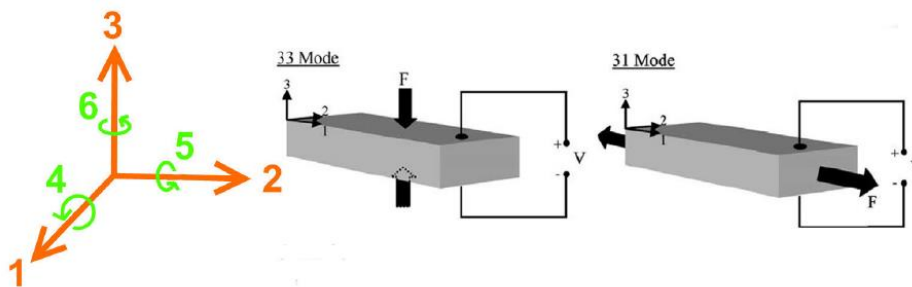
Fig. 2.15 Piezoelectric axes for the crystal orientation and two different modes of 31 and 33 [162].

For the thickness of the sample, axis 3 is placed, and axis 1 is for the length side of the sample. The direction of generated voltage index is *i,* and the *j* index is for the direction of applied stress. There are 36 flexibility coefficients *s*, 18 piezoelectric coefficients *d* and 9 permittivity coefficients ϵ for the piezoelectricity behaviour definition. The matrices of *s, d* and ϵ are shown as Fig. 2.16.

$$s = \begin{bmatrix} s_{11} & s_{12} & s_{13} & 0 & 0 & 0 \\ s_{12} & s_{22} & s_{13} & 0 & 0 & 0 \\ s_{13} & s_{13} & s_{33} & 0 & 0 & 0 \\ 0 & 0 & 0 & s_{44} & 0 & 0 \\ 0 & 0 & 0 & 0 & s_{44} & 0 \\ 0 & 0 & 0 & 0 & 0 & 2(s_{11} - s_{12}) \end{bmatrix} \quad d = \begin{bmatrix} 0 & 0 & 0 & 0 & d_{15} & 0 \\ 0 & 0 & 0 & d_{15} & 0 & 0 \\ d_{31} & d_{32} & d_{33} & 0 & 0 & 0 \end{bmatrix}$$

$$\varepsilon = \begin{bmatrix} \varepsilon_{11} & 0 & 0 \\ 0 & \varepsilon_{22} & 0 \\ 0 & 0 & \varepsilon_{33} \end{bmatrix}$$

Fig. 2.16 All of coefficient matrices for piezoelectric materials [163].

Among all materials, the most common piezoelectric materials are ceramic PZT (Pb [Zr_xTi_{1-x}] O_3,0≤x≤1), natural materials like quartz, and metallic materials such as AlN or $KnbO_3$. Polymeric materials such as Polyvinylidene fluoride (PVDF) and its copolymers are also known as excellent biocompatible piezoelectric materials [162]. The piezoelectricity properties of PVDF, together with its good formability, biocompatibility, flexibility, and low acoustic impedances, made this material very attractive for biomedical applications. Intensive research in this area has been reported for various flexible electroactive devices based on its thin films or one-dimensional (1D) fibers [164-168].

The main feature of piezoelectric materials is to generate electrical charges when exposed to an applied stress or small source of mechanical deformation. The electricity generated could eliminate the need for external power source to power microdevices by providing the electricity under stress/deformation. Lead-based piezo ceramics, including barium titanate, lead titanate and lead zirconate titanate, exhibited good piezo performance, however their toxicity and environmental impacts limit their biomedical applications. In this regard, piezoelectric polymers that are nontoxic, having superb flexible, being light in weight and easy to fabricate, are more suitable for tissue engineering and biomedical applications [169-175].

2.5.2 Polyvinylidene fluoride (PVDF) piezoelectric polymer and its piezoelectricity

PVDF is a chemically stable, semi-crystalline polymer with excellent mechanical properties and high piezoelectric coefficient (d_{33} = 49.6 pm/V) [176-178]. It has five crystalline phases, of which the β phase has three all-trans (TTTT) planar zigzag conformations, the α and δ phases arrange in TGTG' and the γ and Є phases arrange in TTTGTTTG', while (T) and (G) stand as trans and gauche linkages. The α phase is the most common form and is available in commercial films. The β-phase has the orientation of dipole moments in the same direction to allow it responding to stress/deformation to exhibit high piezoelectric properties [176-180]. Among all phases of PVDF, the β-phase exhibits stronger piezo-, ferro- and pyroelectric effects than other phases [179], [181-183]. Furthermore, the β-phase possesses relatively high dipole moment due to the polymer chain arrangement in a single line of hydrogen and fluorine, which endows it with high piezoelectric coefficient. The piezoelectric performance of β-phase PVDF has been widely explored for different applications such as electromechanical actuators, micro-electromechanical devices, and energy harvesters [184-185].

2.5.3 β-phase piezoelectric formation of PVDF polymers

The high piezoelectric performance for PVDF is only achieved by the formation of β-phase. Mechanical stretch is the main technique of polar phase formation in PVDF; however, the β-phase transition of PVDF can be classified as four individual methods, as illustrated in Fig. 2.17, which are melting, solid state drawing, annealing, and high electric field poling processes. From the melt process to produce PVDF thin films, high pressure or high temperature is needed, and subsequent quenching and annealing processes will lead to the crystallization of β-phase, as illustrated in line 1 in Fig. 2.17 [186-191]. In the second line, the stretching annealing, or poling converts α- to β-phase. The uniaxial drawing of α- to β-phase is a typical technique to achieve the piezoelectric character [192-194]. For high pressure crystallized PVDF film, the mechanical drawn PVDF improved its piezoelectric properties, with the maximum β-phase being around 85% [193-194]. The transformation of γ-phase to β-phase happens after poling at 120 °C [195-197]. Finally, as shown in the fourth

line, δ-phase of PVDF can transform to β-phase when an high electric field is applied [194].
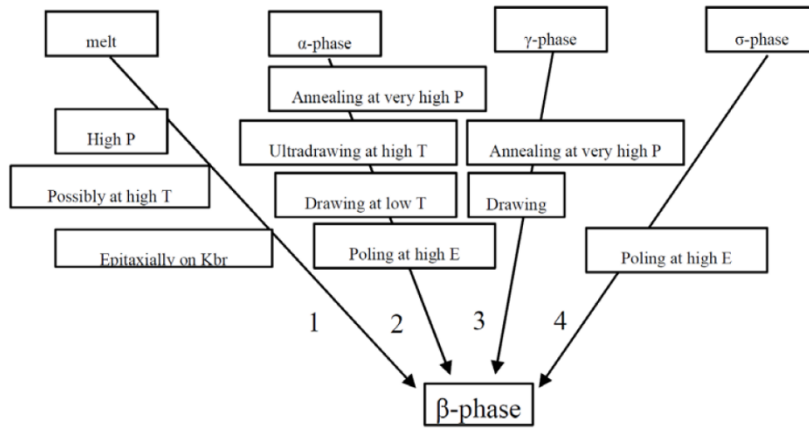
Fig. 2.17 Different routes to achieve β-phase PVDF [180].

Solvent casting in dimethyl formamide (DMF), dimethylacetamide (DMAC) and dimethyl sulfoxide (DMSO), spin-coating and solvent evaporation are the other methods to achieve β-phase PVDF films [197-198]. Among all methods, electrospinning, being simple, low cost, and highly efficient, is a preferred technique to fabricate PVDF nanofibers. In particular, the high voltage applied during the fiber spinning would favour the formation of the desired β-phase, which would omit any extra steps for achieving the piezoelectric phase, and could convert almost all α-phase to β-phase during this process [199-201].

2.5.4 Piezoelectric energy harvesting

Converting mechanical vibration energy from the surrounding environment to electric requires piezoelectric materials [201-202]. Quartz crystal microbalance and PVDF acoustic wave device have been the two main types of piezoelectric energy harvesters, of which PVDF based sensor has been used to measure the variation of the resonance [201-203]. This, together with its excellent biocompatibility, opens the door to construct vibrational and mechanical measurement devices in the body [200]. PVDF has also been studied for the fabrication of other micro electromechanical devices and energy harvesters for medical applications, such as nano transducers interacting with living components, by taking advantage of the mechanical driven piezoelectric properties [179-180]. As a result, electrode implantation is no longer

needed, as the electric signals could be initiated by mechanical forces like compressions, vibrations and sound subjected by the body [204-207].

2.5.5 Improving the piezoelectricity of PVDF

Existing research has reported that a parallel dipole formation will help to increase the β-phase content of PVDF, therefore increase the piezoelectric response [204]. Additives of different nanofillers have an effect on the piezoelectricity properties, such as metallic oxides, graphene oxide, Polyaniline (PANI) and barium titanate [207-208]. While some additives are believed to improve the piezoelectricity in terms of β-phase crystallization in PVDF electrospun fibers, the others could lead to degradation, therefore each material of different concentration in the base PVDF solution needs to be carefully investigated. A nucleating agent will make the transformation from α-phase to β-phase easier. For example, both barium titanate (BT) nanoparticles and graphene could promote the formation of stronger O-HF-C binding with the hydrogen atoms, which leads to more β-phase and smaller diameters for the electrospun fibers [209-217]. On the contrary, adding SiO_2 nanoparticles to the PVDF solution led to thicker electrospun fibers and beads formation, with less β-phase content, due to increased viscosity in the PVDF solution [218].

The conversion of low-frequency mechanical motions from human activity into electricity has been used for the fabrication of piezoelectric Nanogenerators (PENGs) and energy harvesters, which could act as self-powered piezoelectric devices, such as artificial pacemaker, by putting a single crystalline piezoelectric $(1 - x)Pb(Mg_{1/3}Nb_{2/3})O_3 - xPbTiO_3$ on a plastic substrate or by using a hybrid-fiber piezoelectric generator [219-237]. The collection of energy from vibrations, acoustic and mechanical deformations into electrical energy can be realised by using synthetic materials [238-242]. This piezoelectricity property has been applied in numerous devices including transducers, surface acoustic wave (SAW) devices and various fields of engineering and biomedical for the high level of energy conversion efficiency [242-243]. The micro-electro-mechanical-systems (MEMS) based on PVDF electrospun fibers scaffold devices sensors, have been utilized in

biocompatible devices implantable in human body owing to the their piezoelectric properties [243].

Many biocompatible nanoparticles, such as zinc oxide (ZnO), multi-walled CNTs, ttitanium oxide (TiO_2), lithium chloride (LiCl) and tungsten (VI) oxide (WO_3) has been previously reported, which provide useful information for adding them to the PVDF solution to create electrospun fibers [243-246].

2.5.6 Piezoelectric materials in the medical applications

2.5.6.1 Force and vibration detection

PVDF-based sensors have been developed to monitor vibrations of physical movements. To enhance the performance of a Vibrating Intravascular Lung Assist Device (VIVLAD), a PZT actuator along with a PVDF sensor was built to establish the relationship between the increase in the value of output signals of PVDF and the oxygen transfer rate, as shown in Fig. 2.18 [241].
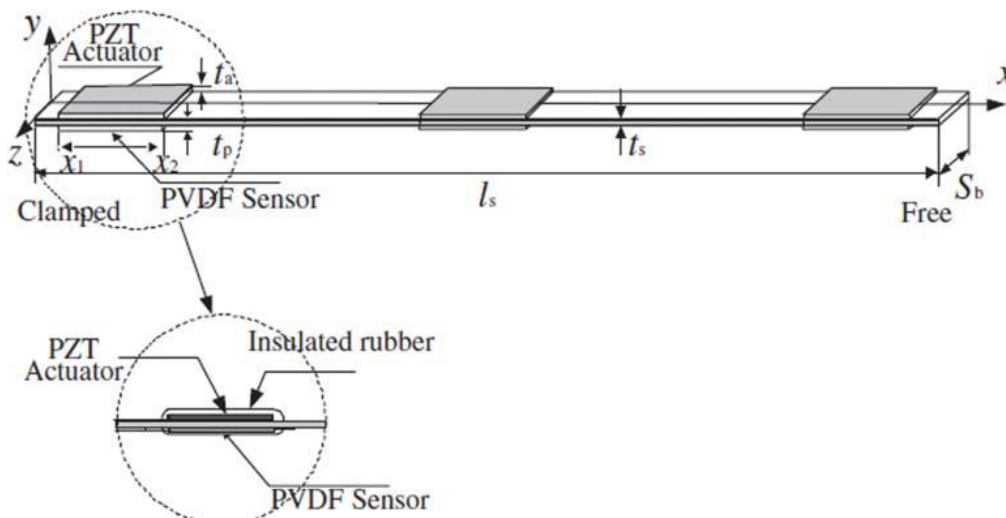
Fig. 2.18 VIVLAD device development for patient having chronic respiratory problems [241].

PVDF film was used to sensing the contact-type vibration, by connecting with a curved silicone rubber to measure the tensile force in the rope [242]. Further improvement by using a curved PVDF film to replace the flat PVDF film led to an 151% improvement in the signal, Fig. 2.19 [243].
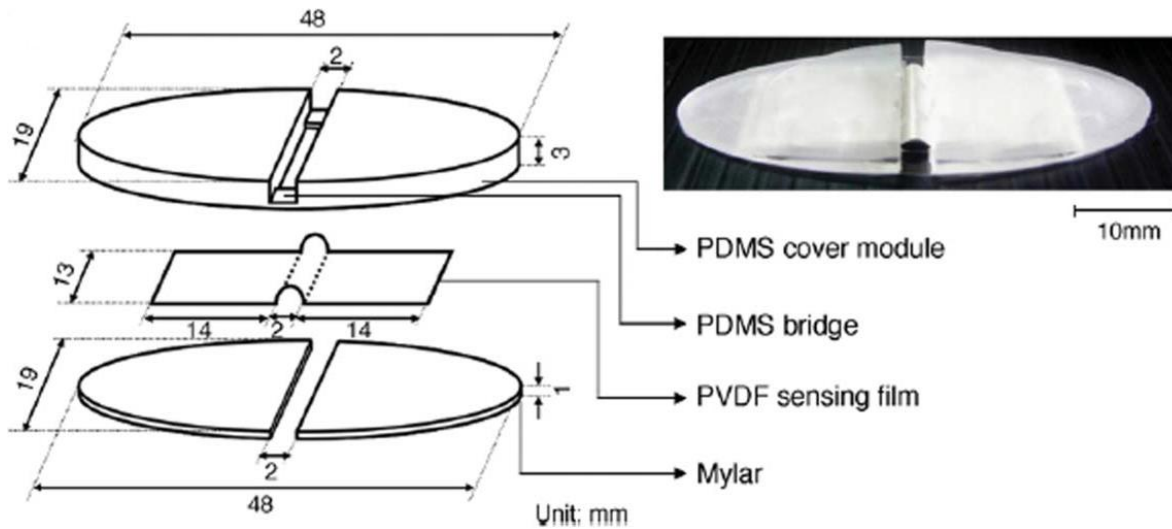
Fig. 2.19 PVDF sensor patch as the curved and flat types [243].

2.5.6.2 Acoustic sensing

PVDF sensor has also been developed to sensing the heartbeats, by linking a microphone with Ag/AgCl electrodes placed under the human's heart [244]. While the sensitivity of the PVDF films for acoustic emission non-destructive testing (NDT) is very high, their application for health monitoring should be reflected very cautiously due to the considerable temperature discrepancies of the PVDF films [245].

The detection of flow turbulence of the air and fluidic medium has been reported based on PVDF fiber arrays, although valid piezoelectricity characterizations of the materials were not completely investigated [246]. A theoretical vibration sensor model based on PVDF films has been proposed to quantify acoustic waves, and its low-frequency performance could be improved by the floor partition, as shown in Fig. 2.20 [247].
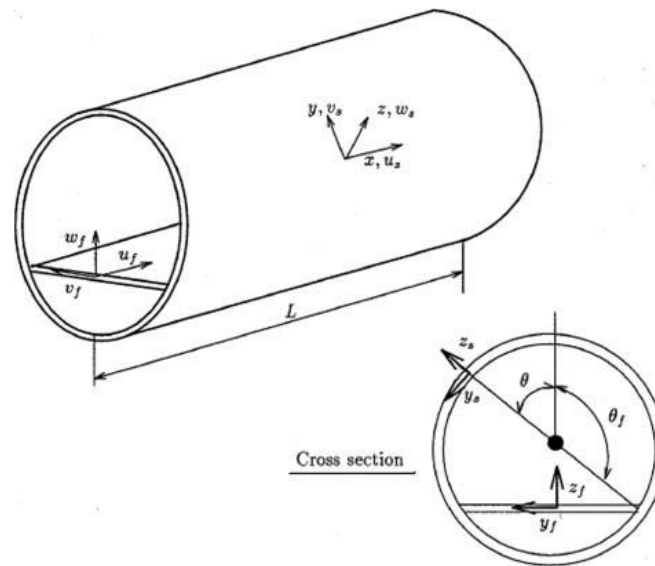
Fig. 2.20 The cylindrical shell and the floor partition cross sectional design schematic [247].

2.5.6.3 Piezoelectric materials applications in hearing devices

An energy efficient artificial structure of hair cells in cochlea can motivate the application of artificial structures in replacing broken natural ones. The transduction mechanisms can be implemented in implantable devices. The types of transduction mechanisms are like piezoelectricity (mechanical strain), electromagnetism (magnetic induction), triboelectricity (frictional contact and electrostaticity), etc. Mechanical energy is related to the materials implantable for hearing systems, as it is directed to the hearing process before converting to electrical power by mechanoelectrical transduction. As the conversion of acoustic energy into electrical energy happens in microphones, the piezoelectric based structures are one of the best choices of transduction method for transformation in making reduced structures instead of the common microphones in HAs. Among all types of HAs, implantable ones can transfer sound into vibration energy which can be driven to the ear. For this purpose, implantable piezoelectric HAs are extremely important in terms of the power and size criteria, because piezoelectric transducers consume less power, are less expensive and completely reliable in electrical signals into mechanical motion conversions [248].

Most of the widely used transducers in HAs are the magnetic air-gap hearing transducers, in which the electrical signal drives a MEMS electromagnetic actuator. Although this technique can be affordable, inadequacies are still present. For instance, the narrow air-gap between large surfaces makes the fabrication process more complicated [249]. In contrast, the simple structure in the piezoelectric HAs could prevent feedback distortion which is common in an air-gap magnetic HA [250]. The power level of piezoelectric transduction transduced mechanical vibrations is in the range of micro and milliwatts. This level of power for piezoelectric energy harvesting is suitably sufficient for an in vivo energy harvester in hearing systems. For wearable biomedical applications, electrospun nanofibers are suitable, due to their flexible and stretchable structures, and high beta-phase content [251].

Koyuncuoğlu et al., applied a PZT piezoelectric energy harvester positioned on the tympanic membrane. This MEMS acoustic energy harvester can transduce the acoustic waves into electrical signal to increase the power of the hearing systems. The device consisted of a PZT thin film layer between gold electrodes, as illustrated in Fig. 2.21. The thin film was deposited with a conductive epoxy using wire bonding in a Si cantilever which was placed on a 40 μm parylene vibrational membrane similar to the ear drum. They have achieved a maximum output power of 16.25 μW and voltage of 2.47 V [252].
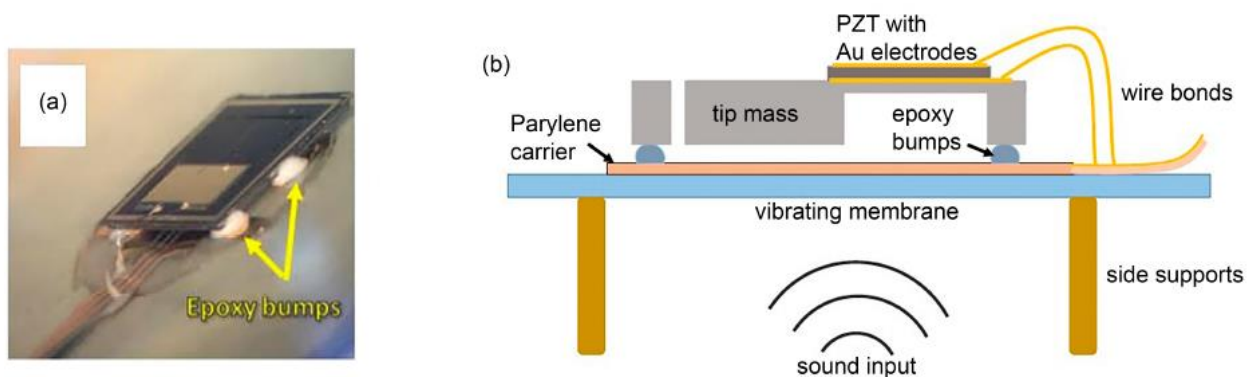
Fig. 2.21 (a) The view of MEMS acoustic energy harvester chip, (b) The piezoelectric transducer mimicking membrane of the ear drum. Adjusted from [252].

Another inorganic piezoelectric acoustic nanosensor (iPANS) and a PZT thin film as biomimetic artificial hair cell was fabricated by Hyun Soo Lee et al. For this structure a silicone-based membrane acts as the natural basilar membrane. A 2-μm thick PZT film was thermally treated at 650 °C for 45 min. A bonding between a flexible supporting substrate (PET) and PZT film was created by ultraviolet (UV) curable polyurethane (PU) adhesive. The pattern of Au deposition was realised by radio frequency (RF) on the PZT film. The silicon-based membrane included a single flexible iPANS attached on its surface with double sided adhesive tape, as shown in Fig. 2.22. The vibrational displacement of iPANS was almost 15 nm and the electrical sensing output was 55 μV. Also, the maximum detected sound frequencies were limited to 1000 Hz which is lower to cover the human hearing range (20 Hz-20 kHz) [253].
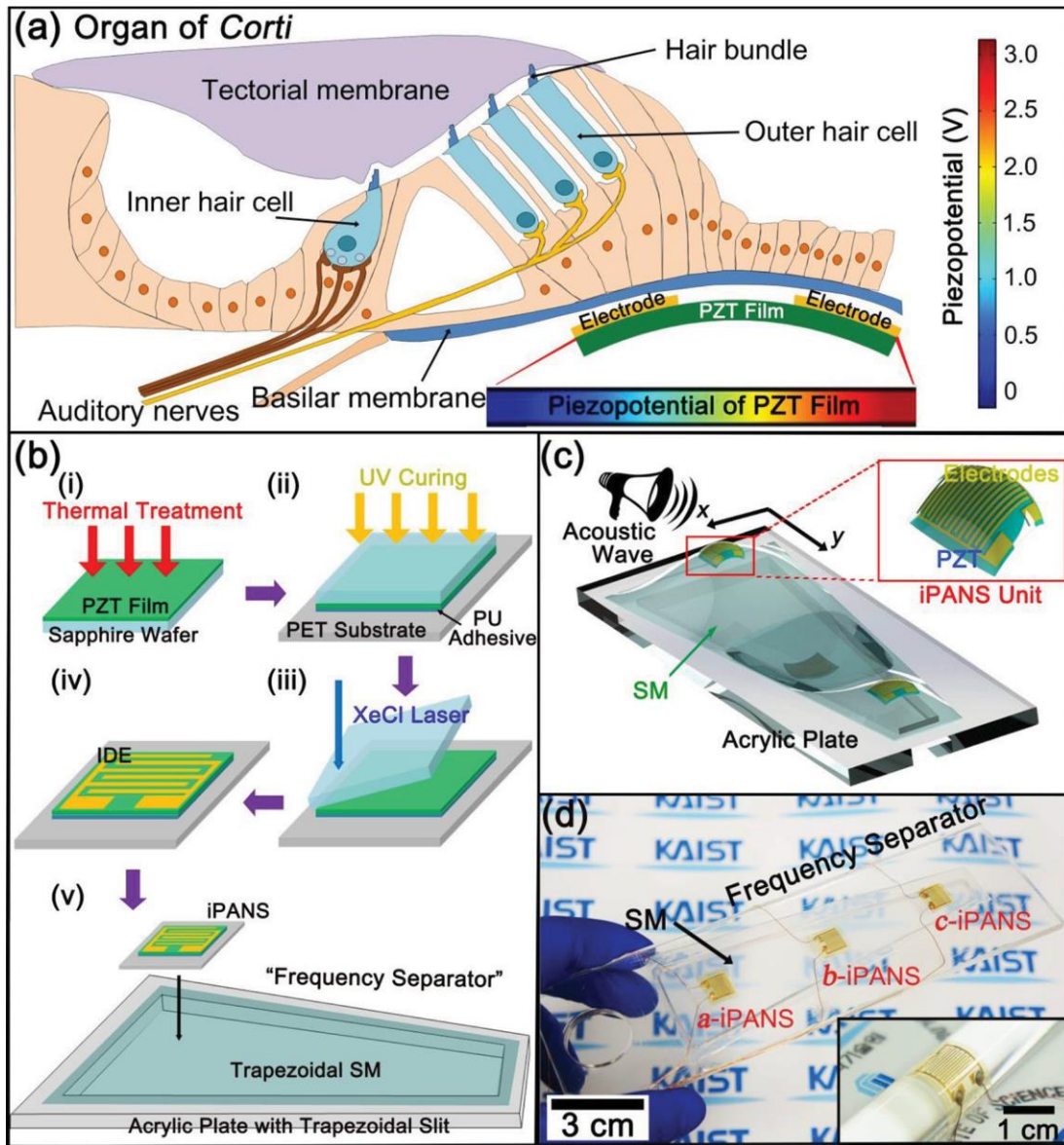
Fig. 2.22 (a) Schematic of Corti in mammalian cochlea and the thin PZT film placed under Basilar Membrane (BM), the PZT film is bending upwards with a height of 600 nm, (b) Steps needed for iPANS fabrication, (c) Silicone based membrane vibration due to acoustic waves for which iPANS is deformed after it is mechanically stressed and converts the vibration deformation into electricity, and (d) The frequency separator with iPANS which is attached to a glass rod [253].

A further PZT-based MEMS system as acoustic energy harvester was reported by Tomioka et al [254]. The device has two top Al electrodes and the whole area was 5×5 mm^2. The lower electrode is Pt/Ti layer. The PZT thin film was spin-coated onto the lower layer of the electrode on the silicon substrate, Fig. 2.23. The wet

etching solution made the electrode patterns on PZT substrate. The power of this acoustic energy harvester is 52.8 pW [255].
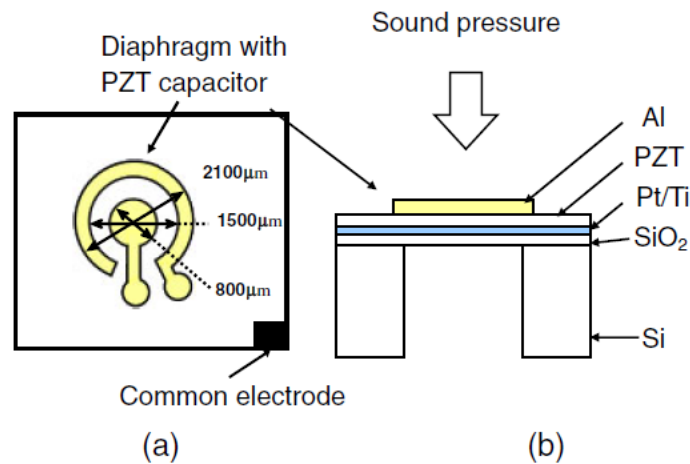
Fig. 2.23 (a) Energy harvester with PZT diaphragm top view, and (b) cross section of the energy harvester device. Modified from [255].

Hyun Han et al. reported a self-powered flexible piezoelectric acoustic sensor, inspired using basilar membrane in cochlea. This acoustic sensor contains Pb $[Zr_{0.52}Ti_{0.48}]$ O_3 (PZT) membrane responsive to the acoustic stimuli. Because of the low sensitivity of this MEMS acoustic sensor, an amplifying circuit was applied which led to the increase in power consumption [255]. These reports showed great progresses in the implementation of PZT in the cochlea, however PZT containing lead is harmful and poisonous to the body and the environment, which therefore cannot be categorized as biocompatible materials.

When PVDF is applied between two electrodes, the generation of voltage is similar to the stimulation of the nerves such as hair cells in the cochlea when the sound hits them. This material can be applied as the source of power for the self-powered devices replacing the stimulus battery in CI. The incident sound pressure waves can initiate the energy source in the cochlea.

Inaoka et al, developed a hypothesis relevant to an artificial cochlear epithelium including a piezoelectric membrane without a battery for a deaf guinea pig (Fig. 2.24). This prototype used a 40 μm PVDF membrane fabricated by

microelectromechanical system. This membrane was positioned at the BM in the cochlea for detection of BM movement when the sound provocation starts, but the electrical output was not enough for auditory nerves stimulation. For the stimulation of auditory neurons, Pt/Ir ball electrodes were inserted into the Scala of the cochlea, which generated electrical output in the range of 0.14 to 5.88 mV [256].
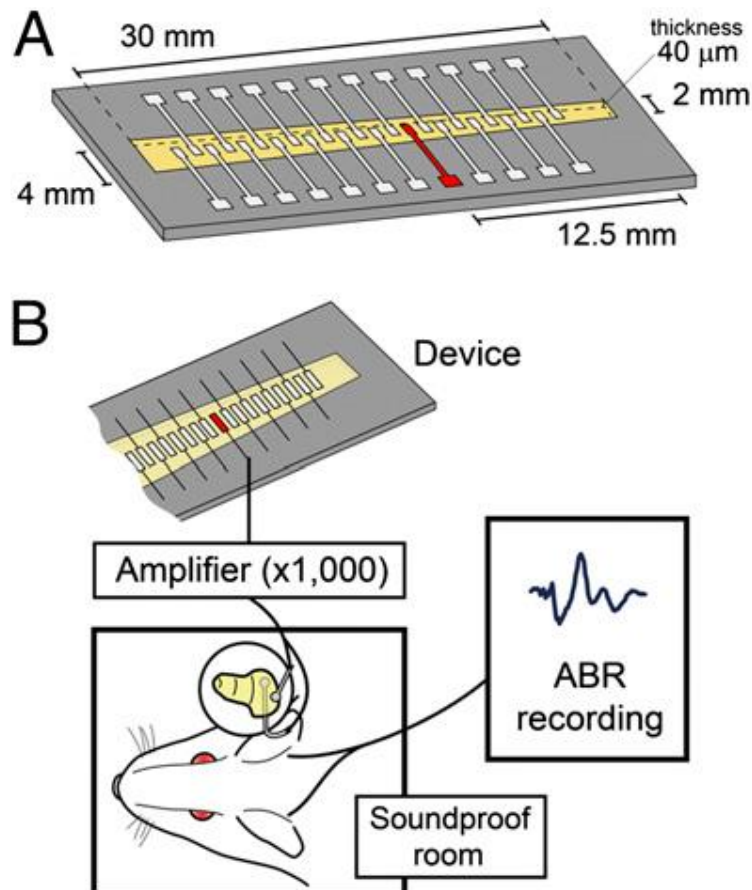
Fig. 2.24 (a) A piezoelectric membrane consisting of an array of 24 aluminum thin film electrodes hearing, and (b) The generation of electrical signal in response of acoustic stimulation [257].

Other reports positioned a PVDF membrane on the basilar membrane of the cochlea to act as auditory hair cells [258], to convert acoustic energy to electrical signals. Harada et al. used the traditional semiconductor fabrication technique to prepare the cantilevers from silicone; while Shen et al, used silicon nitride instead [258-259]. For both studies, the power consumption was high, the device fabrication was not simple, and the processing circuit was complex due to the increase in

numbers of cantilevers to cover the whole audio frequency range. In comparison to these studies, Xu et al. presented an array of polymeric micro-cantilever for the cochlea biological mimicry which can be used in both of advanced hearing aids and in complete cochlear implants. The performance of this product was mechanically similar to the natural organic material in the basilar membrane. The power consumption was less than those used semiconductors [260]. Mota et al., produced a piezoelectric nanocomposite of PVDF fibers and barium titanate nanoparticles to increase the piezoelectric properties of PVDF, and suggested its potential application in cochlea stimulation [261].

2.6 Summary

This Chapter first provided an overview of the recent research on the development of HAs. From the several types of hearing loss, the broken and injured hair cells have been identified as one of the key issues. By developing and implementation of effective HAs, those who suffer from hearing loss will dramatically improve their quality of life, hence an immensely major area of research. It then reviewed several aspects of existing technologies for the development of HAs, which covered the processing of artificial hair cells including the moulding and tip-links, the materials selection, the sensing performance, the toxicity, and their respective limitations. Based on the review, it appears that a PVDF-based HA could offer the advantages of easy fabrication, highly flexible, bio-compatible, low-cost, and exhibiting piezoelectric performance over existing ceramic and metallic materials, which could lead to the creation of next generation of self-powered HAs, benefiting millions of people with hearing loss issues. This therefore inspired me of choosing the relevant research topics of this PhD programme.

As a materials engineer, I hope to make my contribution towards tackling the hearing loss issues by using advanced nanomaterials, to benefit those who need it. I therefore define the current project as a material-focused research activity, although it possesses obvious multidisciplinary features. The overall aim of this dissertation is to study and develop a low cost, highly effective, bio-compatible HA with potential self-powered feature, without the need of external power source. To accomplish this aim, I have accordingly designed separate objectives to address

various challenges that affecting the HA performance. Detailed objectives are outlined as follows:

- To synthesise a SU-8 semi-permanent mould having the desired structures of exposed holes in four arrows, with different depths, starting from the deepest holes to the shortest ones.
- To investigate the morphological structure of SU-8 mould and prepare the right mould for the PDMS solution casting.
- To fabricate the PDMS micropillars of graded heights, so that they could response to various frequencies.
- To observe and investigate the electrospinning process to produce PVDF spun fibers of uniform diameter, smooth and pure, and to understand the reasons.
- To optimise different parameters and obtain PVDF fibers with maximum performance.
- To investigate why some PVDF electrospun fibers could reach the highest piezoelectric properties.
- To understand the effect of additives like WO_3, ZnO, CNTs, TiO_2 and LiCl on the piezoelectric and triboelectric properties of produced nanocomposite fibers and further improvement of piezoelectric properties associated with the β-phase content.
- To construct a HA prototype with the desired acoustic response, biocompatible and self-power functions.

Chapter 3: Experimental methodology

3.1 Introduction

In this Chapter, a generic introduction of different techniques used in this thesis, including the mould fabrication, materials processing, characterisation, property assessments, etc., will be presented. Further specific structure and property characterization techniques for each specific material will be explained in more details later in the relevant Chapters.

To accomplish the overall aim of creating an artificial hair cell-based, self-powered, HA prototype, vast characterization techniques will be involved in different stages to fully understand the materials performance. We first need to create the PDMS polymeric based materials as the vertical micro pillars of different heights, then form the tip-link by using electrospun PVDF nanofibers, to mimic the hair cell functions, with the self-powering ability. Therefore, PDMS materials selection, moulding, and patterning techniques used in the moulding process will be introduced. For tip-link fabrication, to achieve a full understanding of the PVDF polymer, the electrospinning process and the spun fibers, thorough compositional and structural characterization will be required. To further improve the performance of PVDF polymer, different fillers will be used to generate composite fibers, which demands thorough phase, structural and morphology characterizations. For achieving the self-power feature, a fundamental understanding of the piezo- and triboelectric behavior of the resulting PVDF fibers need to be investigated. Finally, to ascertain the biocompatibility and suitability of the HA prototype, cell culture and simulation will be carried out to address the toxicity and performance aspects. Therefore, a diverse technique across multiple disciplines will be used in this thesis, which will be briefly introduced. To have a clear idea of the work packages involved, a flowchart of the materials, processes, and key characterization techniques is shown in Fig 3.1.

(1) UV lithography technique for the SU-8 mould fabrication

(2) PDMS solution preparation and casting on the fabricated SU-8 mould

(3) First step of Au thermal evaporation as the underneath electrode layer on the cured PDMS pillars in different heights

(4) Optical and SEM characterization of SU-8 mould

(1) PVDF solution preparation including pure PVDF powder in DMF/Acetone mixture

(2) Electrospinning technique for electrospun fibers fabrication

(3) Second step of Au thermal evaporation as the above electrode layer on top of electrospun fibers

(4) SEM, TEM, XRD, FTIR XPS, DSC, PFM, Triboelectric test, Raman Spectroscopy

(1) PVDF solution preparation including pure PVDF powder and additives in DMF/Acetone mixture

(2) Electrospinning technique for PVDF composites electrospun fibers fabrication

(3) SEM, TEM, XRD, FTIR XPS, DSC

(1) Pure PVDF and its additives triboelectric and acoustic sensing investigation

(2) Cytotoxicity analysis COMSOL simulation

Au - Top electrode
PVDF and its composites electrospun layer
PDMS micro pillars
Au - Bottom electrode
PDMS substrate

Fig. 3.1 The synthetics and characteristics procedures of produced device and its components presented in Chapters 4, 5, 6 and 7.

3.2 Materials and synthesis technique

3.2.1 Materials

The synthesis of the Polydimethylsiloxane (PDMS) pillars involved three key materials: the negative photoresists of SU-8 2025 and SU-8 2500 series (purchased from MicroChem Corp, USA), the Photoresist developer, and the PDMS SYLGARD(R) 184 Silicone Elastomer kit including the monomer and hardener (purchased from Farnell). Silicon Wafer substrates for the UV lithography of SU-8 were purchased from PI-KEM Limited company (UK). For wafer cleaning, both Isopropyl alcohol (70% in H_2O) and Acetone were used and purchased from Sigma Aldrich.

For the thin film preparation of electrospun polyvinylidene fluoride (PVDF) fibres and their composites, the following raw materials from Sigma Aldrich (UK) were used: PVDF powder with a mean particle size of 20 micron (1×10^{-6} m) and an

average molecular weight of 524,000 g mol^{-1}; N, N-dimethylformamide (DMF) anhydrous, 99.8%, molecular weight 73.09; and Acetone molecular weight 58.08; Tungsten Oxide nanoparticles (WO$_3$, <150 nm particle size); Zinc oxide particles in three different particle sizes (ZnO, <1 μm, <200 nm and <50 nm); Multi-walled Carbon nanotubes (CNTs <300 nm particle size); Titanium (IV) oxide, rutile, (TiO$_2$ <600 nm particle size); and Lithium Chloride (LiCl <1 μm particle size).

For cytotoxicity analysis of the fabricated prototype, cell cultures had been carried out, and materials used for the assessments, including the HCT-116 (human colon cancer) and HEK-293 (embryonic kidney), and Dulbecco's Modified Eagle Medium (DMEM) were purchased from Sigma-Aldrich (UK).

3.2.2 SU-8 mould preparation

3.2.2.1 Preparation of wafer before photolithography procedure

As one of the key steps of wafer preparation prior to any photolithography application, cleaning of wafer is important, as contaminants will have a strong impact on the performance of the device. Contaminants including solvent stains (e.g., methyl alcohol, acetone, trichloroethylene, isopropyl alcohol, and xylene), dust and smoke particles from operator and equipment could complicate further processes, such as oxidation and evaporation of wafers. The process was therefore conducted in clean rooms. The clean-room equipped with a variety of facilities such as wet benches, hotplates, spin-coater, and exposure tool called UV-lithography (Karl Suss MA6BA6) Suss Mask Aligner. 10×10 and 20×20 mm^2 square Si wafers were cleaned and sonicated for around 30 min first in acetone and then in IPA (Piranha etch 70% H$_2$SO$_4$, 30% H$_2$O$_2$) for another 30 min, at room temperature. To remove any moisture on the surfaces of substrate, the cleaned Si wafer were baked for 30 min at 150 °C (Fig. 3.2a and Fig .3.2b), followed with cooling to room temperature on a hot plate, to avoid cracks occurrence on the surface.
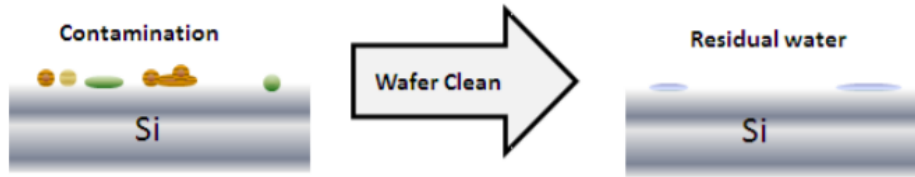
Fig. 3.2a Cleaning of the surface of Si wafers from contaminants.
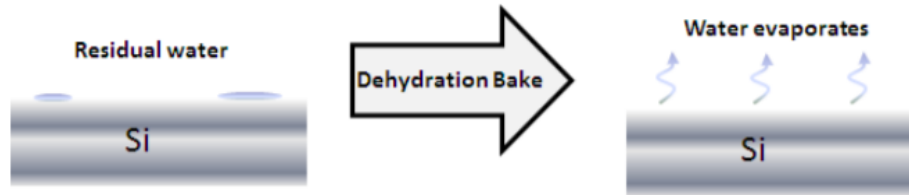
Fig. 3.2b Dehydration bake of Si wafer at 150 °C.

3.2.2.2 Photomasks

The template used for the generation of a desired pattern on photoresist coated wafers is called a mask [262], which was designed by using the CAD software. The absorber metallic pattern on the photomask is opaque to UV light and transparent for the glass or quartz. Masks could be positive or negative like photoresists. For the negative or clear field mask, the pattern is dark, and the background is clear, whereas for the positive or dark field, the pattern is clear, and the background is dark. The mask polarity for different light fields is illustrated in Fig. 3.3.
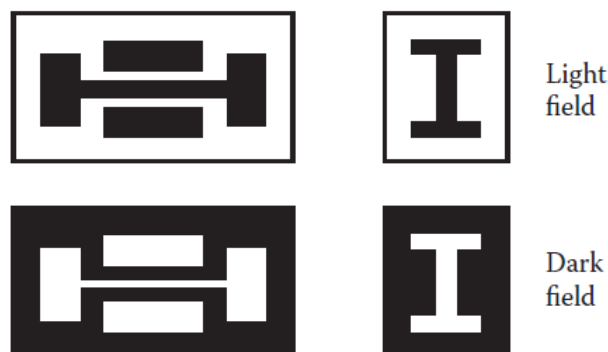
Fig. 3.3 Light and dark fields [148].

3.2.3 Electrospinning for PVDF nanofibers fabrication

The set-up for electrospinning is illustrated in Fig. 3.4, which consists of a feeding pump, high voltage power supply, needle, rotary drum collector, and syringe containing the PVDF fluid. The three voltage 10, 15 and 20 kV, and the feeding rates of 1, 3 and 5 ml h^{-1} are applied. The distance between the needle and the collector has chosen 3 values of 10, 15 and 20 cm. These parameters will be investigated to assess their effects on the final spun fibers. The collector is covered by a piece of aluminium foil of $250 \times 200\ mm^2$ and thickness of 0.163 µm, to collect the electrospun nanofibers for later analysis.

3.2.3.1 The pure electrospun PVDF fibers

Each stock polymer solution of different PVDF concentrations (Sample A:1.50 g, Sample B:1.65 g and Sample C:1.80 g) in the mixture of DMF/Acetone (3/7 volume ratio) solution is fed into the needle gauge 18 (Size: OD:1.27 mm, ID: 0.838 mm) of the electrospinning machine at room temperature, separately. The investigations of different parameter set, including the applying voltages (10, 15 and 20 kV), the distance between the needle and the collector (10, 15 and 20 cm), feeding rates (1, 3 and 5 ml h^{-1}) and rotary speeds of the collector (400, 800 and 1200 rpm) have been conducted. The rotary collector can help to create aligned fibres in large areas. Depending on different characterization purposes, the electrospun fibers were collected. For instance, for SEM characterization, a square of $10\ mm \times 10\ mm$ silicon wafer was used to directly collect the PVDF fibers. For other characterizations, PVDF electrospun fibers were collected by clean tweezers and put into 3 ml vials, from the silicon wafer or Al foil (Fig. 3.4). The diameter of the rotary collector in our study was 100 mm.
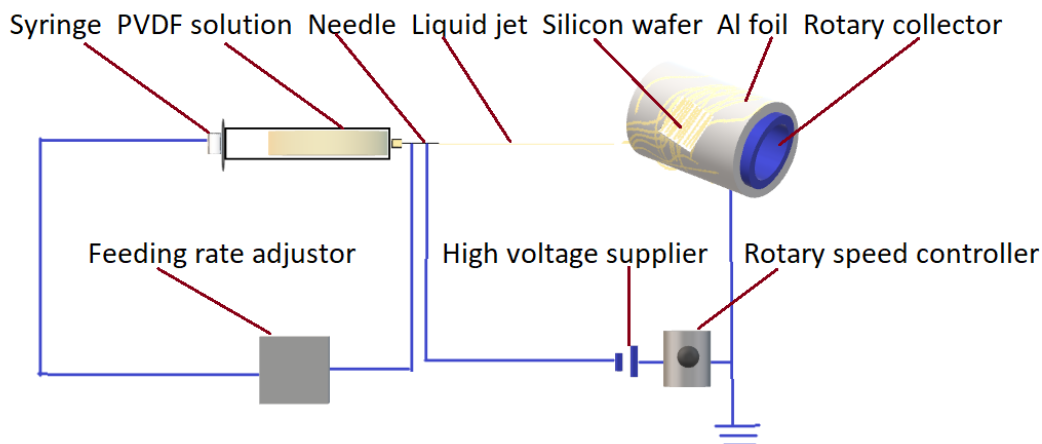
Fig. 3.4 Schematic of the electrospinning set-up.

Pure PVDF electrospun sheet was prepared from 1.50 g of pure PVDF powder with DMF/Acetone (3/7 volume ratio) mixture in a 10 ml vial that was left on a hotplate at 70 °C for 24 h with 600 rpm of magnetic stirrer, to achieve a uniform solution. For the composite mixtures of PVDF, each additive was added to 0.75 g of PVDF powder and after they were mixed and dispersed, (3/7 volume ratio) mixture of DMF and acetone was added to the mixture of powder and the whole container was heated at 70 °C, like the pure PVDF solution preparation routine. Seven types of filler will be investigated in this work, including WO_3, ZnO of varied sizes (<1µm, <200 nm and <50 nm), CNTs, TiO_2 and LiCl. After the solution was ready, the electrospinning machine was set to optimized values for the distance between the needle and collector = 15 cm, applied voltage = 20 kV, feeding rate 3 ml h^{-1} and the rotary collector speed of 1200 rpm for pure PVDF and its composite, at ambient temperature. The whole process takes almost 2 h for each sample to allow for sufficient sample accumulation. The details of each additive will be addressed in Chapter 6.

3.2.4 Thermal evaporation deposition of gold

To form a conductive surface of PDMS substrate as the first electrode and another conductive layer on top of PVDF electrospun fibers, Au coatings are prepared. There

is a piezoelectric sandwich layer between two Au electrode elements on top and underneath of PVDF electrospun sheet.

Two thin films of Au coatings on the surface of the cured PDMS substrate and PVDF electrospun fibers were prepared by using a HHV Edwards Auto306 thermal evaporator. Fig. 3.5a-c shows the HHV Edwards Auto306 thermal evaporator, illustrating the initial round of gold coating and the last step of gold coating.

In each step, the bare PDMS substrate or the finalized prototype was put in the evaporator at a distance of about 8 cm from the boat holding two high pure gold wires 99.99 % around 0.5 g. The chamber was closed and pumped down to better than $2x10^{-6}$ mBar at approximate speed deposition rate of 0.5-1 nm s^{-1}. The chamber was heated up 1100 ºC which was hot enough for the gold evaporation on top of each part in separate step. The heat would not affect both bare PDMS substrate or any other specimens. The bond between the Au and PDMS is strong enough to achieve good conductivities.
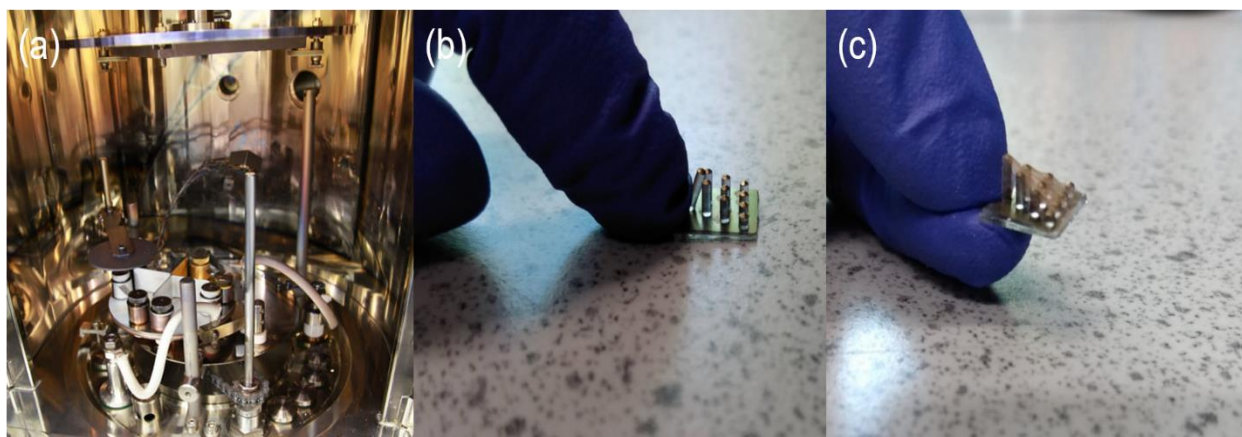
Fig. 3.5 (a) The thermal evaporation chamber, (b) the bare PDMS substrate coated with gold, and (c) the whole artificial device coated with gold on top of the PVDF electrospun fibers.

3.3 Structural and morphological characterization techniques

The structural and morphology of the synthesized materials in this thesis were characterized using several techniques, including X-ray diffraction (XRD), Scanning

Electron Microscopy (SEM), Transmission Electron Microscopy (TEM), Fourier transform infrared radiation (FTIR), Raman Spectroscopy, X-ray Photoelectron Spectroscopy (XPS), laser surface profiler and Optical microscopy.

3.3.1 XRD

To identify the phase of a crystalline material, XRD is a powerful technique. For all different forms either in bulk or powder or thin films, this technique could be applied. Information regarding the structure, phases, preferred crystal orientations and the structural parameters such as the average grain size and crystallinity could be obtained by this non-destructive technique [263]. When a sample is exposed to the X-ray generated in a cathode ray tube, electrons bombard the metal target (anode), and characteristic X-ray spectra will be generated. The constructive interfaces from the incident rays and a diffracted ray interaction is expressed by the Bragg's law: *nλ = 2dsinθ*, where *n* is an integer, *λ* is the wavelength of the X-rays, *d* is the contiguous crystal interplate spacing, and *θ* is the angle between the incident X-ray and the scattering plane (the diffraction angle) [264]. Bragg's law is depicted in Fig. 3.6.
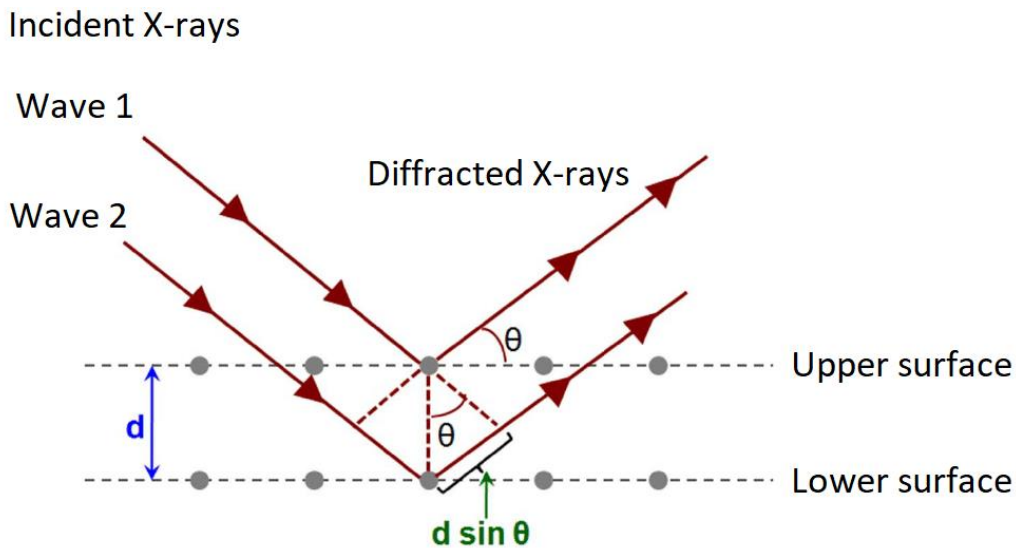
Fig. 3.6 A set of the reflection of an X-ray beam from parallel crystalline phases for the distance travelled (2dsinθ) equal to an integral number of wavelength (nλ) [265].

The constructive interfaces (d_{hkl}) which are produced due to the distance between the crystal lattice planes of the atoms, could be determined by the Bragg's equation [265-266]. Also, the Bragg diffraction peak is related to the average crystallite sizes. The average crystallite size of very finely divided solids can be calculated from Scherrer's formula, $L = \frac{K\lambda}{\beta cos\theta}$, in which K is a constant depending on the particle shape and normally about 0.90, λ is the wavelength of the X-rays, β is the width of the beam at its half maximum value, θ is the half of Bragg angle or the diffraction angle and L is the average size of particle in a direction perpendicular to the Bragg planes [267]. Throughout all testing, the machine will automatically record data including the photon intensity and detector angle 2θ, which will be plotted as 2θ versus intensities, to generate a diffraction profile for a material.

In this thesis, a D8 advanced X-ray diffractometer (XRD, Bruker, UK) working with a Cu-Kα radiation (λ = 0.154 nm) and operating at 40 kV and 40 mA was applied to identify and quantify the powder and electrospun nanofibers we fabricated in this work. About 0.3 g of the fibrous sample was cut with a clean scalpel and collected from the aluminium foil with a pair of tweezers, which was then simply flattened and positioned on the surface of a clean glass substrate for scanning. A 2θ range of 10º -70º and a step size of 0.03º with a dwell time of 1 s scan parameter was generally used for our samples. For analysis and comparison of the results, the EVA (Evaluation) program was applied.

3.3.2 SEM

This system is designed for directly studying the surface of a sample. During investigation, the top surface of the sample is directly hit by a highly concentrated electron beam which is passed through a magnetic lens. An electron gun produces electrons to be accelerated through an anode plate. Scanning coils force the electrons to scan over the surface area of the sample, which can then be viewed in a backscattered or secondary mode on a monitor, using images formed from the primary back scattered electrons, secondary electrons and X-rays [268]. A cathode ray tube receives all signals which are collected by different detectors and translate them to a 2-dimensional image on a screen. Apertures help to define the beam and

prevent electron spray using condenser lenses. Also, the objective aperture controls the contrast in the image which is located below the sample after the objective lens. To control the final focusing of the beam, the objective lens perfects the magnetic field strength and de-magnifies the beam area to around 10 nm. A schematic of an SEM is presented in Fig. 3.7a and b. The primary back scattered, and the secondary electrons are detected by two main detectors in an SEM. The back scattered electrons are the reflection of primary electrons hitting the surface of the sample, while the secondary electrons are from the specimen surface after being excited by the primary electrons. For this thesis, a TESCA VEGA3 combined SEM and Oxford Instrument X-MAXN EDS detector machine (Fig. 3.7c) equipped with a tungsten filament was used, to obtain the morphological and compositional features of samples, operated at 15 kV with a working distance of 15 mm.

For electrospun nanofibers and electrospun coating layer of fibers on a Si wafer, the samples were stuck onto an Al sample holder using a double-sided conductive carbon tape. An ultra-thin Au coating layer (about 2-3 nm) or Cr (around 5 nm) was applied on the sample by a vacuum plasma sputter coater, to grant a better conductivity for the samples. For other samples, such as Si wafer exposed to the UV lithography and negative photoresist, Cr coating of about 6 nm was utilized to eliminate charging.
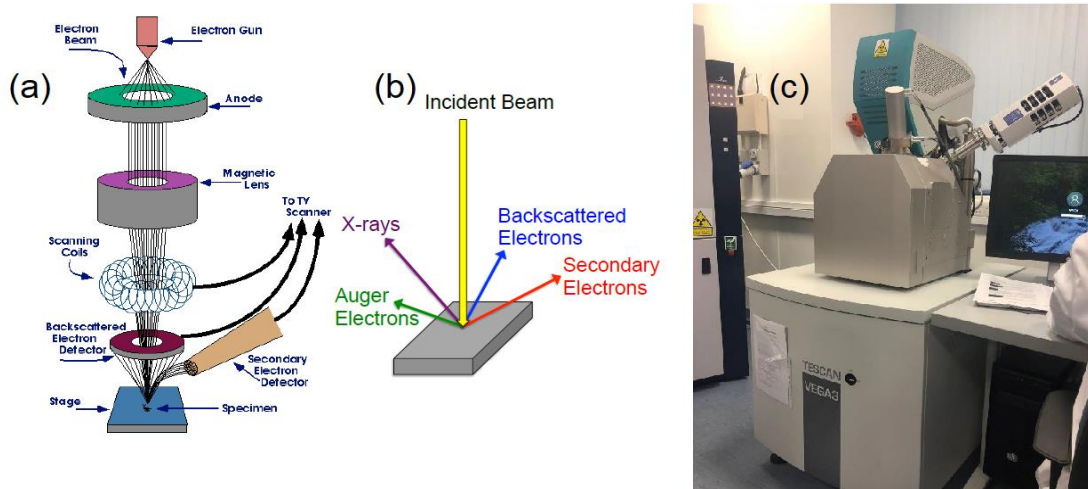
Fig. 3.7 Schematic of (a) an SEM machine column, (b) Interactions between the sample and beam within an SEM [269], and (c) the SEM equipment used in this thesis.

3.3.3 TEM

To achieve a resolution of ~0.1 nm, higher and better resolution than that of SEM, TEM is applied. The internal structure of the specimen in the form of images can be obtained by allowing a beam of electrons passing through the specimen. The electron beam produced by an electron gun was focused onto a thin sample through a condenser, the magnifying system, to obtain the images. It consists of objective lens, movable specimen stage, intermediate and projector lenses [270]. As shown in Fig. 3.8b and c, an accelerated electron beam is like that of the SEM. This beam passes through a very thin specimen to carry information about the structure of the specimens [270]. Part of the beam, which is un-scattered electrons, will be transmitted through an objective aperture and after correction by intermediate lenses on the fluorescence screen, at the bottom of the machine, it will be projected by the projector lens. The thickness of the sample is normally less than 100 nm for better electron transparency allowances.

TEM is one of the most important techniques to allow the beam focusing on one ultra-small area of the sample to present a selected area electron diffraction (SAED) pattern, similar to the X-ray diffraction principles [271]. A ring pattern in TEM-SAED can provide information which can also be seen as an analogous to X-ray diffraction, for which the difference is the use of electrons instead of X-rays. SAED can produce either continuous rings (for multiple crystalline grains) or discrete spots (for a single crystalline grain), depending on the type of grains, to provide detailed information about the phase structure, crystal orientation and lattice spacing for the specimen [272].

To acquire both high resolution transmission electron microscopy (HRTEM) and SAED images in this thesis, a JEM-2100 TEM (STEM) machine is used. It has a 0.25 nm point and 0.14 nm lattice resolutions at 200 kV. TEM samples of the electrospun fibers are prepared on a 3 mm holy carbon coated Cu TEM grid (300 Mesh, Agar). An exceedingly small portion of each sample was suspended in Ethanol (Fisher Chemical) to prevent both contamination and agglomeration of fibers. After probe-sonication for 1 h, a drop of the suspension was transferred by a micropipette onto the top of a TEM grid, which was followed by an overnight drying

at 60 °C in an oven to remove residue solvent, to avoid contamination to the high-vacuum TEM chamber.

Attached to the TEM, an Energy-Dispersive X-ray spectroscopy (EDX, Oxford Instrument System, liquid nitrogen-free SD detector, 80 mm^2, 138 eV) was also used to gain elemental information of our samples.
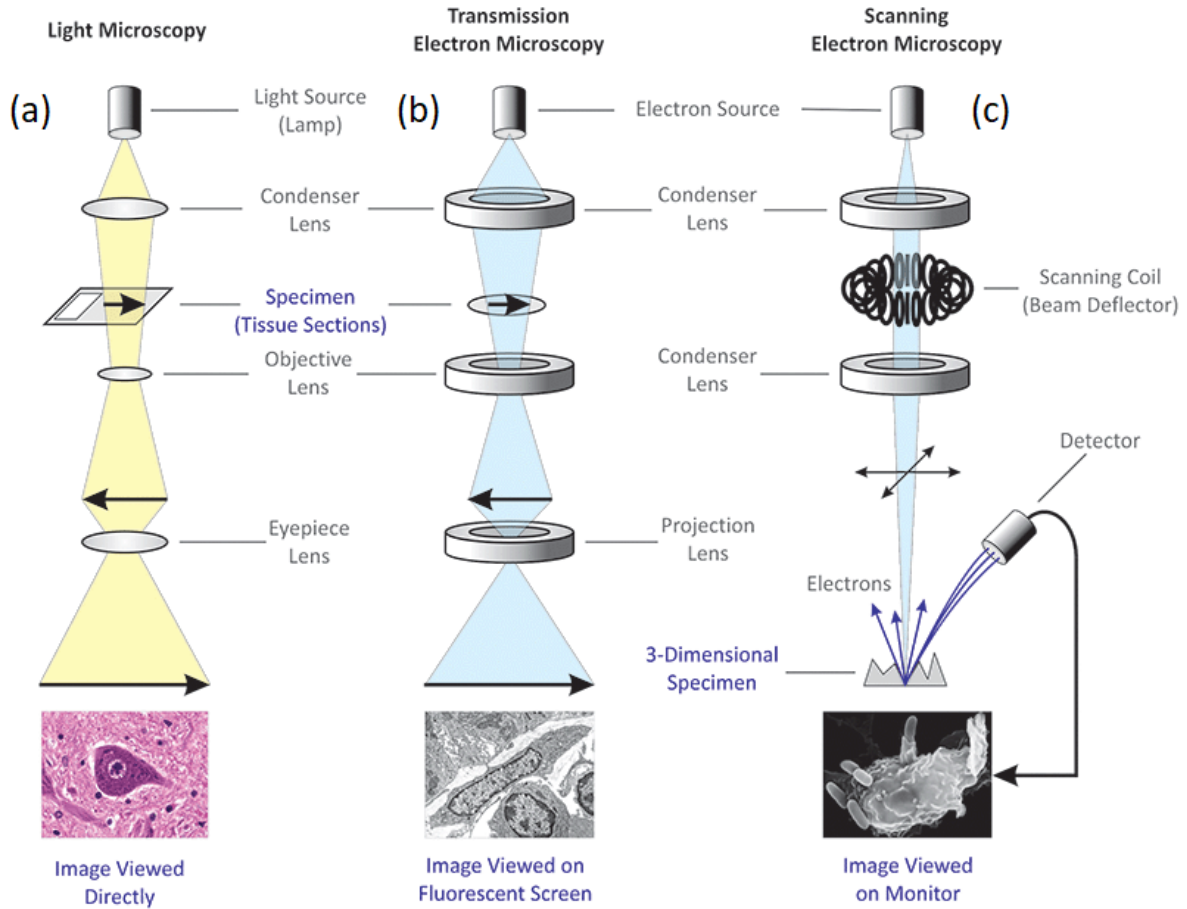
Fig. 3.8 Schematic comparison of different microscopies. (a) an optical microscopy; (b) SEM, and (c) TEM [272].

3.3.4 Optical microscopy

As shown in Fig. 3.7a, this type of microscope allows the user to study sample by the naked eye, after light passing through lenses and curved pieces of glass. In this work, we worked with Nikon LV150 Upright Microscopes with x5, x10, x20, x50 and x100 bright field objective lenses that attached with a digital camera operated with

the Nikon imaging software. The samples were slides of $10\ mm$ x $10\ mm$ Si wafer coated with SU-8 exposed photoresist. On each square, there are several grids of patterns depending on the purpose of each fabrication step. The grids and the holes are micrometer in size, suitable to be observed by an optical microscope.

3.3.5 XPS

XPS, also known as photoelectron spectroscopy, is used for the analysis of surface chemical composition. A solid surface of a specimen has different chemical composition and physical properties. An intense beam of X-ray is an ionizer and can cause photoelectrons to be emitted from initial atomic layers of the surface or the highest valence shell of atoms of the specimen. Spectrum of each sample is obtained from recording of electrons escaping from the surface after hitting the sample with low energy bombardment, ~ 1.5 keV. The interactions between the incident photons and the surface atoms lead to the photoelectric emission of electrons [272]. The determination of both atomic composition and chemical states of a certain element is obtained from atoms emitting electrons of a specific characteristic energy, as peaks in the spectrum. Each spectrum is plotted by the binding energy as a function of the electron counting rate.

In this thesis, sections of the samples were laid on to a double-sided scotch tape attached to a glass microscope slide and pressed flat using a second, solved, rinsed and then ozone cleaned glass slide to ensure samples were clean and flat. A Kratos AXIS ULTRA spectrometer with a mono-chromated Al KR X-ray source (1486.6 eV) operating at 15 kV anode potential and 10 mA emission current, surface penetration of up to 2 nm, spatial resolution as fine as 5 microns, lens magnification of 50x and under high vacuum of p < 10^{-7} Pa condition was applied in this study.

3.3.6 FTIR

To obtain infrared spectrum of absorption, emission, and photoconductivity of solid, liquid and gas samples, FTIR (Fourier transform infrared) can be used. In this technique, the measurements are conducted over a broad spectrum, instead of a narrow band of frequencies, to measure how much light a sample can absorb at each wavelength.

In the current study, FTIR transmittance spectra were obtained between 500 and 2000 cm^{-1} at a resolution of 4 cm^{-1} using 20 co-added scans. 15 mg of nanofibers and particles were thoroughly mixed with 150 mg of potassium bromide (KBr) in an agate mortar. Pellets were formed by pressing the resulting mixtures under 5 tons for 2 min and heated at 60 °C for 2 h, to get rid of residue moisture. Each pellet was placed into an attachment and then analyzed in the optical compartment of the FTIR (Bruker Optics Tensor-27) instrument.

3.3.7 DSC

The melting point, glass transition and crystallization feature of a material are achievable by the DSC (Differential scanning calorimetry) analysis. In this thermoanalytical technique, as a function of temperature, the amount of heat required for increasing the temperature of a sample against a reference, is measured. The temperature of sample and reference is nearly the same during the whole analysis period [273]. Potential thermal transitions of most polymeric materials can be determined by the DSC technique. The most important thermal transitions are the glass transition temperature (T_g), crystallization temperature (T_c), and melting temperature I. The transition from amorphous solid to crystalline solid is an exothermic process, and the melting process is endothermic, which results in different peaks in the DSC signal [273].

A Mettler Toledo DSC 821e/700 was used in this thesis, to analyze different polymeric samples. The electrospun fibrous samples were heated in the DSC machine from 50 to 200 °C and then back to 50 °C at a heating rate of 10 °C min^{-1} under Ar atmosphere at a flow rate of 50 ml min^{-1}. The tests were repeated three times for each sample. % crystallinity values of the resulting PVDF films were calculated using the equation bellow:

$$\text{Crystallinity (\%)} = \frac{\Delta H_{melting}}{\Delta H_{100}} \, x100 \qquad\qquad \text{Eq. 3.3}$$

3.3.8 Raman Spectroscopy

Raman spectroscopy brings a field of major advances in vibrational states of molecules study. As different molecules have different sets of vibrational spectra or

frequencies, this technique can be applied for sample identification and quantification. After irradiation of a light source onto a molecule, photons are absorbed and re-emitted by the molecule [274]. A Raman spectrum will be obtained after the exposure of a sample to the monochromatic source of these exciting photons [274]. There are two modes in Raman scattering including stokes and anti-stokes. In the stoke mode, the photon has lost energy to the molecule, while in the anti-stoke mode, the photon has gained energy from the molecule.

Peak positions in each spectrum illustrate the specific vibration mode of each molecular functional group in the specimen. The energy level changes are different during a Raman scattering, as illustrated in Fig. 3.9.
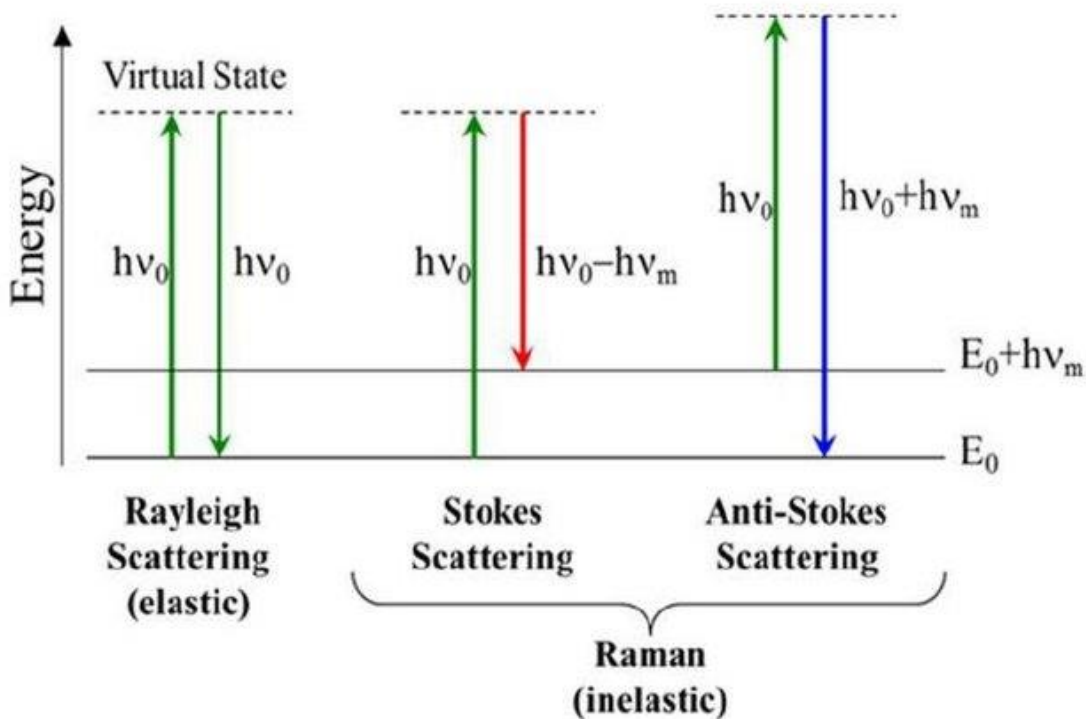
Fig. 3.9 Energy transitions for Rayleigh and Raman scatterings [275].

The molecule prefers to be in the ground state rather than in the excited state, therefore the anti-Stokes scattering is unlikely to occur at room temperature. Also, the majority of the scattered light is of the same frequency as the excitation source, and as a result, there will be no Raman effect, but Rayleigh one.

For the current thesis, an alpha 300 R Confocal Raman Microscope (WITec GmbH) with a laser power of 49 mW was applied to investigate the structure of our samples. A 532 nm laser at 10% power output will be used to excite the sample and scan the wavelength range from 100 to 1000 nm. The solid fibrous sample does not need any specific preparation and will be pressed flat onto a cleaned glass slide, for analysis.

3.4 Property characterization

3.4.1 Piezoelectric property of PVDF fibers

The most important potential of Piezoresponse force microscopy (PFM) in micro and nano scales is its applications for the investigation of sensors, actuators, capacitors, energy harvesting device and microelectromechanical systems (MEMS). As a variant of atomic force microscopy (AFM), PFM can be applied to image and ascertain the piezoelectric or ferroelectric properties of materials, by measuring the accumulation of electric charges of the material when exposed to pressure or other mechanical stresses. This technique is based on the converse piezoelectric effect, for which a very small extension in a sample is resulted from an applied voltage. The deformation is caused by a conductive AFM tip which applies a specified value of voltage on the sample surface. After the deformation, the cantilever is deflected, and the mechanical response is measured. Recently, this technique has been used to characterize nanofibers [276-277].

A piezo response force microscopy (NanoManTM VS, USA) in contact mode of an atomic force microscope was used in this thesis, to characterize the electrospun PVDF nanofibers on a Si wafer substrate, with a conductive platinum/iridium (Pt/Ir)-coated Si cantilever (SCM-PIT). A DC voltage from -12.5 to 12.5 V for all samples of 10 μm x 10 μm square was applied, superimposed on an AC modulation voltage during polarization switching. The PFM amplitude and phase loops were acquired concurrently.

3.4.2 Triboelectric properties of electrospun PVDF fibers

When two different materials coming into contact with each other, both materials' surfaces charge with reverse polarity, which is known as triboelectric charges

[278-279]. Herein the combination of piezoelectric and triboelectric properties for pure PVDF and its composites will be investigated by the set-up shown in Fig. 3.10a. In Fig. 3.10b, the system consists of four main components, a positioning stage power source (Motionlink Ltd), a Galil motion controller (DMC 30012), and a Voice coil actuator/linear motor connected to the KEITHLEY 2612B System (Sourcemeter Instruments). The charges' responses can be measured and collected for the electricity generated by the sensor system, by applying a cyclic compressive load on the sample.
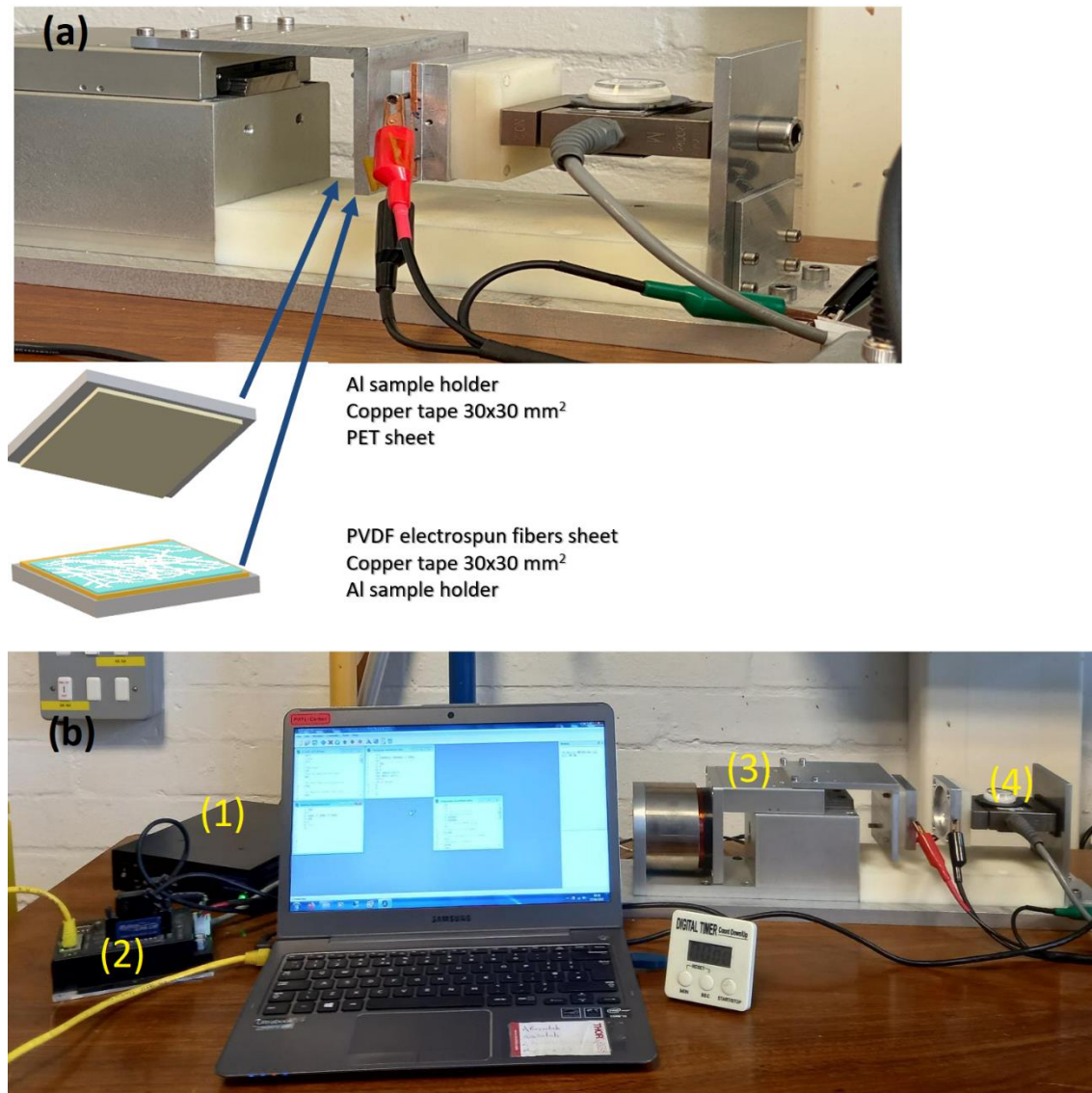
Fig. 3.10 (a) The linear acoustic actuator including two different materials connected to their surfaces, (b) four different components of the system.

To assess the triboelectric performance, we constructed a basic motion sensor to acquire its deformation induced electric signals. The motion sensor includes a thin layer of copper tape, on which a 15 μm thick electrospun PVDF sample is placed. The opposite surface is a thin layer of PET sheet (25 μm thickness) on the other copper sheet. The dimensions of samples vary from $25\ mm \times 15\ mm$, $30\ mm \times 30\ mm$, to $50\ mm \times 50\ mm$, depending on the voltage, electric charge, current outputs, and the machine limitations. For outputs exceeding the machine capacity, the sample was shrunk to $25\ mm \times 15\ mm$ in size. The copper sheet needs

to be cleaned thoroughly with acetone and heated at 60 ºC for 20 min. By applying a repetitive motion load onto the Cu sheet, the PVDF fiber mat will be in contact and apart mode with the PET on the other Cu sheet, and electric signals will be detected. The mean values of 5 peaks for the voltage, current and the electrical charge outputs will be recorded by a Keithley 6514 machine. Pure PVDF and composite PVDF nanofiber mats both were evaluated under the same condition, under the frequency of 1 Hz. A consistent force of 40 N was used, for 2000 cycles during the testing.

The resistance measurement set-up, shown in Fig. 3.11, is based on the Van der Pauw Method, which allows for measuring the average resistivity of the PVDF electrospun sheets.
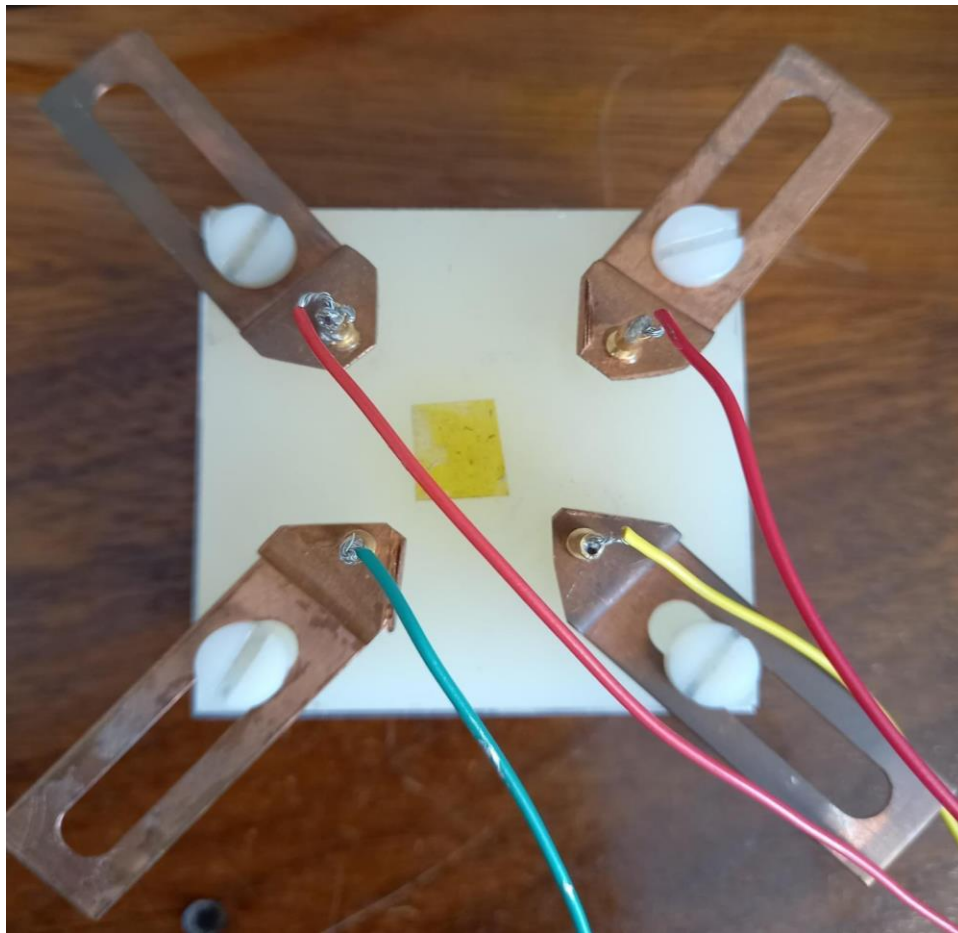
Fig. 3.11 The Van der Pauw sheet resistance setup.

Contacts are numbered from 1 to 4 in an anti-clockwise order, starting at the top-left contact. The current I_{12} is a positive DC current injected into contact 1 and taken

out of contact 2 and is measured in amperes (A) and the voltage V_{34} is a DC voltage measured between contacts 3 and 4, in volts (V). The resistivity ρ is measured in ohms×metres ($\Omega \times m$). The thickness of the sample t is measured in metres (m). The sheet resistance R_s is measured in ohms per square (Ω/sq). Therefore, a current I_{12} causes a flow along one edge of the sample and the voltage across the opposite edge V_{34} and the measurement of a resistance is defined by the following equations:

$$R_{12,34} = \frac{V_{34}}{I_{12}}$$
Eq. 3.4

$$e^{-\pi R_{12,34}/R_S} + e^{-\pi R_{23,41}/R_S} = 1$$
Eq. 3.5

After taking the average of R values, $R_{vertical}$ and $R_{horizontal}$ are calculated, and for the time these two values are equal, the sheet resistance equation will be given as below.

If $R_{vertical} = \frac{R_{12,34}+R_{34,12}+R_{21,43}+R_{43,21}}{4}$ and $R_{horizontal} = \frac{R_{23,41}+R_{41,23}+R_{32,14}+R_{14,32}}{4}$ are equal, then $R_{vertical} = R = R_{horizontal}$, and the sheet resistance Rs is thus defined by the below equation:

$$R_S = \frac{\pi R}{\ln 2}$$
Eq. 3.6

The quotient $\pi.(\ln 2)^{-1}$ is known as the Ven der Pauw constant, as is approximately 4.53236 [280].

3.5 Summary

In this Chapter, we first presented the raw materials used in this thesis, then introduced the generic processes for the synthesis of the electrospun nanofibers, and for the pillar and the complete device fabrication. We also introduced the techniques and instrumentations used in this thesis, to characterise the structural and morphological features of the resulting materials, and to evaluate the piezoelectric/triboelectric performances of the fabricated electrospun fibers.

Chapter 4: The fabrication of PDMS pillars of different heights

4.1 Introduction

The artificial hair cell like sensor prototype is composed of two vital parts, the based PDMS pillars and the artificial tip-links on the top of PDMS pillars. The tip-links are made of PVDF electrospun nanofibers. In this Chapter, we will focus on the first part, the creation of the PDMS pillars of different heights. The fabrication of PDMS pillars by using the SU-8 mould will be presented. Firstly, a female SU-8 mould of different depths of exposed holes on which the male PDMS pillars can be peeled off is designed and produced. This mould is fabricated by a series of steps, including cleaning and preparation of the Si wafer substrates for the negative spin-coated SU-8 photoresist, exposure of the baked photoresist to NanoBeam or UV light for lithography, and finally the development of the exposed SU-8 negative photoresist.

To create the PDMS micropillars as the base sensing part of artificial hair cells, we used a semi-permanent mould. Two lithographic methods by using UV light and NanoBeam have been applied, and better result is achieved from the SU-8 mould under the UV lithography. Using hole sizes of 50 µm for the SU-8 mould, we obtained the resulting PDMS pillars with different heights from 100 to 400 µm, with an increment of almost 100 µm for each row.

4.2 The mould design and creation

The initial step of the PDMS micropillars fabrication is the creation of a mould, which will be used for the fabrication of cured PDMS pillars. The design of the mould should be able to produce the desired structures of the PDMS substrate, and to be re-usable. Photoresist resin, SU-8, has been able to create high aspect ratio features, hence will be used in this study. The key challenge is to create and control the different height of the PDMS pillars in the final structures, so that they can mimic the natural hair cells and response to various frequencies.

4.2.1 SU-8 mould fabrication by NanoBeam lithography (NBL)

Two series of SU-8 photoresist, SU-8 2025 and SU-8 2500, were applied in this work. For the proposed thickness of thin film on the Si wafer around 25 µm, SU-8 2025 series was appropriate and used for the NBL lithography. Table 4.1 illustrates seven steps in the fabrication of the negative SU-8 2025 series (MicroChem, USA) mould by using NanoBeam lithography (NBL). Firstly, a piece of $10\ mm\ \times 10\ mm$ Si wafer was cleaned with acetone and IPA solutions for 30 min, followed by baking at 150 °C for another 30 min. This was necessary for contamination removal from the Si wafer surface. After the Si wafer was cleaned and ready for further steps, it was spin-coated with 25 µm thick SU-8 2025 photoresist dropped by an electronics micropipette at a speed starting from 0 rpm for 15 s and speeding up to 2000 rpm, and then leaving at the constant speed of 2000 rpm for 30 s. The spin-coater was attached to a vacuum pump. To complete the polymerization of SU-8 photoresist, the spin-coated Si wafer was baked at 65 °C for 5 min, heated at 95 °C for 12 min on a hot-plate. Afterward, hole arrays with diameter of 3-5 µm and period of 3 µm would be patterned on the soft-baked SU-8 photoresist.

The patterns were designed by a CAD tool and sent to the software included in the NBL machine, they were then transferred onto the exposed layer of the SU-8 photoresist thin layer. This resist layer was then exposed to the beam with energy in the range of 0.05-1 mW cm^{-2} for different patterns. After the exposure, another step of baking was carried out, at 65 °C for 2 min and then at 95 °C for 10 min on the same hot plate. Finally, after the development step of the wafer in an EC solvent (2-methoxy-1-methylethyl acetate) bath for 2 min at ambient temperature, the sample was rinsed and dried with IPA for 1 min, to obtain the negative arrays of pattern with holes of different diameters and heights.

Table 4.1 The routine steps for the proposed thickness of almost 25 μm by NBL lithography technique.

Step	Process and parameters
Pre-treating of the Si wafer	Cleaning with acetone and IPA solutions for 30 min, then baking at 150 ^{o}C for 30 min
Spin coating	0-2000 rpm for 15 s (speedup) and 2000 rpm for 30 s (speed constant)
Soft baking	65 ^{o}C for 5 min, then 95 ^{o}C for 12 min
Exposure value	Ranging from 0.05-1 mW cm^{-2} for 6 h
Post Exposure Bake (PEB)	65 ^{o}C for 2 min, followed with 95 ^{o}C for 10 min
Development	EC (2-methoxy-1-methylethyl acetate) solvent bath for 2 min at 20 ^{o}C
Rinse and dry	Isopropyl alcohol (IPA) for 1 min

A dose test ranging from 0.05–1 mW cm^{-2} was investigated, in order to achieve the optimal dose for the exposure process, and the results are shown in Fig. 4.1. For exposure doses less than 0.25 mW cm^{-2}, the SU-8 photoresists were not sufficiently exposed, and the surface of the mould did not show any exposed areas. When the value of dose is between 0.05-0.25 mW cm^{-2}, the SU-8 surface was under exposed, as shown in Fig. 4.1a. For the range of 0.25-0.55 mW cm^{-2}, the exposure value is acceptable enough to assess the areas by optical microscope, as presented in Fig. 4.1b. Additionally, Fig. 4.1c shows the over exposed areas in the range of 0.55-1 mW cm^{-2}. The under exposed area is shown in Fig. 4.1d and e at 20x magnification, and the exposed area is shown in Fig. 4.1f at 20x magnification, corresponding to 0.55 mW cm^{-2}. In both Fig. 4.1g and h, over exposed areas are displayed for dose values of 0.60 and 0.65 mW cm^{-2} at 20x magnification. For better illustration of the exposed areas on the SU-8 surface, higher magnifications of 50x and 100x are shown in Fig. 4.1i and j, respectively. The best dose for the exposed areas was therefore 0.55 mW cm^{-2}. Due to the changing of ambient temperature in

the surrounding area in the cleanroom, the time required for the soft and hard baking should be adjusted, and further heating at 95 °C and longer development time might be needed. One principal factor which can be altered during the SU-8 mould fabrication is time.

4.2.2 SU-8 mould characterisation
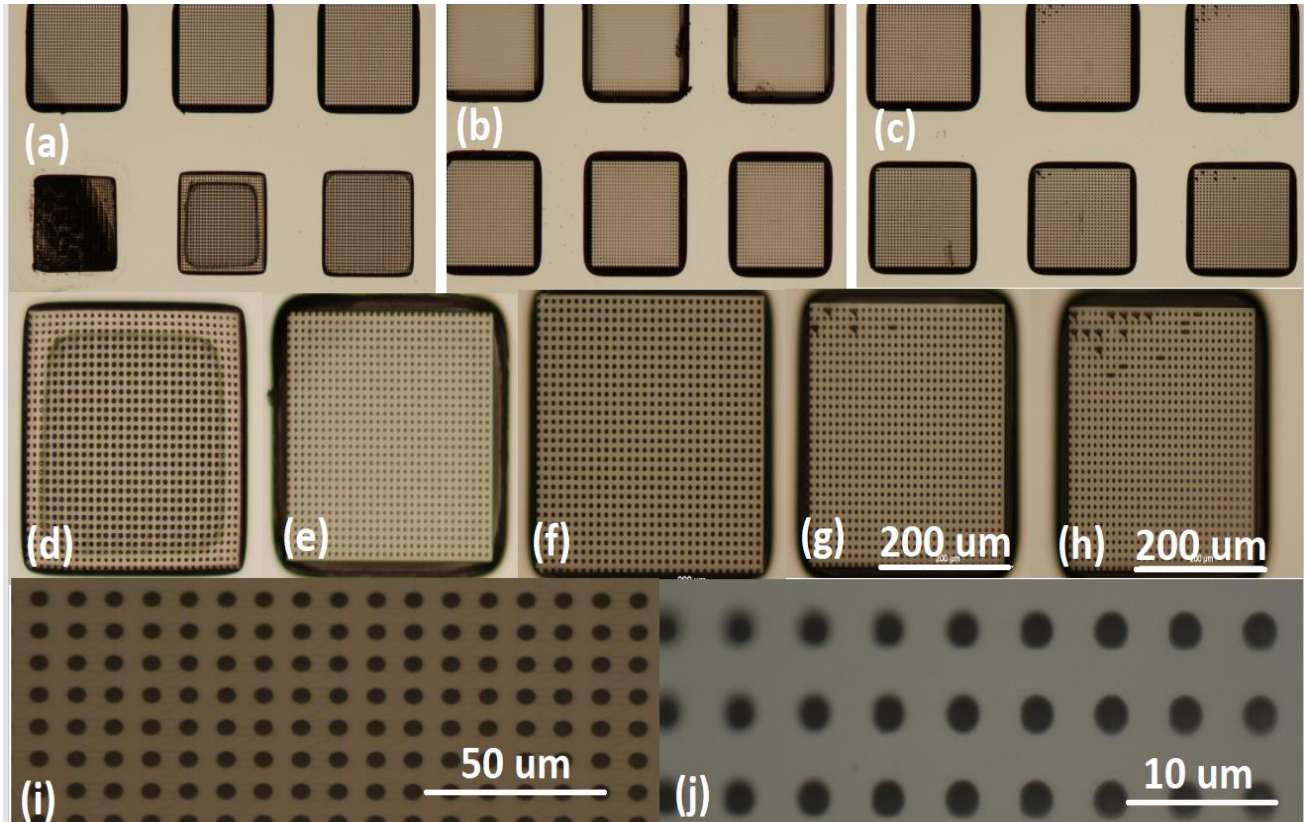
Fig. 4.1 (a) Under exposed surface for dose values between 0.05-0.25 mW cm^{-2} at 5x, (b) exposed surface for dose values between 0.25-0.55 mW cm^{-2} at 5x, and (c) over exposed surface for SU-8 mould at 5 x, (d)Id (e) under exposed surfaces for dose values of 0.05 and 0.1 mW cm^{-2} at 20x, (f) exposed surface of SU-8 for the dose value of 0.55 mW cm^{-2} at 20x, (g) and (h) over exposed surfaces for 0.60 and 0.65 mW cm^{-2} at 20x magnification, (i) exposed surface for 0.55 mW cm^{-2} at for 50x and (j) at 100x magnifications.

The SEM images for 0.55 mW cm^{-2} dose value is shown in Fig. 4.2a-c. Low and high magnifications of SEM images show the rows of the exposed areas of the top

view and side view (Fig. 4.2c) of the Si wafer. The thickness of exposed holes was measured, according to the SEM images, as 3 μm. An illustration of the different status of the exposure, proper exposed, under exposed, and over exposed, is presented in Fig. 4.2d(1-3).
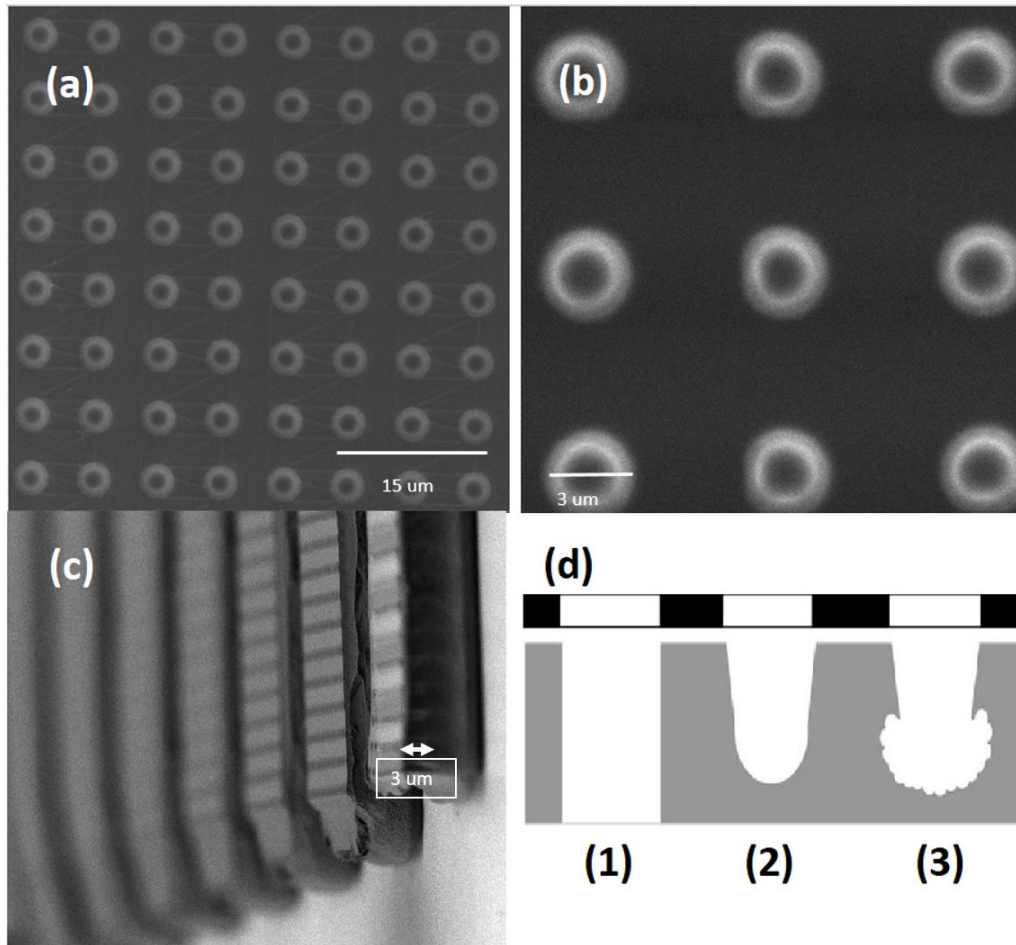
Fig. 4.2 SEM images of the resulting surfaces created by NBL using a dose of 0.55 mW cm^{-2}. (a) lower magnification top view of the exposed grids of the SU-8 mould; (b) higher magnification top view of exposed areas on the SU-8 mould; (c) side view of exposed grids revealing the vertical holes in the SU-8 mould; and (d) A schematic showing the different exposed status. (1) proper exposed, (2) under exposed, and (3) over exposed.

As shown in Fig. 4.2c, although the area was exposed apparently, the thickness was only 3 μm, far less than that of the SU-8 layer on the Si wafer. This dose was sufficient only for the surface, not enough across the entire substrate, only enough

for achieving the highest aspect ratio of 1:1 by the NBL method. To construct artificial hair cells, an aspect ratio around 1:4 between the depth and diameter of the exposed structure is required, hence alternative techniques are needed.

4.2.3 SU-8 mould fabrication by UV lithography (photolithography)

Parallel to the previous microstructure fabrication method, semi-permanent mould with thicker SU-8 layer was fabricated using the photolithography (UV lithography). Table 4.2 summarizes the steps involved in this study. Among these parameters, the power parameter can be varied to achieve different final structures on the SU-8 substrate. This parameter is like the exposure intensity in the NBL method, however, in different unit scale. The first step was to clean the Si wafer to remove contaminations, using similar cleaning steps as in NBL, which was cleaned in acetone and IPA solutions for 30 min and baked at 150 $^{\circ}$C for 30 min. A $10\ mm\ \times 10\ mm$ Si wafer was mounted on the spin-coater that was attached to a vacuum pump. 3-4 ml of SU-8 2500 series was micropipette-dropped onto the wafer center. Then the photoresist was spread around uniformly under low spin velocity of 0-500 rpm for 15 s then speeding up to the constant speed of 1500 rpm for 30 s to cover the whole surface of the wafer and avoid the need of serious edge-beading. After the spin-coating, a pre-exposure baking or soft baking was followed to remove the residual solvent. A SU-8 coating of around 500 μm thick was obtained, which was measured by a clean digital micrometer (MDH-25M with 0.1 μm resolution).

After the pre-exposure bake, the coated wafer was selectively exposed to the UV light through a photomask. Soft baking of the SU-8 was longer than the suggested datasheet, as the conditions used to prepare the sample were different from the datasheet references. The photomasks of different patterns were designed by a CAD software, as shown in Fig. 4.3. The high-quality photomask was created on a soda lime glass substrate coated with a low reflective Cr mask, fabricated by JD Photo Data company (UK). Cr is used to absorb UV rays in later exposure steps. This is the role of the mask which determines the final pattern on the exposed photoresist. The UV radiation is applied to the photomask which was loaded into a mask aligner. A chemical change of the SU-8 happens in the exposure step, which will cause the SU-8 negative photoresist to become less soluble in the developer EC solution. The

Post Exposure Bake (PEB) step is different from the NBL method and takes longer at both temperatures of 65 and 95 °C due to the change of the thickness in the UV lithography method. After placing in the EC solution for 4 min, the SU-8 resist would be dissolved in locations that were not exposed to the UV light, whereas the exposed areas remain intact. Finally, the SU-8 substrate was rinsed with IPA for 1 min and dried with nitrogen, to obtain the negative arrays of pattern with holes of different heights. Another key difference between this method and the previous NBL approach of reaching the final SU-8 mould lies in the development step which will be highlighted in next sections.

Table 4.2 The routine steps used for the UV lithography process.

Step	Process and parameters
Pre-treating of the Si wafer	Cleaning with acetone and IPA solutions for 30 min, then baking at 150 °C for 30 min
Spin coating	0-500 rpm for 15 s (speedup) and 1500 rpm for 30 s (speed constant)
Soft baking	65 °C for 35 min, followed with 95 °C for 20 min
Power density for UV exposure	12.7 mJ cm^{-2} for 120 s
Post expose bake (PEB)	65 °C for 12 min, followed with 95 °C for 8 min
Development	EC solvent bath for 180 s at 20 °C, with a gentle agitation
Rinse and dry	Isopropyl alcohol (IPA) for 1 min and dried with Nitrogen

Fig. 4.3 shows the patterns designed in this thesis, including light field (positive) and dark field (negative) masks. In the light field, islands of lines are in the clear field, and on the contrary in the dark field, holes appear in dark areas. Patterns 1, 3, 5, 7, 9, 10 and 11 are dark field ones, and others are light field masks (Fig. 4.3). Patterns 1 to 8 will be experimented in this thesis.
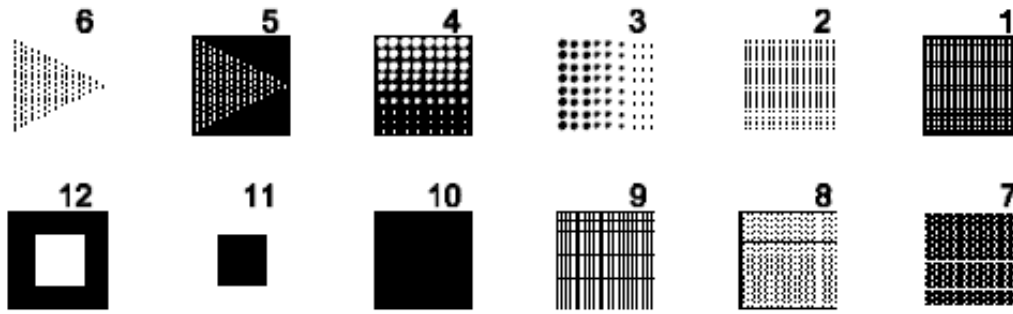
Fig. 4.3 Patterns of photomask designed for the UV lithography experiment, containing both negative and positive masks. Drawn using AutoCAD and Solid Work.

Table 4.3 summarizes the dose tests conducted on the SU-8 substrates, using the same pattern numbers as shown in Fig. 4.3. The maximum intensity for the thickness of 500 μm SU-8 on the Si wafer reached to 14.1 mJ cm^{-2}. The power value is the percentage of intensity value applied in each experiment, starting from 60 % of the total intensity 14.1 mJ cm^{-2}. While the power value was kept constant, different exposure time was investigated. The whole period of development time was 240 s. For the first pattern, obtaining the feature was not possible. When the power was the highest, the time of exposure was the shortest. Higher time of exposure caused the mask to stick to the photoresist. When the pattern changed to positive type, under exposed and none exposed areas were observed on the SU-8 substrate for the same range of power applied in the 1st pattern. When the power was 70%, the area was changed to none exposed substrate. Among all patterns, patterns 4, 5, 6 and 7 were found appropriate in terms of the final features. Other patterns were only used for evaluating the dose for the UV-lithography process. The 5th pattern is similar to the natural structure of hair cell pillar features. The optimal power is 90% of the total intensity, which is 12.7 mJ cm^{-2} for the SU-8 mould in this study.

Table 4.3 The dose tested on the SU-8 substrates using different parameters.

No.	Pattern number	Power value (%)	Time of exposure (s)	Time of development (s)	Pattern description	Final features
1	1	60	300	240	Negative, 50 µm	No figure
2	1	70	240	240	Negative, 50 µm	No figure
3	1	80	180	240	Negative, 50 µm	No figure
4	1	90	120	240	Negative, 50 µm	No figure
5	1	100	60	240	Negative, 50 µm	No figure
6	2	60	300	240	Positive, 50 µm	Under exposed areas and none exposed areas
7	2	70	240	240	Positive, 50 µm	Under exposed areas and none exposed areas
8	2	80	180	240	Positive, 50 µm	Under exposed areas
9	2	90	120	240	Positive, 50 µm	Under exposed areas
10	2	100	60	240	Positive, 50 µm	Under exposed areas
11	3	60	300	240	Positive, including circles from 50 µm to 10 µm with an increment of 10 µm	The whole substrate vanished.
12	3	70	240	240	Positive, including circles from 50 µm to 10 µm with an increment of 10 µm	The whole substrate vanished.
13	3	80	180	240	Positive, including circles from 50 µm to 10 µm with an increment of 10 µm	Over exposed.
14	3	90	120	240	Positive, including circles from 50 µm to 10 µm with an increment of 10 µm	Over exposed
15	3	100	60	240	Positive, including circles from 50 µm to 10 µm with an increment of 10 µm	No figure
16	4	60	300	240	Negative, including circles from 50 µm to 10 µm with an increment of 10 µm	Not completely exposed

17	4	70	240	240	Negative, including circles from 50 µm to 10 µm with an increment of 10 µm	Over and under exposed areas
18	4	80	180	240	Negative, including circles from 50 µm to 10 µm with an increment of 10 µm	Mostly exposed
19	**4**	**90**	**120**	**240**	**Negative, including circles from 50 µm to 10 µm with an increment of 10 µm**	**Exposed**
20	4	100	60	240	Negative, including circles from 50 µm to 10 µm with an increment of 10 µm	Mostly under exposed
21	5	60	300	240	Negative triangles include circles of 50 µm diameter	Under exposed areas
22	5	70	240	240	Negative triangles include circles of 50 µm diameter	Under exposed areas
23	5	80	180	240	Negative triangle includes circles of 50 µm diameter	Mostly exposed
24	**5**	**90**	**120**	**240**	**Negative triangles include circles of 50 µm diameter**	**Exposed**
25	5	100	60	240	Negative triangles include circles of 50 µm diameter	Over exposed
26	6	60	300	240	Positive triangles include circles of 50 µm diameter	Not completely exposed
27	6	70	240	240	Positive triangles include circles of 50 µm diameter	Not completely exposed
28	6	80	180	240	Positive triangles include circles of 50 µm diameter	Nearly exposed
29	6	90	120	240	Positive triangles include circles of 50 µm diameter	Exposed
30	**6**	**100**	**60**	**240**	**Positive triangles include circles of 50 µm diameter**	**Exposed**

31	7	60	300	240	Negative rows of circles of 50 µm diameter	Not completely exposed
32	7	70	240	240	Negative rows of circles of 50 µm diameter	Not completely exposed
33	7	80	180	240	Negative rows of circles of 50 µm diameter	Less under exposed areas
34	7	90	120	240	Negative rows of circles of 50 µm diameter	Almost exposed
35	**7**	**100**	**60**	**240**	**Negative rows of circles of 50 µm diameter**	**Exposed**
36	8	60	300	240	Positive rows of circles of 50 µm diameter	Under exposed
37	8	70	240	240	Positive rows of circles of 50 µm diameter	Mixture of exposed and under exposed areas
38	8	80	180	240	Positive rows of circles of 50 µm diameter	Mostly exposed
39	**8**	**90**	**120**	**240**	**Positive rows of circles of 50 µm diameter**	**Exposed**
40	8	100	60	240	Positive rows of circles of 50 µm diameter	Over exposed

After the exposure step and post-exposure baking process necessary for the completion of chemical reactions induced by the UV exposure, the exposed areas were less soluble in the developing solution (EC solvent). The development procedure was different from the previous NBL method for the direct mould fabrication. The success in reaching different depths for the SU-8 mould was controlled by the development time for each row in the triangular mould (pattern 5 in Fig. 4.3). The development involved four steps. In each step, the first row only having a single hole was developed for longer time than the other rows, which was achieved via staggered development. Initially, the first row was developed for 45 s, followed by three more extra steps of further development for the remaining rows, *i.e.,* the

first row being developed for 180 s, the second row for 135 s, the third row for 90 s, and the fourth row for 45 s. After such a process, we achieved the deepest hole in the top of the triangular mould (single hole), and gradually shallower holes in subsequent rows. After development, the mould was rinsed with IPA, then dried with nitrogen at room temperature.

4.2.4 Optical characterizations of SU-8 mould fabricated by UV lithography (photolithography)

The optical images in Fig. 4.4a and b present the fabricated mould at low and high magnifications. The depth of the hole in the first row on top of the mould was measured by the surface profiler, averaged for three times, being almost 100 µm.
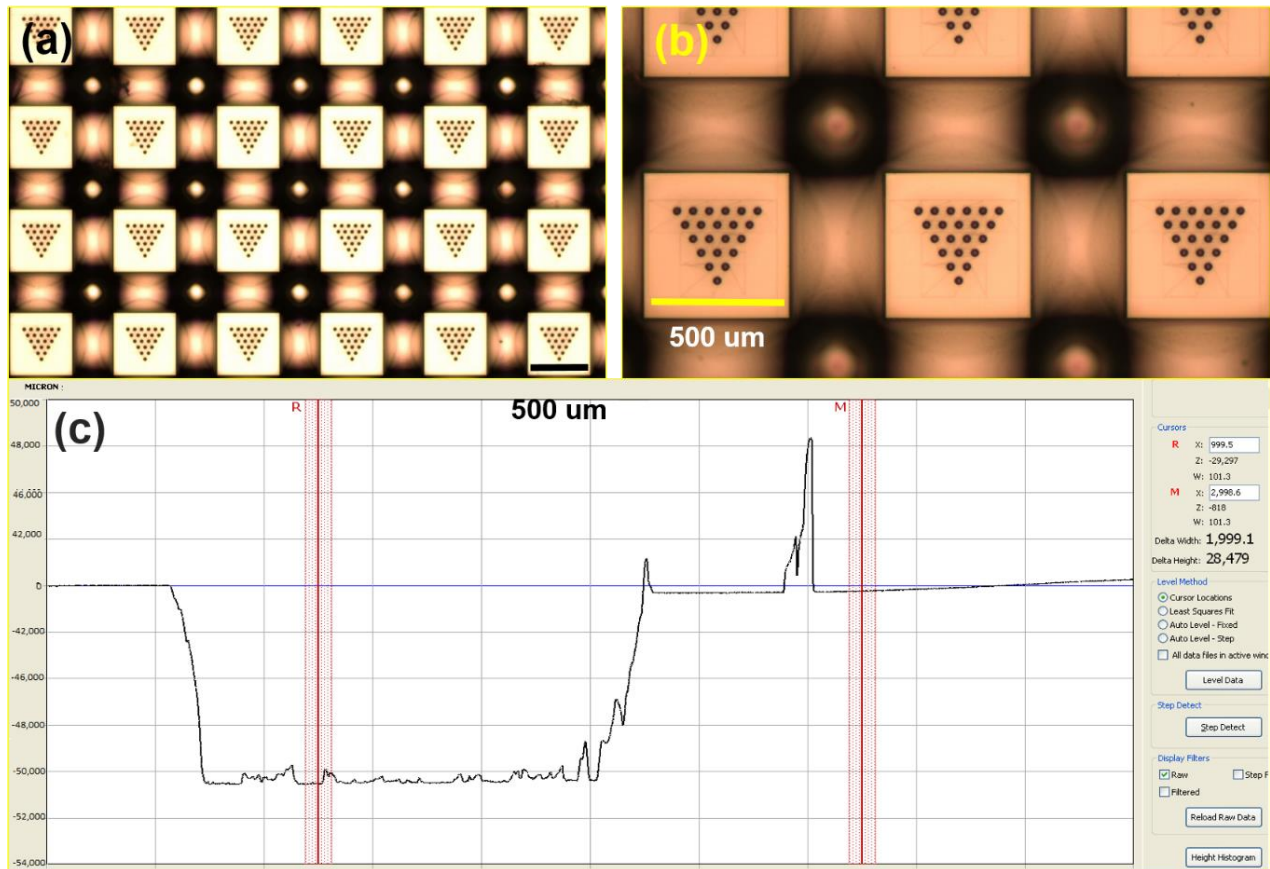
Fig. 4.4 The exposed SU-8 photoresist at the exposure value of 12.7 mJ cm^{-2} for 120 s. (a) 5 x (b) 50 x and (c) The surface profile plot showing the depth of hole.

The above results have confirmed that the refined design and proper processing resulted in semi-permanent SU-8 moulds on a $10\,mm \times 10\,mm$ Si wafer. The deeper holes are suitable for the fabrication of longer PDMS pillars. Using the UV lithography method, we have obtained SU-8 moulds with patterns of graded depths, with lateral dimensions ranging from 100 to 400 µm, with an increment of 100 µm, measured using a digital micrometer (MDH-25M with 0.1 µm resolution). Different heights of PDMS pillars hence could be generated with heights equalling to the depths of the optimized SU-8 mould, under the adjusted exposure and development duration. From the first row with one hole to the last row with four holes, all the holes appeared to be uniform in both diameter and shape after the exposure and development, and the average diameter was around 50 µm, based on three times of measurement using a surface profilometer scanning along the mould surface.

This mould fabrication method offered great reproducibility and fast processing features, and this semi-permanent mould could offer continuous fabrication of PDMS pillars of different heights.

Comparing the two types of mould produced by the two methods, NBL and UV lithography, we can see some advantages and disadvantages, as follows:

- The NBL allowed small submicron features maximum of 5 µm on the SU-8 negative photoresist, however the fabricated PDMS substrate after being cured and peeled off, the surface of SU-8 mould failed to provide the desired PDMS pillars of different heights, instead, it resulted in spots only.
- The diameter of holes in the SU-8 mould produced by NBL is almost one tenth of that fabricated by UV lithography method.
- The UV lithography technique failed to create precise and fine features sufficiently close to the natural type of hair cells, however it worked quickly and was suitable for creating features of larger than 5 µm. The exposure time required by this method was only 120 s, which was much less than that of the NBL which required 6 h.

Therefore, the required aspect ratios up to 4 for 4 rows starting from 100 to 400 μm in depth could be achieved by the UV lithography, which could result in pillars with great resemblance to the natural hair cells geometry.

4.3 PDMS pillar fabrication

4.3.1 PDMS fabrication and demoulding

The fabrication of flexible PDMS structures is another important step towards the overall aim of creating artificial hair cells. The PDMS was synthesised using monomers, following steps illustrated in Fig. 4.5. In this process, two agents, the Silicon monomer (the PDMS elastomer base) and its hardener (curing agent) at a ratio of 10:1, were combined and mixed vigorously in a beaker. The beaker was left in a vacuum chamber for 1 h to remove bubbles inside the solution, prior to spin-coating onto the fabricated SU-8 moulds. The SU-8 moulds were initially spin-coated by 0.2 μl of the releasing agent (WD 40 spray) at the speed of 3000 rpm for 30 s, then 0.25 ml PDMS solution was put on the SU-8 moulds and spin-coated for 20 s at 500 rpm. The polymer solution spin-coated on the SU-8 mould was degassed for another 1 h in a vacuum chamber. After curing at the ambient temperature for 24 h, we obtained the mould filled with PDMS. The treatment period can be shorter or longer depending on the surrounding temperature. We have noted that when the spin-coated specimens were left longer than 24 h, the demoulding (peeling off the pillars) was easier.

To detach the PDMS from the mould, fully cured PDMS in the SU-8 mould was immersed in a breaker containing 30 ml acetone. After 10 min, we used a pair of tweezers to slowly and precisely demould the PDMS pillars, under an optical microscope. Acetone helped to eliminate dust, oil, or other organic contaminations from the surface of the mould and eased off the demoulding process.

The demoulding took 5 min at ambient temperature, which was faster than that required for the NBL method.
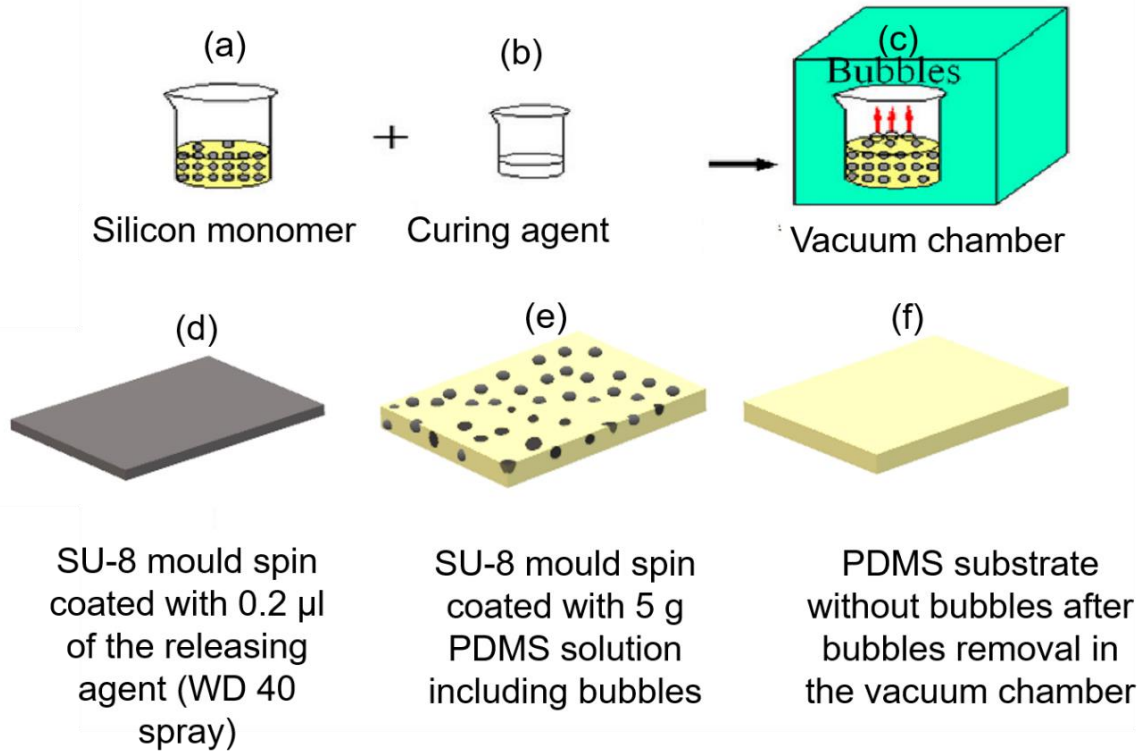
Fig. 4.5 A schematic for the fabrication steps for PDMS microstructure. (a) and (b) mixing Silicon monomer and its curing agent vigorously, followed by (c) degassing in a vacuum chamber at ambient temperature for 1 h, (d) the use of WD 40 (Water Displacement, 40th formula) spray releasing agent on the SU-8 mould, (e) spin-coated PDMS after further degassing for another 1 h in the vacuum chamber at ambient temperature, then left for 24 h at room temperature, and (f) the resulting PDMS after demolding.

4.3.2 Comparison of the resulting PDMS structures between the NBL and UV lithography

For surface morphology, the as-fabricated PDMS substrate was directly left on a microscope glass slide for optical and SEM observations, to prevent any possible contamination. For SEM observation, a 3 nm Cr coating was applied, to avoid charging. Fig. 4.6a-b presents the optical images of the PDMS structures peeled off the SU-8 mould produced by NBL method. Fig. 4.6c-d displays the SEM images of the fine features of the PDMS, which are far from being pillars, just a lump. Although the final PDMS by the NBL did not produce pillars, the mould was still re-useable for further PDMS microstructures fabrication.
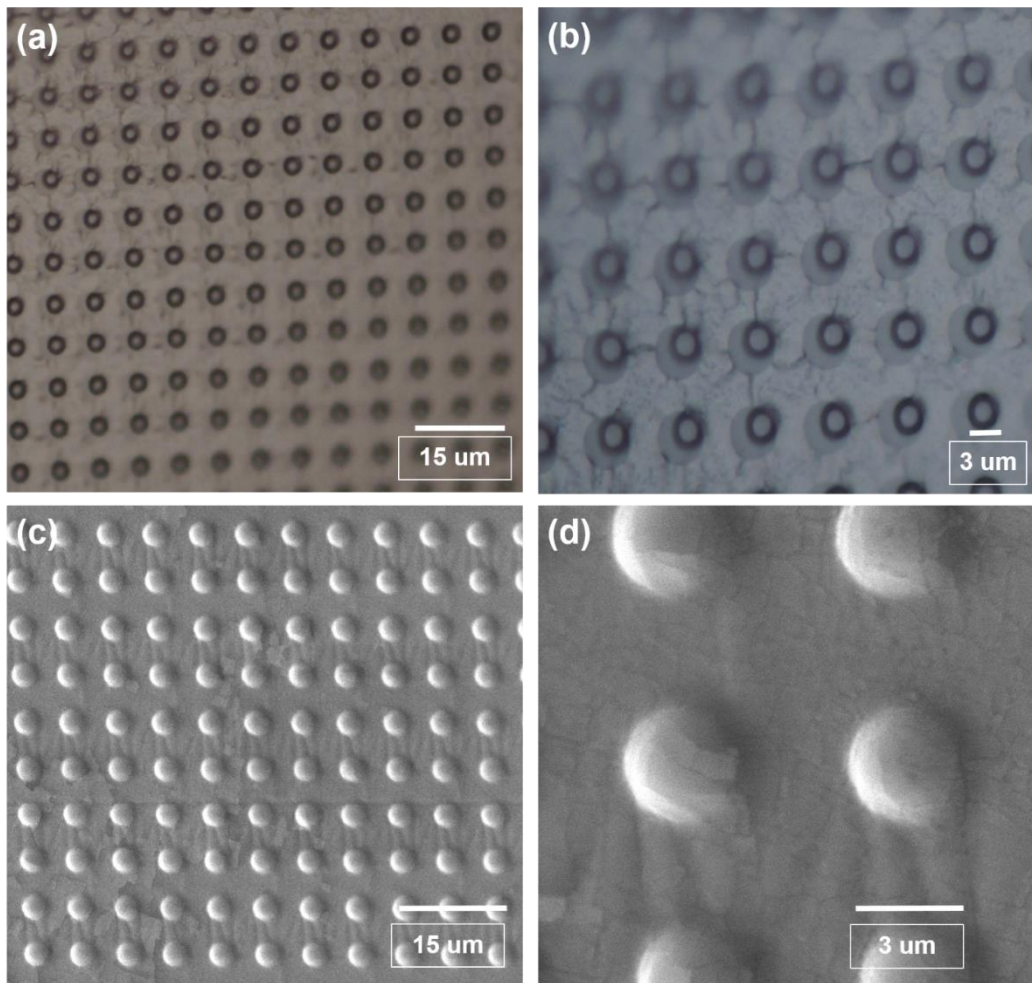
Fig. 4.6 Images of the resulting PDMS microstructures from the SU-8 mould produced by the NBL technique. Optical images (a) 10 x, and (b) 50 x, SEM images (c) low magnification and (d) high magnification.

Fig. 4.7 depicts the final structure of the PDMS micropillars with four rows produced by the UV lithography. The first row from the bottom has four pillars of 100 μm high, the second row three pillars of 200 μm. While the height is increased, the number of pillars in each row is decreased. In the third row, two pillars are 300 μm in height, and the tallest pillar has a height of 400 μm.

Fig. 4.7 The PDMS micropillars peeled off the SU-8 mould, from the UV method.

It was observed that pillars longer than 400 μm would be stuck in the hole of the SU-8 mould and would break while demoulding. In other words, when the aspect ratio was higher than four in this study, the demoulding was not achievable. Conversely, bigger holes in the mould make the pillar demoulding easier.

4.3.3 PDMS micropillars fabricated via thermal evaporating

To make the PDMS substrate electrically conductive as the electrode, an HHV Auto306 thermal evaporator was applied to create a thin metallic layer coating. Two high pure gold wires (99.99 %) were used as the target for the coating. A template was patterned with arrays of microdots on a $10\ mm \times 10\ mm$ aluminum foil. The diameter of each micro hole on the aluminum foil was 50 μm with the gap distance of 100 μm between each hole in each direction.

Au was then evaporated to form a thin layer of ~ 100 nm on the pillars through the aluminium foil template and Au was then deposited onto the whole surface of PDMS micro pillars substrate facing toward the vapor flux. Fig. 4.8 presents the as-fabricated PDMS micropillars, and the Au deposition. This Au coating was strongly deposited and was not damaged or exfoliated by mechanical loading or movements.
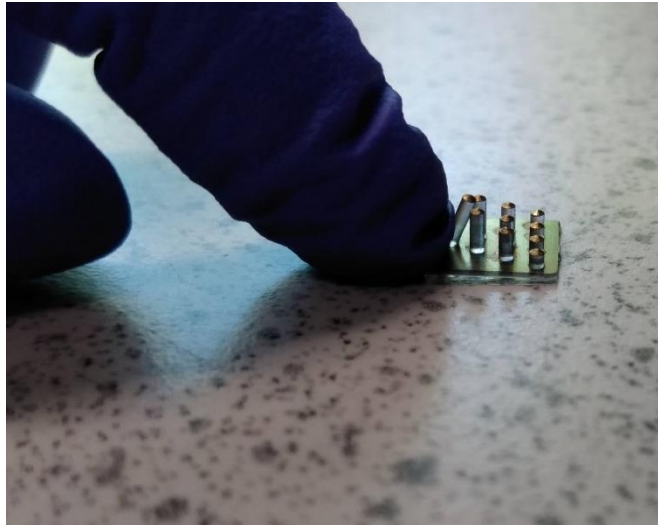
Fig. 4.8 (a) The as-fabricated PDMS micropillars and thermal evaporated layer of Au on its surface.

4.4 Summary

This Chapter presented the fabrication of the PDMS pillars of different heights as the base component of the artificial hair cell device by using two methods, the NBL and UV lithography. To achieve the desirable dimensions and the complete pillars with appropriate features, the processes were optimized, and the outcomes of each method are presented and compared.

- The smallest diameter size of 3 µm has been attained by using the NBL lithography method under the dose of 0.25-0.55 mW cm^{-2}, however the depth was not enough, equalling to the diameter. The desired aspect ratio could not be achieved by this method.
- UV lithography technique led to desired holes with proper aspect ratios on the SU-8 photoresist. A hole diameter of 50 µm, aspect ratio of 1:4 could be achieved by using various exposure time for a constant UV dosage. The parameters involved in the mould and pillar generation processes have been optimized. A sequential exposure process has been introduced for different rows to have different exposure dose, for achieving PDMS pillars of various heights based on the different depths values of the SU-8 mould.

- Four rows of PMDS pillars with different heights on a triangular patterned substrate have been successfully created by the UV lithography technique using the semi-permanent SU-8 mould, with the desired features and resolutions. The dimension of the PDMS substrate was 50 μm diameter and the range of (100-400) μm with an increment of 100 μm for heights in each row of the PDMS substrate.

- The successful production of the pillars could lay down a solid foundation for the underneath part of tip-links, as the key components to create the artificial hair cells.

Chapter 5: Synthesis and characterization of pure PVDF electrospun fibers

5.1 Introduction

Having succeeded in producing the PDMS pillars of different heights in previous Chapter, we will describe the synthesis of tip-links in this chapter. By linking the pillars with proper structures, a solid foundation will be laid down towards the construction of advanced, self-powered, artificial hair cells that could respond to a wide range of frequencies, without side effect to our body.

Briefly, this Chapter will present detailed, specific experimental parameters, step by step preparation of the PVDF electron fibers, which can be separated into 4 sessions. Initially, the syntheses of pure PVDF electrospun for 3 different concentrations will be presented. Secondly, the morphology and structure features will be investigated. Thirdly, Raman spectroscopy, complemented with FTIR and XPS are used to appraise the phase change behavior of the electrospun fibers, against the pure powder PVDF. Fourthly, the piezoelectricity and triboelectric properties of the PVDF electrospun fibers will be investigated using a PFM, which offers fundamental understanding and validates their potential technology aspects for using the PVDF electrospun nanofibers to mimic the tip-links in the hair cells.

5.2 Synthesis

5.2.1 Pure PVDF fibers

Pure PVDF powder, acetone and DMF were used as the precursor and solvent respectively for the synthesis of PVDF fibers via electrospinning. Different concentrations (15, 16.5 and 18 wt%) of PVDF were achieved by dissolving 1.50, 1.65, and 1.80 g PVDF powder into 8.50, 8.35 and 8.20 g DMF/Acetone (3/7 volume ratio for each Sample) solution accordingly. The mixture was heated with the assistance of a hot plate at 70 $^{\circ}$C, under magnetic stirring at 600 rpm, for overnight. The final homogenous and viscous solution was used as the stock solution for further electrospinning experiments.

After electrospinning, as described in Chapter 3, samples were collected on a stationary Si wafer or Al foil fixed on the rotary drum collector, using a pair of small tweezers. The effect of different parameter sets on the morphology and structure of the spun fibers, including the applying voltages (10, 15 and 20 kV), the distance between the needle and the collector (10, 15 and 20 cm), liquid feeding rates (1, 3 and 5 ml h^{-1}), and speeds of the rotary drum collector (400, 800 and 1200 rpm), will be investigated in detail. The rotary drum collector can help to create aligned fibers in large areas. The final products were collected for further characterizations.

5.3 Characterizations

5.3.1 Morphology

5.3.1.1 Precursor concentration effect

Table 5.1 and Fig. 5.1 summarize the effect of the PVDF concentration on the mean nanofiber sizes, obtained while other parameters were kept constant. The thinnest fibers, based on the mean diameter, were achieved using the lowest concentration of PVDF. Fig. 5.1a-c shows the SEM images of the three different PVDF nanofibers. Sample A exhibited a mean nanofiber diameter of 270 nm and was quite uniform, which is the best. Samples B and C exhibited a significantly increased mean diameters of 583 and 989 nm, separately, being non-uniform. When the concentration was higher than 15 wt%, thicker nanofibers were more likely to form. However, when the concentration was lower than 12 wt%, unspinnable products resulted, in the form of droplets to form particles instead of nanofibers. At the proper concentration of 15 wt%, the spinning process was easy, the diameter of the fibers was in the sub-micron scale, and the size distribution was homogenous. At 18 wt% concentration, the spinning was very difficult. From Fig. 5.1a-c, we can see that the diameters and distribution of the fibers were directly affected by the solution concentration. By regulating the stock concentration, we could achieve a good distribution of fibers on the surface. The diameters and uniformity of the electrospun fibers were found to decrease with the increased precursor polymer concentration. Fiber formation was sometimes hindered by the high viscosity of the solution at very high polymer concentration. Fig. 5.1d shows a linear relationship

between the PVDF concentration and diameter of the resulting electrospun fibers, higher concentration leading to larger mean fiber diameters.

Table 5.1 The effect of PVDF concentration on the mean diameter of the nanofibers while fixing other electrospinning parameters.

Samples	Solvent	Concentration (wt%)	Voltage (kV)	Distance (cm)	Feeding rate (ml h^{-1})	Collector speed (rpm)	Mean nanofiber diameter (nm)
A	DMF/Acetone	**15**	20	15	3	1200	270
B	DMF/Acetone	**16.5**	20	15	3	1200	583
C	DMF/Acetone	**18**	20	15	3	1200	989
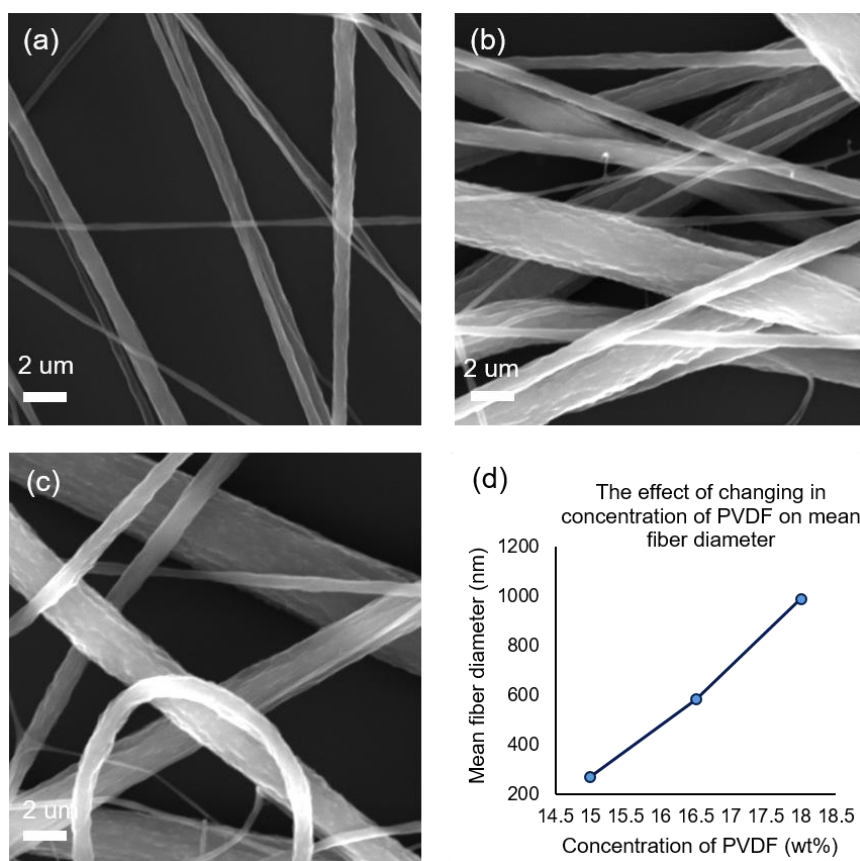
Fig. 5.1 SEM images of the electrospun fibers. (a) Sample A, 15 wt%, (b) Sample B, 16.5 wt%, and (c) Sample C, 18 wt%, prepared at 15 cm between the needle and collector at the same feeding rate of 3 ml·h^{-1}, voltage of 20 kV and collector speed of 1200 rpm, (d) The relationship between the mean fiber diameter (nm) vs concentration of PVDF (wt%).

5.3.1.2 Voltage effect

Table 5.2 summarizes the voltage effects on the morphology, under a constant distance of 15 cm between the needle and the collector, at a feeding rate of 3 ml h^{-1} and a collector rotating speed of 1200 rpm. When the applied voltage was less than 10 kV, the electrospinning could not be realized. Increasing the voltage to 15 kV, the resulting fibers, Sample D, exhibited a mean fiber diameter of 245 nm, as shown in Fig. 5.2a. At 20 kV, a mean fiber diameter of 268 nm was obtained which is assigned to Sample E (Fig. 5.2b). At 25 kV, a mean fiber diameter of 213 nm was observed, accompanied with beads, and bending fibers as marked with red and yellow arrows (Fig. 5.2c, Sample F). At this voltage, non-alignment and poorly distributed diameter distributions became severer.

While some argue that the increase in voltage will lead to an increase in the fiber diameter, others claim the opposite trend. In this thesis, we observed the reduced diameters of the spun fibers at higher voltage, possibly due to the increased electrostatic repulsive force [281]. In this context, no significant differences in diameter were observed for the three voltages, but fewer fibers were spun at lower voltage and more fibers at higher voltage.

The relationship between the applied voltage and the mean diameter of the fibers is shown in Fig. 5.2d, which appears to peak at 20 kV. Although the mean diameter at 20 kV is not the smallest, the spinning is easiest in this case. When the voltage was more than 25 kV, it became unspinnable.

Voltage provides the driving force for the electrospinning process, which supplies the required energy to overcome the surface tension in the polymer solution and drag the ejected solution to form fibers. Higher voltage exerted greater electrostatic forces, therefore dragged more polymeric solution during the spinning, as a result, more fibers were deposited onto the collector. Furthermore, the larger dragging force shortened the time of fiber flying, hence shorter solidification period and ended up with decreased diameters. For the present experimental set-up, the optimum value of applied voltage was 20 kV, which differs from other studies for PVDF electrospun fibers fabrication which were 15 and 10 kV respectively [282-283].

Table 5.2 The effect of voltage on the mean nanofiber diameters while fixing other electrospinning parameters.

Samples	Solvent	Concentration (wt%)	Voltage (kV)	Distance (cm)	Feeding rate (ml h^{-1})	Collector speed (rpm)	Mean nanofiber diameter (nm)
D	DMF/Acetone	15	**15**	15	3	1200	245
E	DMF/Acetone	15	**20**	15	3	1200	268
F	DMF/Acetone	15	**25**	15	3	1200	213
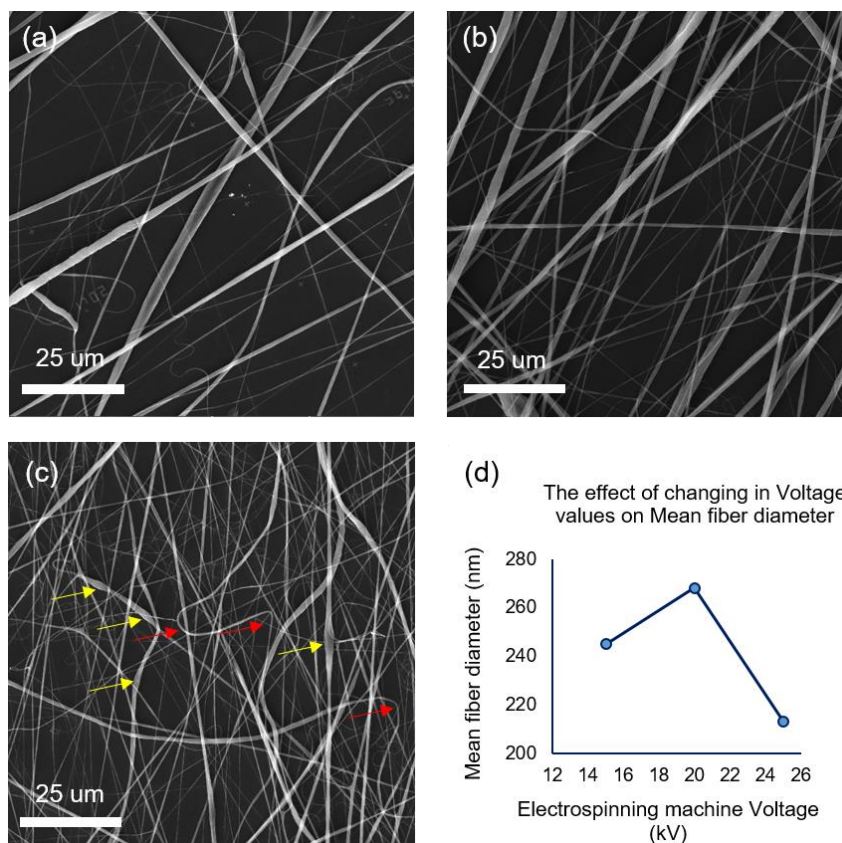
Fig. 5.2 (a-c) SEM images of the electrospun fibers obtained under various voltages. (a) Sample D, 15 kV, (b) Sample E, 20 kV, and (c) Sample F, yellow and red arrows pointing to beads and bendings, 25 kV. All experiments were carried out under a set of fixed parameters: 15 wt% PVDF precursor concentration, 15 cm distance between the needle and collector, 3 ml h^{-1} feeding rate, and 1200 rpm collector rotation speed. (d) The relationship between the mean fiber diameter (nm) and voltage (kV).

5.3.1.3 Distance effect

Table 5.3 shows the influence of needle and collector distances on the mean diameters, and Fig. 5.3 shows the SEM images of the resulting fibers corresponding to three distances (10, 15 and 20 cm). When the distance increased from 10 to 15 cm, a diameter reduction of almost 17%, from 310 to 258 nm, was obtained. At the distance of 20 cm, further reduction of the fibers mean diameter to 209 nm was realized, which is a further 18% reduction. Further increase the distance to more than 25 cm, hardly any fibers were formed on the Al foil collector and the material was not spinnable. The SEM results in Fig. 5.3b and c show fibers with less bead and branched feature when compared with Fig. 5.3a, and they show much uniform distribution in diameters.

Previous studies claimed that there was no significant change in diameter at various distances between the needle and the collector [284-286]. When the distance between the needle tip and the collector is the shortest (10 cm), less spinnable product could be collected, as incomplete fibers. For the highest distance of 20 cm, less aligned and not well distributed fibers with much thinner diameters are produced. Fig. 5.3d illustrates a linear relationship between the distance and diameter of the electrospun fibers, and larger distance corresponds to thinner fibers. However, when the distances are higher than 20 cm, the ejected solution would solidify prior to reaching the collector, making it unspinnable. Thus, the most suitable distance between the needle and the collector was 15 cm.

Table 5.3 Effect of distance between the needle and collector on the fiber diameter while fixing other electrospinning parameters.

Samples	Solvent	Concentration (wt%)	Voltage (kV)	Distance (cm)	Feeding rate (ml h^{-1})	Collector speed (rpm)	Mean nanofiber diameter (nm)
G	DMF/Acetone	15	20	**10**	3	1200	310
H	DMF/Acetone	15	20	**15**	3	1200	258
I	DMF/Acetone	15	20	**20**	3	1200	209
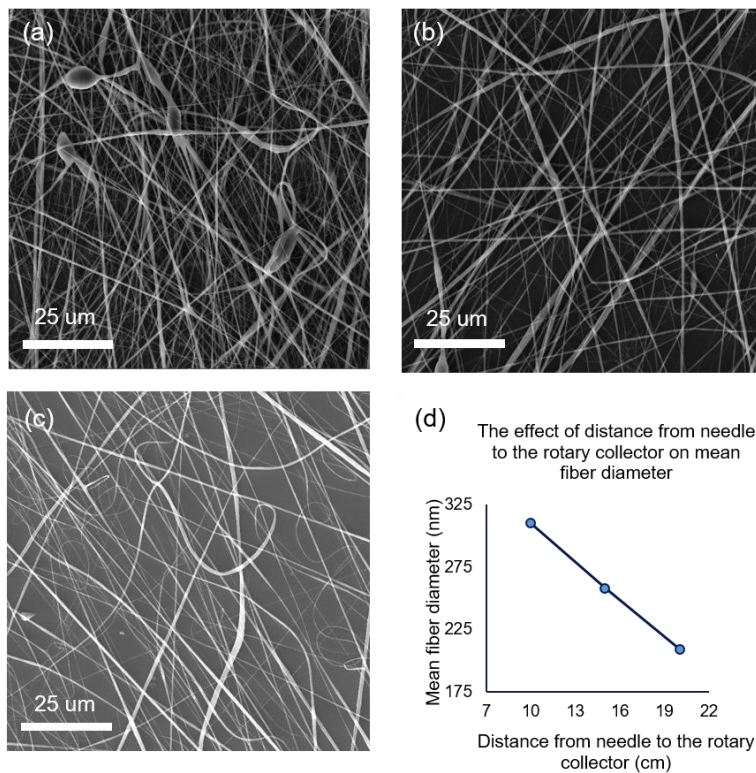
Fig. 5.3 SEM images of sample electrospun using different needle-collector distances. (a) Sample G, 10 cm, (b) Sample H, 15 cm, and (c) Sample I, 20 cm. All samples were spun using 15 wt% PVDF precursors, under 20 kV voltage, at the same feeding rate of 3 ml h^{-1}, and with a collector speed of 1200 rpm. (d) the relationship between the mean fiber diameter (nm) and distance from needle tip to the rotary collector (cm).

5.3.1.4 Effect of solution feeding rates

Three different feeding rates (1, 3 and 5 ml h^{-1} for Samples J, K and L) were investigated and the results are summarized in Table 5.4, and the morphological features of the resulting fibers are presented in Fig. 5.4a-c. At the feeding rate of 1 ml h^{-1}, very fine fibers were formed with a mean diameter of 202 nm, Fig. 5.4a. Increase the feeding rate to 3 ml h^{-1}, led to a 21.70 % increase in size for Sample K, compared with the Sample J. A further increase of 86 % for L was achieved with the highest feeding rate of 5 ml h^{-1}. For higher values of feeding rates than 5 ml h^{-1}, products were not spinnable. For the highest feeding rate of 5 ml h^{-1}, although

electrospun fibers are better aligned than Sample J, nevertheless, the web collected of Sample L consists of the thickest fibers.

While the mean diameter of Sample J is the smallest, there are beads, and the fibers are less aligned. At 3 ml h^{-1}, the diameter distribution of fibers is quite uniform, and no beads are formed. At higher flow rates, more solution is drawn which produces larger droplets at the needle tip, thus forming fibers with larger diameter. At lower feeding rate, the drops forming at the needle tip are smaller, thus the drawn fibers are thinner. The relationship between the feeding rate and the mean diameter is shown in Fig. 5.4d. The sharp rising of the mean diameter starts from 3 ml h^{-1}. In this thesis, 3 ml h^{-1} is the optimal feeding rate, leading to fibers with consistent morphology, being the best among these tested feeding rates.

Table 5.4 Effect of feeding rates on the mean diameter while fixing other electrospinning parameters.

Samples	Solvent	Concentration (wt%)	Voltage (kV)	Distance (cm)	Feeding rate (ml h^{-1})	Collector speed (rpm)	Mean nanofiber diameter (nm)
J	DMF/Acetone	15	20	15	1	1200	202
K	DMF/Acetone	15	20	15	3	1200	258
L	DMF/Acetone	15	20	15	5	1200	480
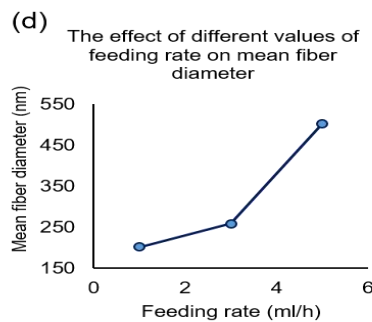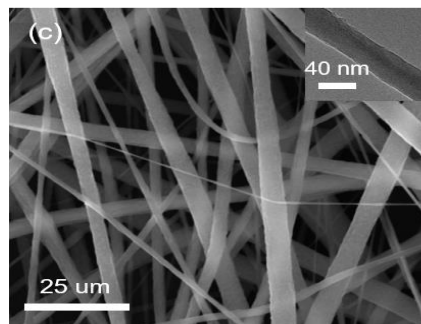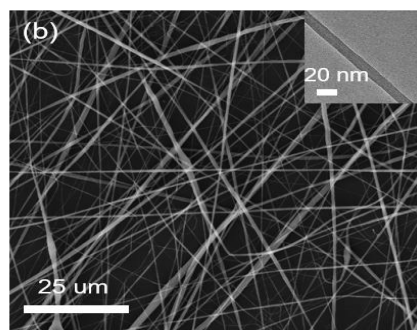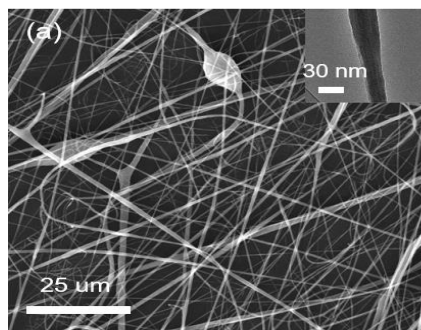
Fig. 5.4 SEM images of samples (a) Sample J, 1 ml h^{-1}, (b) Sample K, 3 ml h^{-1}, and (c) Sample L, 5 ml h^{-1}, for 15 wt% of PVDF under 20 kV and the collector speed of 1200 rpm. (d) The relationship between the mean fiber diameter (nm) and feeding rate (ml h^{-1}).

5.3.1.5 Effect of the rotary speed of the drum collector

Table 5.5 summarizes the mean fiber diameters, distribution and the collector speeds for Samples M, N and O, corresponding to 400, 800 and 1200 rpm, which were obtained while fixing other electrospinning parameters. Their corresponding morphology examined by SEM is shown in Fig. 5.5a-c. At 400 rpm, the mean diameter is 368 nm for Sample M. Double the speed to 800 rpm, the mean diameter reduced to 308 nm for Sample N, which is a decrease of 16.3 %. Further increase the speed to 1200 rpm for Sample O led to further diameter decrease to 271 nm, a further 12.3 % reduction. Furthermore, Fig. 5.5a and b show that the fibers were not aligned, somehow tangled together, however the 1200 rpm Sample O exhibited more alignment feature, Fig. 5.5c. The elongation force during electrospinning is provided by the tangential pulling of the rotary collector. When its speed is increased, this pulling led to a rise in fiber alignment, whilst reducing the fiber diameter.

This relationship between the collector speed and the mean diameter of fibers is plotted in Fig. 5.5d, exhibiting a linear relationship. At the top of the graph, the diameter of the fibers is thicker and reduces to the minimum size at the highest speed of 1200 rpm. It should be noted that the upper allowed safe speed for the rotary drum is 1200 rpm. Therefore, no investigation on further increasing the rotary speed was carried out, which could result in much finer fibers. The most appropriate collector speed is 1200 rpm, which produces fibers with less beads and being more aligned.

Table 5.5 The collector speed and mean nanofiber diameter obtained while fixing other electrospinning parameters.

Samples	Solvent	Concentration (wt%)	Voltage (kV)	Distance (cm)	Feeding rate (ml h⁻¹)	Collector speed (rpm)	Mean nanofiber diameter (nm)
M	DMF/Acetone	15	20	15	3	**400**	368
N	DMF/Acetone	15	20	15	3	**800**	308
O	DMF/Acetone	15	20	15	3	**1200**	271
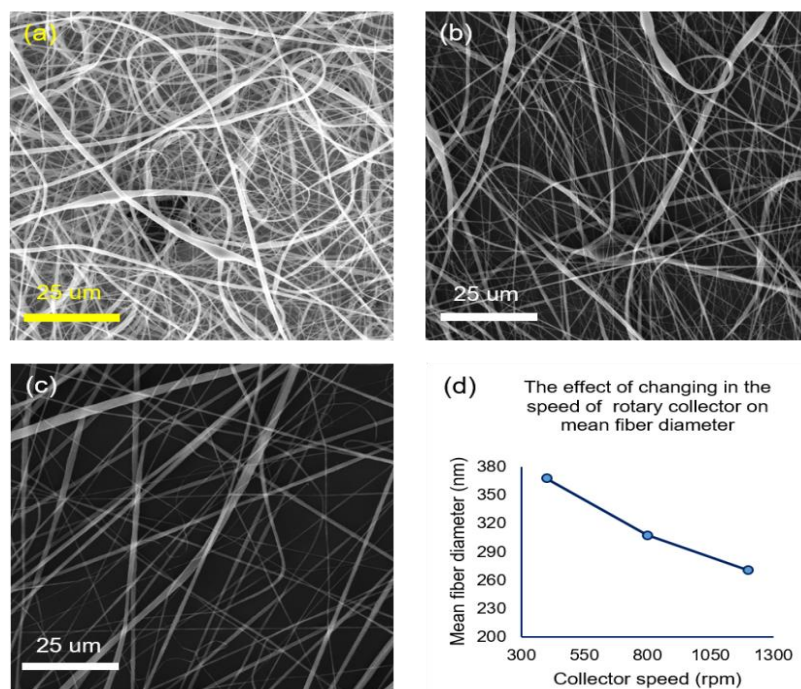
Fig. 5.5 (a-c) SEM images. (a) Sample M, 400 rpm, (b) Sample N, 800 rpm, and (c) Sample O, 1200 rpm, obtained from 15 wt% of PVDF under 20 kV voltage under the same feeding rate of 3 ml h⁻¹. (d) The relationship of mean fiber diameter (nm) vs collector speed (rpm).

5.3.2 Structural and Phase features of the PVDF nanofibers

5.3.2.1 The effect of concentration on structure

The X-Ray diffraction (XRD) profiles shown in Fig. 5.6a present a comparison between the pure semi-crystalline PVDF powder and the electrospun nanofibers from three different PVDF concentrations in the same 10 ml solution, named as

Samples A (15 wt.%), B (16.5 wt.%) and C (18 wt.%). The spun fibers exhibit one intense peak at 20.8° (200), two weak shoulder peaks at 36.6° (120) and 39° (220), and a peak at 56.9° (221), which correspond to the β-phase of PVDF electrospun fibers [287]. The pure PVDF powder exhibits peaks at 18.4° (020), 19.8° (110), 26.4° (001), 33.2° (121), 35.9° (130) and 38.8° (002), which are indexed to α- and γ-phases, but not the β-phase [287-291]. A further comparison of the relative intensity ratios between diffraction peaks at 2θ of 20.8° and 38.8° as indicators for the β-phase content, gives values of 4.73, 4.30 and 3.87 for Samples A, B and C respectively. Interestingly, the β-phase relative intensity at these 2-thetas for Sample B is higher than that of Sample C but lower than that for Sample A. The high content of β-phase for Sample A can be attributed to the better interactions between PVDF and the solvent at this concentration. The change of α-phase to the dominant β-phase occurs due to the high voltage applicator on the stretched polymer jet [287].

As the solvent used in this study is DMF, the dipolar interfaces between C=O and CH_2-CF_2 in the solvent and PVDF in addition to the other weak hydrogen bonding such as C=O…..H-C will make the β-phase formation possible [292-293]. For Sample A, the sharpest β-phase peak is a consequence of the electrospinning that has the highest electric field burst of speed in the stretching of the polymer jet. Therefore, the most suitable concentration for achieving the highest β-phase for optimal piezoelectricity properties is 15 wt%.

The bonding information of the electrospun PVDF fibers and pure PVDF powder was measured by Fourier-Transform Infrared (FTIR), and the results are shown in Fig. 5.6b. In the fiber samples, transmittance bands at 840, 1072, 1170 and 1276 cm^{-1} are corresponding to the β-phase, while the other bonds at 762, 795, 876, and 975 cm^{-1} are from the α-phase in the pure PVDF powder. The powder sample displays a band at 838 cm^{-1} for the γ-phase which is close to the value of the β-phase band in fibers FTIR results. The relative intensity ratio of fixed wavelengths between 840 cm^{-1} and 1170 cm^{-1} for β-phase equals to 0.95 for Sample A, 0.91 for Sample B and 0.90 for Sample C, which provides further evidence that Sample A contains the highest β-phase content of 89%, as shown in Fig. 5.7 and Table 5.6. The detailed calculation is explained as follows.
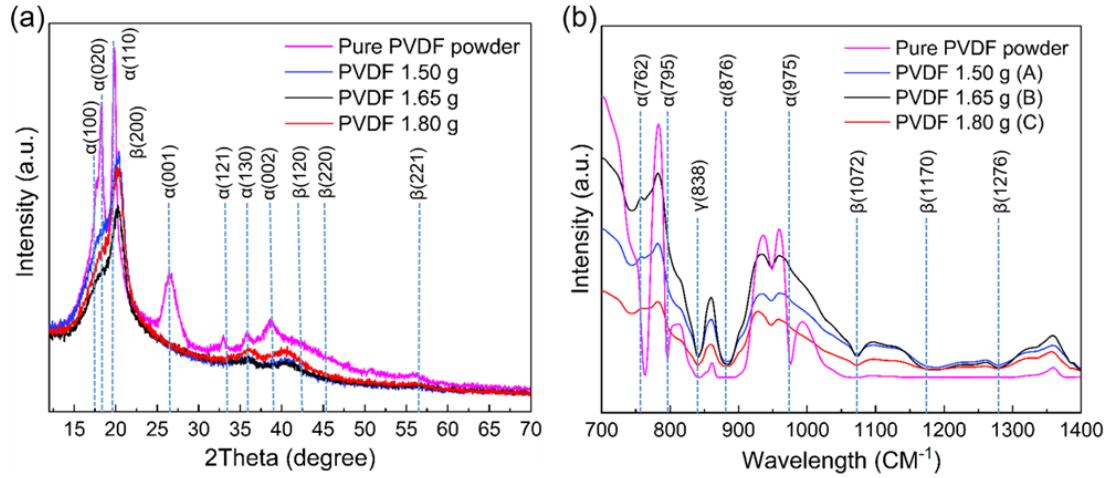
Fig. 5.6 (a) XRD profiles of pure PVDF powder and electrospun fibers from different concentrations of PVDF, and (b) FTIR spectra for PVDF powder containing α and γ phases and, three different concentrations of PVDF electrospun nanofibers with β-phase.

The quantification of β-phase by FTIR results is derived from the Lambert-Beer law and the most promising candidate for achieving the highest piezoelectric properties is Sample A, having the maximum value of F(β) = 0.89, against 0.79 and 0.70 for Samples B and C.

The simplified form of the Lambert Beer law is used to quantify the phase contents in PVDF electrospun fibers. Assuming absorption coefficients as $K_\alpha = 6.1 \times 10^4 \ cm^2 mol^{-1}$ and $K_\beta = 7.7 \times 10^4 \ cm^2 mol^{-1}$ for respective wavenumbers of 766 and 840 cm^{-1} in all electrospun Samples A, B and C, the equation can be expressed as below [294].

$$F(\beta) = \frac{A_\beta}{\left(\frac{K_\beta}{K_\alpha}\right)A_\alpha + A_\beta} \qquad \text{Eq 5.1}$$

With the objective to achieve the highest fraction of β-phase, the best range of electrospinnable production relevant to the optimized range of concentration starting from 15 to 18 wt%, is summarized in Table 5.6, and the relationship between F(β) and the change in concentration is shown in Fig. 5.7. The range of concentrations started from 12 to 18 wt% with an increment equal to 1.5 wt%. For concentrations

lower than 15 wt%, the solutions were not electrospinable, and the products were particles. They were collected only for FTIR analysis. Our results showed that increased concentrations led to higher β fraction, however, it started decreasing from the concentration more than 15 wt%.

Table 5.6 The concentrations of PVDF effect on the content of β-phase.

Samples	Solvent	Concentration (wt %)	A_α	A_β	F(β)
A	DMF/Acetone	15	0.173	0.844	0.89
B	DMF/Acetone	16.5	0.124	0.872	0.79
C	DMF/Acetone	18	0.234	0.701	0.70
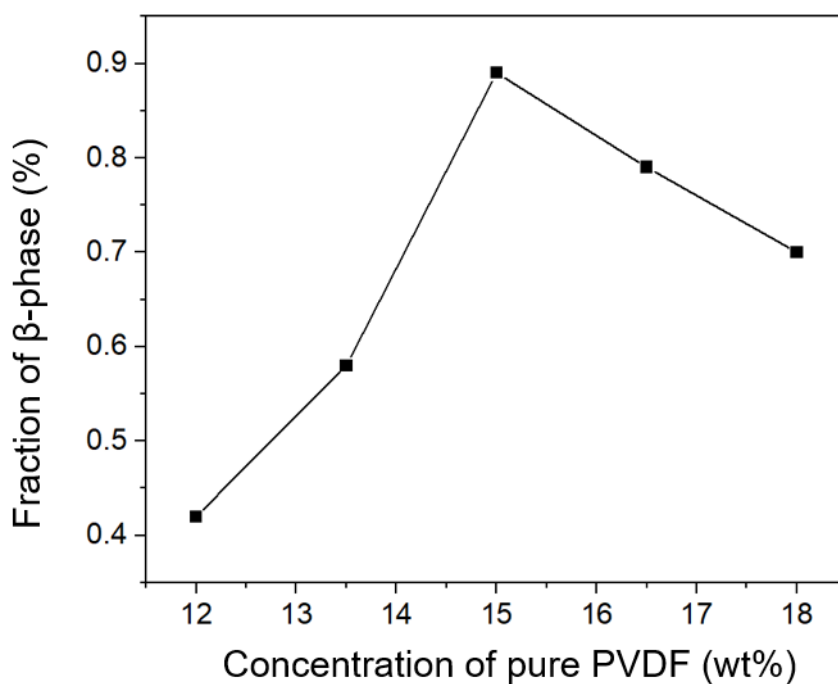
Fig. 5.7 Fraction of β-phase in percentage vs. the concentration of PVDF solution.

XPS was used to analyze the surface elemental composition and chemical state of the raw PVDF powder and different fiber samples (Fig. 5.8). The peaks of F 1s (~688 eV) and C 1s (~286 eV) regions, as well as F KLL Auger transition are

clearly observed in the XPS survey spectrum of all PVDF samples (Fig. 5.8a and c) [295]. The O 1s (~532 eV) of all samples is also observed in low intensity in the survey spectrum. The peak of C 1s of all samples could be deconvoluted into five peaks corresponding to the elements and groups directly boned to carbon atoms (Fig.5.8b and d-f). Two main peaks at about 286 and 290 eV are likely to originate from the –CH$_2$– and –CF$_2$– components in PVDF, respectively [296]. The peaks at about 285 and 288 eV are corresponding to –CH– and carbon atom in strong electron withdrawing environment (For example in ester group, amide group or boned with withdrawing atom such as N or O, assigned with –COO), respectively [281]. A small peak at the highest binding energy of about 293 eV corresponds to –CF$_3$– groups, as seen in perfluorinated ethers [297]. Based on the list of the element composition from both pristine PVDF powder and spun PVDF fibers (Table 5.7), the O 1s/C 1s and F 1s/C 1s ratios of all samples are found to be at the range of 0.016-0.031 and 0.65-0.8, respectively, which fall within the range of PVDF from the literature [298]. The variation of each element might be subjected to contamination during the preparation process or/and dehydrohalogenation of PVDF [281], [299]. The percentage of each component of the C 1s spectrum is also summarized in Table 5.8. The ratios of –CH2– and –CF2– components are 1.3, 1.24, 1.1 and 1.14 for the pristine PVDF, Sample A, B and C, respectively, exhibiting a tread of reducing. The increasing percentage of CH from the fiber samples could be affected by the dimethylformamide (DMF) that was used as the solvent during the fiber preparation. The XPS results have confirmed that the PVDF has been successfully prepared in the fiber form, and the fiber samples remained similar to the pristine PVDF in terms of their elemental composition and chemical states.

Table 5.7 The elemental compositions (in atomic percentage) of the pristine PVDF powder and the as-prepared fiber samples.

Samples	C 1s (At%)	O 1s (At%)	F 1s (At%)	$F.C^{-1}$	$O.C^{-1}$
Pure PVDF powder	54.6	1.8	43.6	0.80	0.032
Sample A	59.6	1.8	38.6	0.65	0.030
Sample B	55.4	0.8	43.8	0.79	0.015
Sample C	57.4	1.0	41.6	0.73	0.018

Table 5.8 Atomic percentage of C 1s surface chemical composition of the pristine PVDF powder and the as-prepared fiber samples.

Samples	CF_2 (At%)	CH_2 (At%)	-COO (At%)	CH (At%)	CF_3 (At%)
Pure PVDF powder	20.2	26.3	2.9	3.0	0.5
Sample A	19.0	23.5	3.1	13	0.4
Sample B	20.6	22.2	2.7	6.1	0.3
Sample C	20.7	23.6	2.8	6.7	0.7

The C:H:F ratio obtained from the spectrum after curve-fitting is 1:1:0.8, respectively, which is in good agreement with the ratio in PVDF molecules (1:1:1) [180].
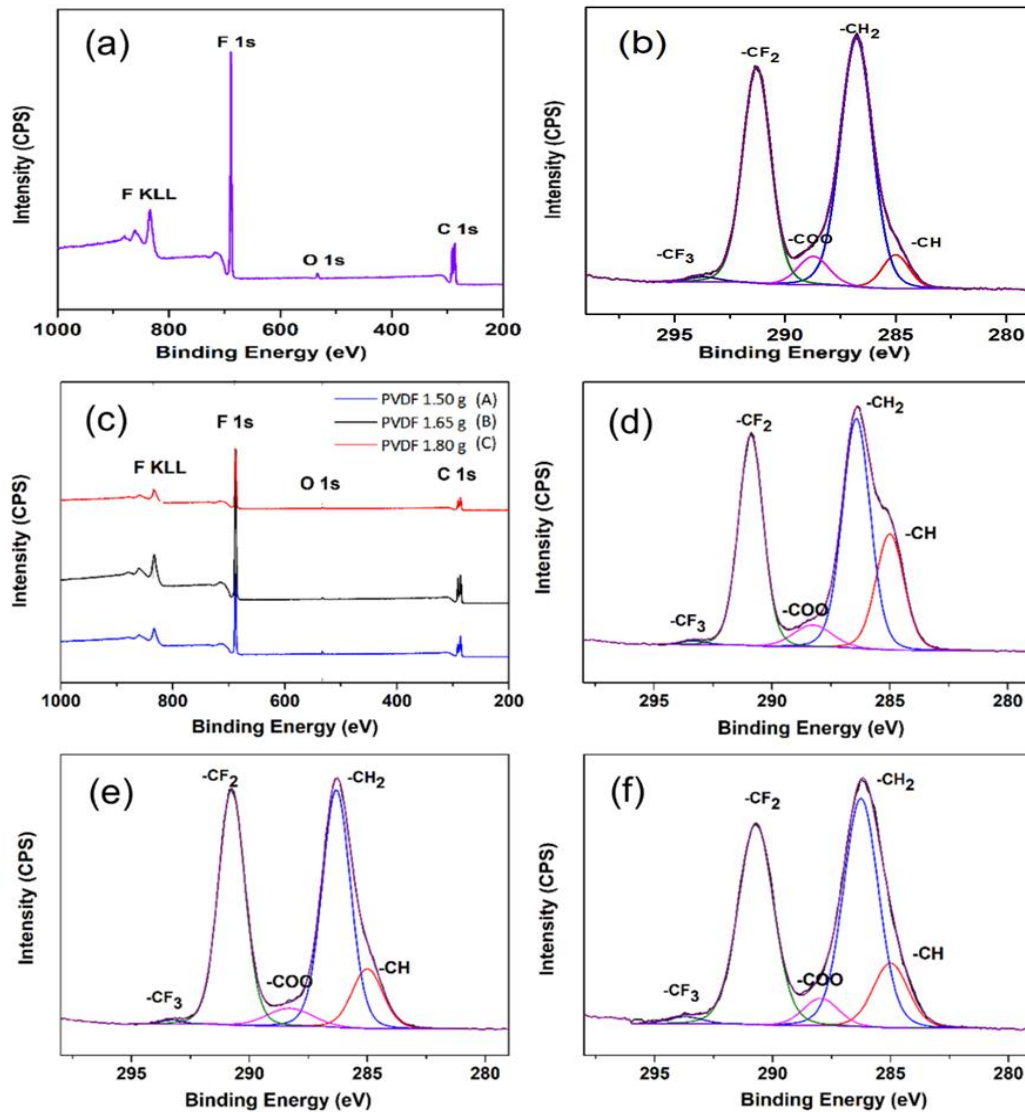
Fig. 5.8 XPS spectra. (a, b) Pure PVDF powder, and (c-f) PVDF electrospun nanofibers for Samples A, B and C.

According to the Raman Spectra (Fig. 5.9), all phases of the electrospun fibers and the powder sample could be distinguished. In the powder sample, both α and γ phases exist; whilst in the electrospun fibers, the major peaks are assigned to the β-phase. The α phase in the powder sample presents Roman shifts at 410, 489, 612, 762, 876, 975,1068,1149 and 1209 cm^{-1} and the shift of the γ phase appears at 838 cm^{-1}. The intensities of the β-phase mode in all samples are relatively higher compared with those of the α-phase for the commercial PVDF powder sample. For the electrospun fibers, the Raman shifts of the β-phase are situated at 795, 840,

1072, 1276 and 1431 cm^{-1}, which are in accordance with the FTIR results (Fig. 5.9b). Most of the CH$_2$ rocking associated to the β-phase is located around 795 cm^{-1}. Therefore, these results have confirmed the higher β-phase content in the present electrospun PVDF fibers than in the commercial powder form.

Furthermore, the relative intensity ratios of two fixed wavelengths, at 1072 and 1276 cm^{-1} for the β-phase, are 1.02, 1.00 and 0.98, respectively, for Samples A, B and C. The highest value in Sample A suggests the highest β-phase content amongst the three samples of different concentrations investigated in this study, which agrees well with the previous calculated results.
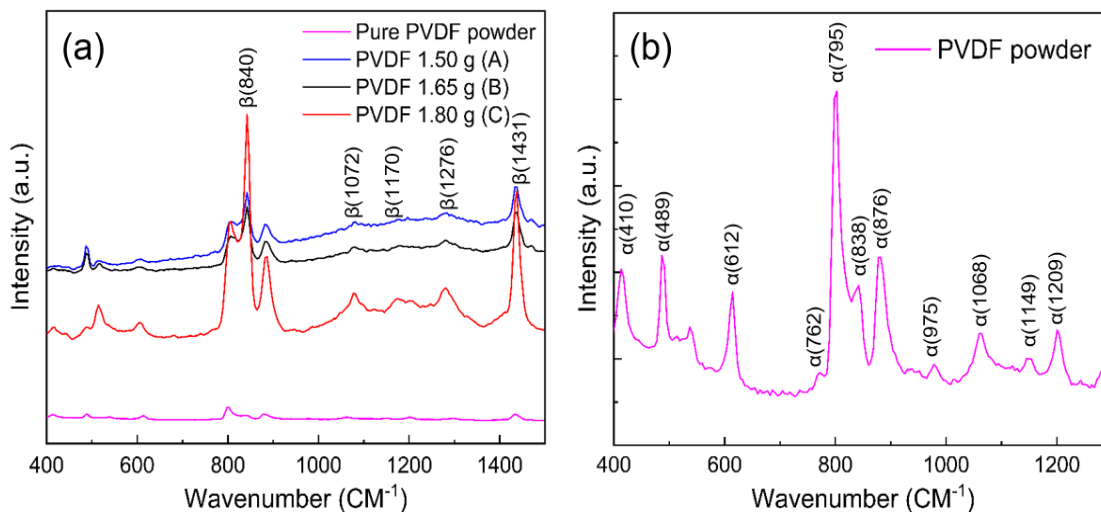
Fig. 5.9 (a) Raman spectra of PVDF electrospun nanofibers for Samples A, B and C, and (b) pure PVDF powder.

The Differential Scanning Calorimetry (DSC) thermograms of electrospun PVDF nanofibers for Samples A, B, C and the pure PVDF powder are shown in Fig. 5.10. The peaks around 155 to 165 °C are similar for all samples, however minor differences in the melting temperatures are still visible which are summarized in Table 5.9 in the thermal analysis results. In the first heating scan, the broad melting endotherms observed for the electrospun nanofibers are in agreement with the literature and all electrospun samples show a melting endotherm, confirming the predominant existence of the β-phase [22],[300-305]. Conversely, for the powder sample, there is a small amount of α-phase present, as revealed in both the XRD

and FTIR analyses. Although the effect of the concentration on the crystallinity of PVDF is multifaceted, the results indicate that the degree of crystallinity of electrospun fibers is the highest for Sample A.

Furthermore, a shift to a lower temperature upon the β-phase formation is observable for all samples except for Sample C, and the melting temperature (T_m) slightly moved to higher temperature for Sample C. Cooling curves have also been affected by the variation of PVDF concentration, and the slight differences between their crystallization temperature (T_c) are summarized in Table 5.9. For the pure PVDF powder, the melting temperature peak is like that of Sample C, whereas its 121.1 °C Tc is slightly lower than that of the electrospun nanofibers (Fig. 5.10). The area of the melting peak is increased when the concentration surges from Sample A to C.

The crystallinity was calculated using the crystallinity equation presented in Chapter 3, Eq. 3.3. The increased 2% crystallinity of electrospun fibers for Sample A, compared with the powder Sample from 44.2 to 45.1, is significantly higher than other samples which is due to the thinner fibers formed. Also, a drop of almost 12% in crystallinity for Samples B and C from 39.7 to 39.1 can be attributed to the shorter solidification period in the electrospinning process. When the loading of PVDF ranges from 15 to 18 wt%, the crystallinity of PVDF chains becomes low and the crystal ability of PVDF will be reduced. Similarly, this can be ascribed to the chain motion restriction of PVDF chains for higher concentration than the moderate one as Sample A [306].
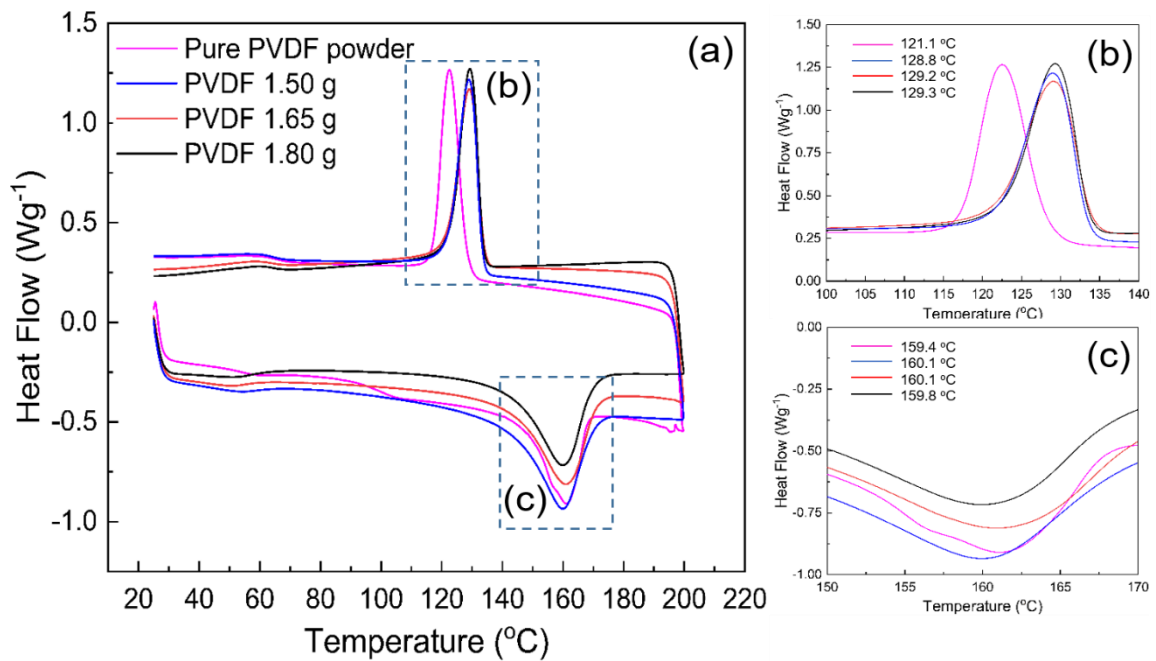
Fig. 5.10 (a) DSC trace of the pure PVDF powder and electrospun PVDF nanofibers including Samples A, B and C. (b) cooling thermograms and (c) heating thermograms of the fibrous and powdery samples.

Table 5.9 DSC analysis of the pure PVDF powder and electrospun fibers, Samples A, B and C. T_m: Melting temperature; ΔH_m: enthalpy of fusion and X_{DSC}: degree of crystallinity.

Samples	T_c [°C]	T_m [°C]	ΔH_m [J g^{-1}]	X_{DSC}
Pure PVDF powder	121.1	160.1	45.2	44.2
Sample A	128.8	159.4	46.7	45.1
Sample B	129.2	159.8	43.3	39.7
Sample C	129.3	160.1	41.1	39.1

5.3.3 Effect of concentrations on the piezoelectric response of the electrospun PVDF fibers

The local amplitude and the piezo-response phase of electrospun samples are shown in Fig. 5.11a-d. A strong piezoelectric contrast is seen in the amplitude image because of the deflection generated by the applied AC field. The negative and positive values of phase image for the nanofiber are relevant to antiparallel ferroelectric nano domains with 180° domain walls for all electrospun nanofiber samples. Under the effect of electric fields, the local hysteresis loops are shown in Fig. 5.11a and b. The forward and backward strong voltages are -12.5 and 12.5 V. The captured data from the PFM images indicate that the magnitude of the amplitude is ~ 170 mV for Sample A at E = 11.5 V, which is the highest amplitude of piezoelectric signal among all samples, and its amplitude and maps of surface height images are shown in Fig. 5.11c. As it is clear in this figure, the phase versus applied voltage for Samples A, B and C exhibited an almost 180° switching hysteresis loop, as well as a complete switch in the polarization of each sample, as a result of the stress generated by the PFM tip.

Furthermore, the highest voltage and current outputs obtained from a square copper sheet of $25\ mm \times 15\ mm$ coated by 15 μm thickness of electrospun PVDF nanofiber facing to the PET sheet attached to another square copper sheet of $25\ mm \times 15\ mm$, are 124 V and 174 nA which are plotted as Fig. 5.11e and f. The effect of piezoelectricity can be seen as the result of transition from the α-phase of the powder to the β-phase in the electrospun fibers. The principle of tip-link activation is to deform them as a static nanofiber membrane through acoustic force, which is like current investigation applied by PFM.

The above results highlight that the use of an appropriate electrospun PVDF nanofiber of pure, biocompatible, and flexible can generate an open circuit voltage (V_{oc}) of 170 mV for a single fiber. This value is sufficient to mimic artificial tip-links, as the natural hair cell's output is only 125 mV (V_{oc}) [307].
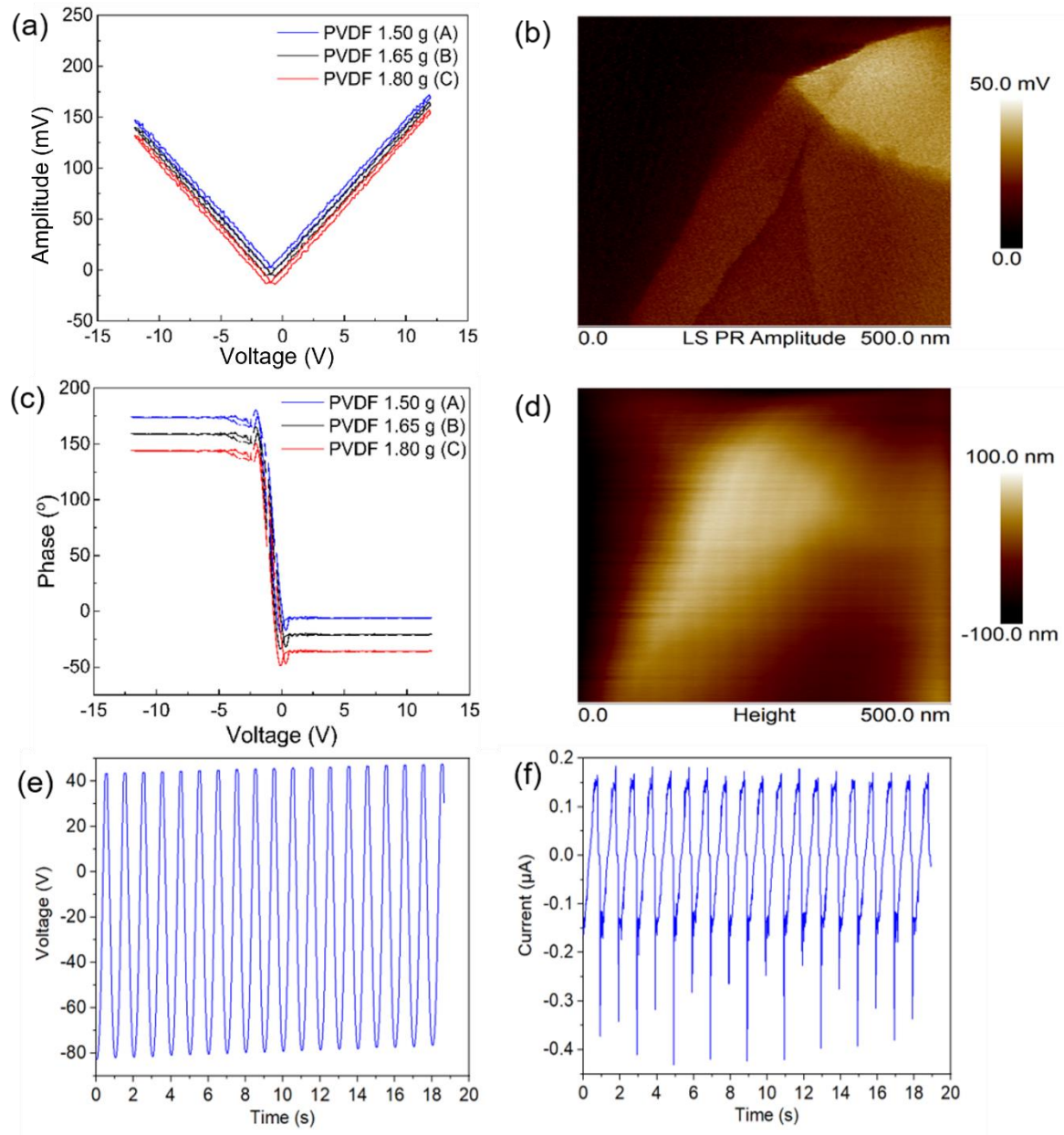
Fig. 5.11 (a-f) Piezoresponse hysteresis loops for Samples A, B and C and piezoresponse force microscope (PFM) phases and corresponding amplitude hysteresis in response of the applied voltage bias for Samples A, B and C and (e-f) electrical response of PVDF electrospun nanofibers mat with 15% wt. PVDF under applied force of 50 N.

There are couple of parameters which need to be discussed here as the main achievements of this Chapter. The highest β-phase fraction and the thinnest electrospun PVDF fibers created in this work, play the most important roles in the piezoelectric properties of the electrospun PVDF fibers, and they are originating from the optimized concentrations of the PVDF solution. Previous reports produced the smallest diameter of 385 nm, with beads, whilst continuous fibers were barely formed, and their highest β-phase fraction is 0.42 [308]. For current electrospun fibers, the mean diameter is 270 nm and the β-phase fraction reached 0.89, achieved when the concentration of PVDF in DMF/Acetone (3/7 volume ratio) mixture was 15%. In another research, the PVDF was dissolved in common ratio of 4/6 DMF/Acetone, and the β-phase fraction was about 0.86, however the concentration of PVDF was 20% [309]. The higher β-phase fraction obtained in this study is believed to originate from the thorough conversion from α-phase to β-phase, which has not been achieved in previous studies.

The effect of PVDF solution concentration on the phase conversion is complicated. When it is increased, the chance to form beaded fibers and thin fibers is equal, as reported. When the concentration is very low, the process of electrospinning changes to electrospraying instead. Although higher concentrations have been suggested in several reports, most of them ended up with beaded areas mixed with fine fibers [310]. To improve the chance of thin fiber formation without bending and beaded parts, the solution we have developed was different from most of previous studies. This higher value of acetone in our study, facilitated the smoother fibers fabrication. This can be assumed that the surface tension is increased when the viscosity and concentration of PVDF are increased. This surface tension is the barrier to the formation of uniform PVDF electrospun fibers. This was carefully controlled by the changing of the concentration rate in this study. The spinnability of PVDF is also dependent upon the concentration of solution. Although it was reduced for the higher concentration of PVDF, in order to reduce the clogged and solidified PVDF solution, the time required to dissolve it was precisely monitored when the solution vial was left on the hot plate. The longer it took, the lower the viscosity of solution, so that PVDF reached the highest solubility in our study. Fig. 5.12(a-c) presents the solutions prepared, which shows after different time of

12, 18 and 24 h Sample A changed from partially to completely dissolved. Red arrows show the residual particles of PVDF powder in the vial containers A and B (Fig. 5.12a and b) which were dissolved completely in vial C after 24 h (Fig. 5.12c).
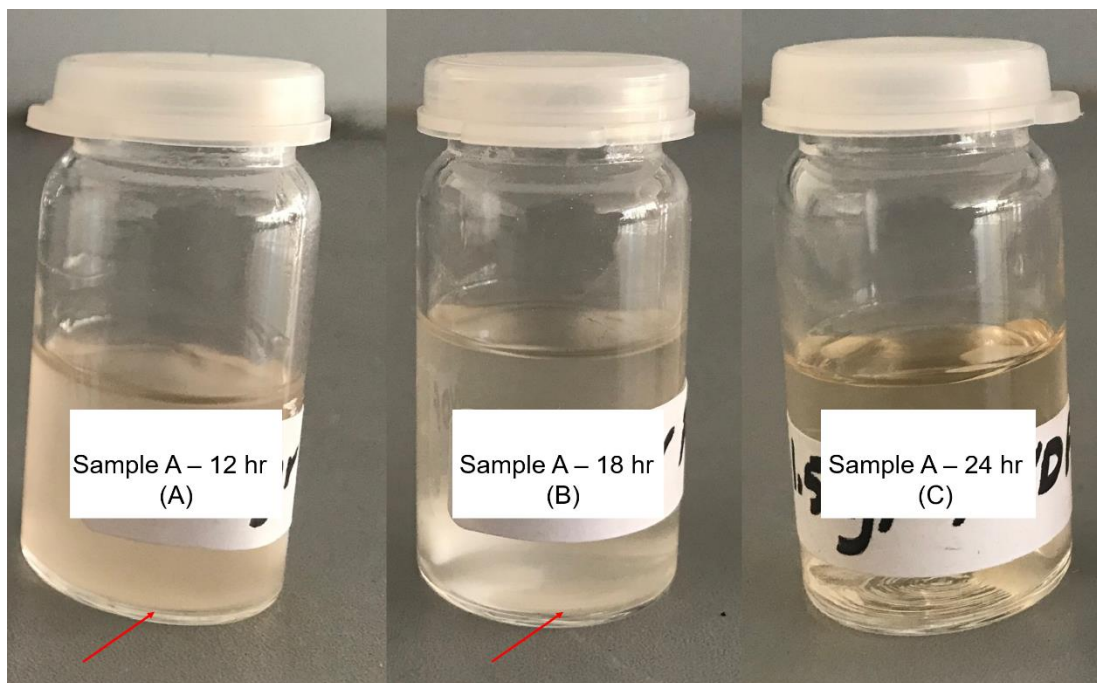
Fig. 5.12 Photographs showing the PVDF dissolved in the solution after various time for Sample A. (a) 12 h, (b) 18 h and (c) 24 h. Red arrows pointing to the suspended powders in the solution.

5.4 Summary

In this Chapter the pure PVDF electrospun nanofibers obtained using different parameters have been thoroughly characterized for their morphological, structural, and compositional features, and their piezoelectric properties have been evaluated, by using combined techniques. These investigations have led to the following findings:

- Finding the setup leading to fabrication of bead-free and smooth electrospun PVDF nanofibers was the most challenging part of this experimental session.
- Optimized conditions of electrospinning in this Chapter for specific values of the distance between the rotary collector and the needle containing the PVDF solution, feeding rate, speed of the aluminum collector and the applied voltage

are 15 cm, 3 ml h^{-1} ,1200 rpm and 20 kV respectively. Furthermore, the role of time was monitored for the homogenous distribution of particles in all solution mixtures.

- Better aligned PVDF fibers have been produced when the concentration was 15 wt%, which can be considered because of well dispersed amount of PVDF particles in the DMF/Acetone mixture solution.

- The reduction in the surface tension can be resulted by the increase in the acetone value in our study compared with previous synthesis protocols. This eased the less beads and thin fibers formation.

- The total polar β-phase content of the produced PVDF was effectively enhanced attributing to the increase in piezoelectric properties of the product.

- The highest relative intensity indicating β-phase according to two sharp diffraction peaks of XRD at 2θ of 20.8° and 38.8° was increased to 4.73 for the sample with the thinnest and well aligned fibers.

- In addition, the fraction of β-phase content based on the FTIR result, approved for the same sample reaching to the value of 0.89 higher than previous studies.

- Reaching to the highest β-phase content is ultimately attributing to the increase in the voltage amplitude value to 170 mV for the purpose of tip-links function in the hair cells when the sample is better aligned and includes less bead fibers.

- Furthermore, the interaction between content of β-phase, current and voltage values for a sheet of PVDF electrospun fibers with the thickness of 15 μm for the piezoelectric properties was essentially proven for the reason of acoustic to electric conversion role in tip-links. These values are 174 nA and 124 V correspondingly.

- All the achieved properties are highly desirable for the self-powered application of the proposed artificial hair cell device.

Chapter 6: PVDF-based composite electrospun fibers

6.1 Introduction

In Chapter 5, the fundamental aspects of pure PVDF electrospun nanofibers have been presented. We first investigated the various effects of different fabrication parameters, particularly the effect of concentrations of the PVDF powder in the DMF/Acetone solution, on the property of the electrospun fibers, which paved the way towards our final goal for device construction.

In this Chapter, the study of specific additives into the pure PVDF, to create composite electrospun fibers and further to enhance the functionalities of these fibers will be introduced. The preparation steps of PVDF electrospun composite fibers, the characterisation of their resulting structures, and the process of TENG/PENG fabrication from the electrospun pure PVDF and its composites are provided in this Chapter. This can be divided into 3 parts. Firstly, the syntheses of composite PVDF electrospun fibers by introducing CNTs, LiCl, TiO_2, WO_3 and ZnO particles to the PVDF solution are presented. Secondly, the morphological and structural analyses of the resulting PVDF/CNTs, PVDF/LiCl, PVDF/TiO_2, PVDF/WO_3, PVDF/ZnO composites will be presented. Finally, the phase constitutions of the composite fibers, against the pure PVDF electrospun nanofibers will be studied.

6.2 PVDF-based composite fibers

In this thesis, we synthesized 6 types of electrospun nanofiber samples, including the pristine PVDF and PVDF reinforced with CNTs, LiCl, TiO_2, WO_3 and ZnO. These nanofillers are chosen due to their biocompatibility, as well as their different nucleation behaviour in the PVDF matrix. The impacts of these additives on the morphology, phase compositions as well as piezoelectric and triboelectric properties of the electrospun fibers will be investigated, for the purpose of artificial tip-links structure connectors. The increase or decrease of the β-phase content as the piezoelectric criterion will be studied.

6.2.1 Synthesis of PVDF composites solutions

WO$_3$ particles, (<150 nm particle size), ZnO particles (in three different particle sizes: <1μm, <200 nm and <50 nm), CNTs (<300 nm), TiO$_2$ (rutile, <600 nm), and LiCl (<1μm), were obtained from Sigma Aldrich (UK). All chemicals and reagents were used as received without further purification. The reason of applying three different particle sizes for the ZnO additive was to ascertain the influence of particle sizes on the processing and properties of the fibers.

Different weight percentages of each additive were investigated, as listed in Table 6.1. The weighted additive was added into DMF/Acetone (3/7 volume ratio) mixture solution containing a constant 0.75 g of pure PVDF powder. The mixture was heated with the assistance of a hot plate at 70 °C, under magnetic stirring at 600 rpm, for overnight. The final homogenous and viscous suspensions (transparent for LiCl, in white for additives such as ZnO, TiO$_2$, in yellow for WO$_3$ and in black for CNTs) were used as the stock solutions, as shown in Fig. 6.1, for further electrospinning experiments.

Table 6.1 Detailed constitutions used to prepare for the electrospinning fibers.

Solution No	Additive	Solution D= DMF, A= Acetone
1	PVDF-12 wt.%	4.4 g D/A (3/7 volume ratio)-0.6 g PVDF
2	PVDF-13.5 wt.%	4.37 g D/A (3/7 volume ratio)-0.68 g PVDF
3	**PVDF-15 wt.%**	**4.25 g D/A (3/7 volume ratio)-0.75 g PVDF**
4	PVDF-16.5 wt.%	4.17 g D/A (3/7 volume ratio)-0.83 g PVDF
5	PVDF-18 wt.%	4.1 g D/A (3/7 volume ratio)-0.9 g PVDF
6	PVDF-15 wt.%-WO$_3$-0.2 wt.%	4.24 g D/A (3/7 volume ratio)-0.75 g PVDF-0.01 g WO$_3$
7	PVDF-15 wt.%-WO$_3$-1 wt.%	4.2 g D/A (3/7 volume ratio)-0.75 g PVDF-0.05 g WO$_3$
8	**PVDF-15 wt.%-WO$_3$-2 wt.%**	**4.15 g D/A (3/7 volume ratio)-0.75 g PVDF-0.10 g WO$_3$**
9	PVDF-15 wt.%-WO$_3$-3 wt.%	4.10 g D/A (3/7 volume ratio)-0.75 g PVDF-0.15 g WO$_3$
10	PVDF-15 wt.%-WO$_3$-4 wt.%	4.05 g D/A (3/7 volume ratio)-0.75 g PVDF-0.20 g WO$_3$
11	PVDF-15 wt.%-ZnO-1 wt.%	4.2 g D/A (3/7 volume ratio)-0.75 g PVDF-0.05 g ZnO
12	PVDF-15 wt.%-ZnO-2 wt.%	4.15 g D/A (3/7 volume ratio)-0.75 g PVDF-0.10 g ZnO
13	**PVDF-15 wt.%-ZnO-3 wt.%**	**4.10 g D/A (3/7 volume ratio)-0.75 g PVDF-0.15 g ZnO**
14	PVDF-15 wt.%-ZnO-4 wt.%	4.05 g D/A (3/7 volume ratio)-0.75 g PVDF-0.20 g ZnO
15	PVDF-15 wt.%-ZnO-5 wt.%	4 g D/A (3/7 volume ratio)-0.75 g PVDF-0.25 g ZnO
16	PVDF-15 wt.%-CNTs-1 wt.%	4.2 g D/A (3/7 volume ratio)-0.75 g PVDF-0.05 g CNT
17	PVDF-15 wt.%-CNTs-2 wt.%	4.15 g D/A (3/7 volume ratio)-0.75 g PVDF-0.10 g CNT
18	PVDF-15 wt.%-CNTs-3 wt.%	4.10 g D/A (3/7 volume ratio)-0.75 g PVDF-0.15 g CNT

19	PVDF-15 wt.%-CNTs-4 wt.%	4.05 g D/A (3/7 volume ratio)-0.75 g PVDF-0.20 g CNT
20	PVDF-15 wt.%-CNTs-5 wt.%	4 g D/A (3/7 volume ratio)-0.75 g PVDF-0.25 g CNT
21	PVDF-15 wt.%-TiO$_2$-0.2 wt.%	4.24 g D/A (3/7 volume ratio)-0.75 g PVDF-0.01 g TiO$_2$
22	PVDF-15 wt.%-TiO$_2$-1 wt.%	4.20 g D/A (3/7 volume ratio)-0.75 g PVDF-0.05 g TiO$_2$
23	PVDF-15 wt.%-TiO$_2$-2 wt.%	4.15 g D/A (3/7 volume ratio)-0.75 g PVDF-0.10 g TiO$_2$
24	**PVDF-15 wt.%-TiO$_2$-3 wt.%**	**4.10 g D/A (3/7 volume ratio)-0.75 g PVDF-0.15 g TiO$_2$**
25	PVDF-15 wt.%-TiO$_2$-4 wt.%	4.05 g D/A (3/7 volume ratio)-0.75 g PVDF-0.20 g TiO$_2$
26	PVDF-15 wt.%-LiCl-0.02 wt.%	4.25 g D/A (3/7 volume ratio)-0.75 g PVDF-0.001 g LiCl
27	PVDF-15 wt.%-LiCl-0.03 wt.%	4.25 g D/A (3/7 volume ratio)-0.75 g PVDF-0.0015 g LiCl
28	PVDF-15 wt.%-LiCl-0.04 wt.%	4.25 g D/A (3/7 volume ratio)-0.75 g PVDF-0.002 g LiCl
29	**PVDF-15 wt.%-LiCl-0.05 wt.%**	**4.25 g D/A (3/7 volume ratio)-0.75 g PVDF-0.0025 g LiCl**
30	PVDF-15 wt.%-LiCl-0.06 wt.%	4.25 g D/A (3/7 volume ratio)-0.75 g PVDF-0.003 g LiCl
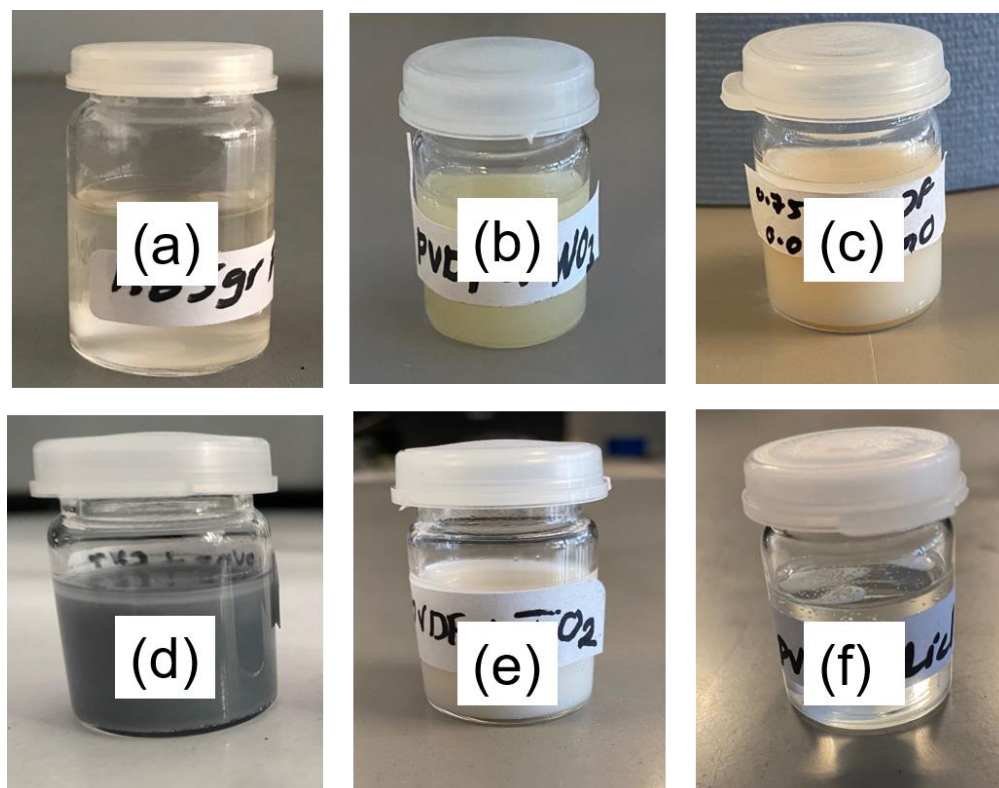
Fig. 6.1 The stocks of (a) pure PVDF, (b-f) WO$_3$, ZnO, CNTs, TiO$_2$ and LiCl suspensions.

6.3 Characterizations

6.3.1 The Morphology

6.3.1.1 Pure PVDF electrospun nanofiber
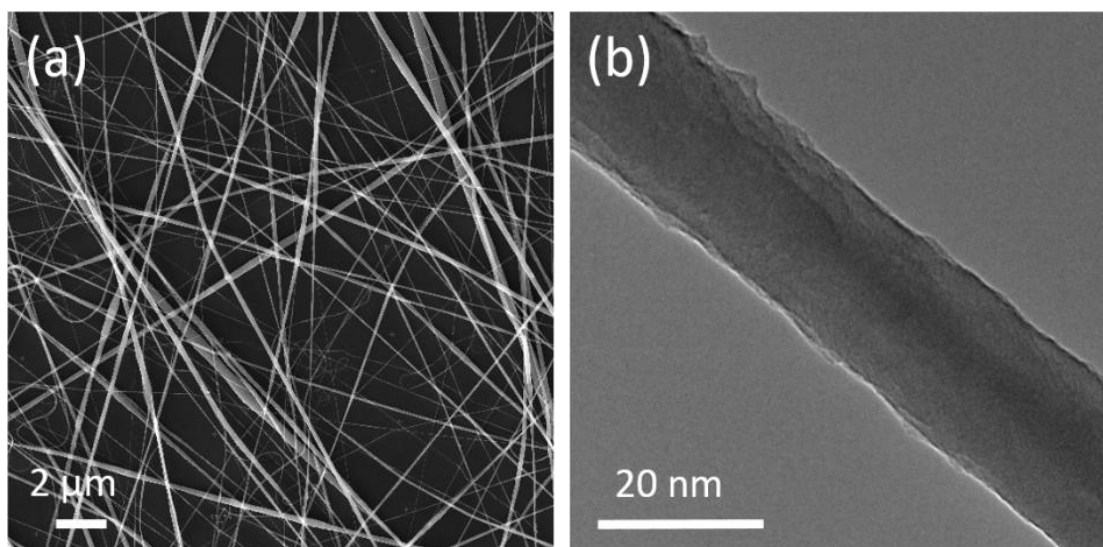
Fig. 6.2 (a) SEM and (b) TEM images of the pristine PVDF electrospun fibers (Sample A) prepared at 15 cm between the needle and collector, at the feeding rate of 3 ml h^{-1}, voltage of 20 kV and collector speed of 1200 rpm.

In Fig. 6.2a, the pure PVDF fibers tend to be aligned which are smoothly electrospun on the Al collector, virtually free of bending and blemish in fibers. The diameter ranges from 30-220 nm for Sample A, with an average of 80 nm, which has been described in detail in previous Chapter. TEM image (Fig. 6.2b) shows a single fiber with a uniform diameter around 20 nm, which is the smallest obtained at this feeding rate.

6.3.1.2 PVDF/WO₃ composite electrospun nanofiber
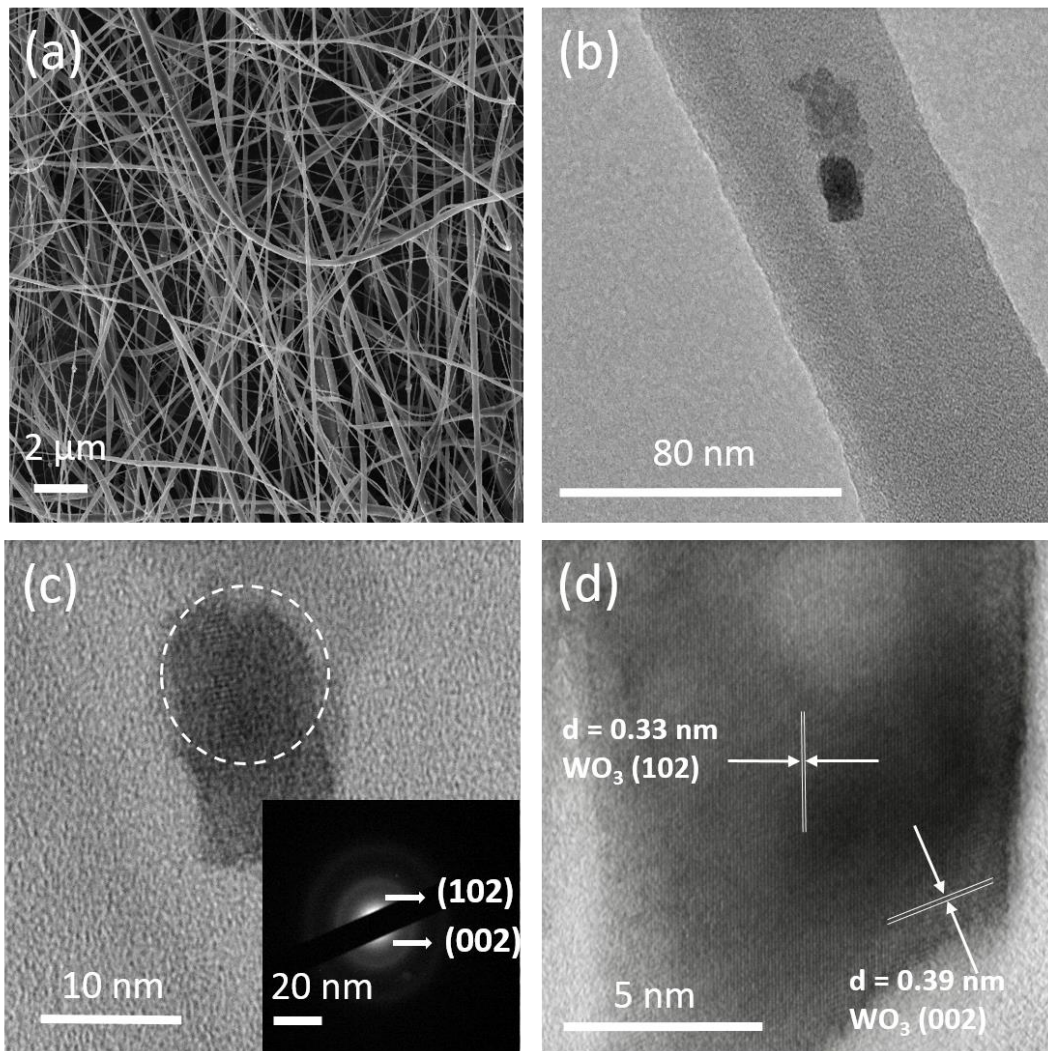
Fig. 6.3 (a) SEM, (b) and (c) low and high magnifications of TEM images and the corresponding SAED pattern of PVDF/WO$_3$ electrospun fibers (Sample P). (d) HRTEM image showing the lattice fringe of the WO$_3$ particle prepared at 15 cm distance between the needle and collector at the same feeding rate of 3 ml h^{-1}, voltage of 20 kV and collector speed of 1200 rpm.

In Fig. 6.3a and b, Sample P with an almost uniform diameter, is free from bead impurities. The diameter ranges 100-480 nm, with an average of 180 nm, which is more than twice of the pure PVDF electrospun fibers. The existence of the WO$_3$ additive within the fiber was confirmed by the HRTEM image and the corresponding

SAED pattern, as shown in Fig. 6.3c. In the picture, the diffraction of the darker particle within the single fiber was indexed to (102) and (002) of orthorhombic WO_3. Further HRTEM image (Fig. 6.3d) shows the lattice spacings of 0.33 nm and 0.39 nm, which are correspondence to the planes of (102) and (002) respectively. Both HRTEM lattice image and SAED pattern have shown that WO_3 additives in the nanofibers are multicrystalline. Sample P did not show any signs of WO_3 agglomeration within or around the fibers, whose morphology is similar to that of the pure PVDF fibers. These results, combined with the XRD result (Fig. A1) presented in the appendix section and Fig. 6.8a which will be discussed in the next section, have confirmed that a composite fiber of $PVDF/WO_3$ was obtained by using the same electrospinning protocol, and that the WO_3 nanoparticles were distributed uniformly within the fiber, with an overall morphology similar to the pure PVDF fiber.

6.3.1.3 PVDF/ZnO composite nanofiber
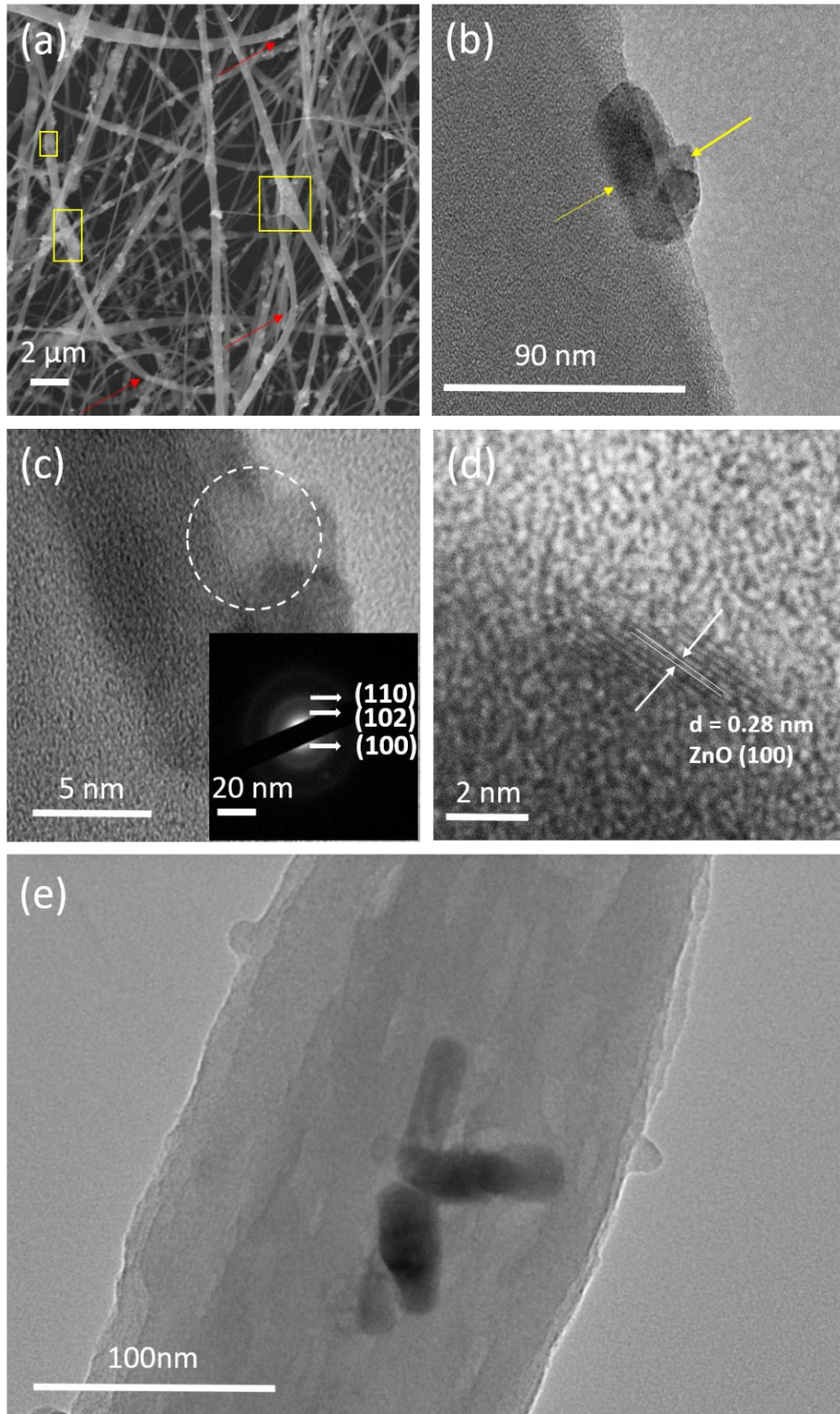
Fig. 6.4 SEM and TEM images of PVDF/ZnO electrospun fibers, Sample Q. (a) SEM image. The red arrows point to bending fibers and yellow frames indicate clogged areas. (b) and (c) Low and high resolution TEM images, showing a ZnO particle at the edge of the fiber. Inset shows the SAED pattern of the particle. (d) HRTEM image showing the lattice fringe of the particle, and (e) The low resolution TEM image of the PVDF/ZnO composite with nanoparticles embedded inside the fiber. The fibers were prepared using the same parameters to the pure PVDF, at a distance of 15 cm between the needle and collector, the same feeding rate of 3 ml h^{-1}, voltage of 20 kV and collector speed of 1200 rpm.

Fig. 6.4a presents the SEM image of PVDF/ZnO composite electrospun fibers, Sample Q. The fibers are randomly distributed and bending, marked by red arrows, against the well-aligned fibers from other samples, with a diameter range of 160 nm-1.60 μm and an average diameter of 780 nm. Clogged ZnO particles are also observed, marked by the yellow frames. The surface of the fibers is not smooth, and the diameter is not uniform for a specific fiber, showing lumps periodically. TEM results of the specific fiber presented in Fig. 6.4b and e show that the ZnO particles are distributed along the surface and within these fibers. The SAED pattern for the particles is indexed to planes of (100), (102) and (110) of the hexagonal ZnO, as shown in Fig. 6.4c, which will be discussed in the next section accompanied with the XRD results. Many fine crystal grains are visible in the ZnO particle for which the polycrystalline feature is apparent in the SAED pattern. According to the HRTEM image of Fig. 6.4d, the lattice spacing of 0.28 nm corresponds to the (100), which is agreed with the XRD result in the appendix section (Fig. A2).

6.3.1.4 PVDF/CNTs composite nanofiber
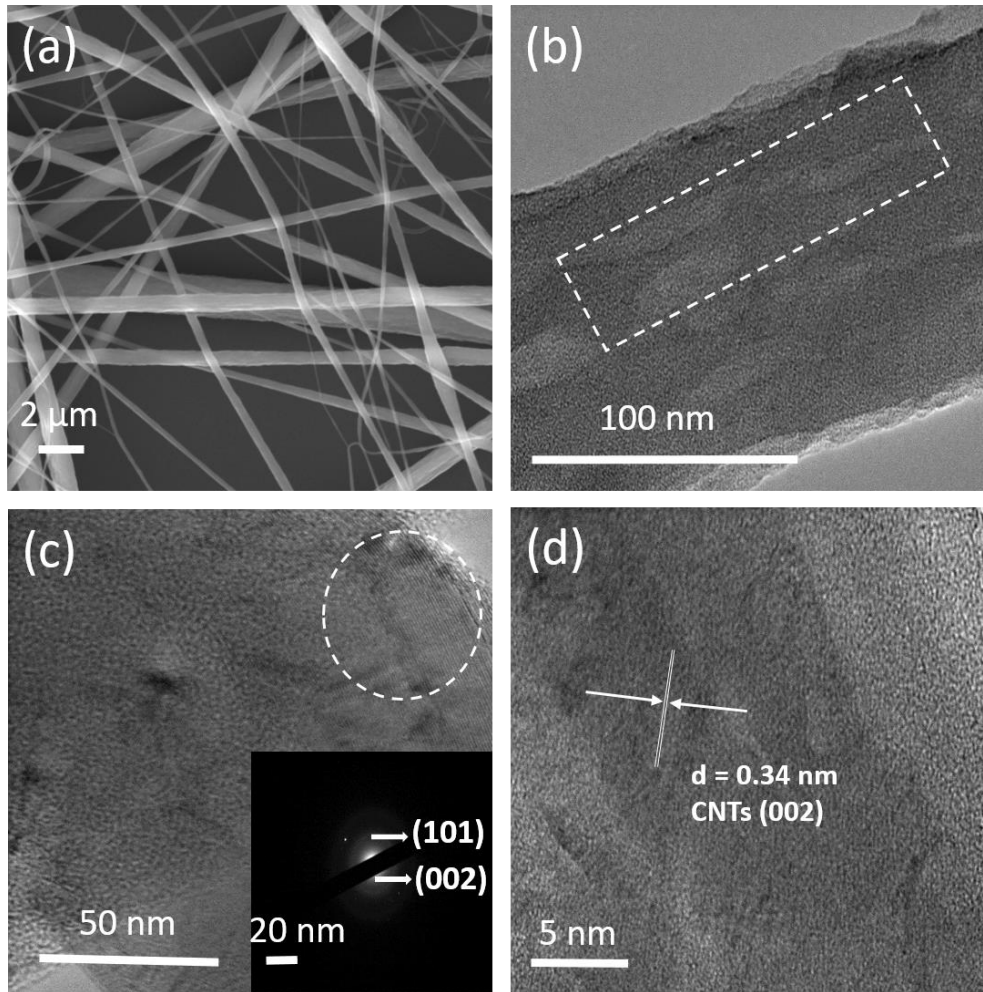
Fig. 6.5 (a) SEM, (b) and (c) low and high magnifications of TEM images, and the corresponding SAED pattern of PVDF/CNTs electrospun fibers and (d) HRTEM image showing the lattice fringe of the particle (Sample R), prepared at 15 cm distance between the needle and collector at the same feeding rate of 3 ml h^{-1}, voltage of 20 kV and collector speed of 1200 rpm.

In Fig. 6.5a, the SEM image shows the PVDF/CNTs composite fibers are quite uniform, having a diameter range of 100 nm-2.40 µm, with an average diameter of 970 nm. According to Fig. 6.5a and b, the CNT additive is mainly dispersed within the fibers, which is free of coarse beads or visible blemish. The SAED pattern taken from an area close to the fiber wall was indexed as (002) and (101) of CNTs, Fig. 6.5c. The HRTEM image shows an interplanar distance of 0.34 nm, which can

be ascribed to the (002) planes of CNTs (Fig. 6.5d). Furthermore, the CNT additive is well-dispersed and surrounded by the polymer, based on the TEM image analyses.

The bonding between CNTs and PVDF polymer seems very strong and the formation of embedded CNTs in the fiber during the electrospinning is evident. Most of CNTs are embedded inside the PVDF nanofiber and are along with the orientation of the fiber without any entanglement of CNT bundles, however, there is a faint contrast between the fiber matrix and the CNT, as marked by the dashed area in Fig. 6.5b, exhibiting the hollow cylindrical structure of CNTs. Unlike other nanofillers (e.g., WO_3, ZnO, TiO_2, and LiCl in this Chapter), CNTs behaved differently. When the 1D CNTs are dispersed in the solution of PVDF prior to spinning, they were embedded within the dissolved PVDF polymer in the mixture. During the electrospinning process, the restriction to fiber shrinkage was more than that exerted by other loosely dispersed 0-D particles when the solvent was evaporated, leaving behind the well-aligned CNTs inside the fibers.

6.3.1.5 PVDF/TiO$_2$ composite nanofiber
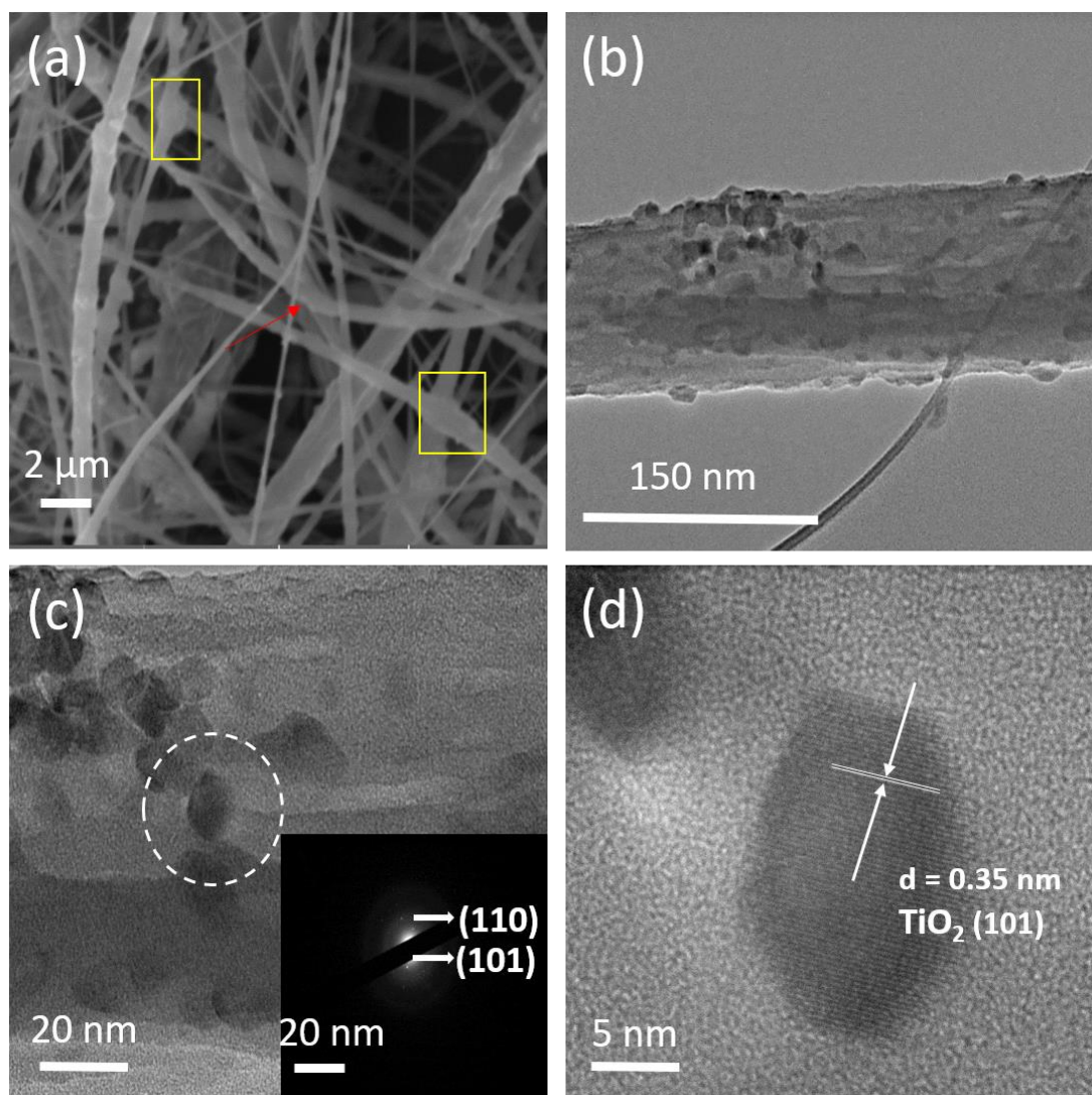
Fig. 6.6 (a) SEM image, (b) and (c) low and high magnifications of TEM images, and (d) the corresponding SAED pattern of PVDF/TiO$_2$ electrospun fibers (Sample S), prepared at 15 cm distance between the needle and collector, at the same feeding rate of 3 ml h^{-1}, voltage of 20 kV and collector speed of 1200 rpm.

Fig. 6.6a and b present the distribution of TiO$_2$ in the composite fiber. These fibers are not smoothly electrospun. Whilst a small number of them are very thin, the majority are extremely bulky, thick, and coarse. Bending fibers marked by red arrow and clogged fibers in yellow frames are shown in Fig. 6.6a. TiO$_2$ particles are thoroughly dispersed and scattered within and around the fiber, Fig. 6.6b. Their

diameter ranges from 110 nm-2.10 μm, with an average of 980 nm. The SAED pattern chosen for the TiO_2 particles embedded in a single electrospun fiber is shown in Fig. 6.6c, which exhibits two diffraction rings of (101) and (110). The HRTEM image shows a d spacing of 0.35 nm, being the (101) plane, as shown in Fig. 6.6d.

6.3.1.6 PVDF/LiCl composite nanofiber
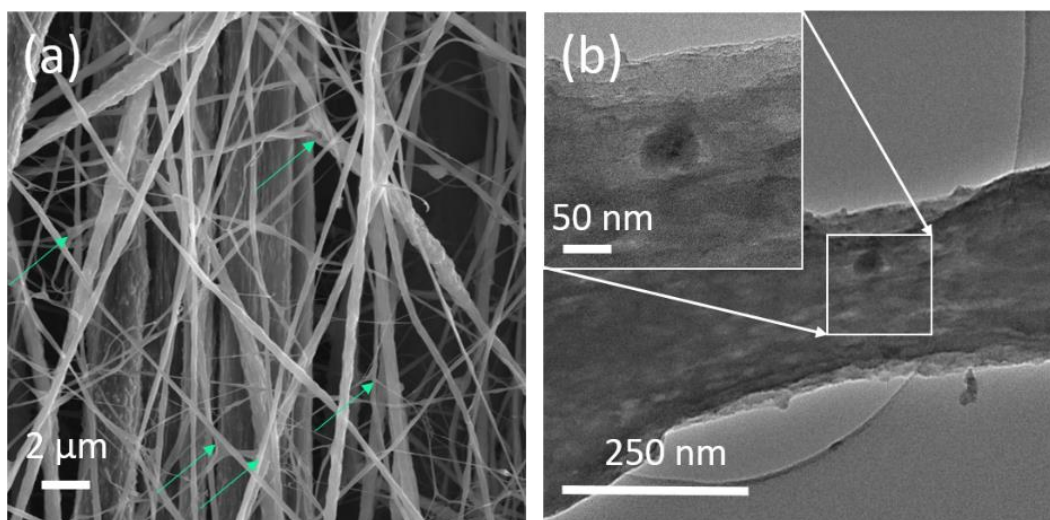
Fig. 6.7 (a) SEM image, green arrows pointing to branched fibers; and (b) low and high (inset) magnification TEM images, showing a particle encapsulated within a fiber. The PVDF/LiCl electrospun fibers (Sample T) were prepared at 15 cm distance between the needle and collector, at the same feeding rate of 3 ml h^{-1}, voltage of 20 kV and collector speed of 1200 rpm.

For Sample T (PVDF/LiCl), the morphology of the composite fibers is shown in Fig. 6.7a and b. The green arrows in the SEM image (Fig. 6.7a) pointed to the branched fibers. The range of diameter is 90 nm-1.80 μm, with an average of 1.20 μm, which is much larger than that of previous composite samples. A single LiCl particle was observed encapsulated within the PDVF fiber. The fiber surface has less bead formation, however the diameter of these fibers is not even, with a variation similar to other samples.

The branch existence in the composite fiber can be due to the balance between electrostatic forces and surface tension of the solution during the electrospinning process. It has been reported that any decrease in the solution's conductivity led to increases in the fiber diameter [311]. This can also be followed by less stretch of fibers due to the reduced tension from the electric field during spinning, as occurred to Sample T (PVDF/LiCl).

The internal balanced positive and negative ions of the LiCl inorganic salt dissolved in the PVDF solution would move in opposite directions under the strong electric field during electrospinning. Based on chemical structure of each additive, we believe that additives such as WO_3, ZnO, CNTs, TiO_2 and LiCl were in free ion form in the DMF/Acetone mixtures. Firstly, for additives of WO_3, ZnO and CNTs, the increase in electrical conductivity of the solution would increase the physical stretching forces. However, for additives such as TiO_2 and LiCl, this effect is absent. Secondly, the higher charge density of the electrified jet (electrically charged liquid of PVDF and its additives) imposed for solution containing WO_3, or CNTs or ZnO, was a result of the induction of positively charged cations of these additives, attached to the negatively charged F ions in the PVDF via electrostatic interactions. In other words, the ionized particles of WO_3, CNTs, ZnO are able to move to conduct electricity much easier than the TiO_2 and LiCl dopants. Both interactions from these fillers resulted in the smaller, better aligned, and more uniform composite fibers, which is in agreement with the higher relative intensities of β-phase contents in Samples P, Q and R, which will be thoroughly discussed in following sections.

Further comparison among pure PVDF (A), PVDF/WO_3 (P), PVDF/ZnO (Q), PVDF/CNTs (R), PVDF/TiO_2 (S) and PVDF/LiCl (T) electrospun Samples, we found that the morphology of PVDF and the WO_3 and CNTs composites was different from those containing ZnO, TiO_2 and LiCl; and similarly, the morphologies of the latter three composites were different in the filler distribution. The resemblance of surface morphology for Samples A, P and R can be seen as bead-free. However, the mean diameter of Sample R is larger than that of both Samples A and P. It is apparent that the size and type of additives played a significant role in governing the morphology of the fibers, including diameter, purity, uniformity, and shape. While the smaller

additives led to finer and smoother fibers, larger additives such as ZnO, TiO_2 and LiCl led to bigger fibers. Whereas the (PVDF/ZnO), (PVDF/TiO_2) and (PVDF/LiCl) composite surfaces ended up with a coarse appearance around the fiber, the (PVDF/WO_3) and (PVDF/CNTs) composite surfaces were smoother, similar to that of pure PVDF fibers.

The fiber diameter varies from 30-220 nm and Avg of 80 nm for Sample A), 100-480 nm and Avg of 180 nm for Sample P, 160 nm-1.60 μm and Avg of 780 nm for Sample Q, 100 nm-2.40 μm and Avg of 970 nm for Sample R, 110 nm-2.10 μm and Avg of 980 nm for Sample S, and finally 90 nm-1.80 μm and Avg of 1.2 μm for Sample T. When the particle size of an additive is smaller (150 nm for WO_3, <200 nm for ZnO and <300 nm for CNTs), the resulting fiber diameter is smaller than those additives with larger particle sizes, such as TiO_2 < 600 nm, and LiCl < 1μm. This result shows that the diameter of the spun fibers is directly affected by the size of the additives. Meanwhile, when WO_3, ZnO and CNTs are mixed with PVDF, the conductivity of the solution increased, which also resulted in thinner fibers, due to the higher charge carrying volume compared with those of TiO_2 and LiCl.

6.4 Structural and compositional characterisations

The XRD pattern of pure PVDF electrospun fibers exhibited one intense peak at 20.81° (200), two weak shoulder peaks at 36.63° (120), 39° (220), and a peak at 56.91° (221) (as shown in Chapter 5 for detail), which matches well with JCPDS No: 38-1638, confirming the dominant β-phase with lattice constants of $a = 4.89$, $b = 4.89$ and $c = 3.88$ nm the electrospun fibers [287]. The strongest intensity of the (200) plane indicates that the electrospun fibers in this sample are perfectly along the <200> direction, and the very week intensities of other planes in the profiles, including (120), (220), and (221), are a typical feature of the 1-D nanofibers.

6.4.1 PVDF/WO₃ composite nanofibers
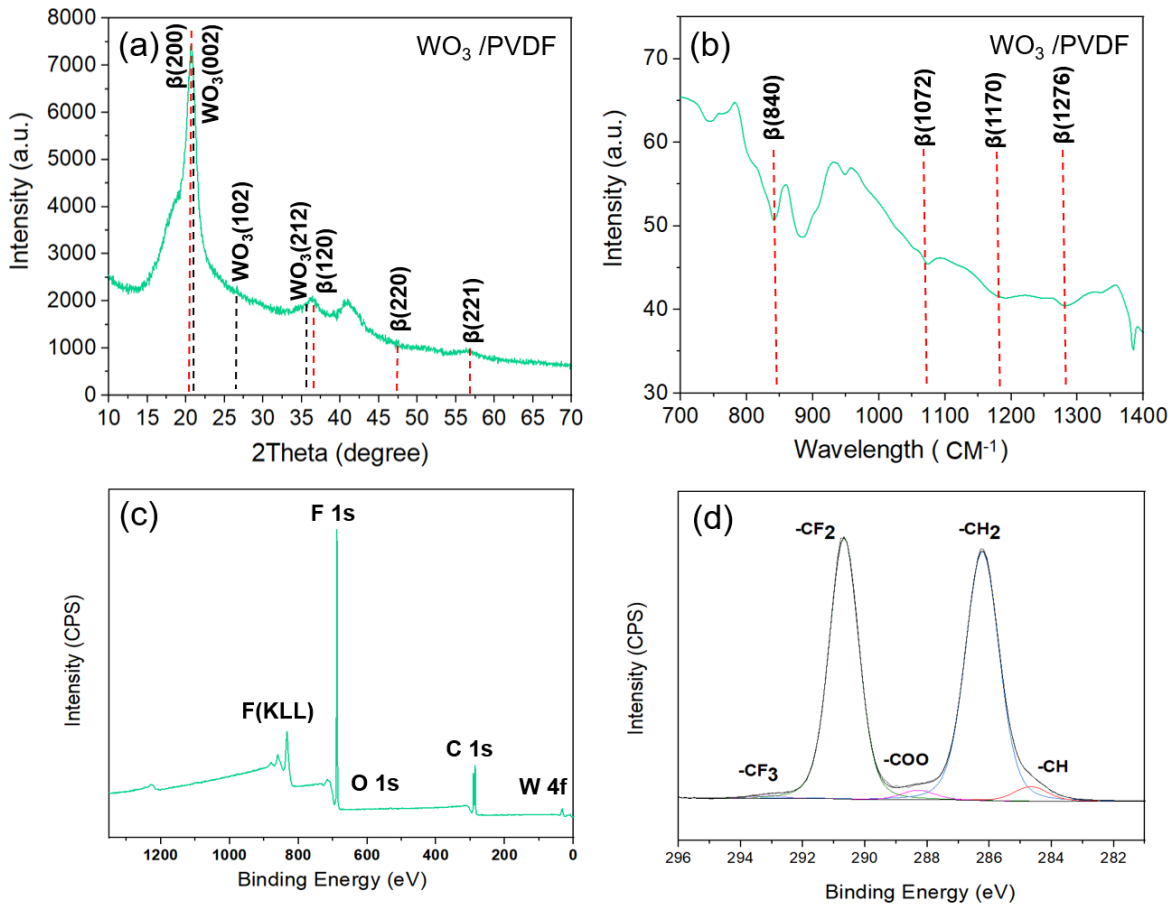
Fig. 6.8 (a) XRD pattern, (b) FTIR spectrum, (c) XPS survey spectrum, and (d) deconvolution of the C 1s peak in (c) of the PVDF/WO₃ electrospun nanofibers, respectively.

The main diffraction peaks for WO₃ appear at 2θ at about 21.24° (001), 22.92° (002), 26.47° (210) and 35.29° (212), which are combined with an intense peak at 20.81° (200), two weak shoulder peaks at 36.63° (120) and 39° (220), and a peak at 56.91° (221) are indexed to the β-phase of PVDF (Fig. 6.8a). The detailed 2θ information of the JCPDS for this sample is listed in Appendix A (Fig. A1). The d values of planes (002) and (102) from the XRD pattern are 0.387 nm and 0.336 nm, respectively, which match well with the d values from the HRTEM pattern of Sample P (as shown in Fig. 6.3d).

The XRD pattern of Sample P (PVDF/WO₃) matches with JCPDS No: 210-7312, confirming the dominant base crystalline feature of WO_3 orthorhombic phase, with lattice constants of $a = 7.7500$, $b = 7.3410$ and $c = 7.7540$ nm.

The FTIR spectrum in Fig. 6.8b shows peaks at 840, 1072, 1170 and 1276 cm^{-1} (marked by red dashed lines), which are corresponding to the β-phase of PVDF, similar to the pure electrospun PVDF nanofibers [312].

The XPS surface composition and chemical states are shown in Fig. 6.8c. The peaks of F1s, O1s and C1s are clearly observed in the XPS survey spectrum and the C1s peak can be deconvoluted into five peaks corresponding to -CF₂ (at ~291 eV), -CH₂ (at ~286 eV) with the chemical characteristics of PVDF (crosslinking of polymer chains). Meanwhile -COO (at ~289 eV) and -CH (at ~284 eV) should be a result from additional dopant elements or contaminant or residual surfactant and environments [313]. The small peak at about 293.5 eV is due to the -CF₃ end groups. The concentration percentage of each peak is presented in Table 6.4.

6.4.2 PVDF/ZnO composite nanofibers
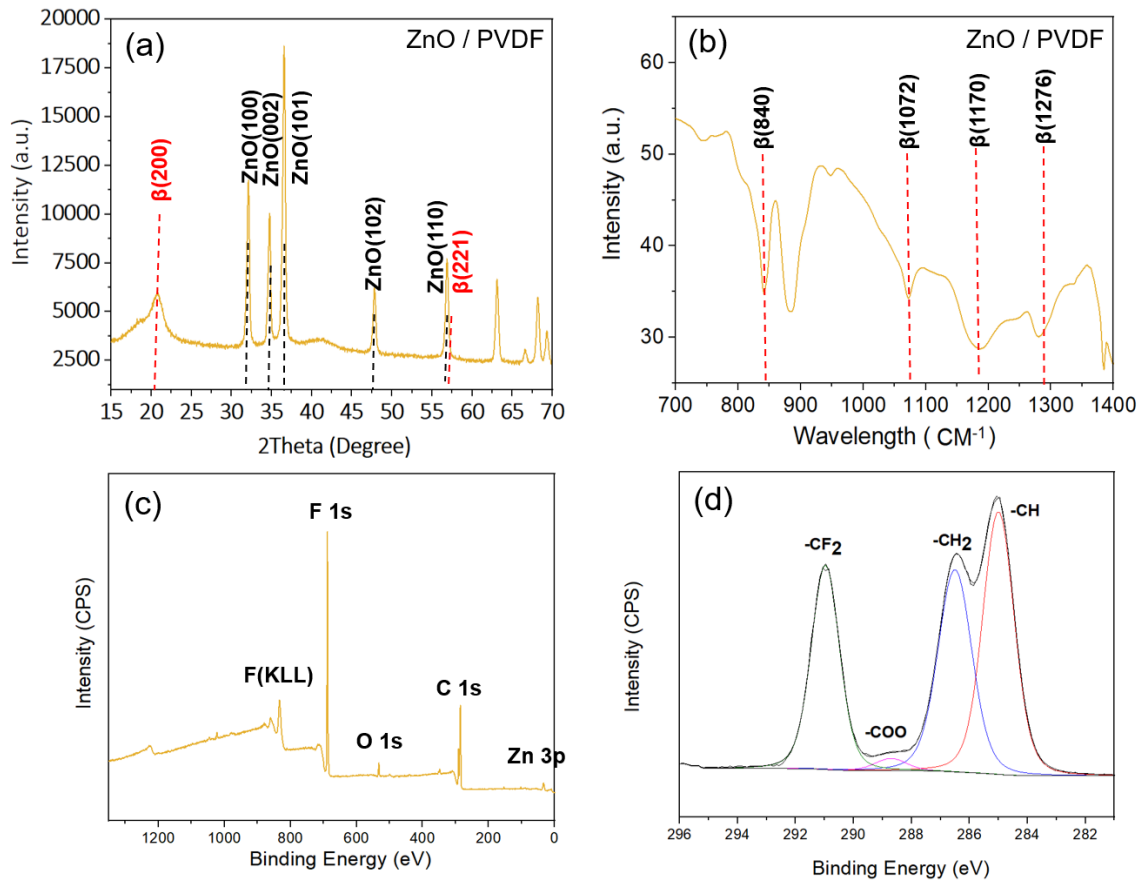
Fig. 6.9 (a) XRD pattern, (b) FTIR spectrum, (c) XPS survey spectrum, and (d) deconvolution of the C 1s peak in (c) of the PVDF/ZnO electrospun nanofibers, respectively.

The XRD pattern displays the main diffraction peaks appeared at 2θ about 31.73° (001), 34.40° (002), 36.23° (101), 47.51° (102) and 56.58° (110), which are assigned to the Hexagonal phase ZnO (JCPDS No: 230–0112); the intense peak at 20.81° (200), two weak shoulder peaks at 36.63° (120) and 39° (220), and a peak at 56.91° (221) are corresponding to the β-phase of PVDF (Fig. 6.9a). The ZnO phase has a lattice constant of a = 3.2494 and c = 5.2054 nm. The detailed 2θ information of the JCPDS for this sample is listed in Appendix A (Fig. A2). The d value of planes (100) from the XRD pattern is 0.281 nm, which agrees with the d value from the HRTEM pattern of Sample Q (as shown in Fig. 6.4d).

The FTIR result in Fig. 6.9b shows the peaks at 840, 1072, 1170 and 1276 cm^{-1}, which originated from the β-phase of the PVDF, similar to the pure electrospun PVDF nanofibers [312].

The XPS survey spectrum for Sample R looks similar to Samples P (Pure PVDF) and Q (PVDF/ WO$_3$). Further details will be addressed in Table 6.4.

6.4.3 PVDF/CNTs composite nanofibers
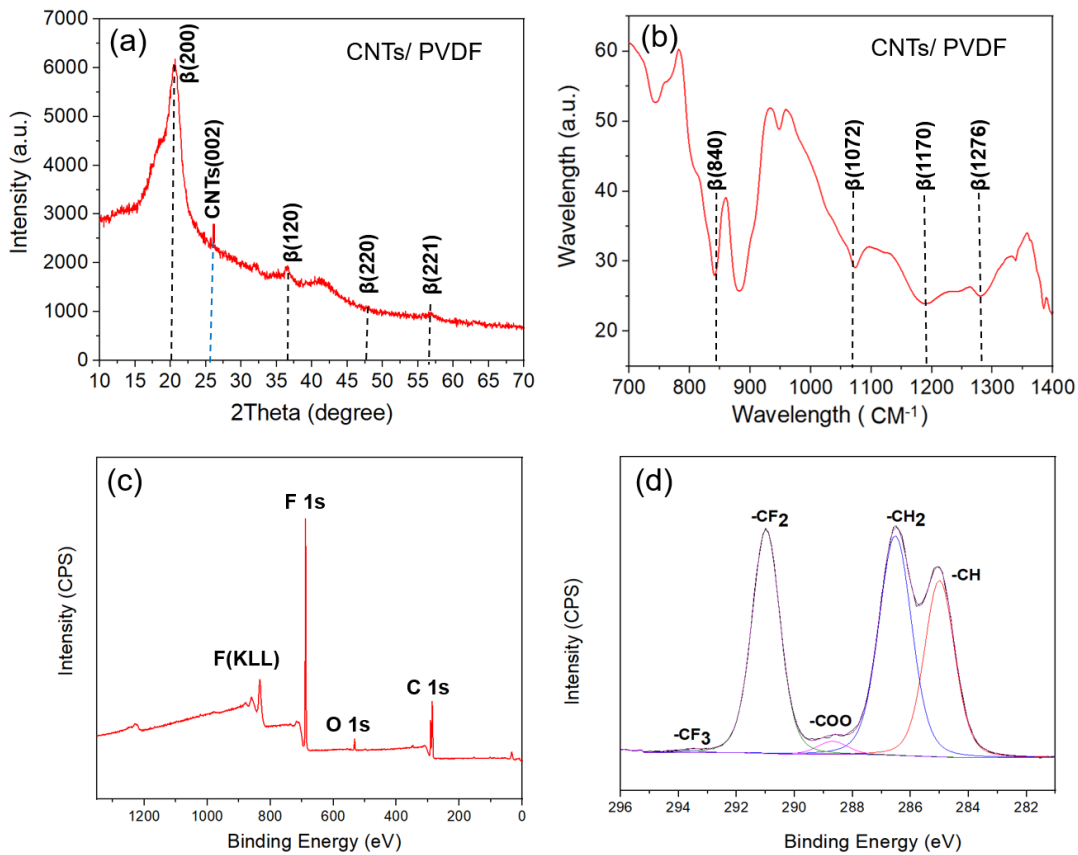
Fig. 6.10 (a) XRD pattern, (b) FTIR spectrum, (c) XPS survey spectrum, and (d) deconvolution of the C 1s peak in (c) of the PVDF/CNTs electrospun nanofibers, respectively.

The XRD pattern in Fig. 6.10a exhibits the main diffraction peaks appeared for this sample. Beside the peaks for β-phase presented in previous sections, the main diffraction peak for CNTs appears at 2θ at about 26.05° (002) which is shown as a blue hatched line in Fig. 6.10a. The XRD pattern for Sample R matches with JCPDS No: 120−0017. This pattern comprises phases of PVDF and CNTs as a combination

of various phases, confirming the hexagonal phase of CNTs, with lattice constants of a = 2.470 and c = 6.790 nm. The other black hatched lines are assigned to the β-phase, similar to previous samples, with an intense peak at 20.81° (200), two weak peaks at 36.63° (120) and 39° (220), and a peak at 56.91° (221). The detailed 2θ information of the JCPDS for this sample is listed in Appendix A (Fig. A3). The d value of plane (002) from the XRD pattern is 0.339 nm, in agreement with the d value obtained from the HRTEM pattern of Sample R (as shown in Fig. 6.5d). In addition, the FTIR results, Fig. 6.10b, show peaks at 840, 1072, 1170 and 1276 cm^{-1}, confirming the existence of β-phase [312].

6.4.4 PVDF/TiO$_2$ composite nanofibers
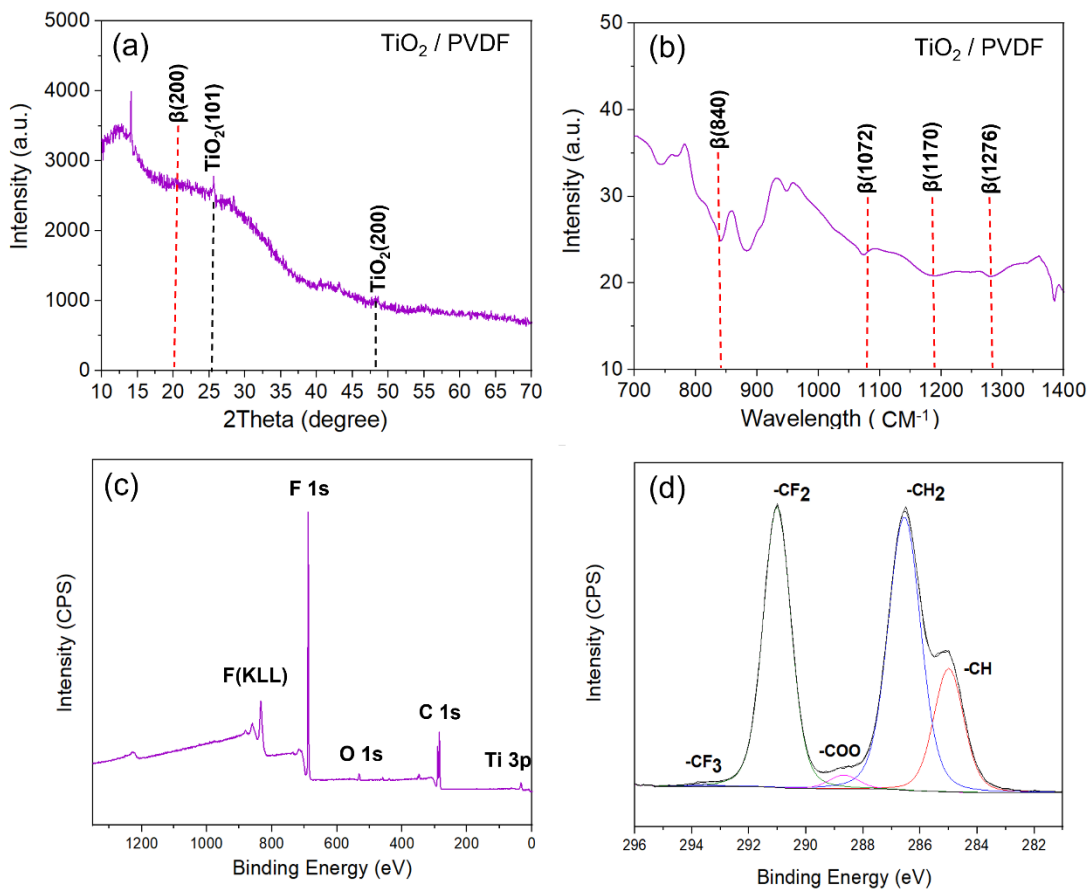
Fig. 6.11 (a) XRD pattern, (b) FTIR spectrum, (c) XPS survey spectrum, and (d) deconvolution of the C 1s peak of the PVDF/TiO$_2$ electrospun nanofibers, respectively.

The XRD pattern of the PVDF/TiO$_2$ composite nanofibers matches well with JCPDS No: 152−6931 listed in Appendix A (Fig. A.4), confirming the Tetragonal crystalline phase of TiO$_2$, with lattice constants of a = 3.785 and c = 9.514. Correspondingly, it exhibits one intense peak at 20.81° (200), being allocated to the β-phase. The main diffraction peaks for TiO$_2$ appeared at 2θ about 25.27° (101) and 48.01° (200), as shown in Fig. 6.11a. Moreover, the d value of plane (101) from the XRD pattern is 0.35 nm, which is in line with the d value obtained from the HRTEM pattern for Sample S (PVDF/TiO$_2$), as shown in Fig. 6.6d. Red hatched lines in Fig. 6.11b mark the peak position assigned to the β-phase.

6.4.5 PVDF/LiCl composite nanofibers
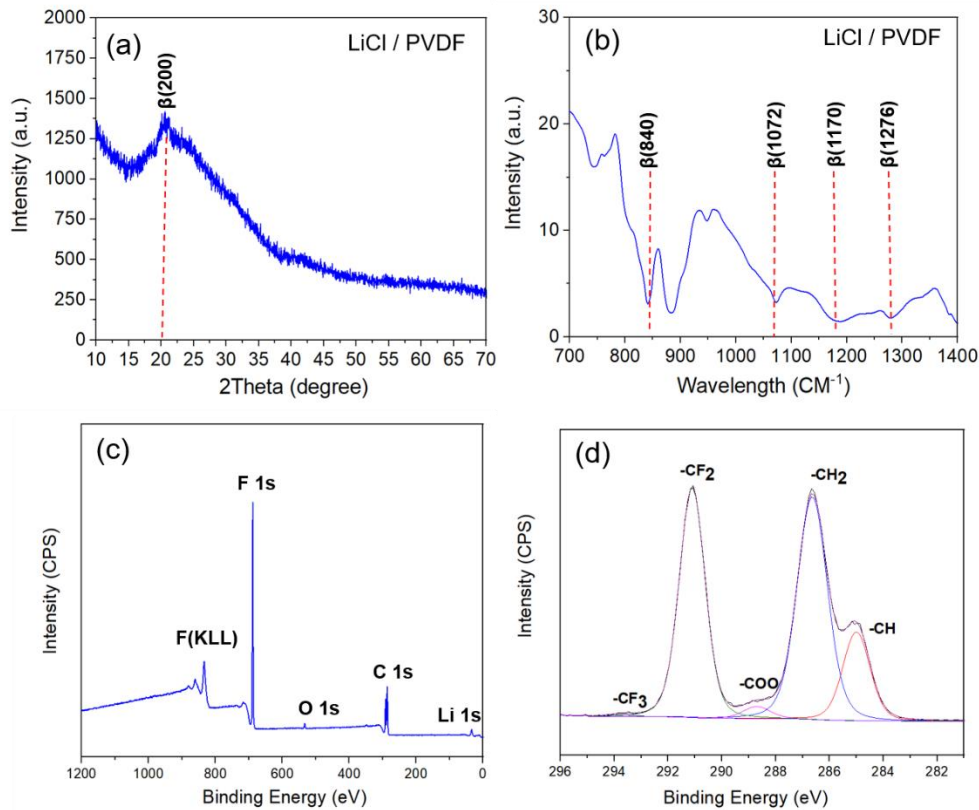
Fig. 6.12 (a) XRD pattern, (b) FTIR spectrum, (c) XPS survey spectrum, and (d) deconvolution of the C 1s peak of the PVDF/LiCl electrospun nanofibers, respectively.

For the PVDF/LiCl composite, the XRD and FTIR (Fig. 6.12a and b) results are similar to those of Sample S (PVDF/TiO$_2$). In the XRD pattern, only an intensive peak

at 20.81° (200) is visible. The FTIR spectrum in Fig. 6.12b exhibits peaks at 840, 1072, 1170 and 1276 cm^{-1} (marked by red dashed lines), correspond to the β-phase of PVDF, which matches well with literature and other samples [312].

The weakened peaks for the β-phase, with only one main peak remained, show that the formation of β-phase in this LiCl composite was reduced, similar to that observed for Sample S (PVDF/TiO$_2$). These results demonstrate the weaker β-phase promotion ability by these two fillers, against other fillers discussed earlier. The SEM and TEM investigations, as well as the XRD and FTIR characterizations, are hard to detect the Li elements, however the XPS survey spectra indeed confirmed the existence of Li in the fibers.

XRD patterns altogether show that the (200) peak position of the β-phase remained unchanged for all of composites, however its (120) peak is not sharp enough for Samples S (PVDF/TiO$_2$) and T (PVDF/LiCl). This indicates a decrease in the crystallinity of β-phase for those two samples. On the contrary, for other fillers, including WO$_3$, ZnO, CNTs, the crystallinity of the β-phase of the PVDF was enhanced. Details of the crystallinity will be discussed in XPS analysis, to support the results of XRD.

A summary of the XRD results for all samples is presented in Table 6.2.

Table 6.2 A summary of the relative peak intensity of β-phase for Samples A, P, Q, R, S and T, achieved based on the XRD results.

Samples	Intensity at 2θ ≈ 20.81°=I_1 (200)	Intensity at 2θ ≈ 36.63°= I_2 (120)	The relative intensity between 2θ ≈ 20.81° and 2θ ≈ 36.63°(I_1/I_2)	FWHM (200)
Pure PDVF (A)	3781	1637	2.30	0.34
PVDF/WO$_3$ (P)	7398	2021	3.66	0.21
PVDF/ZnO (Q)	4554	1890	2.40	0.29
PDVF/CNTs (R)	6174	1876	3.29	0.31
PVDF/TiO$_2$ (S)	2892	910	1.87	0.45
PVDF/LiCl (T)	1342	808	1.66	0.52

Note: FWHM = Full width half maximum of the peak (unit = Theta degree)

In Table 6.2, the intensities of two main peaks allocated to the β-phase, the relative intensities of these peaks, and the FWHM of the main peak (200) are summarised. The relative intensity ratios of (200)/(120) are increased for Samples P (PVDF/WO$_3$), Q (PVDF/ZnO) and R (PVDF/CNTs) but reduced for Samples S (PVDF/TiO$_2$) and T (PVDF/LiCl) compared with the pristine PVDF Sample. The full-width at half-maximum (FWHM) of the (200) plane in Samples P (PVDF/WO$_3$), Q (PVDF/ZnO) and R (PVDF/CNTs) is slightly decreased, compared with that of the pure PVDF nanofibers. However, the FWHM value for Samples S (PVDF/TiO$_2$) and T (PVDF/LiCl) is increased, representing thicker fibers are formed.

Interestingly, if we consider the β-phase content of the composites against the values of the FWHM, or intensity ratios in Table 6.2, there seems to have some type of relationship: smaller FWHM or larger (200)/(120) intensity ratios correlate with higher β-phase content. For example, the smallest FWHM corresponds to Sample P that has the highest β-phase content. This correlation appears to suggest that the incorporation of WO$_3$, ZnO and CNTs into the PVDF solution promoted the growth along the <200> direction, resulting in more (200) planes in the composite fibers, whilst hindered the growth along <120> direction and consequently less (120) planes in the fibers. As this is associated with the β-phase formation, therefore we believe these values (FWHM and intensity ratios) are associated with the β-phase content. This analysis is backed up with the SEM and TEM results that, thinner fibers are associated with higher β-phase content, as verified by the XRD and FTIR analyses.

The reason behind that link could lie in the molecular interactions between the different filler and the PVDF during the electrospun processing. These finer fillers were well-mixed with the polymer solution due to the weak Van der Waals forces between them, and the jet during the spin could easily be stretched to form finer fibers, with features of well--aligned and less beads and bending, than those of the larger fillers such as Samples S and T. For that reason, the alignment of molecules in the direction of the fiber axis is better perceived, so the β-phase crystalline formed subsequently, for finer additives such as WO$_3$, ZnO and CNTs. Further evidence of this aspect can be explained in next session relevant to the DSC analysis. On the contrary, thicker nanofibers with the clogged areas were obtained with less β-phase

content for the larger TiO_2 and LiCl fillers. Having said that, we believe that new evidence is required to verify if the fillers themselves have direct promoting function as nuclei agent, to promote the solidification of the polymers, and whether to form as α-phase first, then promoted its conversion to β-phase, or directly promoted the beta-phase formation by hindering the alpha-phase formation. Nevertheless, the finer fillers lead to finer fibers with good morphology and higher β-phase content in the composite fibers which will be discussed below.

6.5 Phase characterization

The introduction of WO_3, ZnO and CNT fillers to the PVDF solution increased the β-phase content, as evidenced by the enhanced intensities of the absorption peaks of β-phase in the FTIR graphs (Fig. 6.8b, 6.9b and 6.10b), whilst the introduction of TiO_2 and LiCl led to the attenuation of absorption peaks (Fig. 6.11b and 6.12b). The crystalline proportion of α- and β-phases of the PVDF electrospun fibers can be calculated based on the Lambert-Beer law, Eq. 6.1 [294].

$$F(\beta) = \frac{A_\beta}{\left(\frac{K_\beta}{K_\alpha}\right)A_\alpha + A_\beta}$$
Eq 6.1

where A_α and A_β are absorbances of α and β phases at 766 and 840 cm^{-1}, respectively, and the constant value of $\frac{K\beta}{K\alpha}$ equals to 1.26, which are derived from K_α (6.1 × 10^4 cm^2.mol^{-1}) and K_β (7.7 × 10^4 cm^2.mol^{-1}), the absorption coefficients at the corresponding wavenumbers [313]. In this thesis, for all PVDF composite samples, A_α and A_β equal to 0.173 and 0.8443, respectively (shown as Table 5.6 in Chapter 5).

The calculated β-phase contents for all samples are shown in Fig. 6.13(a-f) and summarized in Table 6.3.
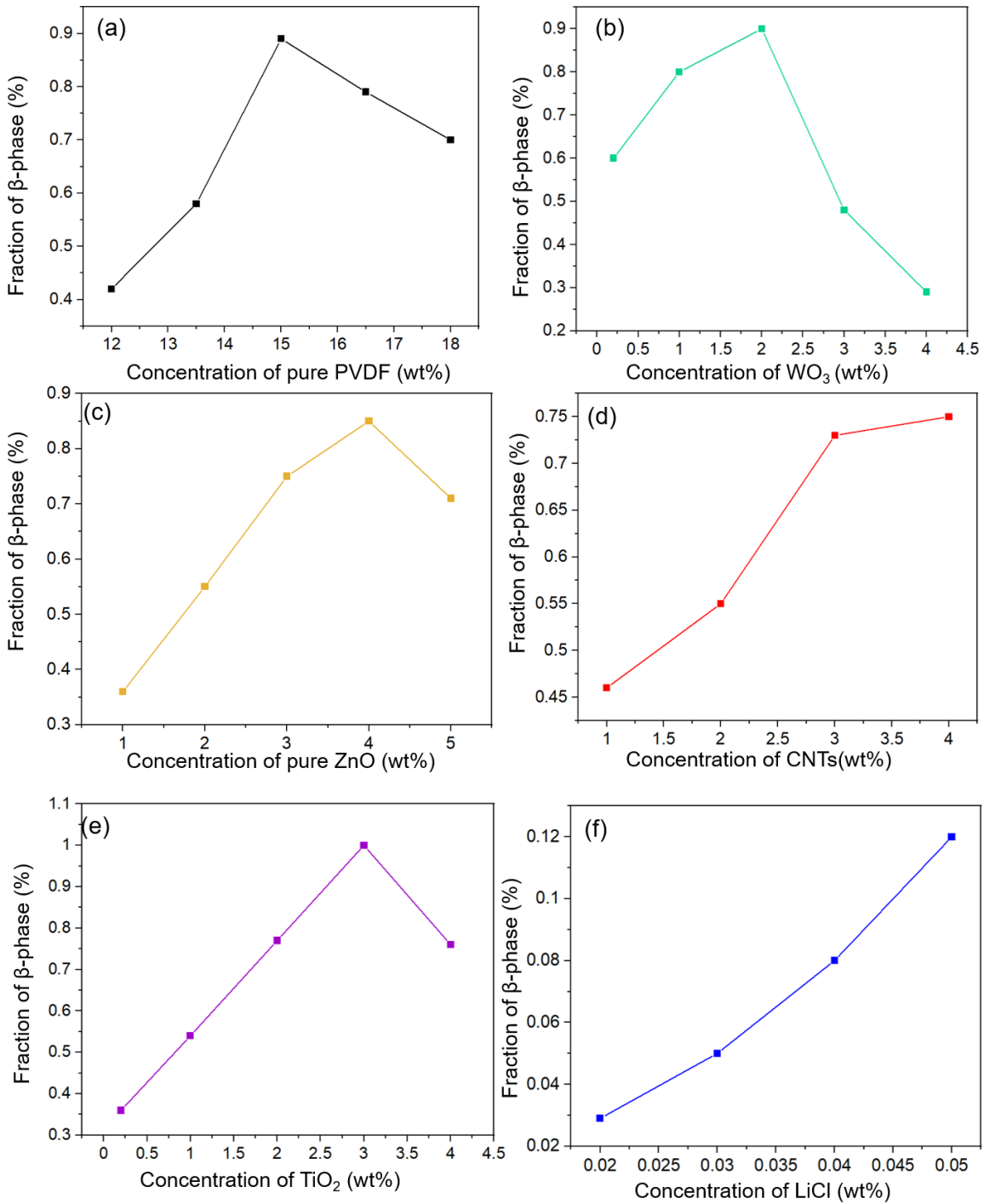
Fig. 6.13 (a-f) Fraction of β-phase (%) vs. concentration for pure PVDF, and different composite fibers, as marked, WO_3, ZnO, CNTs, TiO_2 and LiCl.

From Fig. 6.13, we can see that a rapid increment of the β-phase fraction occurred to all samples, with the increase of filler content, although the maximum β-phase content occurred at different filler concentrations for different fillers. For pure PVDF,

the maximum β-phase occurred at 15 wt%, 4 wt% CNTs, 4 wt% ZnO, 2 wt% WO_3, 3 wt% TiO_2 and 0.05 wt% LiCl respectively, all obtained at a fixed PVDF concentration of 15 wt%. However, among these additives, further increase CNTs and LiCl led to non-spinnable products, and no fibers were produced. Additional rise in concentration of WO_3, ZnO and TiO_2 reduced the β-phase fraction.

This enhancement of the β-phase fraction with each filler can be justified by the interaction between the filler and the polymer matrix. In other words, at low filler content of each additive, the amount of interfacial area between the polymer and the filler is low, while the interfacial area increases with the increasing filler content in PVDF, as these additives are homogeneously dispersed in the polymer matrix. After reaching the maximum β-phase for additives of WO_3, ZnO and TiO_2, the interaction between the polymer and nanoparticles starts to decline and the β-phase fraction is dropped by 22 % for pure PVDF, 66 % for PVDF/WO_3, 18 % for PVDF/ZnO and 64 % for PVDF/TiO_2. For Samples S and T, this was even unable to investigate, due to their severely deteriorated spinning behavior at higher filler contents.

Table 6.3 The optimal concentration for maximum relative β-phase content for various additives.

Solution No	Additive	Results for relative β phase intensity based on FTIR graphs
1	PVDF-12 wt%	0.23
2	PVDF-13.5 wt%	0.67
3	**PVDF-15 wt% (Sample A)**	**1.00**
4	PVDF-16.5 wt%	0.84
5	PVDF-18 wt%	Not spinnable
6	WO_3-0.2 wt%	0.67
7	WO_3-1 wt%	0.89
8	**WO_3-2 wt% (Sample P)**	**1.00**
9	WO_3-3 wt%	0.54
10	WO_3-4 wt%	0.32
11	ZnO-1 wt%	0.43
12	ZnO-2 wt%	0.65
13	ZnO-3 wt%	0.88
14	**ZnO-4 wt% (Sample Q)**	**1.00**
15	ZnO-5 wt%	0.84
16	CNTs-1 wt%	0.62
17	CNTs-2 wt%	0.76
18	CNTs-3 wt%	0.97
19	**CNTs-4 wt% (Sample R)**	**1.00**

20	CNTs-5 wt%	Not spinnable
21	TiO$_2$-0.2 wt%	0.36
22	TiO$_2$-1 wt%	0.54
23	TiO$_2$-2 wt%	0.77
24	**TiO$_2$-3 wt% (Sample S)**	**1.00**
25	TiO$_2$-4 wt%	0.76
26	LiCl-0.02 wt%	0.24
27	LiCl-0.03 wt%	0.43
28	LiCl-0.04 wt%	0.79
29	**LiCl-0.05 wt% (Sample T)**	**1.00**
30	LiCl-0.06 wt%	Not spinnable

In Table 6.3, the optimal concentration for maximum β-phase content for each additive is defined as 1, specifying the highest intensity in the FTIR spectra. This was then used as a reference to obtain other relative values at different concentrations based on their intensity, by using Eq. 6.1. For Samples A, P, Q, R and S, after reaching a maximum concentration, their β-phase contents decreased, at various speeds.

For finer fillers, a better interfacial connection between the filler and the PVDF would be achieved due to easier to be dissolved and dispersed than those of larger fillers. Three of these fillers, WO$_3$, ZnO and CNTs, orient the -CH$_2$/-CF$_2$ dipoles differently, which could facilitate the transformation of the α-phase to β-phase. The addition of such fillers could lead to the formation of strong O-HF-C bond oriented to the -CH$_2$/-CF$_2$ dipoles along with the F atoms near the WO$_3$, ZnO and CNTs nanoparticles. The strong interactions of these particles with F on the PVDF chains could compel the PVDF chains to be arranged into trans-configuration with the F atoms. These fundamental interactions have been discussed in detail in Ref [314-315].

Table 6.4 The relative intensities of β-phase of Samples A, P, Q, R, S and T, based on the FTIR results.

Samples	Intensity at wavelength 840 CM^{-1} = I$_1$	Intensity at wavelength 1170 CM^{-1} = I$_2$	The relative intensity between wavelengths 840 and 1170 CM^{-1} (I$_1$/I$_2$)
Pure PDVF (A)	27.54	23.05	1.19
PVDF/WO$_3$ (P)	52.65	40.84	1.28
PVDF/ZnO (Q)	34.77	31.43	1.10
PDVF/CNTs (R)	27.94	24.53	1.13
PVDF/TiO$_2$ (S)	24.82	22.90	1.07
PVDF/LiCl (T)	3.06	2.89	1.05

For further comparison of the additive influence, the intensities of two main absorption peaks at wavelength of 840 and 1170 CM^{-1} of the β-phase are compared for different composites, summarized in Table 6.4. For both intensities, Samples P, Q and R are greater than those of the pristine PVDF, but Samples S and T are lower than that of the PVDF. The relative intensities of the two peaks, *i.e.*, the ratios, are somehow complicated. Starting from 1.19 for the pristine PVDF, the ratios for Samples P, Q and R are increased or similar (being 1.28, 1.1. and 1.13), considering the system error, however Samples S and T are obviously reduced to 1.07 and 1.05, respectively. Nevertheless, the smallest value 1.05 corresponds to Sample T (PVDF/LiCl), whilst the highest value 1.28 is obtained for Sample P (PVDF/WO₃). To establish a convincing relationship between the β-phase content and intensity ratio, further investigations are required in the future.

The higher β-phase content for the WO_3 containing sample, based on the XRD and FTIR results, is believed to arise from its smaller particle size which leads to better distribution within the nanofibers, than other fillers. To verify this, further investigations on the effect of different particle sizes were conducted, using three different sizes of ZnO, <1 µm, < 100 nm and < 50 nm, and the XRD and FTIR results are shown in Fig. 6.14a and b.
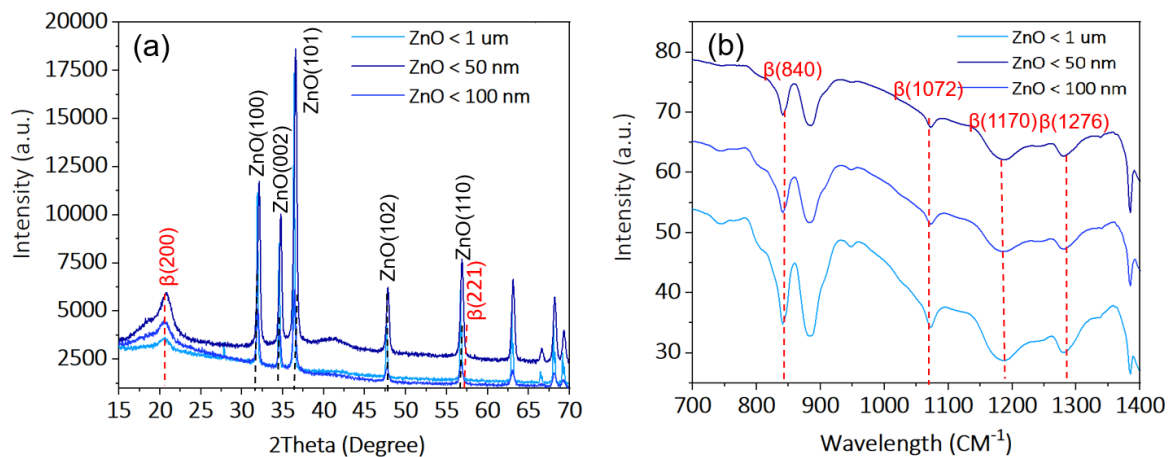
Fig. 6.14 (a) The XRD profiles and (b) FTIR spectra. Obtained from composite fibers containing ZnO of different particle sizes.

In Fig. 6.14, the relative peak intensity ratios between diffraction peaks at 2θ of 20.8° and 56.91° for varied sizes of ZnO, < 50 nm, < 100 nm and < 1 μm are used as the indicator for the β-phase content, which gives values of 2.71, 1.80 and 0.87, respectively. In addition, the relationship between F(β) and the change in the particle sizes of ZnO is shown in Table 6.5, based on the FTIR results.

Table 6.5 The particle size of ZnO effect on the content of β-phase.

Samples	Solvent	Concentration (wt %)	A_α	A_β	F(β)
ZnO < 50 nm	DMF/Acetone	PVDF 15 wt%- ZnO 4 wt%	0.114	0.876	0.86
ZnO < 100 nm	DMF/Acetone	PVDF 15 wt%- ZnO 4 wt%	0.211	0.758	0.74
ZnO < 1 μm	DMF/Acetone	PVDF 15 wt%- ZnO 4 wt%	0.250	0.703	0.69

The FTIR spectra revealed that transmittance bands at 840, 1072, 1170 and 1276 cm^{-1} are corresponding to the β-phase. According to Table 6.5 and using technique described earlier, we quantified the β-phase content based on the FTIR results by using the Lambert-Beer law and obtained the maximum value of F(β) = 0.86 for ZnO < 50 nm, against 0.74 and 0.69 for ZnO samples < 100 nm and < 1 μm correspondingly.

It is obvious that the smallest particle size led to the highest β-phase content in the PVDF matrix, and vice versa the largest ZnO fillers resulted in lowest β-phase. Therefore, the particle size indeed exhibited a strong effect on the β-phase content and a direct link exists between them. It is possible that when the particle size is increased, for the same weight percentage, the number of particles inside the PVDF solution will be drastically reduced. As a result, the electrostatic effect of PVDF solution during the electrospinning is thus significantly declined. Consequently, the final β-phase in the PVDF is reduced.

Meanwhile, when the particles are smaller, they will be easier to be embedded in the PVDF jet during electrospinning, rather than stay on the surface, as for larger particles. In this case, they could act as nucleation agents in the jet during elongation, so the TGTG molecular chains could stick to ZnO surfaces and crystalise

around them, driving by the stronger electrostatic interactions between the particles and the CF_2 and/or CH_2 groups of the PVDF, as discussed above. Thus, resulting in higher β-phases. This explanation is in an excellent agreement with previous studies on CNTs additive [316].

In general, it is challenging to establish a precise relationship between the type of additive and different features of the resulting electrospun fibers, such as the morphology and β-phase content. In addition, when a specific additive is higher in concentration, the morphology will get worsened, and different forms of bead and defect will be generated. Severe agglomeration of additives decreases the β-phase formation and widen the diameter of fabricated electrospun fibers.

The incorporation of additives within the PVDF electrospun nanofibers is further confirmed by EDX elemental mapping under the STEM mode, as shown in Fig. 6.15. The results for all samples except Sample T (PVDF/LiCl), confirm the homogeneous distribution of the constituent elements, and that F, O and C are dominant within all electrospun fibers in Samples A (Pure PVDF), P ($PVDF/WO_3$), Q (PVDF/ZnO), R (PVDF/CNTs) and S ($PVDF/TiO_2$). For Sample T (PVDF/LiCl), we can rely on the XPS results only. Furthermore, these element mapping results have shown that C is present across the entire nanowires and is most likely existing inside the parental PVDF electrospun nanofibers. The elemental composition of Sample A revealed that carbon (63%), fluoride (26%) and oxygen (11%) were spread all over the nanofiber. Sample P exhibited homogeneous spatial distributions throughout the nanofiber body, and carbon (62%), fluoride (24%), oxygen (12%), and tungsten (2 %) were spread all over the nanofiber. For Sample Q, these values were carbon (61 %), fluoride (24%), oxygen (11 %), and zinc (4%). For Sample R, we have obtained values of carbon (67%), fluoride (23%), oxygen (10%). And finally, for Sample S, the distribution is carbon (61%), fluoride (24%), oxygen (10%), and titanium (5%).
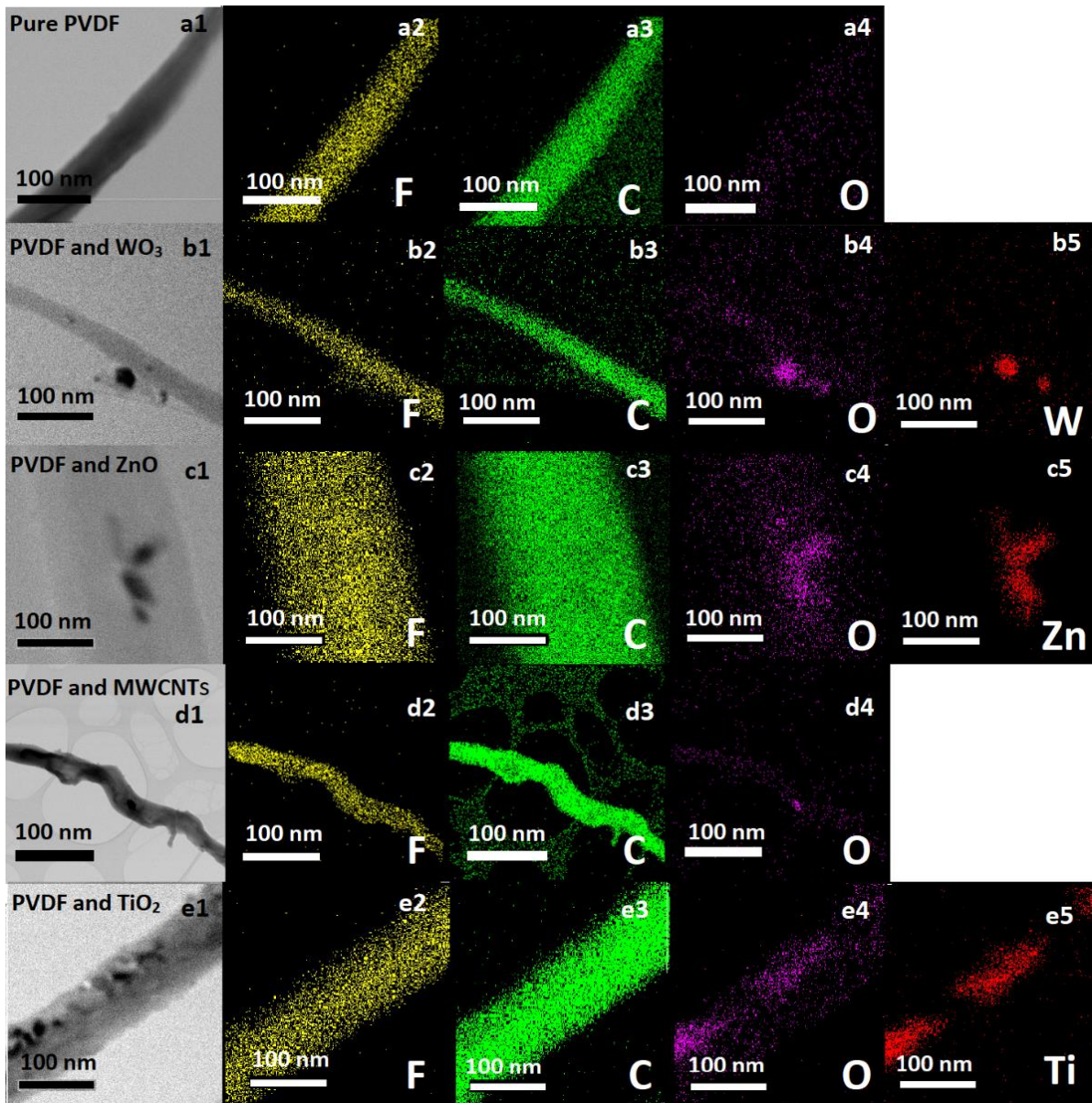
Fig. 6.15 EDX elemental mapping images. (a1-4), pure PVDF, (b1-5), WO₃/PVDF composite, (c1-5), ZnO/PVDF composite, (d1-4), CNTs/PVDF composite, (e1-5), TiO₂/PVDF composite. Yellow, green, and purple dots represent the distribution of F, C and O, and red dots represent the key metallic element of corresponding additives.

A summary of surface composition and the chemical state of the composite samples is presented in Table 6.6.

Table 6.6 The percentage of carbon species obtained from the XPS peaks for the PVDF electrospun fibers for Samples A, P, Q, R, S and T.

Samples	-CH	-CH$_2$	-COO	-CF$_2$/-CN	-CF$_3$
Pure PDVF (A)	20.69	40.54	5.31	32.85	0.62
PVDF/WO$_3$ (P)	27.68	37.38	2.04	32.58	0.31
PVDF/ZnO (Q)	15.62	43.60	2.09	38.39	0.29
PDVF/CNTs (R)	18.52	40.88	3.39	36.33	0.88
PVDF/TiO$_2$ (S)	2.89	49.35	1.87	45.42	0.47
PVDF/LiCl (T)	39.19	30.76	2.97	26.50	0.58

The XPS results indicate that the PVDF composites have been successfully prepared with different fillers in the fiber form. The fiber samples were remained similar in their elemental composition and chemical state compared with the pristine PVDF. All composites fiber samples remained similar in their elemental compositions and chemical states, compared with the pristine PVDF, which is in good agreement with the XRD and FTIR results for interfacial interactions.

Based on the XPS, XRD and FTIR results for all samples, it clear that the effect of TiO$_2$ and LiCl addition on the β-phase formation is different from those fillers in Samples P (PVDF/WO$_3$), Q (PVDF/ZnO) and R (PVDF/CNTs). Whilst the interactions between the molecular dipoles (CH$_2$ or CF$_2$) of PVDF and the fillers of WO$_3$, ZnO and CNTs improved the β-phase content, the interaction of TiO$_2$ and LiCl additives with them deteriorated the nucleation and β-phase formation in the PVDF matrix.

From SEM and TEM results, when the additive was one of WO$_3$, ZnO, CNTs, the saturation of nanofillers did not significantly change the diameter of fabricated electrospun fibers, conversely, TiO$_2$ and LiCl affected the diameter of the fibers. The increase in the diameter lessened the β-phase content. The increase of the diameter can be due to the nonsolvent capacity of specific additives such as TiO$_2$ and LiCl. When the spinnability of fibers reduced, less interaction occurred between the

electron donating groups such as Ti^{4+} and PVDF segments in Sample S and donating groups Li^+ and PVDF segments for Sample T.

6.6 Thermophysical characterisations

The influence of additives on the melting enthalpy (ΔH_m), melting temperature (T_m), cooling temperature (T_c) and degree of crystallinity (X_c) is studied using DSC thermograms for the pristine PVDF and PVDF composite nanofibers, and the results are shown in Fig. 6.16 a-c. Cooling and heating curves are shown in Fig. 6.16b and c correspondingly. In Fig. 6.16c, peaks in the range of 157 to 163 °C are similar for Samples A, P, Q, R, S and T. The minor differences among the melting temperature of each sample are summarized in Table 6.7. While the melting temperatures for Samples P, Q and R equal to 157.75, 158.65 and 158.85 °C, slightly lower than that of the pure PVDF spun fibers or Sample A (161.83 °C), the melting temperatures of Samples S and T(162.43 and 162.56 °C) are higher than that of Sample A. Beside the main melting point for all samples, both Samples P (PVDF/WO$_3$) and S (PVDF/TiO$_2$) have shown extra shoulders in the profile. The slight differences between the two crystallization temperatures (T_c) are also summarized in Table 6.7.

There is still an ongoing dispute on melting temperatures of different crystalline phases of PVDF, however in this work, the range between 158-166 °C has been allocated to the melting point of β-phase. While the pristine PVDF electrospun fibers show $T_m = 161.83$ °C, a reduction to 157.75 °C is assigned to Sample P(PVDF/WO$_3$), which is lower than the other five samples. Depending on each sample, the melting point is decreased and less than that of the pristine PVDF electrospun fibers, except for Samples S (PVDF/TiO$_2$) and T (PVDF/LiCl).

Similar to the previous Chapter, the value of crystallinity was calculated using the crystallinity equation presented in Chapter 3, Eq. 3.3. The crystallinity percent of the Sample P is 68.3 % which is the highest among all additives such as Sample Q (PVDF/ZnO) (64.6 %), Sample R (PVDF/CNTs) (58.5 %), Sample A (pure PVDF) (45.1 %), Sample S (PVDF/TiO$_2$) (44.7 %) and Sample T (PVDF/LiCl) (37.4 %), as shown in Table. 6.7.
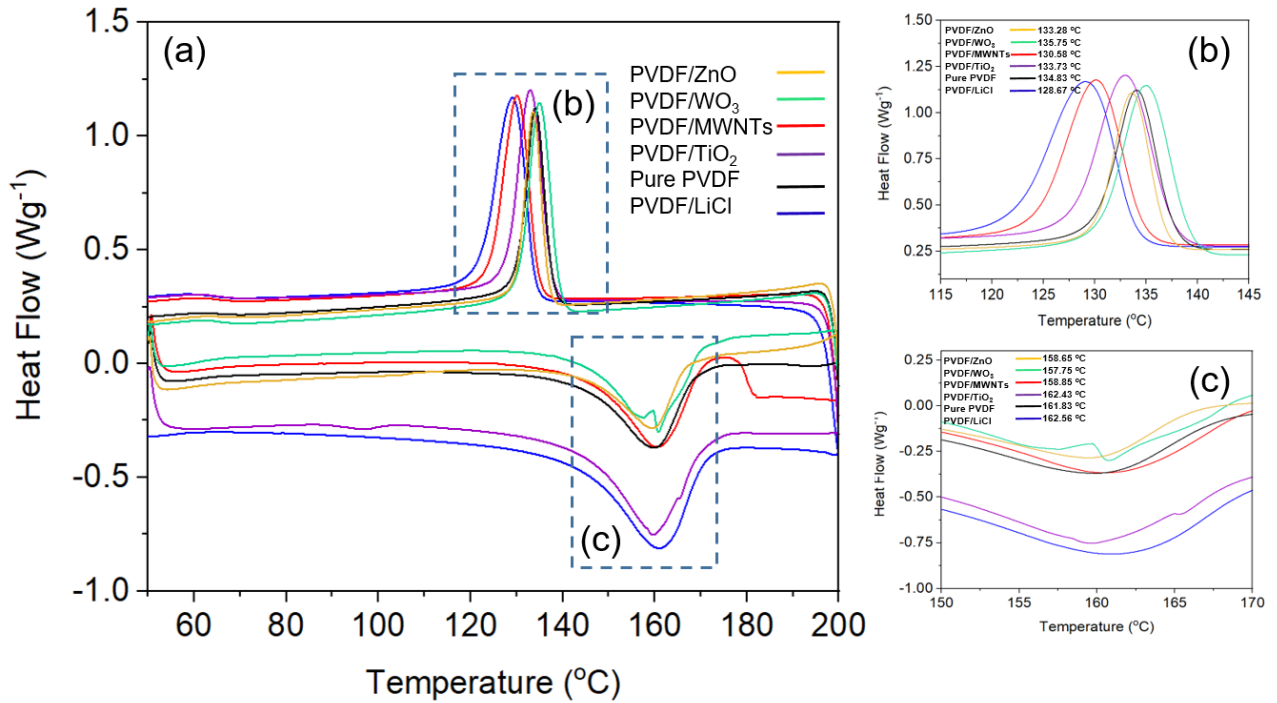
Fig. 6.16 (a) DSC profiles, (b) cooling thermograms, and (c) heating thermograms of the pristine PVDF and composite nanofibers of Samples A, P, Q, R, S and T.

Table 6.7 A summary of the T_m: Melting temperature; ΔH_m: enthalpy of fusion and X_{DSC}: degree of crystallinity for the pure and composite nanofibers of Samples A, P, Q, R, S and T, obtained from the DSC measurements.

Samples	T_m [°C]	T_c [°C]	ΔH_m [J g^{-1}]	X_{DSC}
Pure PDVF (A)	161.83	134.83	46.7	45.1
PVDF/WO$_3$ (P)	157.75	135.75	48.1	68.3
PVDF/ZnO (Q)	158.65	133.28	47.3	64.6
PDVF/CNTs (R)	158.85	130.58	44.3	58.5
PVDF/TiO$_2$ (S)	162.43	133.73	40.2	44.7
PVDF/LiCl (T)	162.56	128.67	39.1	37.4

Fillers added to the PVDF solution can play two separate roles in the spinning process, which are acting as the PVDF nucleation sites and the chains formation constraints. These opposite effects will increase the crystallinity by forming more amount of small crystals and by delaying the crystal growth via chain immobilization.

However, Samples S and T failed to exhibit this feature, which could be due to the poor dispersion of these two additives compared with others, therefore neither the nucleation promotion nor the chain restrains could effectively function. As a result, these two composites showed lower crystallinity than that of Samples P, Q and R.

Upon adding nanofillers to PVDF matrix, the T_m of the composite films for Samples P (PVDF/WO$_3$), Q (PVDF/ZnO) and R (PVDF/CNTs) are slightly less than that of the pristine PVDF fibers. The decrease in the T_m could be caused by the β-phase enrichment, particularly for the WO$_3$ composite. This is again originating from the smaller size of WO$_3$ particles, as discussed earlier. The change in T_c is ascribed to different groups of interactions between each single additive and the PVDF during the crystallization. The interaction of each filler is different from each other, hence the promotion effect on the nucleation of PVDF is different for each sample. Thus, T_c is decreased the most for Sample T (PVDF/LiCl), due to the poorest interaction, which resulted in the remarkable increase in the beadings formation and coarse appearance of the fibers.

The resulted samples with additives such as WO$_3$, ZnO and CNTs significantly facilitated the phase transformation from α-phase to β-phase. This mechanism is exactly the nucleating agents' function as discussed in the DSC analysis part. Additionally, the stronger interactions at the interfaces between PVDF/WO$_3$, PVDF/ZnO and PVDF/CNTs promoted stronger O-HF-C hydrogen atoms formation. Furthermore, regarding the addition of WO$_3$, ZnO, CNTs, H atoms of –CH$_2$/-CF$_2$ dipoles are willing to reach the WO$_3$, ZnO and CNTs surfaces, whilst for TiO$_2$ and LiCl, this tendency is not achieved therefore the intensity of β-phase is weak.

6.7 Summary

This Chapter has studied the morphological, structural, and phase compositional features of various electrospun composite fibers, including WO$_3$, ZnO, CNTs, TiO$_2$ and LiCl reinforced PVDF, with comparison to the pristine PVDF spun fibers. The reasons for choosing these additives are several folded, including their promotion to enhance the β-phase conversion, their conductivity, and their biocompatibility, which

could benefit for them to be used in the artificial HAs. The investigations have led to the following new findings:

- After the investigation of different concentrations of each additive, optimal concentration for each additive has been obtained, in terms of diameters, morphology, β-phase contents of the resulting fibers.

- Different fillers behaved differently: the minimum diameter of the composite fibers is 180, 780 and 970 nm for WO_3, ZnO and CNTs fibers, whilst larger TiO_2 and LiCl additives led to much larger diameters, all larger than the pristine PVDF fibers of 80 nm. WO_3 and CNTs were dispersed within the electrospun fibers evenly, ZnO additive was dispersed around and within the fibers, and TiO_2 and LiCl fillers are poorly dispersed along the fibers.

- Sample P (PVDF/WO_3) resulted in the highest β-phase content of 0.91, followed by Samples Q (PVDF/ZnO) and R (PVDF/CNTs) of 0.85 and 0.74 respectively, whilst TiO_2 and LiCl acted as inhibitors and only led to a β-phase of 0.61 and 0.13, correspondingly. The 0.91 for PVDF/WO_3 is the highest β-phase obtained so far, against existing literatures, which could lead to excellent piezoelectric performance for those composite fibers.

- Particle size exhibited a significant impact on the β-phase content. By using different ZnO particles, we have confirmed that finer fillers lead to higher β-phase conversion with smaller diameters for the composite fiber.

- By analyzing the crystallinity, we have explained that filler WO_3, ZnO and CNTs exhibited two roles in the composite fibers, promoting the nucleation and restraining the chain growth which are both originating from stronger interactions between the filler and PVDF molecules, hence led to the higher crystallinity than those of TiO_2 and LiCl fillers in the composite electrospun fibers.

Chapter 7: Prototype construction, acoustic characterization, and biocompatibility assessment

7.1 Introduction

In Chapter 4, we presented the use of UV lithography for the preparation of SU-8 semi-permanent mould of different depths, for the fabrication of PDMS micropillars with different heights, which formed the foundation of artificial hair cells prototype. In Chapter 5, we achieved PVDF fibers with the highest piezoelectric properties, to act as the tip-links, linking the pillars to mimic the function of artificial hair cells. Beyond pure PVDF electrospun fibers, WO_3, ZnO, CNTs, TiO_2 and LiCl additives were used to produce PVDF composites, expecting to have enhanced piezoelectric and triboelectric properties, which were thoroughly investigated in Chapter 6. In this Chapter, firstly the fundamental aspects of TENG/PENG properties of the pure PVDF and its composite fibers relevant to their triboelectric and piezoelectric performance will be presented, leading to an effective guidance towards the selection of optimal PVDF-based composites. Secondly, the final structure of artificial hair cells prototype is constructed. Thirdly, the acoustic sensing behavior of the pure PVDF and its composites samples will be validated. Fourthly, the cytotoxicity of the resulting fibers towards biomedical device application will be assessed. Finally, a COMSOL simulation will be conducted to investigate the structures similar to the dimensions of natural hair cells, in order to provide support for utilizing those electrospun fibers in further device construction.

7.2 The properties of artificial hair cells prototype

The piezoelectric characterisation was conducted in collaboration with Drs. Zakaria Saadi and Ana I. S. Neves, by using their facilities at the University of Exeter.

7.2.1 The preparation of TENG/PENG sheets

On the aluminium collector attached to the rotary drum, clean copper tapes ($25\ mm \times 15\ mm \times 0.05\ mm$) are also stuck onto the collector. After 2 h spun using

the same set of parameters optimised in Chapter 5, a uniform sheet of fibers was obtained. To fabricate specimens for the TENG/PENG characterisations, copper tapes spun with the pure PVDF, and its composites were separated by a pair of clean tweezers from the surface of aluminium collector on the rotary drum. Fig. 7.1 illustrates the steps for the preparation of substrates. The collected substrates for each additive were stored in drying cabinet at 40 °C for 2 h for further use. After thorough drying, each copper sheet with electrospun fibers was stuck on a clean aluminium holder $(30\ mm \times 30\ mm \times 6\ mm)$.

Mixture of additive in the solution heated for 24 hrs

Electrospinning For 2 hrs at ambient temperature

Preparation of TENG piezoelectric devices

Al sample holder

PET tape 30x30 mm²

PVDF electrospun fibers sheet

Copper tape 30x30 mm²

Al sample holder
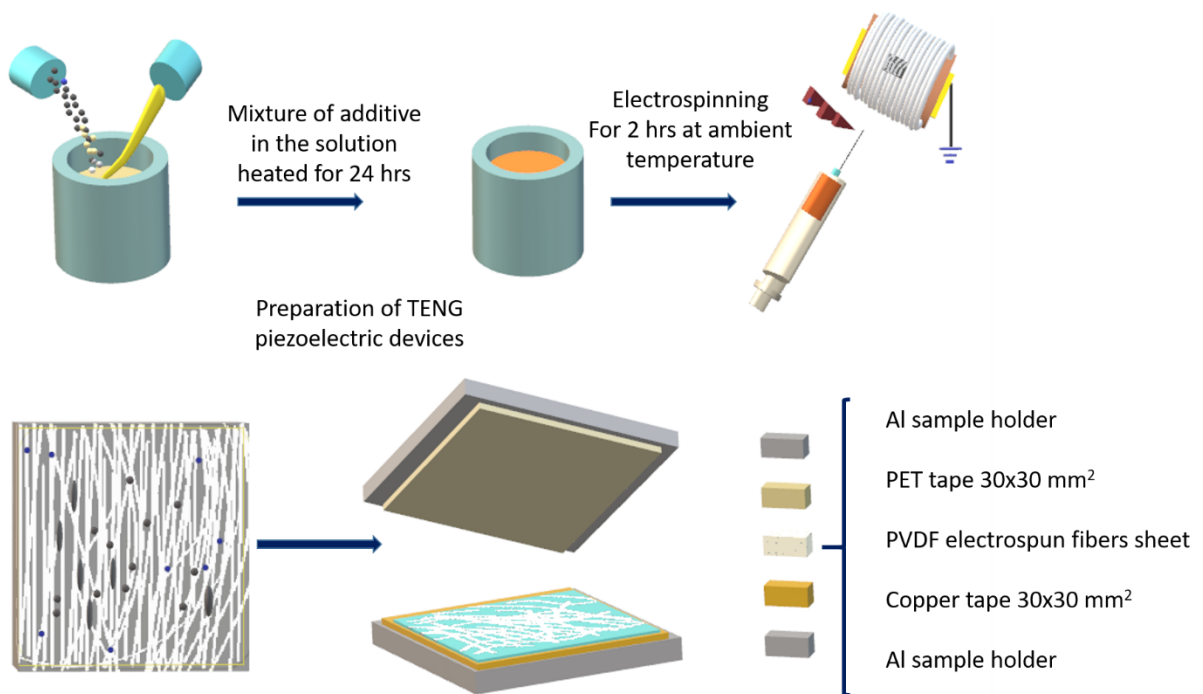
Fig. 7.1 The schematic steps of TENG piezoelectric devices preparation for pure PVDF electrospun fibers and its additives.

7.2.2 The experimental procedure of TENG/PENG sheets

After electrospinning, the pure PVDF and its composite spun fibers on $25\ mm \times 15\ mm \times 0.05\ mm$ copper sheets were collected from the rotary collector. This fiber mat will combine with a PET plate on another copper plate (as shown in Fig. 3.9a in Chapter 3), and the two plates are mutually made into contact. The thickness of PET layer was 25 μm, measured by a digital micrometer. The copper

side of both plates was stuck on two aluminium holders, separately, allowing the fiber mat to make good contact with the PET surface in the device assembly. Both the fiber and the PET layers should adhere securely onto the copper plates and remain stable for later characterization. After contact and release motion repetitions of the fibers against the PET, the peak voltage, current and the electrical charge outputs were measured, under the condition of 1 Hz and a consistent compression force of 40 N, for 2000 cycles. The frequency could be 1 Hz or 2 Hz and choosing 1 Hz was to preserve the integrity of the sample, avoid damage. To reach the maximum threshold of voltage, current and electrical charge for all samples, the contact force was kept constant. The mean voltage, current and charge values of samples are taken for 5 initial peaks.

In Fig. 7.2a-f, the voltage output values of the TENG substrates are presented for the Pure PVDF electrospun nanofibers (Sample A), and different composite fibers, including PVDF/WO$_3$ (Sample P), PVDF/ZnO (Sample Q), PVDF/CNTs (Sample R), PVDF/TiO$_2$ (Sample S), and (Sample T) PVDF/LiCl, respectively. The peak voltages of 125, 280, 160, 90, 80 and 21 V are assigned to Samples A, P, Q, R, S and T within 20 s, correspondingly.
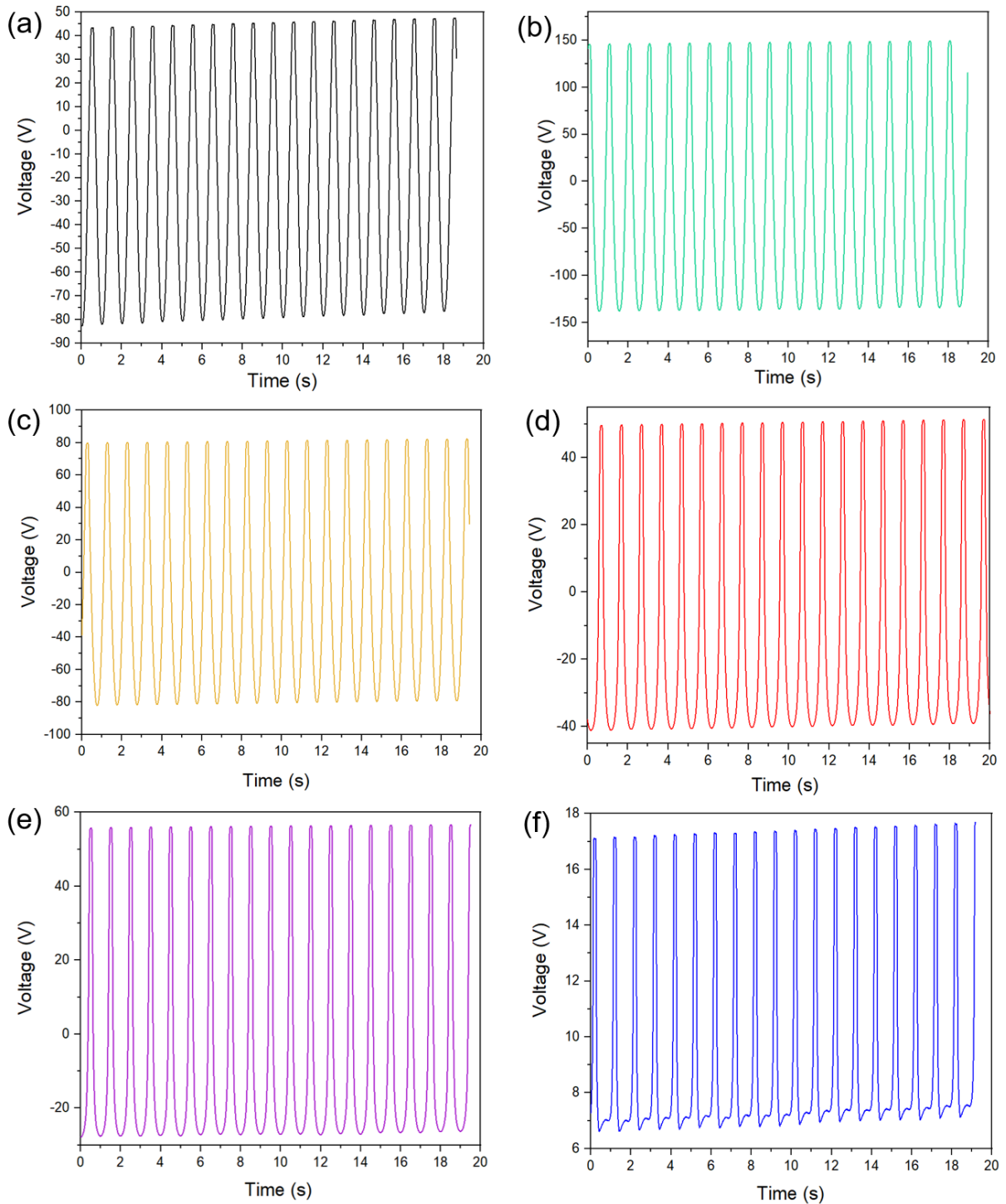
Fig. 7.2 Electrical responses in terms of voltage output. (a) Pure PVDF electrospun nanofibers, (b) PVDF/WO₃, (c) PVDF/ZnO, (d) PVDF/CNTs, (e) PVDF/TiO₂, and (f) PVDF/LiCl composites.

The output current values of Samples A (Pure PVDF), P (PVDF/WO₃), Q (PVDF/ZnO), R (PVDF/CNTs), S (PVDF/TiO₂) and T (PVDF/LiCl) are presented

in Fig. 7.3a-f, respectively. These values are 180, 580, 248, 400, 370 and 100 nA for Samples A, P, Q, R, S and T, respectively.
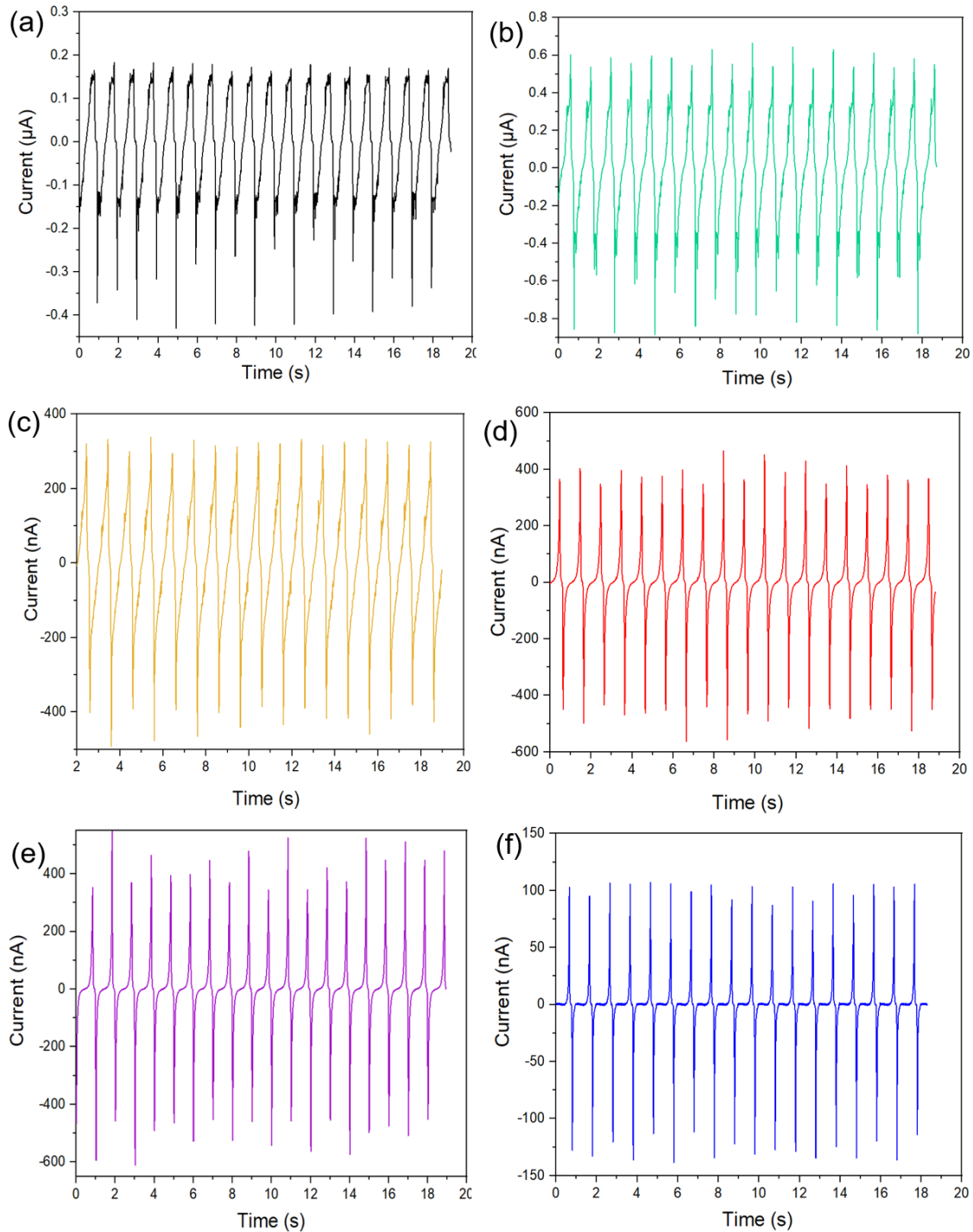
Fig. 7.3 Electrical response in terms of current output. (a) Pure PVDF electrospun nanofibers, (b) PVDF/WO₃, (c) PVDF/ZnO, (d) PVDF/CNTs, (e) PVDF/TiO₂, and (f) PVDF/LiCl composites.

Fig. 7.4a-f shows the peak values of electric charge for the pure PVDF and its composite samples, and the electric charge recorded output values of 4, 100, 55, 36, 30 and 5 nC for Samples A, P, Q, R, S and T, respectively.

Fig. 7.4 Electrical response in terms of electric charge output. (a) Pure PVDF electrospun nanofibers, (b) PVDF/WO$_3$, (c) PVDF/ZnO, (d) PVDF/CNTs, (e) PVDF/TiO$_2$, and (f) PVDF/LiCl composites.
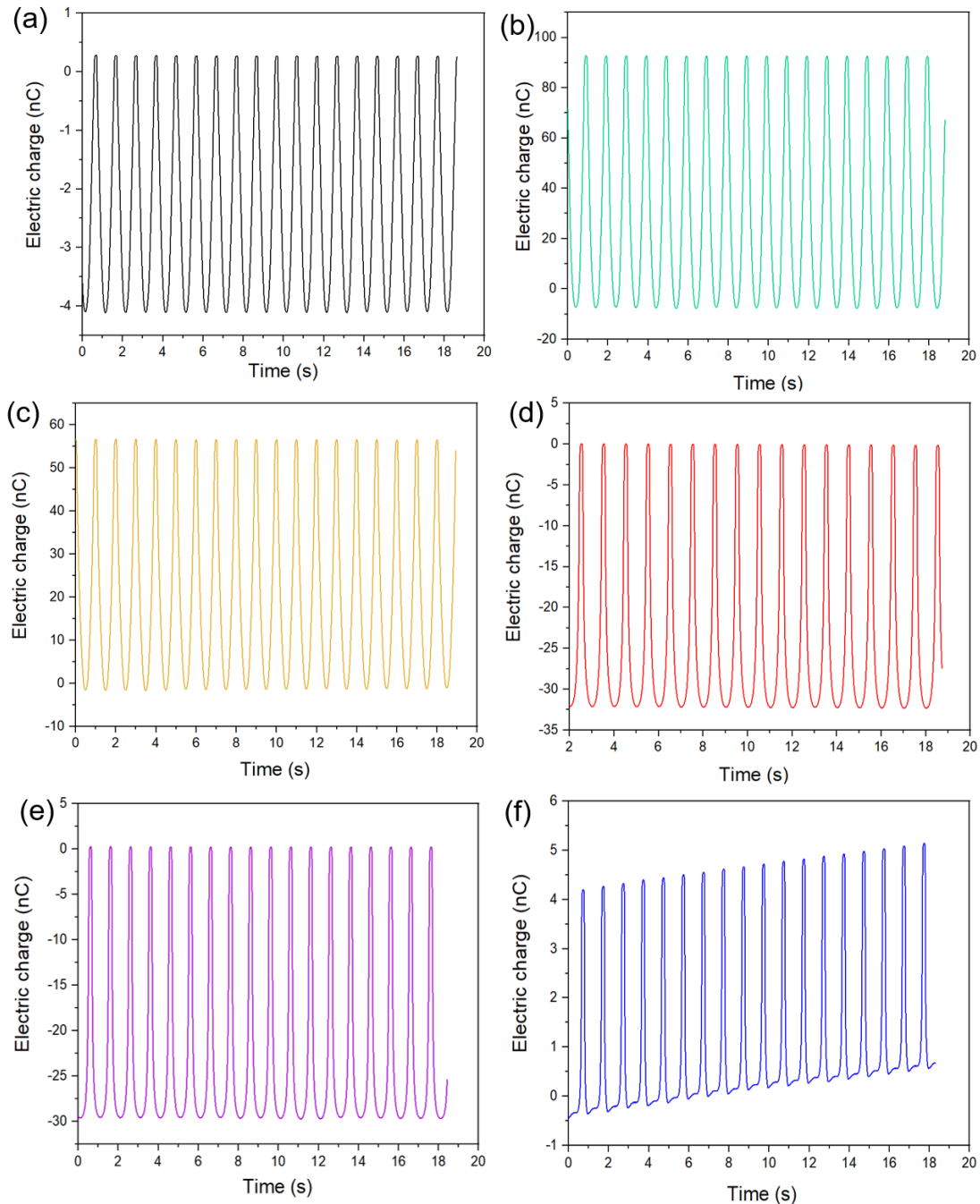
The TENG/PENG piezoelectric energy harvesting characterization of different PVDF electrospun fibers is presented in Fig. 7.5a. The values are extracted from Figs. 7.2-7.4, for better comparison among all samples. In Fig. 7.5a, starting from the pure PVDF (Sample A), the voltage, charge and current values are 125 V, 180 nA and 4 nC, accordingly. These values changed to 280 V, 580 nA and 100 nC for Sample P (PVDF/WO$_3$). For Sample Q (PVDF/ZnO), compared with Sample P, the voltage, current and electrical charge output values dropped by 43 %, 57 % and 45%, separately. When the additive is CNTs (Sample R), the output values of voltage, current and electrical charge are 90 V, 400 nA and 36 nC, respectively. For samples containing TiO$_2$ (Sample S) and LiCl (Sample T), the voltage outputs are 80 and 21 V, the current values are 370 and 100 nA, and the electrical charge values are 30 and 5 nC, respectively. Sample P (PVDF/WO$_3$) showed the highest output values, followed by Sample Q (PVDF/ZnO). Whilst the voltage output for pure PVDF electrospun fibers (Sample A) is higher than that of Samples R (PVDF/CNTs), S (PVDF/TiO$_2$) and T (PVDF/LiCl), its current output is only 22% of Sample P (PVDF/WO$_3$), and the electrical charge is barely 4% of Sample P, being the lowest. Furthermore, Samples R and S are almost equal in all output values, with current and electrical charge values being twice of the pure PVDF elactrospun fibers (Sample A). Sample T (PVDF/LiCl) behaved differently from other samples, with its voltage, current and electrical charge outputs reduced by 83 %, 83 % and 95 %, respectively, compared with Sample P.

Since material's intrinsic properties are the main determining factor of the charge transfer, better known as the triboelectric series, it is important to take into consideration the surface charge density of the dielectrics, thus selecting the best additive WO$_3$ for this work.

To characterise the potential applicability of this PVDF composite as a power source, the output current was measured against different load resistances, with incrementing values ranging from 10 KΩ to 10 GΩ, in order to get the optimum output power as stated by the "Maximum power transfer theorem" which is shown in Fig. 7.5b. It is observed that a maximum instantaneous power was obtained at load resistance of 212 MΩ, which is quite high, however such resistance can be reduced

by using a larger area of the tribomaterials to achieve a significantly higher output power. This value is around 140 µW for Sample P (PVDF/WO$_3$).
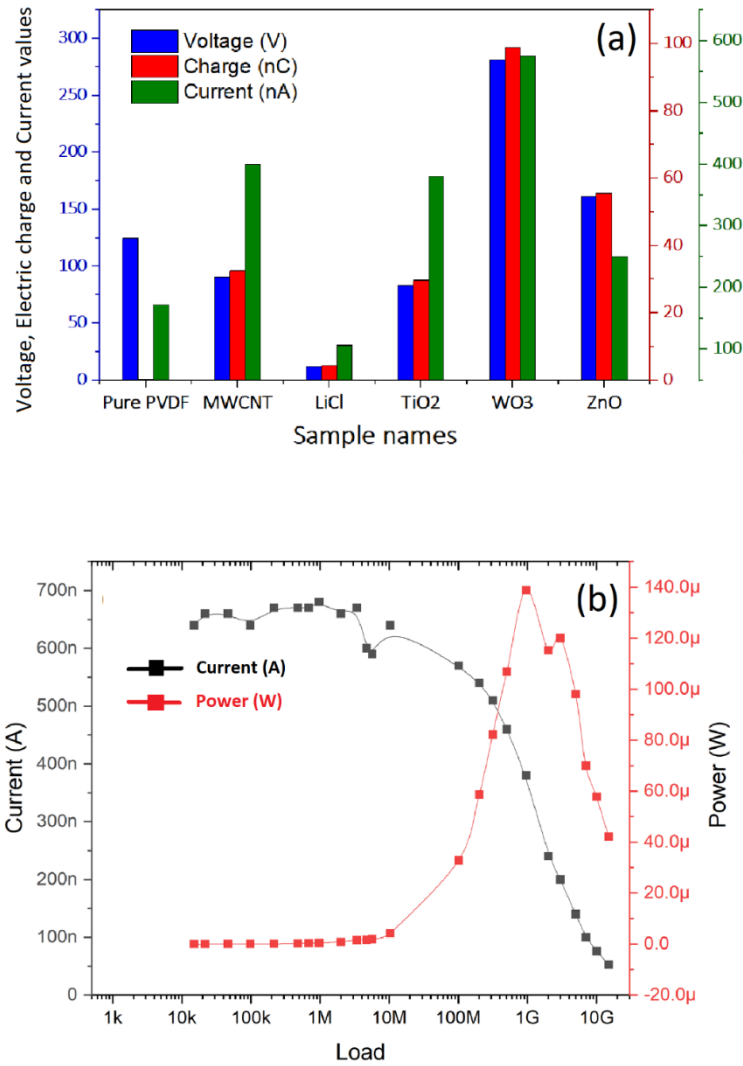
Fig. 7.5 (a) Voltage, current and charge outputs for each sample, and (b) the power graph derived from the current *vs* resistance power measurements for Sample P.

The piezoelectric properties of PVDF composites obtained by electrospinning have been highlighted in previous studies. Among those additives, barium titanate (BaTiO$_3$ or BT), Gr/GO, and CNTs, the highest β-phase formation occurred by using CNTs as the filler, achieved an voltage output of 0.9 V from a web [317]. It was reported that although BT enhanced the chance of β-phase crystallization in the PVDF web, its dispersion was inconstant [317]. By incorporating 15 wt% BT and

0.15 wt% Gr hybrid filler, an highest voltage output reached 11 V, with a maximum electric power of 4.1 µW, measured under a mechanical strain of 4 mm at 2 Hz [318]. Abdolhasani et al. obtained the highest proportion of β-phase of 76 % by using Gr, which exhibited an increase in voltage from 3.8 to 7.9 V.[319] Other study reported various concentrations of CNTs (3, 5, 7, and 10 wt%) in PVDF, reached a maximum content of β-phase of only 68.4%, by using electrospinning method, and obtained a highest voltage value of only 6 V [320]. The improved output in both the piezoelectric and triboelectric of PVDF/WO$_3$ composite is contributed to the homogenous dispersion of WO$_3$ nanoparticles. This study demonstrates that Sample P nanocomposite fiber-based PENG could be an effective power source for acoustic wearable devices.

The increase in the output for Samples A (pure PVDF), P (PVDF/WO$_3$), Q (PVDF/ZnO) and R (PVDF/CNTs) confirms the importance role of these additives in the piezoelectric performance of PVDF electrospun composite nanofibers. The energy harvesting property of composite TENG is strongly affected by both the surface chemistry and structural properties of the fibers, such as the crystallinity. The decrease in fiber diameters is relevant to the type of additive, and it can cause a major enhancement in the output. When the size of additive is nanoscale, the shape of nanofillers is more uniform, and their distribution within the fibers are better than those of TiO$_2$ and LiCl micro-scale flakes. For that reason, the polarization of the fibers would be stronger, which contributed to the increased piezoelectric outputs.

The distribution of various fillers is shown in Fig. 7.6, which was acquired after the triboelectric experiment.
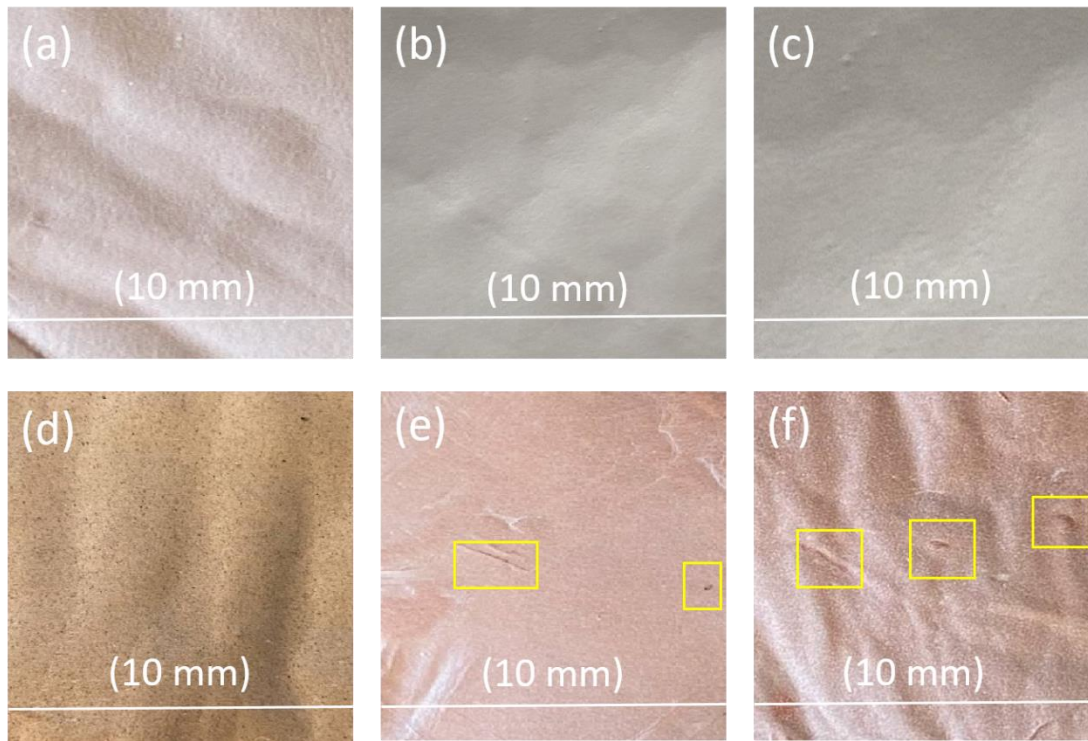
Fig. 7.6 2x digital image of various electrospun fiber mats on a copper collector after the triboelectric experiment. (a) Pure PVDF, (b) PVDF/WO$_3$, (c) PVDF/ZnO, (d) PVDF/CNTs, (e) PVDF/TiO$_2$, and (f) PVDF/LiCl, under the frequency of 1 Hz and a consistent force of 40 N, tested for 2000 cycles.

As it is clear in Fig. 7.6a-f, the post-test electrospun mat on the substrate is different from each other in terms colour, due to the original colour of the filler. Samples A, P, Q, S and T are relatively whiter, whilst Sample R appears darker (Fig. 7.6d).

For the pure PVDF, PVDF/WO$_3$, PVDF/ZnO and PVDF/CNTs (Fig. 7.6a-d), they appear to be flat and no obvious damage to the mat, suggesting a good adhesion and good stability. Conversely, damaged areas occurred to composite mat of PVDF/TiO$_2$ and PVDF/LiCl after the triboelectric experiment, as marked with yellow frames in Fig. 7.6e-f. For the former samples, they can undergo the repetitive mechanical friction tests from the linear acoustic actuator without issues, however this step cannot be conducted for the latter samples, as the copper surface was exposed after a few triboelectric tests, which could cause errors for the conductivity and make the results unreliable.

The reasons for this difference were two folded, the inhomogeneous fiber structures of the micro-sized fillers and the non-uniform charge distribution in the latter composite mats, as shown in Fig. 7.6 and in the SEM images of the pre-test samples presented earlier. During the pressing/releasing process, some micro flakes within the $PVDF/TiO_2$ and PVDF/LiCl composites might be broken, due to friction. On the contrary, finer fillers within the former smoother mats consisting of finer fibers could sustain such testing process, leading to higher charge, voltage and current values, as seen in Sample P ($PVDF/WO_3$) composite.

7.3 The construction of the artificial hair cell prototype

The mat of PVDF electrospun fibers can be used to cover the vertical, sequential pillars of various height, acting as tip links in an artificial hearing aid device prototype, as shown in Fig. 7.7a, mimicking the artificial hair cell functions. This artificial structure is inspired by the natural structure of hair cells which is illustrated in Fig. 7.7b.

So far, separate elements of the artificial hair cell have been prepared and studied in specific Chapters of 4, 5 and 6. These comprise the PDMS base in different heights and PVDF electrospun sheet on top of the PDMS substrate. To construct the proposed structure, initially the clean PDMS substrate (pillars) as fabricated by the methodology explained in Chapter 4 (section 4.3.3) was stuck on the aluminum collector of the electrospinning machine, by using a pair of clean tweezers. After 2 h of electrospinning, 15 μm thickness of pure PVDF or its composites were electrospun on the surface of the PDMS pillar substrate. A thin layer of gold of ~ 100 nm was then deposited onto the surface of the spun structure by using a HHV Edwards Auto306 thermal evaporator, which took another 6 h under the same condition described in Chapter 4. This is the upper electrode layer on top of electrospun fiber sheet.
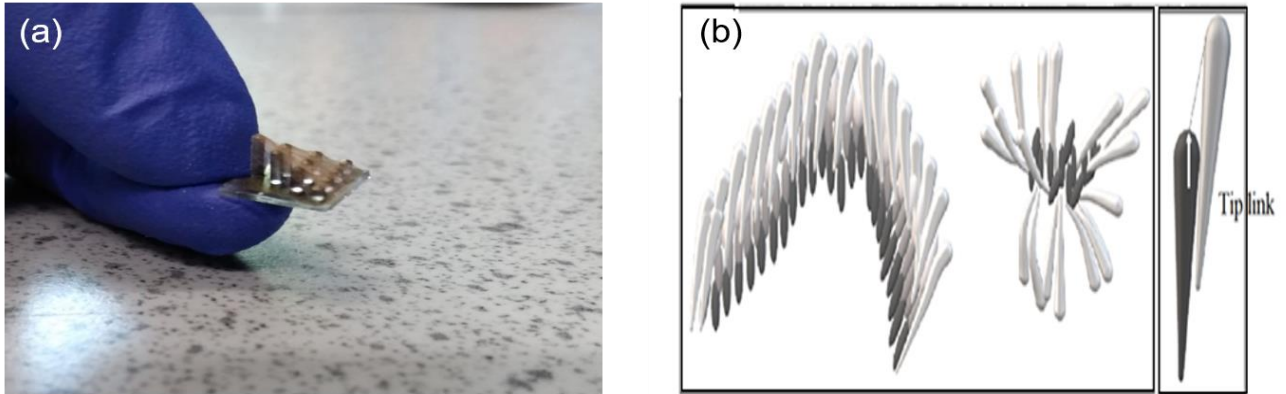
Fig. 7.7 (a) A prototype of the device with the PVDF electrospun nanofiber mat on the Au coated PDMS, and (b) An illustration of the structure of natural hair cell and tip-links.

7.4 The acoustic response

7.4.1 Set-up for the acoustic sensing characterizations

This section of acoustic analysis was obtained in collaboration with Mr. Konstantinos-Andreas Anastasiou and Ms. Agnes Bacon of the Physics department at the University of Exeter.

In Fig. 7.8a, a schematic setup for measuring the artificial hair cell is presented. A hypothetical graphic structure for the proposed artificial hair cells and their acoustic response is displayed in Fig. 7.8b. The setup consists of a faraday cage to eliminate external noise, a louder speaker as the sound source, an amplifier, and the sensing device. The sensing device comprises a sheet of the PVDF, or its composite placed between two parallel aluminium sheets $(10\ mm \times 10\ mm)$ acting as electrodes, which are mounted on the acoustic sensing device, stacked on an insulated sheet of clean room non dust wiper (superfine fiber). It is sitting across a rectangular opening directly above the speaker, with a distance $d = 11.6 \pm 0.5\ cm$ from it, as shown in Fig. 7.8c.

The speaker used is a VISATON FX 10 – 4692 coaxial loudspeakers, connected with a Sound Lab G097 180W Amplifier. Both frequency and amplitude of the applied

acoustic signal are controlled by a Tektronix AFG1022 arbitrary function generator. The device along with the speaker is enclosed in a grounded aluminium box (Faraday box) to avoid pick-up noise. A piece of tape on the top surface of the opening is set and the sample is stuck there. The PVDF and its composites layer are facing the speaker. The input voltage is applied by the function generator. A thin golden thread as the top electrode was stacked on the specimen surface with the help of a very small amount of conductive silver paste, whilst a copper wire was similarly attached to the bottom surface of the specimen as the counter electrode.

By using two shielded copper wires to connect the golden top and counter electrodes, the acoustic sensing signals were acquired on a Stanford Research Systems SR560 Low noise preamplifier.

7.4.2 The acoustic sensing characterizations

The correlation between the output voltage (mV) and input frequency (Hz) for pure PVDF and its composites is presented in Fig. 7.8d. Fig. 7.9a and b depicts the enlarged images of acquired output voltages shown in Fig. 7.8d under an input voltage of 6V.
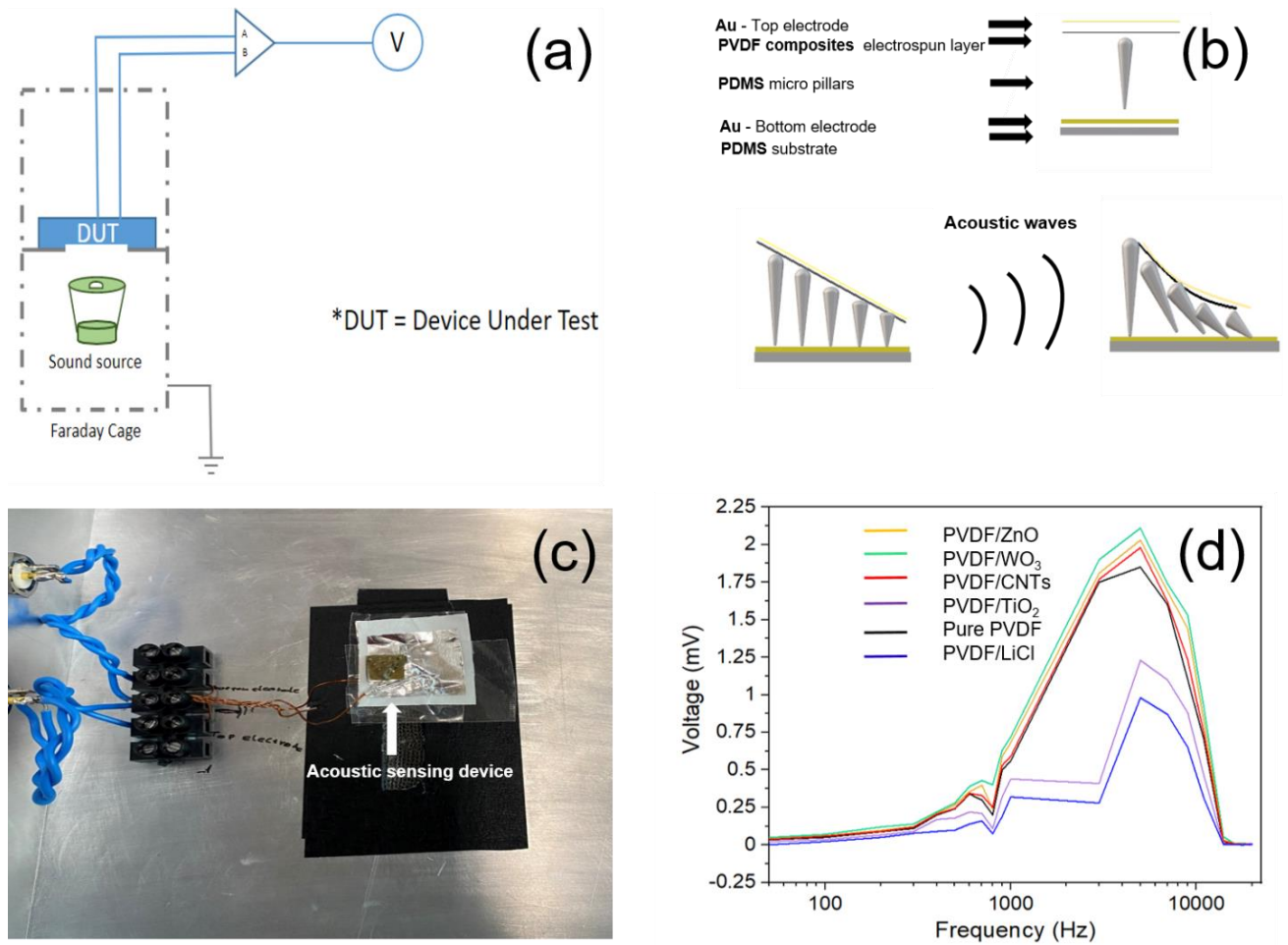
Fig. 7.8 (a) The schematic of acoustic measurement setup, (b) the theoretical function of acoustic waves on the proposed structure of artificial hair cells, (c) the actual acoustic sensing measurement setup for the artificial hair cell sensing prototype. and (d) the relationship between the output voltage (mV) and input frequency (Hz) for various samples under an input voltage of 6V.
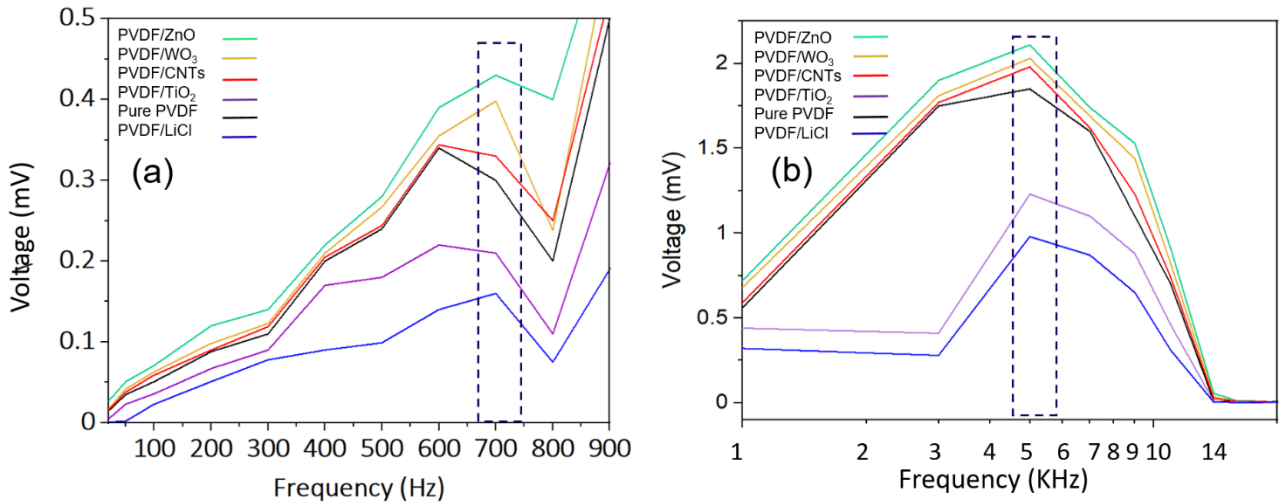
Fig. 7.9 (a) The relationship between the output voltage (mV) and input frequency (Hz) for various samples under an input voltage of 6 V for frequencies less than 1 kHz and, (b) and frequencies more than 1 kHz.

The amplified signal was recorded by a Tektronix TDS 2024C oscilloscope. For the acoustic response measurements, we applied a wide range of audio frequencies, from 50 Hz to 20 kHz, and amplitudes (2, 4 and 6V) to the specimen, to record their response against each combination of input frequency and amplitude by an oscilloscope connected to it. During the measurements, no signs of pick-up voltage outputs from noise were detected, which showed that the setup was properly shielded. Initial parameters for taking measurements had to be set during the experiment which are summarized in Table 7.1. Herein, the input value range of V_{pp} (the amplitude of the oscillating) was 2, 4 and 6 V. Gain was about the number of times for which the measured signal was magnified. High F_c (Frequency) and low F_c were parameters for setting up the filter of the voltage amplifier correctly. The definition of High and low F_c is highlighted when the filter to the corresponding position is set, either only low ($F < F_c$) or high ($F > F_c$) is measured.

The acoustic wave signals responses of all mat samples between 50 Hz and 20 kHz show two main maxima, the main one at about 5 kHz and the secondary one around 600 -700 Hz, depending on the composite, a similar output behavior. Regarding Figs. 7.8d and 7.9a, between 20 Hz and 700 Hz there is a region of gradual increase in the output voltage, until the appearance of the secondary peak

in the range 600 -700 Hz (shown as black dashed frame in Fig. 7.9a). This is followed by a drop until 800 Hz where a steep rise begins, reaching the dominant peak at approximately 6 kHz (shown as black dashed frame in Fig. 7.9b). For the TiO_2 and LiCl composite samples, they showed slightly different features, in the frequency range value of 1-3 kHz, the sensitivity is stopped, and it starts increasing once again after reaching to the frequency of 3 kHz. The lower responses were recorded (V_{out}^{max} = 1.25 mV for TiO_2 composite), compared with other samples that exhibited comparable output voltages for the main peak (Frequency = 6 kHz). In particular, the WO_3 composite sample showed consistently the highest output voltage (V_{out}^{max} = 2.13 mV) amongst all samples.

After the main maximum, all specimens showed a steep decline after 6 kHz, and at 14 kHz they are not responsive to the external sound wave. The voltage was almost zero for frequencies higher than 14kHz for all composite and pure samples.

Table 7.1 The initial parameters of acoustic sensing measurements for all samples.

Frequency	V_{pp}	Gain	High F_C	Low F_C	Soundlab Sound amplifier Power knob position
10 Hz	2	X200	1	100	3rd live CHH
50 Hz	2	X200	1	30	3rd live CHH
100 Hz	2	X200	10	100	3rd live CHH
200 Hz	2	X200	10	1 K	3rd live CHH
300 Hz	2	X200	10	1 K	3rd live CHH
400 Hz	2	X200	30	3 K	3rd live CHH
500 Hz	2	X200	100	3 K	3rd live CHH
600 Hz	2	X200	100	3 K	3rd live CHH
700 Hz	2	X200	300	3 K	3rd live CHH
800 Hz	2	X200	100	3 K	3rd live CHH
900 Hz	2	X200	100	3 K	3rd live CHH
1 kHz	2	X200	1 K	30 K	3rd live CHH
3 kHz	2	X200	1 K	30 K	3rd live CHH
5 kHz	2	X200	1 K	30 K	3rd live CHH
7 kHz	2	X200	3 K	10 K	3rd live CHH
9 kHz	2	X200	3 K	30 K	3rd live CHH
11 kHz	2	X200	3 K	100 K	3rd live CHH
14 kHz	2	X200	1 K	30 K	3rd live CHH
16 kHz	2	X200	3 K	100 K	3rd live CHH
18 kHz	2	X200	3 K	30 K	3rd live CHH
20 kHz	2	X200	3 K	30 K	3rd live CHH

Minor deformations associated with reflection of the detected signal on the walls of the enclosure were observed but their effect on the device's output was significant only in the very low frequency regime where the device is less sensitive.

The acoustic response of each single device during the frequency changings application is an acoustic sine wave. The frequency range (20 Hz-20 kHz) is facilitating the change in the output voltages matching to each frequency and is shown in detail for three different voltages of 2, 4 and 6 V in (Fig. 7.10-12). For input voltages higher than 6 V, the device was failed to response, and it started burning during the experiment.
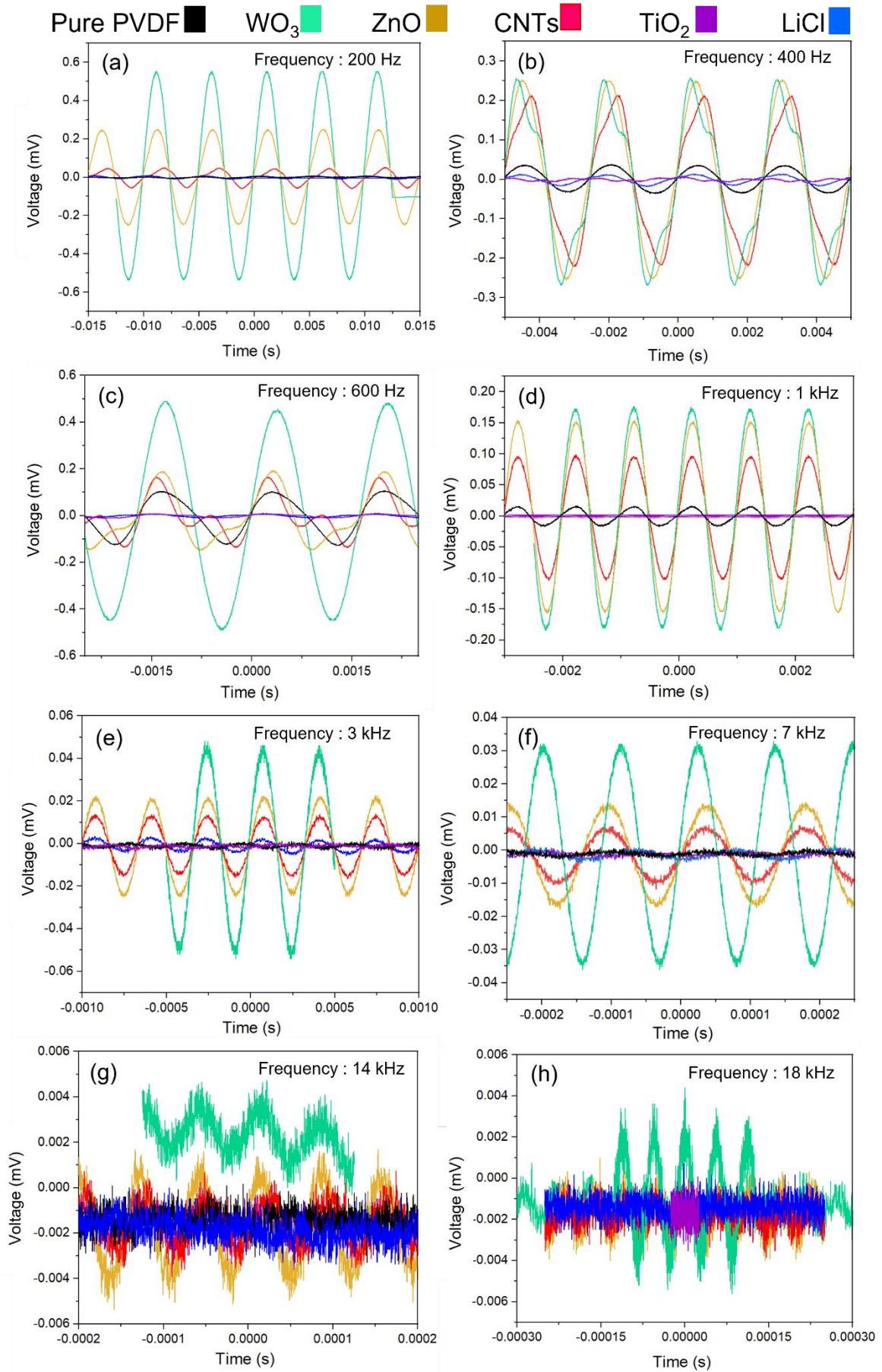
Fig. 7.10 Acoustic wave output voltage *vs* time, acquired at an applied voltage of 2 V for Samples A, P, Q, R, S, and T shown in black, green, golden, red, purple, and blue, under different input frequencies of (a) 200 Hz, (b) 400 Hz, (c) 600 Hz, (d) 1 kHz, (e) 3 kHz, (f) 7 kHz, (g) 14 kHz and (h) 18 kHz.

In Fig. 7.10a-h, the acoustic response under different frequencies from low to high values (200 Hz-18 kHz) for the pristine PVDF and its composite sensing device at a fixed applied voltage of 2 V is presented. The highest output voltage under similar conditions is obtained under the applied frequency of 200 HZ, being 0.6 mV, for Sample P (Fig. 7.10a). Other samples do not show any peak values of the voltage output, which is clearly distinguishable in the figure. The second and third highest voltage outputs are obtained from the ZnO and CNTs composites, respectively, and reducing following sequence of TiO_2, LiCl composites and the pristine PVDF.
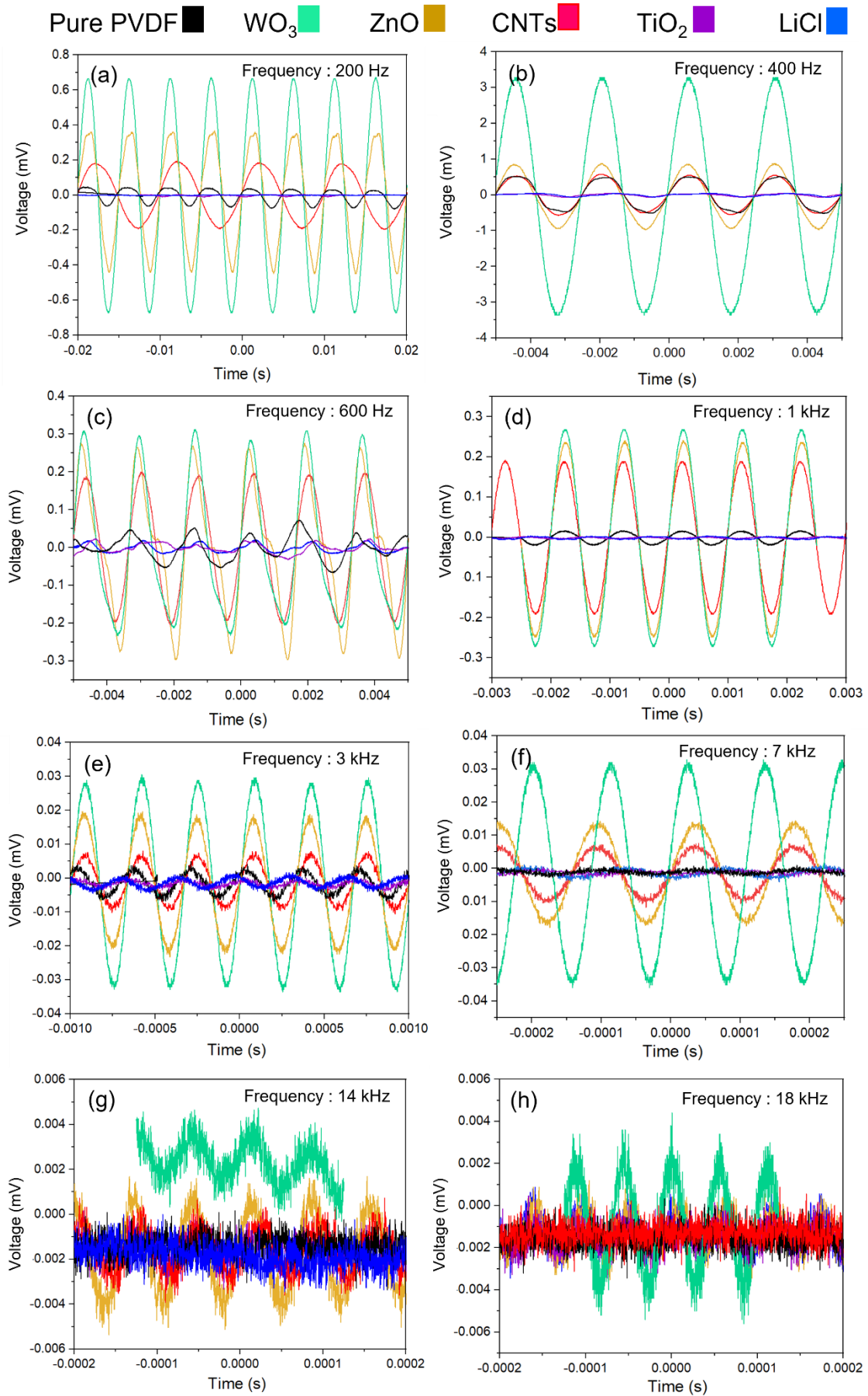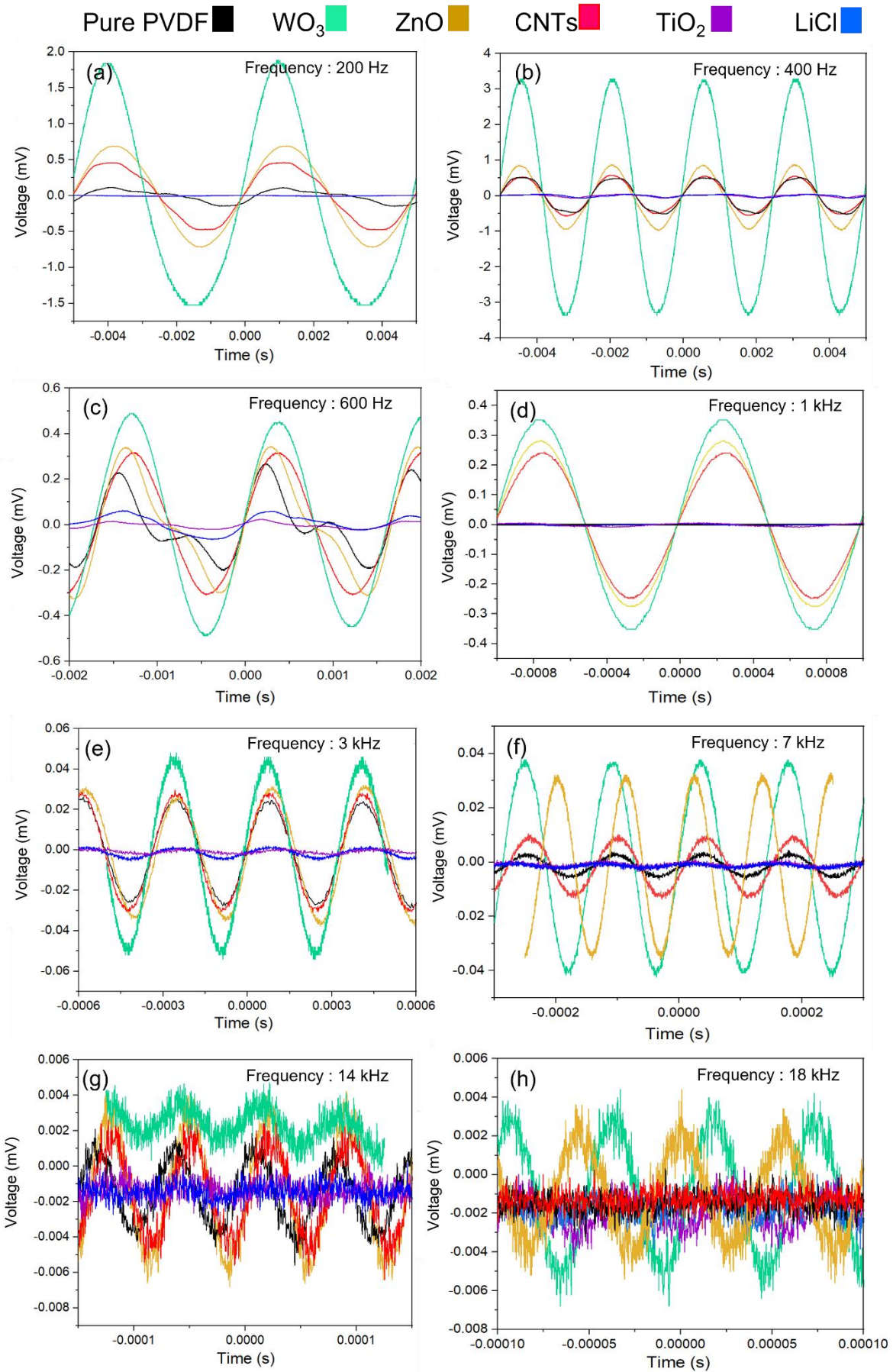
Fig. 7.11 Acoustic wave output voltage *vs* time, acquired at an applied voltage of 4 V for Samples A, P, Q, R, S, and T shown in black, green, golden, red, purple and blue, under different input frequencies of (a) 200 Hz, (b) 400 Hz, (c) 600 Hz, (d) 1 kHz, (e) 3 kHz, (f) 7 kHz, (g) 14 kHz and (h) 18 kHz.

Fig. 7.11a-h shows the output voltage values for the pure PVDF and its composite device under a fixed applied input voltage of 4 V. Different from the previous 2 V results, the highest output voltage, 3.3 mV for Sample P, is seen when the applied frequency is 400 Hz. Samples Q and R are followed in the voltage attainment. Samples S and T see clear drop, from 0.2 mV to almost 0. The difference between the pristine PVDF sample and its composite devices are still distinguishable, as shown in Fig. 7.11a-f. The outputs of specimens under frequencies of 14 and 18 kHz are similar, higher than other samples. Sample P shows highest output near 0.004 mV and the rest samples' acoustic output voltage are between (0-0.002 mV).

Pure PVDF ■ WO₃ ■ ZnO ■ CNTs ■ TiO₂ ■ LiCl ■

Fig. 7.12 Acoustic wave output voltage *vs* time, acquired at an applied voltage of 6 V for Samples A, P, Q, R, S, and T shown in black, green, golden, red, purple and blue, under different input frequencies of (a) 200 Hz, (b) 400 Hz, (c) 600 Hz, (d) 1 kHz, (e) 3 kHz, (f) 7 kHz, (g) 14 kHz and (h) 18 kHz.

Fig. 7.12 shows the device responses under 6 V voltage input, which shows different features from the responses under 2 V and 4 V input voltages. When the applied input voltage is 2 V, the disfigurement of waves happens from frequencies higher than 14 kHz. At 4 V, a similar trend of deformation is observed. Further rising the voltage to 6 V, more increased distortion rate at higher frequencies of 14 and 18 kHz is observed. Sample P (PVDF/WO$_3$) exhibits the highest output voltage of 1.65 mV, whereas Samples Q (PVDF/ZnO), R (PVDF/CNTs), S (PVDF/TiO$_2$) and T (LiCl) showed a linear decrease, as shown in Fig. 7.12. Sample Q at low frequency of 200 Hz exhibits an output voltage of 0.55 mV, and Sample R 0.48 mV. Both Samples of S and T show almost no voltage, lower than Sample A, the pure PVDF Sample, which exhibits 0.15 mV.

Based on above studies, under different ranges of frequencies at different amplitudes, some composite samples transduced the acoustic signals into good electric potentials, which originated from their enhanced piezoelectric and triboelectric properties than those of pure PVDF mat sample. In particular, Sample P, the WO$_3$ composite sample, showed the maximum output voltage. These results have validated that these composite samples have great potentials in harvesting acoustic signals and noise and transducing them into electrical energy.

The best energy harvesting feature demonstrated by Sample P, the WO$_3$ composite, can be attributed to its highest piezoelectric properties that originated from its highest β-phase crystallinity, as concluded in the previous Chapter. This result strengthens the direct perception of generating piezoelectricity from sound energy to electricity, for the construction of future generation of self-powered HAs.

7.5 Cytotoxicity analysis of the device

The experiments presented and analysed in this section were performed in collaboration with Ms. Evelina Lucinskaite in the Soeller Lab, Biophysics and Advanced Imaging from University of Exeter.

7.5.1 Experimental set-up of cell cultures

Materials used in these experiments include: HCT-116 (human colon cancer), HEK-293 (embryonic kidney), McCoy's 5a Modified Medium (DMEM, D6429) which were purchased from Sigma-Aldrich, and fetal bovine serum (10500064), and Antibiotic-Antimycotic solution (15240062) that were purchased from Gibco.

Cell cultures of the HCT-116 (human colon cancer) and HEK-293 (embryonic kidney) were grown under standard conditions of 5% CO_2 and 37 ^{o}C in a controlled humidified incubator to reach 70–80% confluence. The HCT-116 was grown in DMEM, and the HEK-293 was grown in McCoy's 5a Modified Medium. The HCT-116 and HEK-293 cell lines were maintained in a high glucose Dulbecco's modified Eagle's medium (DMEM), supplemented with 10% fetal bovine serum and 1% Antibiotic-Antimycotic solution, as provided in Fig. 7.13.
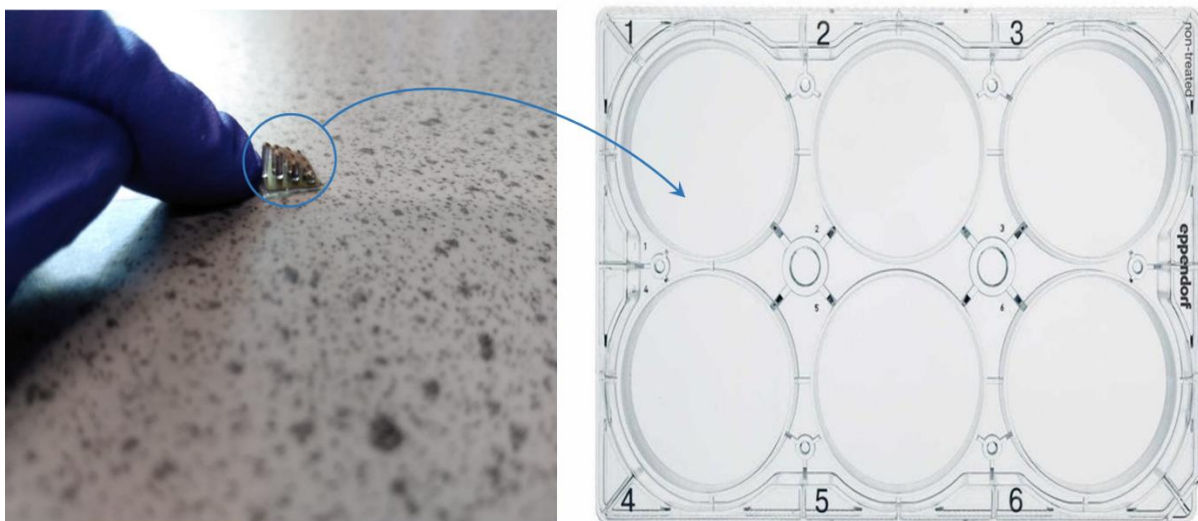

Fig. 7.13 The final device and proposed cell lines.

7.5.2 Cell images and investigation of positive and negative controls

The cells were plated in 6-well plates and grown for 24 h. After 24-hour incubation period of cell growth, the devices were added to the wells (one device per well) and were left for further growth and potential toxicity observation. Control wells did not contain any devices (Fig. 7.14a-b). As a reference of how a toxic substance could affect the cell lines, a drop of toluene was added to the HCT-116 containing well. When cells were exposed to this toxic material, they instantaneously started breaking up from their colonies and detached from the surface. When observed under the microscope (Fig. 7.14c), the cell morphology changed, and the dead cells were floating which indicates high toxicity. Also, a lot of debris was excreted from the dying stressed cells. Contrastively, the cells which were in presence of the device remained healthy, continued growing, and showed no signs of toxicity. These preliminary results suggest the viability for these devices to be used in an inner ear as a completely implantable and safe device.
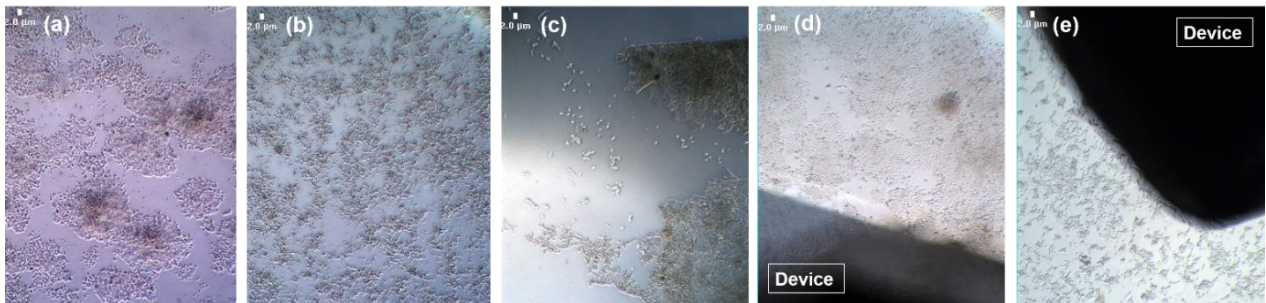

Fig. 7.14 (a) Cell line: HCT-116 (human colon cancer), (b) Cell line: HEK-293 (human embryonic kidney), (c) a drop of toluene in the HCT-116 cell line as an evidence of negative control, (d) the growth of cells after 2 days in the HCT-116 cell line around the device, and (e) the growth of cells around the device after 2 days in the HEK-293 cell line.

7.6 COMSOL model of device prototype

To estimate the performance of piezoelectric nanofibers on an elastic PDMS substrate for the purpose of mimicking hair cell structures, COMSOL simulation was conducted, in collaboration with Dr. William Ferguson at the University of Exeter.

COMSOL Multiphysics® was used to model the harvester's output by finite element analysis. Fig. 7.15 shows the layout of the model. For computational purpose, the piezoelectric fibers were assumed to be a flat sheet. The raked pillars were arranged in four rows in a pyramidal arrangement (with the single pillar being the tallest, h_p in height, and the four shortest ones all being $h_p \times H$ in height). The gap between rows was controlled by the spacing ratio, R, of the substrate length, and the arrangement was positioned relative to the middle of the substrate. The top of every cylindrical pillar was shaved (preserving its height at the high end) at an angle calculated to allow the flat face of the piezoelectric layer to meet all of them. All values used for the model is summarized as Table 7.2.
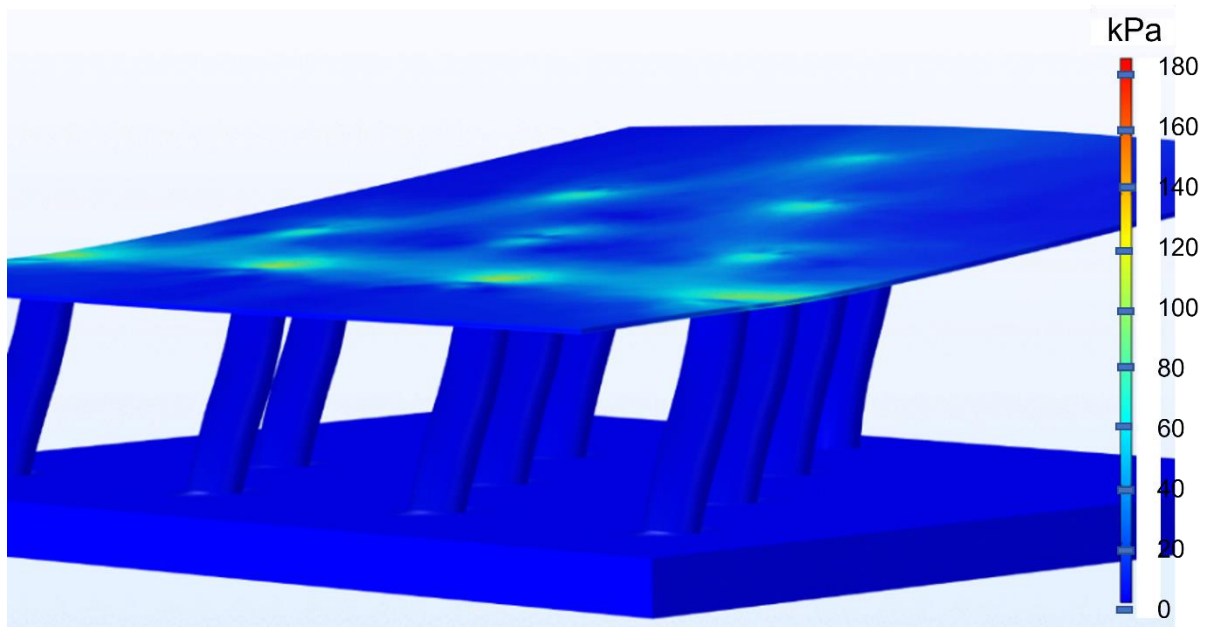
Fig. 7.15 View of model under an applied force.

Table 7.2 Parameter values used in the COMSOL model.

Part	Parameters	Value	Unit
PVDF layer	Length (L_p) Width (W_p) Thickness (t_p)	1000 850 5	nm nm nm
PDMS substrate	Length (L_s) Width (W_s) Thickness (t_s)	1250 850 50	nm nm nm
PDMS pillars	Radius (r_p) Base height (h_p) Height ratio (H) Spacing ratio (R)	50 100 0.9 0.2	nm nm - -

The model had two components: the PDMS polymer substrate and pillars, and the PVDF as the piezoelectric layer; all material parameters used in their modelling are listed in Table 7.3. To measure the electrical output of the piezoelectric layer under excitation, a sinusoidal force of 5 N (middle-to-peak) was applied to the piezoelectric layer parallel to the length of the substrate, at an oscillating rate of 10 Hz. A virtual resistor was connected across the top and bottom surfaces of the PVDF layer (emulating its electrodes); its load is set to maximise the power transfer. The power output was calculated from the voltage and current in this resistor.

The power output from this setup was found to be 2.44 μW, though this can only be an estimate of the practical devices' spun fibres and changing parameters can suggest different suggestive values.

Table 7.3 Parameter values used in the COMSOL model.

Material	Property	Value	Unit
PVDF	Density (ρ_p) Coupling (d_{31}) Matrix (d_{32}) (d_{33}) Relative Permittivity (ε_{33})	1780 23 2 -33 136	Kg.m^{-3} m.V^{-1} m.V^{-1} m.V^{-1} 10^{-12} F.M^{-1}
PDMS	Density (ρ_s) Poisson's Ratio (v_s) Elastic Modulus (E_s)	965 0.5 0.57-3.7	Kg.m^{-3} - Mpa

7.7 Summary

In this Chapter, a prototype of artificial hair cells sensor device consisting of the PDMS pillars and PVDF composite fiber mat has been constructed. Its acoustic responses and cytotoxicity as a medical device have been investigated, and the performance has been simulated by using the COMSOL model. In detail:

- After the triboelectric experiment towards the PENG/TENG substrate application for all of hybrid composite samples, the output values of voltage, charge and current for each specimen have been obtained, and Sample P (PVDF/WO$_3$) resulted in values of 280 V, 580 nA and 100 nC as the most suitable candidate for the tip-links function purpose.

- Different composite fibers performed differently with regard to the acoustic sensing investigation.

- For the specified set of frequencies and input voltages, Sample P (PVDF/WO$_3$), exhibited the highest output voltage of 2.12 mV, which could be the optimal choice as acoustic signal to electrical potential transducer based on its highest piezoelectric and triboelectric properties.

- The distortion rate for the acoustic waves of all fibrous ends up in the higher frequency range of 14 and 18 kHz for all composite samples. In the other frequency ranges, the input acoustic signals with less alteration and distortion can be chosen as a suggestive harvesting acoustic signals to transduce them into electrical energy mimicking the role of artificial tip-links.

- The viability of the fabricated device was characterized by two cell cultures of HCT-116 (human colon cancer) and HEK-293 (embryonic kidney). Both preliminary cell cultures proved that in the presence of the device, they were remained healthy, they continued growing, and showed no signs of toxicity.

- The developed COMSOL simulation of the artificial hair cell exhibited a power output as high as 2.44 µW. This available finding points out that the elaboration of this novel piezoelectric structure which should be based on the size of proposed structure controlled.

Chapter 8: Conclusion and suggestions for future work

8.1 Conclusions

The main aim of this PhD study was to fabricate an artificial hair cell like sensor prototype for the next generation of HAs. This investigation included the synthesis procedures and the properties of related materials fabricated. In this thesis, the whole structure of device was prepared and the morphologies, crystal structures, piezoelectric, triboelectric, and acoustic properties were investigated and analyzed in further details.

In Chapter 4, several trials of fabrication for achieving semi-permanent SU-8 moulds in an appropriate geometrical structure close to the proposed shape were performed. Changing parameters like the time of exposure, the exposure intensity value while the lithography was performed, the time of development for the SU-8 photoresist were mainly listed. The proper structure was obtained when the SU-8 was exposed to the UV-lithography as it was more sensitive to the UV light. To get different heights for the PDMS flexible micro pillars, the development of SU-8 moulds after being exposed was done partially and not completely. This helped to get the different depth of holes developed in the SU-8 photoresist semi-permanent mould. After the mould was ready, PDMS solution including the elastomer and its hardener were mixed thoroughly and degassing was done to inhibit bubbles trapping while seeping the solution on the mould. The whole mould and the solution on top were left at ambient temperature for longer than 24 h. The PDMS micro pillars were peeled off from the mould in an acetone container to remove all possible contamination.

In Chapter 5, PVDF electrospun nanofibers were synthesised by the electrospinning method. For the electrospinning process, the appropriate parameters affecting on the morphology of the products were completely compared and the best values were chosen among each group of parameters as optimized values. They were the change in concentration of PVDF into DMF/Acetone (3/7) volume ratio of solution, voltage values of the process, changing the distance between the needle and the collector, feeding rate and the collector speed values. The effect of concentration among all parameters was significantly monitored as it

was proven that other properties can be affected by the change in the concentration of PVDF powder in the solution. For instance, the highest β-phase content was allocated to the solution containing 1.50 g PVDF in DMF/Acetone (3/7 volume ratio) solution. This proved the highest piezoelectric property of the obtained nanofibers among the rest samples. Also, minimum diameter mean size was 213 nm for the sample including the higher β-phase content generating the highest V_{oc} of 170 mV sufficient for the artificial tip-links functionality. Furthermore, the highest voltage and current outputs for a thickness of 15 µm of PVDF electrospun fibers was 124 V and 174 nA respectively.

In Chapter 6, for the purpose of additive roles on the piezoelectric and triboelectric properties of electrospun fibers studying, different material with different particle sizes were chosen. They were WO_3, ZnO, CNTs, TiO_2 and LiCl. The optical, structural, piezoelectric, triboelectric, and acoustic sensing properties of all samples including additives were compared with the pure PVDF electrospun fiber sample. The increase in the diameter of samples was for two additives including TiO_2 and LiCl, while the lowest mean diameter sizes were for samples including WO_3, ZnO and CNTs which are around 80, 180, 780 and 970 accordingly. The change in the diameter was followed to the change in the content of β-phase fraction which is directly relevant to the piezoelectric properties. For the sample including WO_3, this value was 0.91 which was the highest among all samples while it was only 0.13 for the composite including LiCl.

In Chapter 7, TENG/PENG species generated for each additive were used for acoustic excitation waves at different amplitudes and frequencies. As an acoustic signals harvester, the device with WO_3 additive, showed higher values of output which is around 2.12 mV at a frequency of 6 kHz. In this Chapter, the fundamental aspects of TENG/PENG properties of the pure PVDF and its composite fibers relevant to their triboelectric and piezoelectric performance was presented and, the optimal PVDF based composite was chosen. Furthermore, the final artificial hair cells prototypes were grown in two different cell lines including HCT-116 (human colon cancer, ATCC: CCL-247) and HEK-293 (human embryonic kidney, ATCC: CRL-1573), under the standard conditions of 5% CO_2 and 95% air at 37°C in a

controlled humidified incubator to reach 70–80% confluence. The results showed that the cells which were in presence of the device remained healthy, continued growing, and showed no signs of toxicity. These preliminary results suggest the viability for these devices to be used in an inner ear as a completely implantable and safe devices. Moreover, a COMSOL simulation helped with an estimate of power output equal to 2.44 µW. The measurement of the electrical output of the piezoelectric layer under excitation, a sinusoidal force of 5 N (middle-to-peak) was applied to the piezoelectric layer parallel to the length of the substrate, at an oscillating rate of 10 Hz.

8.2 Future

Based on the results, my observations, and expectations, I would like to suggest following works for future works to improve the direction of research. Some of them are not included due to lack of equipment access or sufficient time.

- While producing SU-8 semi-permanent mould, using NanoBeam lithography was not very helpful. However, the precise shape for the circle structure was obviously achievable by this method. The problem was that the SU-8 is not sensitive to electron beam but the UV. The lack of exposed areas resulting in use of NanoBeam lithography is due to the SU-8 behavior to electron beam. This might be possible and time taking if two of UV and NanoBeam lithographies were applied. As a suggestion, starting from Nanobeam lithography following to a short development step. Next, using patterns similar to the surface of produced SU-8 developed layer by using UV lithography. This might present smaller dimensions and more precise PDMS pillars following to the next steps.

- The use of additives in the pure PVDF solution changed the properties significantly. The investigation of two additives into the pristine PVDF solution can be suggested. These additives can be mainly WO_3, ZnO and CNTs. The preparation can be initially started with a constant value of ZnO while the concentration of WO_3 is adding with a standard increment. This can be repeated when the concentration of WO_3 is unvarying and ZnO concentration is changeable. Next batch of experiments can include WO_3 and CNTs, and

ZnO and CNTs separately. The effect of the strongest additives in this study on the piezoelectric, triboelectric as well as accosting sensing can be investigated thoroughly and the best combination of two additives together can be suggested.

- It is very well noted that cell line completely like the inner ear medium will work better than introduced cell lines. Although, the preliminary information in this regard was sufficient to convince that the device is not toxic, however a very well cell line similar to the inner ear environment will make a stark difference in presentation of this artificial device for future generations of completely implantable artificial hair cell sensor devices.

References

[1] J. Tao and X. Yu, "Hair flow sensors: From bio-inspiration to bio-mimicking - A review," *Smart Mater. Struct.*, vol. 21, no. 11, 2012, doi: 10.1088/0964-1726/21/11/113001.

[2] S. A. (2017). Gelfand, *Hearing: An Introduction to Psychological and Physiological Acoustics (6th ed.). CRC Press.* .

[3] T. Inaoka *et al.*, "Piezoelectric materials mimic the function of the cochlear sensory epithelium," *Proc. Natl. Acad. Sci. U. S. A.*, vol. 108, no. 45, pp. 18390–18395, 2011, doi: 10.1073/pnas.1110036108.

[4] S. Kim, W. J. Song, J. Jang, J. H. Jang, and H. Choi, "Mechanical frequency selectivity of an artificial basilar membrane using a beam array with narrow supports," *J. Micromechanics Microengineering*, vol. 23, no. 9, 2013, doi: 10.1088/0960-1317/23/9/095018.

[5] A. F. Ryan, "Protection of auditory receptors and neurons: Evidence for interactive damage," *Proc. Natl. Acad. Sci. U. S. A.*, vol. 97, no. 13, pp. 6939–6940, 2000, doi: 10.1073/pnas.97.13.6939.

[6] N. Hirokawa, Y. Tanaka, Y. Okada, and S. Takeda, "Nodal Flow and the Generation of Left-Right Asymmetry," *Cell*, vol. 125, no. 1, pp. 33–45, 2006, doi: 10.1016/j.cell.2006.03.002.

[7] J. Sirohi and I. Chopra, "Fundamental understanding of piezoelectric strain sensors," *J. Intell. Mater. Syst. Struct.*, vol. 11, no. 4, pp. 246–257, 2000, doi: 10.1106/8BFB-GC8P-XQ47-YCQ0.

[8] J. S. Park, "Electrospinning and its applications," *Adv. Nat. Sci. Nanosci. Nanotechnol.*, vol. 1, no. 4, 2010, doi: 10.1088/2043-6262/1/4/043002.

[9] E. Daniel, "Noise and hearing loss: A review," *J. Sch. Health*, vol. 77, no. 5, pp. 225–231, 2007, doi: 10.1111/j.1746-1561.2007.00197.x.

[10] W. J. Murphy and J. R. Franks, "Revisiting the NIOSH Criteria for a Recommended Standard: Occupational Noise Exposure," *J. Acoust. Soc. Am.*, vol. 111, no. 5, p. 2397, 2002, doi: 10.1121/1.4778162.

[11] M. R. Serra *et al.*, "Recreational noise exposure and its effects on the hearing of adolescents. Part I: An interdisciplinary long-term study," *Int. J. Audiol.*, vol. 44, no. 2, pp. 65–73, 2005, doi: 10.1080/14992020400030010.

[12] T. Zahnert, "The Differential Diagnosis of Hearing Loss," *Dtsch. Aerzteblatt Online*, vol. 108, no. 25, pp. 433–445, 2011, doi: 10.3238/arztebl.2011.0433.

[13] M. Giles and P. Dawes, "Introduction to Hearing Loss," *Symptom Oriented Otolaryngol. Neck Surg. Otol. Pediatr. (Volume 3)*, pp. 94–94, 2017, doi:

10.5005/jp/books/12951_9.

[14] A. J. Hudspeth, "How the ear's works work: Mechanoelectrical transduction and amplification by hair cells," *Comptes Rendus - Biol.*, vol. 328, no. 2, pp. 155–162, 2005, doi: 10.1016/j.crvi.2004.12.003.

[15] D. Howard and J. Angus, "The anatomy of the hearing system," *Acoust. Psychoacoustics*, no. April 2016, pp. 66–74, 2001.

[16] A. O. Diefendorf, "Introduction to Audiology.," *Ear Hear.*, vol. 7, no. 4, pp. 276–277, 1986, doi: 10.1097/00003446-198608000-00011.

[17] R. W. Cantrell, *Auditory System: Anatomy, Physiology (Ear)*, vol. 233, no. 11. 1975.

[18] J. I. Matsui, M. a Parker, B. M. Ryals, and D. a Cotanche, "Regeneration and replacement in the vertebrate inner ear cochlear hair cells , which could lead to therapies for treating deafness in humans," *Rev. - Drug Discov. Today*, vol. 10, no. 19, pp. 1307–1312, 2005.

[19] J. Isamu and D. Allen, "Current opinion in otolaryngology {&} head and neck surgery Allen," pp. 418–425, 2004.

[20] J. Martin, F.; Clark, *Introduction to Audiology (with CD-ROM)*. Needham Heights, MA, USA, 2005.

[21] G. Newby, H.; Popelka, *Audiology*. Englewood Cliffs; Prentice-Hall, Upper Saddle River, NJ, USA, 1992.

[22] J. Sataloff, *Hearing Loss*. Lippincott: Philadephia, PA, USA, 1966.

[23] A. Kharlamova and N. L. Aarts, "A Review of Past and Present Hair Cell Regeneration Techniques," *Contemp. Issues Commun. Sci. Disord.*, vol. 34, no. Fall, pp. 134–144, 2007, doi: 10.1044/cicsd_34_f_134.

[24] J. F. Willott, "Anatomy, Physiology and Psychophysics," in *Aging and the Auditory System*, London, UK: Whurr Pub Ltd, 1991.

[25] R. Fettiplace and C. M. Hackney, "The sensory and motor roles of auditory hair cells," *Nat. Rev. Neurosci.*, vol. 7, no. 1, pp. 19–29, 2006, doi: 10.1038/nrn1828.

[26] D. C. Emanuel, T. Letowski, and S. Maroonroge, "Auditory function: Physiology and function of the hearing system," *Helmet-Mounted Displays Sensory, Perceptual, Cogn. Issues*, no. April 2016, pp. 307–334, 2009.

[27] R. Fettiplace, "Hair cell transduction, tuning, and synaptic transmission in the mammalian cochlea," *Compr. Physiol.*, vol. 7, no. 4, pp. 1197–1227, 2017, doi: 10.1002/cphy.c160049.

References

[28]   M. LeMasurier and P. G. Gillespie, "Hair-cell mechanotransduction and cochlear amplification," *Neuron*, vol. 48, no. 3, pp. 403–415, 2005, doi: 10.1016/j.neuron.2005.10.017.

[29]   E. P. Hong, M. K. Kim, I. Y. Park, S. H. Lee, Y. Roh, and J. H. Cho, "Vibration modeling and design of piezoelectric floating mass transducer for implantable middle ear hearing devices," *IEICE Trans. Fundam. Electron. Commun. Comput. Sci.*, vol. E90-A, no. 8, pp. 1620–1627, 2007, doi: 10.1093/ietfec/e90-a.8.1620.

[30]   L. E. Cross *et al.,* "Piezoelectric and Electrostrictive Materials for Transducer Applications," p. 390, 1991.

[31]   S. L. Shotwell, R. Jacobs, and A. J. Hudspeth, "Directional Sensitivity of Individual Vertebrate Hair Cells To Controlled Deflection of Their Hair Bundles," *Ann. N. Y. Acad. Sci.*, vol. 374, no. 1, pp. 1–10, 1981, doi: 10.1111/j.1749-6632.1981.tb30854.x.

[32]   D. J. Lim, "Cochlear anatomy related to cochlear micromechanics. A review," *J. Acoust. Soc. Am.*, vol. 67, no. 5, pp. 1686–1695, 1980, doi: 10.1121/1.384295.

[33]   D. N. Furness and C. M. Hackney, "Cross-links between stereocilia in the guinea pig cochlea," *Hear. Res.*, vol. 18, no. 2, pp. 177–188, 1985, doi: 10.1016/0378-5955(85)90010-3.

[34]   J. O. Pickles, S. D. Comis, M. P. Osborne, D. N. Furness, and C. M. Hackney, "Cross-links between stereocilia in the guinea pig cochlea," *Hear. Res.*, vol. 18, no. 2, pp. 177–188, 1985, doi: 10.1016/0378-5955(85)90010-3.

[35]   J. Corwin, "Auditory Hair Cells: Structure, Function, Development, And Regeneration," *Annu. Rev. Neurosci.*, vol. 14, no. 1, pp. 301–333, 1991, doi: 10.1146/annurev.neuro.14.1.301.

[36]   A. Flock and D. Strelioff, "Graded and nonlinear mechanical properties of sensory hairs in the mammalian hearing organ," *Nature*, vol. 310, no. 5978, pp. 597–599, 1984, doi: 10.1038/310597a0.

[37]   A. C. Crawford and R. Fettiplace, "The mechanical properties of ciliary bundles of turtle cochlear hair cells.," *J. Physiol.*, vol. 364, no. 1, pp. 359–379, 1985, doi: 10.1113/jphysiol.1985.sp015750.

[38]   A. M. Dunn, O. S. Hofmann, B. Waters, and E. Witchel, "Cloaking malware with the trusted platform module," *Proceedings of the 20th USENIX Security Symposium*. pp. 395–410, 2011.

[39]   D. P. Corey and A. J. Hudspeth, "Kinetics of the receptor current in bullfrog saccular hair cells.," *J. Neurosci.*, vol. 3, no. 5, pp. 962–76, 1983.

[40]   D. P. Corey and A. J. Hudspeth, "Response latency of vertebrate hair cells,"

References

          Biophys. J., vol. 26, no. 3, pp. 499–506, 1979, doi: 10.1016/S0006-3495(79)85267-4.

[41]   S. S. Narayan, "Frequency Tuning of Basilar Membrane and Auditory Nerve Fibers in the Same Cochleae," *Science (80-.).*, vol. 282, no. 5395, pp. 1882–1884, 1998, doi: 10.1126/science.282.5395.1882.

[42]   D. P. Walker, "No Title," *Stud. Music. Sci. Late Renaiss.*, pp. 136–138., 1978.

[43]   G. Tartini Broude Brothers and pp. 4–5. 1967, "D.P. Walker," in *De' Principj dell' Armonia Musicale (Facsimile Edition of 1767 Padova book),* New York, 1767, pp. 4–5.

[44]   E. G. Walsh, "Experiments in Hearing," *Q. J. Exp. Physiol. Cogn. Med. Sci.*, vol. 45, no. 3, pp. 324–325, 1960, doi: 10.1113/expphysiol.1960.sp001484.

[45]   M. Mills, "Hearing aids and the history of electronics miniaturization," *IEEE Ann. Hist. Comput.*, vol. 33, no. 2, pp. 24–44, 2011, doi: 10.1109/MAHC.2011.43.

[46]   V. Nwadinobi, "Chapter eight hearing impairment," no. September, 2019.

[47]   Burkey, John M., *Overcoming Hearing Aid Fears : the road to better hearing*. Rutgers University Press New Brunswick, New Jersey, and London, 1959.

[48]   M. S. Almeida-Branco, S. Cabrera, and J. A. Lopez-Escamez, "Perspectives for the Treatment of Sensorineural Hearing Loss by Cellular Regeneration of the Inner Ear," *Acta Otorrinolaringol. (English Ed.*, vol. 66, no. 5, pp. 286–295, 2015, doi: 10.1016/j.otoeng.2015.08.006.

[49]   J. Agnew, "Acoustic Feedback and Other Audible Artifacts in Hearing Aids," *Trends Amplif.*, vol. 1, no. 2, pp. 45–82, 1996, doi: 10.1177/108471389600100202.

[50]   G. E. Moore, "Cramming more components onto integrated circuits, Reprinted from Electronics, volume 38, number 8, April 19, 1965, pp.114 ff.," *IEEE Solid-State Circuits Soc. Newsl.*, vol. 11, no. 3, pp. 33–35, 2009, doi: 10.1109/n-ssc.2006.4785860.

[51]   M. C. Killion and E. V. Carlson, "a Sbuminiature Condenser.Pdf," *Journal of the audio engineering society*, vol. 22, no. 4. pp. 237–243, 1974.

[52]   H. H. Kim and D. M. Barrs, "Hearing aids: A review of what's new," *Otolaryngol. - Head Neck Surg.*, vol. 134, no. 6, pp. 1043–1050, 2006, doi: 10.1016/j.otohns.2006.03.010.

[53]   M. T. Maltby, "Principles of Hearing Aid Audiology, Second Edition."

[54]   C. C. Sarli, R. M. Uchanski, A. Heidbreder, K. Readmond, and B. Spehar, "19Th-Century Camouflaged Mechanical Hearing Devices," *Otol. Neurotol.*,

vol. 24, no. 4, pp. 691–698, 2003, doi: 10.1097/00129492-200307000-00027.

[55] "APA Sarli, Cathy C.; Uchanski, Rosalie M.; Heidbreder, Arnold; Readmond, Kimberly; Spehar, Brent 19th-Century Camouflaged Mechanical Hearing Devices, Otology & Neurotology: July 2003 - Volume 24 - Issue 4 - p 691-698."

[56] S. D.G. Stephens & J. C. Goodwin, "Non-Electric Aids to Hearing: A Short History, Audiology," vol. 23, no. 2, pp. 215–240, 1984.

[57] P. Stark, L. Hickson, and P. Stark, "Outcomes of hearing aid fitting for older people with hearing impairment and their significant others Outcomes of hearing aid fitting for older people with hearing impairment and their Resultados de la adaptación de audífonos en," vol. 2027, 2009, doi: 10.1080/14992020400050050.

[58] C. D. Mulrow and M. R. Tuley, "Sustained Benefits of Hearing Aids," vol. 35, no. December 1992, pp. 1402–1405, 2016.

[59] M. M. Nafady and H. M. Bukhary, "Enhancement of solubility and release of ibuprofen from witepsol W35 suppository base by inclusion with lyophilized skimmed milk," *Int. J. Pharm. Pharm. Sci.*, vol. 5, no. SUPPL.1, pp. 376–382, 2013, doi: 10.1109/RBME.2008.2008250.

[60] N. K. Prenzler, E. Kludt, T. Giere, R. Salcher, T. Lenarz, and H. Maier, "Middle Ear Transducer : Long Term Stability of the Latest Generation T2," vol. 2019, 2019.

[61] M. H. Khosravi, A. Kouhi, S. Dabiri, P. Borghei, and M. Saeedi, "Cochlear Implants: An Excursus into the Technologies and Clinical Applications," *An Excursus into Hear. Loss*, 2018, doi: 10.5772/intechopen.74266.

[62] H. D.S., Y. J.A., W. G.B., and G. I. I. M.E., "Middle ear implantable hearing devices: An overview," *Trends Amplif.*, vol. 13, no. 3, pp. 206–214, 2009, doi: 10.1177/1084713809346262.

[63] S. T. Woo *et al.*, "A new trans-tympanic microphone approach for fully implantable hearing devices," *Sensors (Switzerland)*, vol. 15, no. 9, pp. 22798–22810, 2015, doi: 10.3390/s150922798.

[64] H. P. Zenner and H. Leysieffer, "Total implantation of the implex TICA hearing amplifier implant for high-frequency sensorineural hearing loss: The Tübingen University experience," *Otolaryngol. Clin. North Am.*, vol. 34, no. 2, pp. 417–446, 2001, doi: 10.1016/S0030-6665(05)70340-6.

[65] H. A. Jenkins *et al.*, "U.S. Phase I preliminary results of use of the Otologics MET Fully-Implantable Ossicular Stimulator," *Otolaryngol. - Head Neck Surg.*, vol. 137, no. 2, pp. 206–212, 2007, doi: 10.1016/j.otohns.2007.03.012.

[66] R. J. S. Briggs *et al.*, "Initial clinical experience with a totally implantable cochlear implant research device," *Otol. Neurotol.*, vol. 29, no. 2, pp. 114–119,

2008, doi: 10.1097/MAO.0b013e31814b242f.

[67]   Ian M. Smith., D. Cook, and B. P. Smith., *Second Edition Second Edition*, no. June. 2001.

[68]   N. Mehendale and sneha venkateshwar, "Smart hearing aid," *Technofocus*, vol. 4, no. October 2013, p. 38, 2013.

[69]   M. J. Goupell, D. Eisenberg, and K. DeRoy Milvae, "Dichotic listening performance with cochlear-implant simulations of ear asymmetry is consistent with difficulty ignoring clearer speech," *Attention, Perception, Psychophys.*, vol. 83, no. 5, pp. 2083–2101, 2021, doi: 10.3758/s13414-021-02244-x.

[70]   D. H. Kirkwood, "Hearing aid sales slip back to norm, but leaders see growth potential," *Hear. J.*, vol. 58, no. 12, pp. 11–20, 2005, doi: 10.1097/01.HJ.0000285903.40878.28.

[71]   R. Hampson, "Hearing aids," *Eur. Geriatr. Med.*, vol. 3, no. 3, pp. 198–200, 2012, doi: 10.1016/j.eurger.2012.03.003.

[72]   B. S. Kochkin, "10-Year Customer Satisfaction Trends," *Hear. Rev.*, vol. 9, no. 10, pp. 14–46, 2002.

[73]   R. M. Cox, "Assessment of subjective outcome of hearing aid fitting: Getting the client's point of view," *Int. J. Audiol.*, vol. 42, no. SUPPL. 1, 2003, doi: 10.3109/14992020309074629.

[74]   B. Edwards, "The Future of Hearing Aid Technology," *Trends Amplif.*, vol. 11, no. 1, pp. 31–45, 2007, doi: 10.1177/1084713806298004.

[75]   B. S. Kochkin, "MarkeTrak VII : Customer satisfaction with hearing," vol. 58, no. 9, 2005.

[76]   H. Dai, "Feedback Cancellation for Hearing Aids Fitted to Open Ear Canals," pp. 1606–1609.

[77]   J. H. Won, S. M. Schimmel, W. R. Drennan, P. E. Souza, L. Atlas, and J. T. Rubinstein, "Hearing Research," vol. 239, pp. 1–11, 2008, doi: 10.1016/j.heares.2008.01.009.

[78]   V. V. Pokropivny and V. V. Skorokhod, "New dimensionality classifications of nanostructures," *Phys. E Low-Dimensional Syst. Nanostructures*, vol. 40, no. 7, pp. 2521–2525, 2008, doi: 10.1016/j.physe.2007.11.023.

[79]   G. Oberdörster, E. Oberdörster, and J. Oberdörster, "NANOTOXICOLOGY : An Emerging Discipline Evolving from Studies of Ultrafine Particles Supplemental Web Sections," *Environ. Med.*

[80]   H. Qiao, L. Wang, J. Han, Y. Chen, D. Wang, and D. Li, "The mutual beneficial effect between medical imaging and nanomedicine," *J. Nanomater.*, vol. 2013,

2013, doi: 10.1155/2013/764095.

[81] C. R. Martin, "Membrane-based synthesis of nanomaterials," *Chem. Mater.*, vol. 8, no. 8, pp. 1739–1746, 1996, doi: 10.1021/cm960166s.

[82] V. L. Colvin, "The potential environmental impact of engineered nanomaterials," *Nat. Biotechnol.*, vol. 21, no. 10, pp. 1166–1170, 2003, doi: 10.1038/nbt875.

[83] C. R. Martin, "Nanomaterials : A Membrane-Based Synthetic Approach," vol. 266, no. December, 1994.

[84] R. Freitas, "Volume I: Basic Capabilities Return to Nanomedicine Book Site Nanomedicine," *Landes Biosci.*, vol. I, 1999.

[85] J. J. Davis, K. S. Coleman, B. R. Azamian, C. B. Bagshaw, and M. L. H. Green, "Chemical and biochemical sensing with modified single walled carbon nanotubes," *Chem. - A Eur. J.*, vol. 9, no. 16, pp. 3732–3739, 2003, doi: 10.1002/chem.200304872.

[86] S. Sotiropoulou, V. Gavalas, V. Vamvakaki, and N. A. Chaniotakis, "Novel carbon materials in biosensor systems," *Biosens. Bioelectron.*, vol. 18, no. 2–3, pp. 211–215, 2002, doi: 10.1016/S0956-5663(02)00183-5.

[87] D. N. Nguyen and W. Moon, "Piezoelectric polymer microfiber-based composite for the flexible ultra-sensitive pressure sensor," *J. Appl. Polym. Sci.*, vol. 137, no. 29, 2020, doi: 10.1002/app.48884.

[88] J. Wang, "Nanoparticle-based electrochemical DNA detection," *Anal. Chim. Acta*, vol. 500, no. 1–2, pp. 247–257, 2003, doi: 10.1016/S0003-2670(03)00725-6.

[89] E. Katz, I. Willner, and J. Wang, "Electroanalytical and Bioelectroanalytical Systems Based on Metal and Semiconductor Nanoparticles," *Electroanalysis*, vol. 16, no. 1–2, pp. 19–44, 2004, doi: 10.1002/elan.200302930.

[90] X. Luo, A. Morrin, A. J. Killard, and M. R. Smyth, "Application of nanoparticles in electrochemical sensors and biosensors," *Electroanalysis*, vol. 18, no. 4, pp. 319–326, 2006, doi: 10.1002/elan.200503415.

[91] Y. Huang, W. Zhang, H. Xiao, and G. Li, "An electrochemical investigation of glucose oxidase at a CdS nanoparticles modified electrode," *Biosens. Bioelectron.*, vol. 21, no. 5, pp. 817–821, 2005, doi: 10.1016/j.bios.2005.01.012.

[92] J. Wang, G. Liu, R. Polsky, and A. Merkoçi, "Electrochemical stripping detection of DNA hybridization based on cadmium sulfide nanoparticle tags," *Electrochem. commun.*, vol. 4, no. 9, pp. 722–726, 2002, doi: 10.1016/S1388-2481(02)00434-4.

References

[93] A. Merkoçi, M. Aldavert, S. Marín, and S. Alegret, "New materials for electrochemical sensing V: Nanoparticles for DNA labeling," *TrAC - Trends Anal. Chem.*, vol. 24, no. 4, pp. 341–349, 2005, doi: 10.1016/j.trac.2004.11.007.

[94] E. Stern *et al.*, "Label-free immunodetection with CMOS-compatible semiconducting nanowires," *Nature*, vol. 445, no. 7127, pp. 519–522, 2007, doi: 10.1038/nature05498.

[95] Y. Cui, Q. Wei, H. Park, and C. M. Lieber, "Nanowire nanosensors for highly sensitive and selective detection of biological and chemical species," *Science (80-.).*, vol. 293, no. 5533, pp. 1289–1292, 2001, doi: 10.1126/science.1062711.

[96] S. Ramanathan, S. Patibandla, S. Bandyopadhyay, J. D. Edwards, and J. Anderson, "Fluorescence and infrared spectroscopy of electrochemically self assembled ZnO nanowires: Evidence of the quantum confined Stark effect," *J. Mater. Sci. Mater. Electron.*, vol. 17, no. 9, pp. 651–655, 2006, doi: 10.1007/s10854-006-0021-4.

[97] A. V. Kabashin *et al.*, "Plasmonic nanorod metamaterials for biosensing," *Nat. Mater.*, vol. 8, no. 11, pp. 867–871, 2009, doi: 10.1038/nmat2546.

[98] C. K. O.T. Wolf, B.M. Kudielka, D.H. Hellhammer, J. Hellhammer, "Opposing effects of DHEA replacement in elderly subjects on declarative memory and attention after exposure to a laboratory stressor," *Psychoneuroendocrinology*, vol. 23, pp. 617–629, 1999.

[99] E. L. Wagner and J. B. Shin, "Mechanisms of Hair Cell Damage and Repair," *Trends Neurosci.*, vol. 42, no. 6, pp. 414–424, 2019, doi: 10.1016/j.tins.2019.03.006.

[100] Z. Wang, M. Gerstein, and M. Snyder, "Nrg2484-1," *Nat. Rev. | Genet.*, vol. VOLUME 10, no. jANUARy 2009, pp. 57–63, 2009.

[101] X. Shi and C. H. Cheng, "Artificial hair cell sensors using liquid metal alloy as piezoresistors," *8th Annu. IEEE Int. Conf. Nano/Micro Eng. Mol. Syst. IEEE NEMS 2013*, vol. 1, pp. 978–981, 2013, doi: 10.1109/NEMS.2013.6559886.

[102] M. R. Maschmann *et al.*, "Bioinspired carbon nanotube fuzzy fiber hair sensor for air-flow detection," *Adv. Mater.*, vol. 26, no. 20, pp. 3230–3234, 2014, doi: 10.1002/adma.201305285.

[103] J. E. Han, D. Kim, and K. S. Yun, "All-polymer hair structure with embedded three-dimensional piezoresistive force sensors," *Sensors Actuators, A Phys.*, vol. 188, pp. 89–94, 2012, doi: 10.1016/j.sna.2012.03.045.

[104] N. Chen, C. Tucker, J. M. Engel, Y. Yang, S. Pandya, and C. Liu, "Design and characterization of artificial haircell sensor for flow sensing with ultrahigh velocity and angular sensitivity," *J. Microelectromechanical Syst.*, vol. 16, no.

References

5, pp. 999–1014, 2007, doi: 10.1109/JMEMS.2007.902436.

[105] A. G. P. Kottapalli, M. Asadnia, J. M. Miao, G. Barbastathis, and M. S. Triantafyllou, "A flexible liquid crystal polymer MEMS pressure sensor array for fish-like underwater sensing," *Smart Mater. Struct.*, vol. 21, no. 11, 2012, doi: 10.1088/0964-1726/21/11/115030.

[106] Y. Bian, Y. Zhang, and X. Xia, "Design and Fabrication of a Multi-electrode Metal-core Piezoelectric Fiber and Its Application as an Airflow Sensor," *J. Bionic Eng.*, vol. 13, no. 3, pp. 416–425, 2016, doi: 10.1016/S1672-6529(16)60314-1.

[107] H. Droogendijk, M. J. De Boer, R. G. P. Sanders, and G. J. M. Krijnen, "A biomimetic accelerometer inspired by the cricket's clavate hair," *J. R. Soc. Interface*, vol. 11, no. 97, 2014, doi: 10.1098/rsif.2014.0438.

[108] A. Alfadhel, B. Li, A. Zaher, O. Yassine, and J. Kosel, "A magnetic nanocomposite for biomimetic flow sensing," *Lab Chip*, vol. 14, no. 22, pp. 4362–4369, 2014, doi: 10.1039/c4lc00821a.

[109] Z. Han *et al.*, "Artificial Hair-Like Sensors Inspired from Nature: A Review," *J. Bionic Eng.*, vol. 15, no. 3, pp. 409–434, 2018, doi: 10.1007/s42235-018-0033-9.

[110] J. T. Muth *et al.*, "Embedded 3D printing of strain sensors within highly stretchable elastomers," *Adv. Mater.*, vol. 26, no. 36, pp. 6307–6312, 2014, doi: 10.1002/adma.201400334.

[111] Ninla Elmawati Falabiba *et al.*, "済無No Title No Title No Title," *Pap. Knowl. . Towar. a Media Hist. Doc.*, vol. 5, no. 2, pp. 40–51, 2014.

[112] Sang-Soo Je, "MICRO DEVICES FOR HEARING AID APPLICATIONS."

[113] N. Mukherjee, A. Shukla, R. D. Roseman, and D. F. Thompson, "Experimental determination of bending resonances of millimeter size PVF2 cantilevers," *Sensors*, vol. 3, no. 7, pp. 263–275, 2003, doi: 10.3390/s30700263.

[114] S. Hur, J. H. Kwak, Y. Jung, and Y. H. Lee, "Biomimetic acoustic sensor based on piezoelectric cantilever array," *IEICE Electron. Express*, vol. 9, no. 11, pp. 945–950, 2012, doi: 10.1587/elex.9.945.

[115] R. Latif, M. M. Noor, J. Yunas, and A. A. Hamzah, *Mechanical energy sensing and harvesting in micromachined polymer-based piezoelectric transducers for fully implanted hearing systems: A review*, vol. 13, no. 14. 2021.

[116] H. Kreft and W. Jetz, "Global patterns and determinants of vascular plant diversity," *Proc. Natl. Acad. Sci. U. S. A.*, vol. 104, no. 14, pp. 5925–5930, 2007, doi: 10.1073/pnas.0608361104.

[117] Q. Shao *et al.*, "High-performance and tailorable pressure sensor based on

ultrathin conductive polymer film," *Small*, vol. 10, no. 8, pp. 1466–1472, 2014, doi: 10.1002/smll.201303601.

[118] P. J. Chen, D. C. Rodger, S. Saati, M. S. Humayun, and Y. C. Tai, "Microfabricated implantable parylene-based wireless passive intraocular pressure sensors," *J. Microelectromechanical Syst.*, vol. 17, no. 6, pp. 1342–1351, 2008, doi: 10.1109/JMEMS.2008.2004945.

[119] H. Lee, B. P. Lee, and P. B. Messersmith, "A reversible wet/dry adhesive inspired by mussels and geckos," *Nature*, vol. 448, no. 7151, pp. 338–341, 2007, doi: 10.1038/nature05968.

[120] Z. Pan, C. Yan, R. Peng, Y. Zhao, Y. He, and J. Ding, "Control of cell nucleus shapes via micropillar patterns," *Biomaterials*, vol. 33, no. 6, pp. 1730–1735, 2012, doi: 10.1016/j.biomaterials.2011.11.023.

[121] D. Chandra, S. Yang, A. A. Soshinsky, and R. J. Gambogi, "Biomimetic ultrathin whitening by capillary-force-induced random clustering of hydrogel micropillar arrays," *ACS Appl. Mater. Interfaces*, vol. 1, no. 8, pp. 1698–1704, 2009, doi: 10.1021/am900253z.

[122] H. J. Kim, S. H. Song, and S. H. Ahn, "A turtle-like swimming robot using a smart soft composite (SSC) structure," *Smart Mater. Struct.*, vol. 22, no. 1, 2013, doi: 10.1088/0964-1726/22/1/014007.

[123] N. Vogel *et al.*, "Color from hierarchy: Diverse optical properties of micron-sized spherical colloidal assemblies," *Proc. Natl. Acad. Sci. U. S. A.*, vol. 112, no. 35, pp. 10845–10850, 2015, doi: 10.1073/pnas.1506272112.

[124] K. Liu, X. Yao, and L. Jiang, "Recent developments in bio-inspired special wettability," *Chem. Soc. Rev.*, vol. 39, no. 8, pp. 3240–3255, 2010, doi: 10.1039/b917112f.

[125] S. Franssila, *Introduction to Microfabrication*. Director of Microelectronics Centre, Helsinki University of Technology, Finland.

[126] J. E. Park *et al.*, "Fabrication and applications of stimuli-responsive micro/nanopillar arrays," *J. Polym. Sci.*, vol. 59, no. 14, pp. 1491–1517, 2021, doi: 10.1002/pol.20210311.

[127] B. Volland, F. Shi, P. Hudek, H. Heerlein, and I. W. Rangelow, "Dry etching with gas chopping without rippled sidewalls," *J. Vac. Sci. Technol. B Microelectron. Nanom. Struct.*, vol. 17, no. 6, p. 2768, 1999, doi: 10.1116/1.591061.

[128] I. W. Rangelow, "Critical tasks in high aspect ratio silicon dry etching for microelectromechanical systems," *J. Vac. Sci. Technol. A Vacuum, Surfaces, Film.*, vol. 21, no. 4, pp. 1550–1562, 2003, doi: 10.1116/1.1580488.

[129] E. W. Becker, W. Ehrfeld, P. Hagmann, A. Maner, and D. Münchmeyer,

"Fabrication of microstructures with high aspect ratios and great structural heights by synchrotron radiation lithography, galvanoforming, and plastic moulding (LIGA process)," *Microelectron. Eng.*, vol. 4, no. 1, pp. 35–56, 1986, doi: 10.1016/0167-9317(86)90004-3.

[130] C. K. Malek and V. Saile, "Applications of LIGA technology to precision manufacturing of high-aspect-ratio micro-components and -systems: A review," *Microelectronics J.*, vol. 35, no. 2, pp. 131–143, 2004, doi: 10.1016/j.mejo.2003.10.003.

[131] R. F. W. Pease, "Electron beam ilthography," *Contemp. Phys.*, vol. 22, no. 3, pp. 265–290, 1981, doi: 10.1080/00107518108231531.

[132] A. A. Leonardi, M. J. Lo Faro, and A. Irrera, "Silicon nanowires synthesis by metal-assisted chemical etching: A review," *Nanomaterials*, vol. 11, no. 2, pp. 1–24, 2021, doi: 10.3390/nano11020383.

[133] Y. Hu *et al.*, "Laser printing hierarchical structures with the aid of controlled capillary-driven self-assembly," *Proc. Natl. Acad. Sci. U. S. A.*, vol. 112, no. 22, pp. 6876–6881, 2015, doi: 10.1073/pnas.1503861112.

[134] C. Maibohm, O. F. Silvestre, J. Borme, M. Sinou, K. Heggarty, and J. B. Nieder, "Multi-beam two-photon polymerization for fast large area 3D periodic structure fabrication for bioapplications," *Sci. Rep.*, vol. 10, no. 1, pp. 1–10, 2020, doi: 10.1038/s41598-020-64955-9.

[135] D. Bäuerle, R. Denk, J. D. Pedarnig, K. Piglmayer, J. Heitz, and G. Schrems, "Perspectives of laser processing and chemistry," *Appl. Phys. A Mater. Sci. Process.*, vol. 77, no. 2, pp. 203–207, 2003, doi: 10.1007/s00339-003-2155-z.

[136] J. H. Daniel, A. Sawant, M. Teepe, C. Shih, R. A. Street, and L. E. Antonuk, "Fabrication of high aspect-ratio polymer microstructures for large-area electronic portal X-ray imagers," *Sensors Actuators, A Phys.*, vol. 140, no. 2, pp. 185–193, 2007, doi: 10.1016/j.sna.2007.06.027.

[137] J. H. Park, S. O. Choi, S. Seo, Y. Bin Choy, and M. R. Prausnitz, "A microneedle roller for transdermal drug delivery," *Eur. J. Pharm. Biopharm.*, vol. 76, no. 2, pp. 282–289, 2010, doi: 10.1016/j.ejpb.2010.07.001.

[138] R. Zhang, A. Liberski, F. Khan, J. J. Diaz-Mochon, and M. Bradley, "Inkjet fabrication of hydrogel microarrays using in situ nanolitre-scale polymerisation," *Chem. Commun.*, no. 11, pp. 1317–1319, 2008, doi: 10.1039/b717932d.

[139] B. J. De Gans and U. S. Schubert, "Inkjet printing of well-defined polymer dots and arrays," *Langmuir*, vol. 20, no. 18, pp. 7789–7793, 2004, doi: 10.1021/la049469o.

[140] J. J. Dong *et al.*, "Controllable growth of highly ordered ZnO nanorod arrays via inverted self-assembled monolayer template," *ACS Appl. Mater.*

Interfaces, vol. 3, no. 11, pp. 4388–4395, 2011, doi: 10.1021/am2010288.

[141] P. Abgrall and A. Gu, "Lab-on-chip technologies : making a microfluidic network and coupling it into a complete microsystem — a review," 2007, doi: 10.1088/0960-1317/17/5/R01.

[142] V. Jokinen *et al.*, "Basic Neuroscience A microfluidic chip for axonal isolation and electrophysiological measurements," *J. Neurosci. Methods*, vol. 212, no. 2, pp. 276–282, 2013, doi: 10.1016/j.jneumeth.2012.10.013.

[143] A. A. Tseng, K. Chen, C. D. Chen, and K. J. Ma, "Electron beam lithography in nanoscale fabrication: Recent development," *IEEE Trans. Electron. Packag. Manuf.*, vol. 26, no. 2, pp. 141–149, 2003, doi: 10.1109/TEPM.2003.817714.

[144] G. Marin, "Inclined lithography and photoresist optimization for fabrication of 3D mesh structures," 2014.

[145] J. Nilsson, M. Evander, B. Hammarström, and T. Laurell, "Analytica Chimica Acta Review of cell and particle trapping in microfluidic systems," vol. 649, pp. 141–157, 2009, doi: 10.1016/j.aca.2009.07.017.

[146] W. H. Grover, A. M. Skelley, C. N. Liu, E. T. Lagally, and R. A. Mathies, "Monolithic membrane valves and diaphragm pumps for practical large-scale integration into glass micro ‾ uidic devices," vol. 89, pp. 315–323, 2003, doi: 10.1016/S0925-4005(02)00468-9.

[147] *Semiconductor Lithography: Principles, Practices, and Materials*. .

[148] M. J. Madou, *Manufacturing Techniques for Microfabrication and Nanotechnology*. 2011.

[149] V. Linder, H. Wu, X. Jiang, and G. M. Whitesides, "Rapid prototyping of 2D structures with feature sizes larger than 8 μm," *Anal. Chem.*, vol. 75, no. 10, pp. 2522–2527, 2003, doi: 10.1021/ac026441d.

[150] J. C. McDonald and G. M. Whitesides, "Poly(dimethylsiloxane) as a material for fabricating microfluidic devices," *Acc. Chem. Res.*, vol. 35, no. 7, pp. 491–499, 2002, doi: 10.1021/ar010110q.

[151] M. W. Montgomery, "Photomask Technology 2010," vol. 7823, no. September, 2010.

[152] A. Del Campo and C. Greiner, "SU-8: A photoresist for high-aspect-ratio and 3D submicron lithography," *J. Micromechanics Microengineering*, vol. 17, no. 6, 2007, doi: 10.1088/0960-1317/17/6/R01.

[153] W. H. Teh, U. Dürig, U. Drechsler, C. G. Smith, and H. J. Güntherodt, "Effect of low numerical-aperture femtosecond two-photon absorption on (SU-8) resist for ultrahigh-aspect-ratio microstereolithography," *J. Appl. Phys.*, vol. 97, no. 5, 2005, doi: 10.1063/1.1856214.

References

[154] R. W. Jaszewski, H. Schift, P. Gröning, and G. Margaritondo, "Properties of thin anti-adhesive films used for the replication of microstructures in polymers," *Microelectron. Eng.*, vol. 35, no. 1–4, pp. 381–384, 1997, doi: 10.1016/S0167-9317(96)00203-1.

[155] J. Takahashi, *An Introduction to the Theory of Social Control*, vol. 11, no. 2. 1960.

[156] N. Galopin, "Modelling and characterisation of smart materials for the design of magneto-electric devices," Université Paris Sud-Paris, 2007.

[157] Y. Cui *et al.*, "Lead-free (Ba 0.85Ca 0.15)(Ti 0.9Zr 0.1)O 3-CeO 2 ceramics with high piezoelectric coefficient obtained by low-temperature sintering," *Ceram. Int.*, vol. 38, no. 6, pp. 4761–4764, 2012, doi: 10.1016/j.ceramint.2012.02.063.

[158] B. Jaffe, *Piezoelectric ceramics. Vol. 3. Elsevier*. 2012.

[159] W. G. Cady, "'Piezoelectricity (McGraw-Hill, New York.,'" 1946.

[160] J. M. Herbert, "'Ferroelectric Transducers and Sensors;.' New York (1982).," *Gordon Breach Sci. Publ.*, 1982.

[161] S. L. Swartz, "'Topics in electronic ceramics.,'" *IEEE Trans. Electr. Insul. 25.5*, pp. 935–987, 1990.

[162] B. Gusarov, "PVDF piezoelectric polymers : characterization and application to thermal energy harvesting PVDF polymères piézoélectriques : caractérisation et application pour la récupération d ' énergie thermique," 2015.

[163] S. Committee, I. Ultrasonics, and F. C. Society, "An American National Standard: IEEE Standard on Piezoelectricity," *IEEE Trans. Sonics Ultrason.*, vol. 31, no. 2, pp. 8–10, 1984, doi: 10.1109/T-SU.1984.31464.

[164] Q. Zheng, B. Shi, Z. Li, and Z. L. Wang, "Recent Progress on Piezoelectric and Triboelectric Energy Harvesters in Biomedical Systems," pp. 1–23, 2017, doi: 10.1002/advs.201700029.

[165] A. H. Rajabi, M. Jaffe, and T. L. Arinzeh, "Acta Biomaterialia Piezoelectric materials for tissue regeneration : A review," *Acta Biomater.*, vol. 24, pp. 12–23, 2015, doi: 10.1016/j.actbio.2015.07.010.

[166] P. Martins, A. C. Lopes, and S. Lanceros-mendez, "Progress in Polymer Science Electroactive phases of poly (vinylidene fluoride): Determination , processing and applications," *Prog. Polym. Sci.*, vol. 39, no. 4, pp. 683–706, 2014, doi: 10.1016/j.progpolymsci.2013.07.006.

[167] M. Acosta *et al.*, "BaTiO3-based piezoelectrics: Fundamentals, current status, and perspectives," *Appl. Phys. Rev.*, vol. 4, no. 4, 2017, doi:

10.1063/1.4990046.

[168] C. Ribeiro, V. Sencadas, D. M. Correia, and S. Lanceros-Méndez, "Piezoelectric polymers as biomaterials for tissue engineering applications," *Colloids Surfaces B Biointerfaces*, vol. 136, pp. 46–55, 2015, doi: 10.1016/j.colsurfb.2015.08.043.

[169] V. F. Cardoso, D. M. Correia, C. Ribeiro, M. M. Fernandes, and S. Lanceros-Méndez, "Fluorinated polymers as smart materials for advanced biomedical applications," *Polymers (Basel).*, vol. 10, no. 2, pp. 1–26, 2018, doi: 10.3390/polym10020161.

[170] T. Soulestin, V. Ladmiral, F. D. Dos Santos, and B. Améduri, "Vinylidene fluoride- and trifluoroethylene-containing fluorinated electroactive copolymers. How does chemistry impact properties?," *Prog. Polym. Sci.*, vol. 72, pp. 16–60, 2017, doi: 10.1016/j.progpolymsci.2017.04.004.

[171] Y. S. Lee, G. Collins, and T. Livingston Arinzeh, "Neurite extension of primary neurons on electrospun piezoelectric scaffolds," *Acta Biomater.*, vol. 7, no. 11, pp. 3877–3886, 2011, doi: 10.1016/j.actbio.2011.07.013.

[172] and S. L.-M. Martins, P. (2014). a. C. Lopes, "Electroactive phases of poly (vinylidene fluoride): Determination, processing and applications," *Prog. Polym. Sci*, vol. 39, no. 4, pp. 683–706.

[173] J. W. Judy, "Microelectromechanical systems (MEMS): fabrication , design and," vol. 10, pp. 1115–1134, 2001, doi: 10.1088/0964-1726/10/6/301.

[174] F. R. Fan, W. Tang, and Z. L. Wang, "Flexible Nanogenerators for Energy Harvesting and Self-Powered Electronics," *Adv. Mater.*, vol. 28, no. 22, pp. 4283–4305, 2016, doi: 10.1002/adma.201504299.

[175] C. M. Wu and M. H. Chou, "Polymorphism, piezoelectricity and sound absorption of electrospun PVDF membranes with and without carbon nanotubes," *Compos. Sci. Technol.*, vol. 127, pp. 127–133, 2016, doi: 10.1016/j.compscitech.2016.03.001.

[176] E. L. V. Lewis and I. M. Ward, "A study of the mechanical anisotropy in shear of high-draw, low-draw, and voided poly(vinylidene fluoride)," *J. Polym. Sci. Part B Polym. Phys.*, vol. 27, no. 7, pp. 1375–1388, 1989, doi: 10.1002/polb.1989.090270701.

[177] A. G. Holmes-Siedle, P. D. Wilson, and A. P. Verrall, "PVdF: An electronically-active polymer for industry," *Mater. Des.*, vol. 4, no. 6, pp. 910–918, 1983, doi: 10.1016/0261-3069(84)90003-7.

[178] L. Mateu and F. Moll, "<title>Review of energy harvesting techniques and applications for microelectronics (Keynote Address)</title>," *VLSI Circuits Syst. II*, vol. 5837, no. June 2005, pp. 359–373, 2005, doi: 10.1117/12.613046.

References

[179] B. Dutta, E. Kar, N. Bose, and S. Mukherjee, "Significant enhancement of the electroactive β-phase of PVDF by incorporating hydrothermally synthesized copper oxide nanoparticles," *RSC Adv.*, vol. 5, no. 127, pp. 105422–405434, 2015, doi: 10.1039/c5ra21903e.

[180] L. Ruan, X. Yao, Y. Chang, L. Zhou, G. Qin, and X. Zhang, "Properties and applications of the β phase poly(vinylidene fluoride)," *Polymers (Basel).*, vol. 10, no. 3, pp. 1–27, 2018, doi: 10.3390/polym10030228.

[181] S. Chen, K. Yao, F. E. H. Tay, and C. L. Liow, "Ferroelectric poly(vinylidene fluoride) thin films on Si substrate with the B phase promoted by hydrated magnesium nitrate," *J. Appl. Phys.*, vol. 102, no. 10, 2007, doi: 10.1063/1.2812702.

[182] R. Song, D. Yang, and L. He, "Effect of surface modification of nanosilica on crystallization, thermal and mechanical properties of poly(vinylidene fluoride)," *J. Mater. Sci.*, vol. 42, no. 20, pp. 8408–8417, 2007, doi: 10.1007/s10853-007-1787-3.

[183] D. Yang and Y. Chen, "B-Phase Formation of Poly(Vinylidene Fluoride) From the Melt Induced By Quenching," *J. Mater. Sci. Lett.*, vol. 6, no. 5, pp. 599–603, 1987, doi: 10.1007/BF01739296.

[184] W. W. Doll and J. B. Lando, "The Polymorphism of Poly(vinylidene fluoride) IV. the Structure of High-Pressure-Crystallized Poly(vinylidene fluoride)," *J. Macromol. Sci. Part B*, vol. 4, no. 4, pp. 889–896, 1970, doi: 10.1080/00222347008217130.

[185] C. Wan and C. R. Bowen, "Multiscale-structuring of polyvinylidene fluoride for energy harvesting: the impact of molecular-, micro- and macro-structure," *J. Mater. Chem. A*, vol. 5, no. 7, pp. 3091–3128, 2017, doi: 10.1039/c6ta09590a.

[186] Y. J. Yu and A. J. H. McGaughey, "Energy barriers for dipole moment flipping in PVDF-related ferroelectric polymers," *J. Chem. Phys.*, vol. 144, no. 1, 2016, doi: 10.1063/1.4939152.

[187] W. M. P. Jr, D. J. Luca, W. M. Prest, and D. J. Luca, "The morphology and thermal response of high - temperature – crystallized poly (vinylidene fluoride) The morphology and thermal response of high-temperature- crystallized poly (vinylidene fluoride)," vol. 4136, no. 1975, 2016, doi: 10.1063/1.321438.

[188] S. P. Bao, G. D. Liang, and S. C. Tjong, "Effect of mechanical stretching on electrical conductivity and positive temperature coefficient characteristics of poly(vinylidene fluoride)/carbon nanofiber composites prepared by non-solvent precipitation," *Carbon N. Y.*, vol. 49, no. 5, pp. 1758–1768, 2011, doi: 10.1016/j.carbon.2010.12.062.

[189] H. Kawai, "The Piezoelectricity of Poly (vinylidene Fluoride)," *Jpn. J. Appl. Phys.*, vol. 8, no. 7, pp. 975–976, 1969, doi: 10.1143/jjap.8.975.

References

[190] B. Mohammadi, A. A. Yousefi, and S. M. Bellah, "Effect of tensile strain rate and elongation on crystalline structure and piezoelectric properties of PVDF thin films," *Polym. Test.*, vol. 26, no. 1, pp. 42–50, 2007, doi: 10.1016/j.polymertesting.2006.08.003.

[191] T. Hattori, M. Kanaoka, and H. Ohigashi, "Improved piezoelectricity in thick lamellar β-form crystals of poly(vinylidene fluoride) crystallized under high pressure," *J. Appl. Phys.*, vol. 79, no. 4, pp. 2016–2022, 1996, doi: 10.1063/1.361055.

[192] A. You, M. A. Y. Be, and I. In, "Improved piezoelectricity in thick lamellar β-form crystals of poly (vinylidene fluoride) crystallized under high pressure," vol. 2016, no. November 1995, 2016.

[193] J. Martı, D. Zhao, T. Lenz, I. Katsouras, and D. M. De Leeuw, "Materials Horizons," pp. 408–414, 2017, doi: 10.1039/C7MH00007C.

[194] B. A. C. Rastogi and S. B. Desu, "Ferroelectric Poly (vinylidene fluoride) Thin Films Grown by Low-Pressure Chemical Vapor Polymerization," pp. 742–750, 2006, doi: 10.1002/cvde.200606505.

[195] M. Benz, W. B. Euler, and O. J. Gregory, "The Role of Solution Phase Water on the Deposition of Thin Films of Poly (vinylidene fluoride)," pp. 2682–2688, 2002.

[196] J. Joseph, M. Kumar, S. Tripathy, G. D. V. S. Kumar, S. G. Singh, and S. R. K. Vaniari, "A Highly Flexible Tactile Sensor with Self-Poled Electrospun PVDF Nanofiber," *Proc. IEEE Sensors*, vol. 2018-Octob, pp. 3–6, 2018, doi: 10.1109/ICSENS.2018.8589807.

[197] C. Chang, Y. Fuh, and L. Lin, "(c) (d) (a) (b)," pp. 1485–1488, 2009.

[198] M. Kitsara *et al.*, "Permanently hydrophilic, piezoelectric PVDF nanofibrous scaffolds promoting unaided electromechanical stimulation on osteoblasts," *Nanoscale*, vol. 11, no. 18, pp. 8906–8917, 2019, doi: 10.1039/c8nr10384d.

[199] G. K. Knopf, *Smart Biosensor Technology, Second Edition*.

[200] Y. Xin *et al.*, "The use of polyvinylidene fluoride (PVDF) films as sensors for vibration measurement: A brief review," *Ferroelectrics*, vol. 502, no. 1, pp. 28–42, 2016, doi: 10.1080/00150193.2016.1232582.

[201] P. Mehrotra, "Biosensors and their applications - A review," *J. Oral Biol. Craniofacial Res.*, vol. 6, no. 2, pp. 153–159, 2016, doi: 10.1016/j.jobcr.2015.12.002.

[202] F. Jianqing, Y. Huipin, and Z. Xingdong, "Promotion of osteogenesis by a piezoelectric biological ceramic," *Biomaterials*, vol. 18, no. 23, pp. 1531–1534, 1997, doi: 10.1016/S0142-9612(97)80004-X.

References

[203] Jiashi Yang, *An Introduction to the Theory of Piezoelectricity*, Second Edi. .

[204] S. H. Bae *et al.*, "Graphene-P(VDF-TrFE) multilayer film for flexible applications," *ACS Nano*, vol. 7, no. 4, pp. 3130–3138, 2013, doi: 10.1021/nn400848j.

[205] E. S. Cozza, O. Monticelli, and P. Cebe, "On the electrospinning of PVDF : influence of the experimental conditions on the nanofiber properties," no. March 2012, pp. 41–48, 2013, doi: 10.1002/pi.4314.

[206] B. Nw, "Wireless piezoelectric devices based on," pp. 17751–17760, 2018, doi: 10.1039/c8nr05292a.

[207] R. Khajavi, A. A. Yousefi, M. Abbasipour, and F. Razaghian, "Improving piezoelectric and pyroelectric properties of electrospun PVDF nanofibers using nanofillers for energy harvesting application," no. August 2018, pp. 279–291, 2019, doi: 10.1002/pat.4463.

[208] S. A. Haddadi, A. R. S. A, S. Talebi, S. Fattahpour, and M. Hasany, "Investigation of the E ff ect of Nanosilica on Rheological , Thermal , Mechanical , Structural , and Piezoelectric Properties of Poly (vinylidene fl uoride) Nano fi bers Fabricated Using an Electrospinning Technique," pp. 12596–12607, 2017, doi: 10.1021/acs.iecr.7b02622.

[209] M. Lee *et al.*, "A hybrid piezoelectric structure for wearable nanogenerators," *Adv. Mater.*, vol. 24, no. 13, pp. 1759–1764, 2012, doi: 10.1002/adma.201200150.

[210] L. L. Zhang, J. X. Liu, X. Q. Fang, and G. Q. Nie, "Surface effects on the scattering of compressional waves by a piezoelectric nano-cylinder," *J. Appl. Phys.*, vol. 115, no. 24, 2014, doi: 10.1063/1.4885059.

[211] Z. H. Lin, Y. Yang, J. M. Wu, Y. Liu, F. Zhang, and Z. L. Wang, "BaTiO3 nanotubes-based flexible and transparent nanogenerators," *J. Phys. Chem. Lett.*, vol. 3, no. 23, pp. 3599–3604, 2012, doi: 10.1021/jz301805f.

[212] K. S. Hong, H. Xu, H. Konishi, and X. Li, "Direct water splitting through vibrating piezoelectric microfibers in water," *J. Phys. Chem. Lett.*, vol. 1, no. 6, pp. 997–1002, 2010, doi: 10.1021/jz100027t.

[213] L. Gu *et al.*, "Flexible fiber nanogenerator with 209 v output voltage directly powers a light-emitting diode," *Nano Lett.*, vol. 13, no. 1, pp. 91–94, 2013, doi: 10.1021/nl303539c.

[214] X. Chen, S. Xu, N. Yao, and Y. Shi, "1.6 v nanogenerator for mechanical energy harvesting using PZT nanofibers," *Nano Lett.*, vol. 10, no. 6, pp. 2133–2137, 2010, doi: 10.1021/nl100812k.

[215] G. Zhu, A. C. Wang, Y. Liu, Y. Zhou, and Z. L. Wang, "Functional electrical stimulation by nanogenerator with 58 v output voltage," *Nano Lett.*, vol. 12, no.

References

6, pp. 3086–3090, 2012, doi: 10.1021/nl300972f.

[216] K. Y. Lee *et al.*, "P-Type Polymer-Hybridized High-Performance Piezoelectric Nanogenerators," 2012.

[217] Y. Hu, L. Lin, Y. Zhang, and Z. L. Wang, "Replacing a battery by a nanogenerator with 20 v output," *Adv. Mater.*, vol. 24, no. 1, pp. 110–114, 2012, doi: 10.1002/adma.201103727.

[218] E. Zampetti, A. Bearzotti, and A. Macagnano, "Flexible piezoelectric transducer based on electrospun PVDF nanofibers for sensing applications," *Procedia Eng.*, vol. 87, pp. 1509–1512, 2014, doi: 10.1016/j.proeng.2014.11.585.

[219] M. S. Jayalakshmy and J. Philip, "Pyroelectric figures of merit and associated properties of LiTaO 3/poly vinylidene difluoride nanocomposites for thermal/infrared sensing," *Sensors Actuators, A Phys.*, vol. 206, pp. 121–126, 2014, doi: 10.1016/j.sna.2013.12.004.

[220] A. V. Shirinov and W. K. Schomburg, "Pressure sensor from a PVDF film," *Sensors Actuators, A Phys.*, vol. 142, no. 1, pp. 48–55, 2008, doi: 10.1016/j.sna.2007.04.002.

[221] C. Wang, S. K. Lai, Z. C. Wang, J. M. Wang, W. Yang, and Y. Q. Ni, "A low-frequency, broadband and tri-hybrid energy harvester with septuple-stable nonlinearity-enhanced mechanical frequency up-conversion mechanism for powering portable electronics," *Nano Energy*, vol. 64, no. May, p. 103943, 2019, doi: 10.1016/j.nanoen.2019.103943.

[222] K. Fan, Z. Liu, H. Liu, L. Wang, Y. Zhu, and B. Yu, "Scavenging energy from human walking through a shoe-mounted piezoelectric harvester," *Appl. Phys. Lett.*, vol. 110, no. 14, 2017, doi: 10.1063/1.4979832.

[223] Y. Kuang and M. Zhu, "Characterisation of a knee-joint energy harvester powering a wireless communication sensing node," *Smart Mater. Struct.*, vol. 25, no. 5, 2016, doi: 10.1088/0964-1726/25/5/055013.

[224] J. Cao, W. Wang, S. Zhou, D. J. Inman, and J. Lin, "Nonlinear time-varying potential bistable energy harvesting from human motion," *Appl. Phys. Lett.*, vol. 107, no. 14, 2015, doi: 10.1063/1.4932947.

[225] K. Zhang, X. Wang, Y. Yang, and Z. L. Wang, "Hybridized Electromagnetic-Triboelectric Nanogenerator for Scavenging Biomechanical Energy for Sustainably Powering Wearable Electronics," *ACS Nano*, vol. 9, no. 4, pp. 3521–3529, 2015, doi: 10.1021/nn507455f.

[226] Y. Wu, X. Wang, Y. Yang, and Z. L. Wang, "Hybrid energy cell for harvesting mechanical energy from one motion using two approaches," *Nano Energy*, vol. 11, pp. 162–170, 2015, doi: 10.1016/j.nanoen.2014.10.035.

References

[227] M. G. Kang, W. S. Jung, C. Y. Kang, and S. J. Yoon, "Recent progress on PZT based piezoelectric energy harvesting technologies," *Actuators*, vol. 5, no. 1, 2016, doi: 10.3390/act5010005.

[228] A. You, M. A. Y. Be, and I. In, "Properties of aluminum nitride thin films for piezoelectric transducers and microwave filter applications," vol. 3032, no. March 1999, pp. 11–14, 2004.

[229] I. Introduction, "Characteristics Of Relaxor-based Piezoelectric Single Crystals For Ultrasonic Transducers - Ultrasonics, Ferroelectrics and Frequency Control, IEEE Transactions on," vol. 44, no. 5, pp. 1140–1147, 1997.

[230] S. Chu, T. Chen, I. Tsai, and W. Water, "Doping effects of Nb additives on the piezoelectric and dielectric properties of PZT ceramics and its application on SAW device," vol. 113, pp. 198–203, 2004, doi: 10.1016/j.sna.2004.02.020.

[231] I. Tang, H. Chen, W. C. Hwang, Y. C. Wang, M. Houng, and Y. Wang, "Applications of piezoelectric ZnO film deposited on diamond-like carbon coated onto Si substrate under fabricated diamond SAW filter," vol. 262, pp. 461–466, 2004, doi: 10.1016/j.jcrysgro.2003.10.081.

[232] Y. Jiang, Z. Ma, J. Fu, and D. Zhang, "Development of a flexible artificial lateral line canal system for hydrodynamic pressure detection," *Sensors (Switzerland)*, vol. 17, no. 6, 2017, doi: 10.3390/s17061220.

[233] Z. Pi, J. Zhang, C. Wen, Z. bin Zhang, and D. Wu, "Flexible piezoelectric nanogenerator made of poly(vinylidenefluoride-co-trifluoroethylene) (PVDF-TrFE) thin film," *Nano Energy*, vol. 7, pp. 33–41, 2014, doi: 10.1016/j.nanoen.2014.04.016.

[234] Y. Cho *et al.*, "Enhanced energy harvesting based on surface morphology engineering of P(VDF-TrFE) film," *Nano Energy*, vol. 16, pp. 524–532, 2015, doi: 10.1016/j.nanoen.2015.07.006.

[235] V. Bhavanasi, V. Kumar, K. Parida, J. Wang, and P. S. Lee, "Enhanced Piezoelectric Energy Harvesting Performance of Flexible PVDF-TrFE Bilayer Films with Graphene Oxide," *ACS Appl. Mater. Interfaces*, vol. 8, no. 1, pp. 521–529, 2016, doi: 10.1021/acsami.5b09502.

[236] O. Oleshko *et al.*, "Biocompatibility and Antibacterial Properties of ZnO-Incorporated Anodic Oxide Coatings on TiZrNb Alloy," pp. 1–15.

[237] L. Wen, L. Chen, S. Zheng, J. Zeng, G. Duan, and Y. Wang, "Ultrasmall Biocompatible WO 3 − x Nanodots for Multi-Modality Imaging and Combined Therapy of Cancers," doi: 10.1002/adma.201506428.

[238] "Why is Titanium Biocompatible ?," vol. 11, no. 0981, p. 6597, 2012.

[239] F. Saleem, A. Khan, N. M. Mubarak, M. Khalid, and R. Walvekar, "Functionalized multi - walled carbon nanotubes and hydroxyapatite nanorods

reinforced with polypropylene for biomedical application," *Sci. Rep.*, pp. 1–10, 2021, doi: 10.1038/s41598-020-80767-3.

[240] M. Technology, "Lithium Chloride-Releasing 3D Printed Scaffold for Enhanced Cartilage Regeneration," pp. 4041–4050, 2019, doi: 10.12659/MSM.916918.

[241] G. B. Kim, C. U. Hong, and T. K. Kwon, "Vibration characteristics of piezoelectric lead zirconate titanate by fluid flow in intravascular oxygenator," *Japanese J. Appl. Physics, Part 1 Regul. Pap. Short Notes Rev. Pap.*, vol. 45, no. 4 B, pp. 3811–3817, 2006, doi: 10.1143/JJAP.45.3811.

[242] M. Toda and M. L. Thompson, "Contact-type vibration Sensors using curved clamped PVDF film," *IEEE Sens. J.*, vol. 6, no. 5, pp. 1170–1177, 2006, doi: 10.1109/JSEN.2006.881407.

[243] Y. Y. Chiu, W. Y. Lin, H. Y. Wang, S. Bin Huang, and M. H. Wu, "Development of a piezoelectric polyvinylidene fluoride (PVDF) polymer-based sensor patch for simultaneous heartbeat and respiration monitoring," *Sensors Actuators, A Phys.*, vol. 189, pp. 328–334, 2013, doi: 10.1016/j.sna.2012.10.021.

[244] and K. S. P. Won Kyu Lee, Gih Sung Chung, Hyun Jae Baek, "Heart sounds measurement using PVDF film sensor and their comparison with RR intervals of ECG signals," *Proc. IEEE-EMBS Int. Conf. Biomed. Heal. Informatics*, 2012.

[245] L. F. Brown and J. L. Mason, "Disposable PVDF ultrasonic transducers for nondestructive testing applications," *IEEE Trans. Ultrason. Ferroelectr. Freq. Control*, vol. 43, no. 4, pp. 560–568, 1996, doi: 10.1109/58.503716.

[246] W. Liu *et al.*, "A novel artificial hair receptor based on aligned PVDF micro/nano fibers," *2008 IEEE Int. Conf. Robot. Biomimetics, ROBIO 2008*, pp. 49–54, 2009, doi: 10.1109/ROBIO.2009.4912978.

[247] D. S. Li, L. Cheng, and C. M. Gosselin, "The design of structural acoustic sensors for active control of sound radiation into enclosures," *Smart Mater. Struct.*, vol. 13, no. 2, pp. 371–383, 2004, doi: 10.1088/0964-1726/13/2/016.

[248] E. P. Hong, M. K. Kim, I. Y. Park, S. H. Lee, Y. Roh, and J. H. Cho, "Vibration modeling and design of piezoelectric floating mass transducer for implantable middle ear hearing devices," *IEICE Trans. Fundam. Electron. Commun. Comput. Sci.*, vol. E90-A, no. 8, pp. 1620–1627, 2007, doi: 10.1093/ietfec/e90-a.8.1620.

[249] S. A. Saleh, H. Elsimary, A. Z. Mohamed, and H. F. Hamed, "Design of Piezoelectric Cantilever Microphone and Its MEMS- Acoustical Circuit for Hearing Aid Devices," pp. 897–900, 2006, doi: 10.1109/mwscas.2003.1562431.

[250] H. Tang, "MEMS Transducer for Hearing Aid Device," 2008.

[251] S. M. Damaraju, S. Wu, M. Jaffe, and T. L. Arinzeh, "Structural changes in

References

PVDF fibers due to electrospinning and its effect on biological function," *Biomed. Mater.*, vol. 8, no. 4, 2013, doi: 10.1088/1748-6041/8/4/045007.

[252] A. Koyuncuoğlu *et al.*, "Bulk PZT Cantilever Based MEMS Acoustic Transducer for Cochlear Implant Applications," *Proceedings*, vol. 1, no. 10, p. 584, 2017, doi: 10.3390/proceedings1040584.

[253] H. S. Lee *et al.*, "Flexible inorganic piezoelectric acoustic nanosensors for biomimetic artificial hair cells," *Adv. Funct. Mater.*, vol. 24, no. 44, pp. 6914–6921, 2014, doi: 10.1002/adfm.201402270.

[254] S. Tomioka *et al.*, "Lead – Zirconate – Titanate Acoustic Energy Harvesters with Dual Top Electrodes," 2011, doi: 10.1143/JJAP.50.09ND16.

[255] S. Tomioka *et al.*, "Lead-zirconate-titanate acoustic energy harvesters with dual top electrodes," *Jpn. J. Appl. Phys.*, vol. 50, no. 9 PART 3, 2011, doi: 10.1143/JJAP.50.09ND16.

[256] J. H. Han *et al.*, "Basilar membrane-inspired self-powered acoustic sensor enabled by highly sensitive multi tunable frequency band," *Nano Energy*, vol. 53, no. July, pp. 198–205, 2018, doi: 10.1016/j.nanoen.2018.08.053.

[257] T. Inaoka *et al.*, "Piezoelectric materials mimic the function of the cochlear sensory epithelium," *Proc. Natl. Acad. Sci.*, vol. 108, no. 45, pp. 18390–18395, 2011, doi: 10.1073/pnas.1110036108.

[258] J. Moersch, T. Hare, J. Mustard, R. Clark, and V. Hamilton, "417266a," vol. 417, no. May, pp. 266–269, 2002.

[259] T. Harada, S. Ito, and A. Tsukazaki, "Electric dipole effect in PdCoO2/β-Ga2O3 Schottky diodes for high-temperature operation," *Sci. Adv.*, vol. 5, no. 10, pp. 1–8, 2019, doi: 10.1126/sciadv.aax5733.

[260] T. Xu, M. Bachman, F. G. Zeng, and G. P. Li, "Polymeric micro-cantilever array for auditory front-end processing," *Sensors Actuators, A Phys.*, vol. 114, no. 2–3, pp. 176–182, 2004, doi: 10.1016/j.sna.2003.11.035.

[261] C. Mota *et al.*, "Design, fabrication and characterization of composite piezoelectric ultrafine fibers for cochlear stimulation," *Mater. Des.*, vol. 122, pp. 206–219, 2017, doi: 10.1016/j.matdes.2017.03.013.

[262] and A. V. Silver, Richard M., "'Photomask Metrology, Photomask Fabrication Technology.,'" pp. 281–342, 2005.

[263] N. Widjonarko, "Introduction to Advanced X-ray Diffraction Techniques for Polymeric Thin Films," *Coatings*, vol. 6, no. 4, p. 54, 2016, doi: 10.3390/coatings6040054.

[264] C. G. Pope, "X-ray diffraction and the bragg equation," *J. Chem. Educ.*, vol. 74, no. 1, pp. 129–131, 1997, doi: 10.1021/ed074p129.

References

[265] B. A. Pederson, "Structure and Regulation of Glycogen Synthase in the Brain," *Adv. Neurobiol.*, vol. 23, no. January 2010, pp. 83–123, 2019, doi: 10.1007/978-3-030-27480-1_3.

[266] A. Val, "Usage of Scherrer ' s formula in X-ray diffraction analysis of size distribution in systems of monocrystalline nanoparticles," pp. 1–9.

[267] A. A. Bunaciu, E. gabriela Udriştioiu, and H. Y. Aboul-Enein, "X-Ray Diffraction: Instrumentation and Applications," *Crit. Rev. Anal. Chem.*, vol. 45, no. 4, pp. 289–299, 2015, doi: 10.1080/10408347.2014.949616.

[268] D. C. Joy, "Scanning electron microscopy for materials characterization," *Curr. Opin. Solid State Mater. Sci.*, vol. 2, no. 4, pp. 465–468, 1997, doi: 10.1016/S1359-0286(97)80091-5.

[269] "Principles of Nanometrology." [Online]. Available: https://www.scribd.com/presentation/178475268/Principles-of-Nanometrology.

[270] D. Fields, "'What is transmission electron microscopy?.' News Medical Life Sciences (2019).," in *News Medical Life Sciences*, 2019.

[271] "Jurado, Susana B., and Miguel Ángel Petruccelli. 'Aplicaciones de la microscopía electrónica de transmisión en el diagnóstico microbiológico.' Analecta Veterinaria 25 (2005)."

[272] J. M. H. Brent Fultz, "1 . Diffraction and the X-Ray Powder," 2001, pp. 1–2.

[273] M. Chiu and E. Prenner, "Differential scanning calorimetry: An invaluable tool for a detailed thermodynamic characterization of macromolecules and their interactions," *J. Pharm. Bioallied Sci.*, vol. 3, no. 1, pp. 39–59, 2011, doi: 10.4103/0975-7406.76463.

[274] and G. G. Colomban, Philippe, *"Raman scattering theory and elements of Raman instrumentation." Raman Spectroscopy for Soft Matter Applications.* .

[275] T. B. Limbu, "Developing a Novel Approach for Layer Controlled Graphene Synthesis and Tailoring the Properties for Applications," no. August, 2017, doi: 10.13140/RG.2.2.26125.18407.

[276] V. Sencadas, C. Ribeiro, I. K. Bdikin, A. L. Kholkin, and S. Lanceros-Mendez, "Local piezoelectric response of single poly(vinylidene fluoride) electrospun fibers," *Phys. Status Solidi Appl. Mater. Sci.*, vol. 209, no. 12, pp. 2605–2609, 2012, doi: 10.1002/pssa.201228136.

[277] B. J. Rodriguez, A. Gruverman, A. I. Kingon, R. J. Nemanich, and O. Ambacher, "Piezoresponse force microscopy for polarity imaging of GaN," *Appl. Phys. Lett.*, vol. 80, no. 22, pp. 4166–4168, 2002, doi: 10.1063/1.1483117.

References

[278] S. S. Kwak *et al.*, "Triboelectrification-Induced Large Electric Power Generation from a Single Moving Droplet on Graphene/Polytetrafluoroethylene," *ACS Nano*, vol. 10, no. 8, pp. 7297–7302, 2016, doi: 10.1021/acsnano.6b03032.

[279] U. Khan, T. H. Kim, H. Ryu, W. Seung, and S. W. Kim, "Graphene Tribotronics for Electronic Skin and Touch Screen Applications," *Adv. Mater.*, vol. 29, no. 1, 2017, doi: 10.1002/adma.201603544.

[280] QuantumDesign, "Performing Van Der Pauw Resistivity Measurements," *Appl. Note 1076-304*, vol. 1, no. March, p. 3, 2007.

[281] T. Sultana, G. L. Georgiev, G. Auner, G. Newaz, H. J. Herfurth, and R. Patwa, "XPS analysis of laser transmission micro-joint between poly (vinylidene fluoride) and titanium," *Appl. Surf. Sci.*, vol. 255, no. 5 PART 2, pp. 2569–2573, 2008, doi: 10.1016/j.apsusc.2008.07.149.

[282] T. Mazoochi, M. Hamadanian, M. Ahmadi, and V. Jabbari, "Investigation on the morphological characteristics of nanofiberous membrane as electrospun in the different processing parameters," *Int. J. Ind. Chem.*, vol. 3, no. 1, pp. 1–8, 2012, doi: 10.1186/2228-5547-3-2.

[283] L. A. Can-Herrera, A. I. Oliva, M. A. A. Dzul-Cervantes, O. F. Pacheco-Salazar, and J. M. Cervantes-Uc, "Morphological and mechanical properties of electrospun polycaprolactone scaffolds: Effect of applied voltage," *Polymers (Basel).*, vol. 13, no. 4, pp. 1–16, 2021, doi: 10.3390/polym13040662.

[284] M. Nasir *et al.*, "Control of diameter, morphology, and structure of PVDF nanofiber fabricated by electrospray deposition," *J. Polym. Sci. Part B Polym. Phys.*, vol. 44, no. 5, pp. 779–786, 2006, doi: 10.1002/polb.20737.

[285] A. S. Motamedi, H. Mirzadeh, F. Hajiesmaeilbaigi, S. Bagheri-Khoulenjani, and M. Shokrgozar, "Effect of electrospinning parameters on morphological properties of PVDF nanofibrous scaffolds," *Prog. Biomater.*, vol. 6, no. 3, pp. 113–123, 2017, doi: 10.1007/s40204-017-0071-0.

[286] J. Bae, I. Baek, and H. Choi, "Efficacy of piezoelectric electrospun nanofiber membrane for water treatment," *Chem. Eng. J.*, vol. 307, pp. 670–678, 2017, doi: 10.1016/j.cej.2016.08.125.

[287] P. Sajkiewicz, A. Wasiak, and Z. Goclowski, "Phase transitions during stretching of poly(vinylidene fluoride)," *Eur. Polym. J.*, vol. 35, no. 3, pp. 423–429, 1999, doi: 10.1016/S0014-3057(98)00136-0.

[288] A. You, M. A. Y. Be, and I. In, "An infrared study of phase-III poly (vinylidene fluoride)," vol. 6106, no. July, 2008.

[289] T. Boccaccio, A. Bottino, G. Capannelli, and P. Piaggio, "Characterization of PVDF membranes by vibrational spectroscopy," *J. Memb. Sci.*, vol. 210, no. 2, pp. 315–329, 2002, doi: 10.1016/S0376-7388(02)00407-6.

References

[290] A. C. Lopes, C. M. Costa, C. J. Tavares, I. C. Neves, and S. Lanceros-Mendez, "Nucleation of the electroactive γ phase and enhancement of the optical transparency in low filler content poly(vinylidene)/clay nanocomposites," *J. Phys. Chem. C*, vol. 115, no. 37, pp. 18076–18082, 2011, doi: 10.1021/jp204513w.

[291] R. Gregorio, "Determination of the α, β, and γ crystalline phases of poly(vinylidene fluoride) films prepared at different conditions," *J. Appl. Polym. Sci.*, vol. 100, no. 4, pp. 3272–3279, 2006, doi: 10.1002/app.23137.

[292] L. E. Cross, "Ferroelectric materials for electromechanical transducer applications," *Mater. Chem. Phys.*, vol. 43, no. 2, pp. 108–115, 1996, doi: 10.1016/0254-0584(95)01617-4.

[293] Y. Xin *et al.*, "PVDF tactile sensors for detecting contact force and slip: A review," *Ferroelectrics*, vol. 504, no. 1, pp. 31–45, 2016, doi: 10.1080/00150193.2016.1238723.

[294] R. Gregorio, "Effect of crystalline phase , orientation and temperature on the dielectric properties of poly (vinylidene fluoride) (PVDF)," *J. Mater. Sci. 34 4489 – 4500*, no. September 1999, 2014, doi: 10.1023/A.

[295] Y. Zhu *et al.*, "Zwitterionic Nanohydrogel Grafted PVDF Membranes with Comprehensive Antifouling Property and Superior Cycle Stability for Oil-in-Water Emulsion Separation," *Adv. Funct. Mater.*, vol. 28, no. 40, pp. 1–10, 2018, doi: 10.1002/adfm.201804121.

[296] A. L. Cordeiro *et al.*, "Fluorination of poly(dimethylsiloxane) surfaces by low pressure CF 4 plasma - Physicochemical and antifouling properties," *Express Polym. Lett.*, vol. 3, no. 2, pp. 70–83, 2009, doi: 10.3144/expresspolymlett.2009.11.

[297] N. G. P. Chew, S. Zhao, C. Malde, and R. Wang, "Superoleophobic surface modification for robust membrane distillation performance," *J. Memb. Sci.*, vol. 541, no. June, pp. 162–173, 2017, doi: 10.1016/j.memsci.2017.06.089.

[298] M. Serhan *et al.*, "Total iron measurement in human serum with a smartphone," *AIChE Annu. Meet. Conf. Proc.*, vol. 2019-Novem, 2019, doi: 10.1039/x0xx00000x.

[299] J. H. Li, X. S. Shao, Q. Zhou, M. Z. Li, and Q. Q. Zhang, "The double effects of silver nanoparticles on the PVDF membrane: Surface hydrophilicity and antifouling performance," *Appl. Surf. Sci.*, vol. 265, pp. 663–670, 2013, doi: 10.1016/j.apsusc.2012.11.072.

[300] J. G. Gualtieri, J. A. Kosinski, and A. Ballato, "Piezoelectric Materials for Acoustic Wave Applications," *IEEE Trans. Ultrason. Ferroelectr. Freq. Control*, vol. 41, no. 1, pp. 53–59, 1994, doi: 10.1109/58.265820.

[301] Z. L. Wang, G. Zhu, Y. Yang, S. Wang, and C. Pan, "Progress in

nanogenerators for portable electronics," *Mater. Today*, vol. 15, no. 12, pp. 532–543, 2012, doi: 10.1016/S1369-7021(13)70011-7.

[302] K. Shimamura, H. Takeda, T. Kohno, and T. Fukuda, "Growth and characterization of lanthanum gallium silicate La3Ga5SiO14 single crystals for piezoelectric applications," *J. Cryst. Growth*, vol. 163, no. 4, pp. 388–392, 1996, doi: 10.1016/0022-0248(95)01002-5.

[303] A. Klimov *et al.*, "Magnetoelectric write and read operations in a stress-mediated multiferroic memory cell," *Appl. Phys. Lett.*, vol. 110, no. 22, 2017, doi: 10.1063/1.4983717.

[304] P. Paruch, T. Tybell, and J. M. Triscone, "Nanoscale control of ferroelectric polarization and domain size in epitaxial Pb(Zr0.2Ti0.8)O3 thin films," *Appl. Phys. Lett.*, vol. 79, no. 4, pp. 530–532, 2001, doi: 10.1063/1.1388024.

[305] D. T. Le *et al.*, "Effects of the domain size on local d33 in tetragonal (Na 0.53 K 0.45 Li 0.02)(Nb 0.8 Ta 0.2) O 3 ceramics," *J. Am. Ceram. Soc.*, vol. 96, no. 1, pp. 174–178, 2013, doi: 10.1111/j.1551-2916.2012.05445.x.

[306] P. Solutions, *An Introduction to Physical Properties*, vol. 3. 2002.

[307] M. LeMasurier and P. G. Gillespie, "Hair-cell mechanotransduction and cochlear amplification," *Neuron*, vol. 48, no. 3, pp. 403–415, 2005, doi: 10.1016/j.neuron.2005.10.017.

[308] A. A. Shah, Y. H. Cho, S. E. Nam, A. Park, Y. I. Park, and H. Park, "High performance thin-film nanocomposite forward osmosis membrane based on PVDF/bentonite nanofiber support," *J. Ind. Eng. Chem.*, vol. 86, no. February, pp. 90–99, 2020, doi: 10.1016/j.jiec.2020.02.016.

[309] H. Shao, J. Fang, H. Wang, and T. Lin, "RSC Advances concentrations on mechanical-to-electrical energy poly (vinylidene fl uoride) nano fi ber mats †," pp. 14345–14350, 2015, doi: 10.1039/c4ra16360e.

[310] G. Kalimuldina, N. Turdakyn, I. Abay, and A. Medeubayev, "Electrospinning and Its Applications," 2020.

[311] S. Huang *et al.*, "Electrospinning of polyvinylidene difluoride with carbon nanotubes: Synergistic effects of extensional force and interfacial interaction on crystalline structures," *Langmuir*, vol. 24, no. 23, pp. 13621–13626, 2008, doi: 10.1021/la8024183.

[312] C. V. Chanmal and J. P. Jog, "Electrospun PVDF/BaTiO3 nanocomposites: Polymorphism and thermal emissivity studies," *Int. J. Plast. Technol.*, vol. 15, no. 1, pp. 1–9, 2011, doi: 10.1007/s12588-011-9001-5.

[313] X. Zhang *et al.*, " An Extremely Simple Method for Protecting Lithium Anodes in Li-O 2 Batteries ," *Angew. Chemie*, vol. 130, no. 39, pp. 12996–13000, 2018, doi: 10.1002/ange.201807985.

References

[314] P. Martins, A. C. Lopes, and S. Lanceros-Mendez, "Electroactive phases of poly(vinylidene fluoride): Determination, processing and applications," *Prog. Polym. Sci.*, vol. 39, no. 4, pp. 683–706, 2014, doi: 10.1016/j.progpolymsci.2013.07.006.

[315] M. Zeyrek Ongun, S. Oguzlar, U. Kartal, M. Yurddaskal, and O. Cihanbegendi, "Energy harvesting nanogenerators: Electrospun β-PVDF nanofibers accompanying ZnO NPs and ZnO@Ag NPs," *Solid State Sci.*, vol. 122, no. November, p. 106772, 2021, doi: 10.1016/j.solidstatesciences.2021.106772.

[316] S. Wang, Y. Wan, B. Sun, L. Liu, and W. Xu, "Mechanical and electrical properties of electrospun PVDF / MWCNT ultrafine fibers using rotating collector," pp. 1–7, 2014.

[317] F. Mokhtari, M. Shamshirsaz, M. Latifi, and S. Asadi, "Comparative evaluation of piezoelectric response of electrospun PVDF (polyvinilydine fluoride) nanofiber with various additives for energy scavenging application," *J. Text. Inst.*, vol. 108, no. 6, pp. 906–914, 2017, doi: 10.1080/00405000.2016.1202091.

[318] K. Shi, B. Sun, X. Huang, and P. Jiang, "Synergistic effect of graphene nanosheet and BaTiO3 nanoparticles on performance enhancement of electrospun PVDF nanofiber mat for flexible piezoelectric nanogenerators," *Nano Energy*, vol. 52, no. May, pp. 153–162, 2018, doi: 10.1016/j.nanoen.2018.07.053.

[319] M. M. Abolhasani, K. Shirvanimoghaddam, and M. Naebe, "PVDF/graphene composite nanofibers with enhanced piezoelectric performance for development of robust nanogenerators," *Compos. Sci. Technol.*, vol. 138, pp. 49–56, 2017, doi: 10.1016/j.compscitech.2016.11.017.

[320] H. Yu, T. Huang, M. Lu, M. Mao, Q. Zhang, and H. Wang, "Enhanced power output of an electrospun PVDF/MWCNTs-based nanogenerator by tuning its conductivity," *Nanotechnology*, vol. 24, no. 40, 2013, doi: 10.1088/0957-4484/24/40/405401.

Appendix

Pattern: COD 2107312　Radiation: 1.54060　Quality: Quality Unknown

Formula	O3 W		
Name			
Name (mineral)			
Name (common)			

Lattice:	Orthorhombic	Mol. weight =	
S.G.:	P n m a (62)	Volume [CD] =	430.9
		Dx =	
		Dm =	
		I/Icor =	7.650

a = 7.57000
b = 7.34100
c = 7.75400
a/b = 1.03119　　Z = 8
c/b = 1.05626

Primary Reference
Salje E., "The orthorhombic phase of W O3", Acta Crystallographica B (24,1968-38,1982) 33 (1977) 574-577.

Filter	Not specified
d-spacing:	

Wavelength: 1.54060
SS/FOM:

d	2θ	I fix	h	k	l	d	2θ	I fix	h	k	l
3.8770	22.920	986	0	0	-2	1.6821	54.508	107	-4	-2	0
3.7850	23.485	958	-2	0	0	1.6796	54.596	20	-2	-1	-4
3.6705	24.229	999	0	-2	0	1.6718	54.872	7	-1	-2	-4
3.4508	25.797	7	-1	0	-2	1.6588	55.339	157	0	-4	-2
3.3642	26.473	159	-2	-1	0	1.6568	55.412	132	-4	-1	-2
3.1229	28.560	280	-1	-1	-2	1.6514	55.609	160	-2	-4	0
2.7083	33.049	452	-2	0	-2	1.6203	56.772	2	-1	-4	-2
2.6654	33.596	487	0	-2	-2	1.6001	57.555	27	-3	-3	-2
2.6350	33.995	489	-2	-2	0	1.5615	59.116	90	-2	-2	-4
2.5409	35.295	111	-2	-1	-2	1.5431	59.893	89	-4	-2	-2
2.5142	35.682	7	-1	-2	-2	1.5372	60.146	18	-3	0	-4
2.1793	41.398	300	-2	-2	-2	1.5193	60.930	149	-2	-4	-2
2.1149	42.720	14	-3	0	-2	1.5046	61.589	89	-3	-1	-4
2.0550	44.029	40	-2	-3	0	1.4970	61.936	58	-4	-3	0
2.0496	44.151	3	-2	-1	-3	1.4898	62.269	116	-1	-3	-4
2.0322	44.549	60	-3	-1	-2	1.4179	65.813	26	-3	-2	-4
1.9961	45.400	77	-1	-3	-2	1.4103	66.213	9	-5	0	-2
1.9385	46.828	113	0	0	-4	1.4101	66.223	12	-2	-3	-4
1.8925	48.037	116	-4	0	0	1.3965	66.953	71	-4	-3	-2
1.8779	48.434	5	-1	0	-4	1.3861	67.522	7	-3	-4	-2
1.8353	49.633	172	0	-4	0	1.3850	67.583	9	-5	-1	-2
1.8326	49.711	123	-4	-1	0	1.3688	68.493	10	-2	-5	0
1.8324	49.717	18	-3	-2	-2	1.3542	69.336	34	-4	0	-4
1.8193	50.099	238	-1	-1	-4	1.3510	69.524	20	-1	-5	-2
1.8157	50.206	40	-2	-3	-2	1.3327	70.620	54	0	-4	-4
1.7254	53.032	101	-2	0	-4	1.3317	70.681	38	-4	-1	-4
1.7141	53.409	101	0	-2	-4	1.3175	71.559	58	-4	-4	0
1.7007	53.864	97	-4	0	-2	1.3165	71.622	13	-5	-2	-2

Fig. A.1 The detailed 2θ information of the JCPDS for Sample P (PVDF/WO₃).

Pattern: COD 2300112   Radiation: 1.54060   Quality: Quality Unknown

Formula	O Zn						
		d	2θ	I fix	h	k	l
		2.81410	31.773	519	-1	0	0
		2.60270	34.430	397	0	0	-2
		2.47550	36.259	999	-1	0	-1
		1.91070	47.551	224	-1	0	-2
		1.62470	56.604	332	-2	1	0
		1.47690	62.875	305	-1	0	-3
		1.40700	66.388	48	-2	0	0
		1.37820	67.962	265	-2	1	-2
		1.35830	69.097	135	-2	0	-1
		1.30130	72.591	23	0	0	-4
		1.23770	76.978	43	-2	0	-2
		1.18120	81.405	25	-1	0	-4
		1.09290	89.630	97	-2	0	-3
		1.06360	92.811	34	-3	1	0
		1.04210	95.323	109	-3	1	-1
		1.01570	98.646	61	-2	1	-4

Lattice: Hexagonal
S.G.: P 63 m c (186)
Mol. weight =
Volume [CD] = 47.6
Dx =
Dm =
I/Icor = 7.120
a = 3.24940
c = 5.20540
a/t 1.00000   Z = 2
c/h 1.60196

Color: colourless: Temperature of data collection: 293.00 K:

Primary Reference
Sowa Heidrun, Ahsbahs Hans, "High-pressure X-ray investigation of zincite ZnO single crystals using diamond anvils with an improved shape", Journal of Applied Crystallography 39(2) (2006) 169-175.

Filter   Not specified
d-spacing:
Wavelength: 1.54060
SS/FOM:

Fig. A.2 The detailed 2θ information of the JCPDS for Sample Q (PVDF/ZnO).

Pattern: COD 1200017   Radiation: 1.54060   Quality: Quality Unknown

			d	2θ	I fix	h	k	l
Formula		C	3.39500	26.228	1000	0	0	-2
Name			2.13910	42.213	33	-1	0	0
Name (mineral)	Graphite 2H		2.04020	44.365	159	-1	0	-1
Name			1.80980	50.381	32	-1	0	-2
(common)			1.69750	53.974	61	0	0	-4
			1.55460	59.405	46	-1	0	-3
			1.32970	70.803	9	-1	0	-4
Lattice: Hexagonal	Mol. weight =		1.23500	77.177	44	-2	1	0
S.G.: P 63 m c (186)	Volume [CD] = 35.88		1.16060	83.167	68	-2	1	-2
	Dx =		1.14650	84.423	13	-1	0	-5
	Dm =		1.13170	85.790	11	0	0	-6
	I/Icor = 2.580		1.06950	92.149	3	-2	0	0
a = 2.47000			1.05650	93.623	9	-2	0	-1
c = 6.79000			1.02010	98.072	4	-2	0	-2

a = 2.47000

c = 6.79000

a/b = 1.00000   Z = 4

c/b = 2.74899

- from Kropfm}hl, Bavaria:

Primary Reference
Hassel O, "Ueber die Kristallstruktur des Graphits", Zeitschrift fuer Physik 25 (1924) 317-337.

Wavelength: 1.54060
SS/FOM:

Filter: Not specified
d-spacing:

Fig. A.3 The detailed 2θ information of the JCPDS for Sample R (PVDF/CNT).

Pattern: COD 1526931   Radiation: 1.54060   Quality: Quality Unknown

Formula	O2 Ti						
Name							
Name (mineral)							
Name (common)							

d	2θ	I fix	h	k	l
3.50140	25.418	999	-1	0	-1
2.41450	37.209	63	-1	0	-3
2.35750	38.143	202	0	0	-4
2.32100	38.766	67	-1	-1	-2
1.88550	48.226	269	-2	0	0
1.68680	54.344	164	-1	0	-5
1.66010	55.292	163	-2	-1	-1
1.48610	62.441	27	-2	-1	-3
1.47250	63.084	126	-2	0	-4
1.35400	69.348	50	-1	-1	-6
1.33320	70.589	59	-2	-2	0
1.26860	74.775	5	-1	0	-7
1.25710	75.579	88	-2	-1	-5
1.24600	76.372	24	-3	0	-1
1.17880	81.606	5	0	0	-8
1.16710	82.602	5	-3	0	-3
1.16050	83.175	44	-2	-2	-4
1.15610	83.563	16	-3	-1	-2
1.05260	94.076	5	-2	-1	-7
1.04600	94.855	21	-3	0	-5
1.03950	95.638	25	-3	-2	-1
1.00950	99.468	17	-1	0	-9

Lattice: Tetragonal
S.G.:   I 41/a m d (141)

Mol. weight =
Volume [CD] =   134.1
Dx =
Dm =
I/Icor =   5.290

a =   3.77100

c =   9.43000
a/b =   1.00000   Z =   4
c/h =   2.50066

Primary Reference
Weirich T.E., Winterer M., Seifried S., Fuess H., Hahn H., "Rietveld analysis of electron powder diffraction data from nanocrystalline anatase, Ti O2", Ultramicroscopy 81 (2000) 263-270.

Filter   Not specified
Wavelength: 1.54060
d-spacing:
SS/FOM:

Fig. A.4 The detailed 2θ information of the JCPDS for Sample S (PVDF/TiO₂).